Numerical Simulation of Turbulent Combustion in Situations Relevant to Scramjet Engine Propulsion

Fábio Henrique Eugênio Ribeiro

THESE

Pour l'obtention du Grade de

DOCTEUR DE L'ECOLE NATIONALE SUPERIEURE DE MECHANIQUE ET D'AEROTECHNIQUE

(Diplôme National - Arrêté du 25 mai 2016)

Ecole Doctorale :
Sciences et Ingénierie en Matériaux, Mécanique, Energétique

Secteur de Recherche : Energétique, Thermique, Combustion

Présentée par :

Fábio Henrique EUGÊNIO RIBEIRO

****

NUMERICAL SIMULATION OF TURBULENT COMBUSTION IN SITUATIONS RELEVANT TO SCRAMJET ENGINE PROPULSION

****

Directeur de thèse : Arnaud MURA

Co-encadrant : Vincent ROBIN

****

Soutenue le 8 mars 2019

devant la Commission d'Examen

****

JURY

Président :

M.	HALTER Fabien	Professeur - Université d'Orléans, France

Rapporteurs :

M.	HALTER Fabien	Professeur - Université d'Orléans, France
M.	BAI Xue-Song	Professeur - Université de Lund, Suède

Membres du jury :

M.	SABELNIKOV Vladimir	Directeur de recherche émérite - ONERA, Palaiseau, France
Mme.	LEITE Valéria	Chercheur - Instituto de Estudos Avançados, Brésil
Mme.	FORTUNE Véronique	Maître de conférences - Institut P', CNRS, Poitiers
M.	ROBIN Vincent	Maître de conférences - ISAE ENSMA, Institut P', Chasseneuil
M.	MURA Arnaud	Directeur de recherche - CNRS, Institut P', Chasseneuil

If I have seen further it is by standing on the shoulders of giants

Isaac Newton

Acknowledgements

First, I would like to thank God, who gave me strength, wisdom and health to overcome all the adversities encountered throughout my life.

I would like to thank my wife Vanessa, who always supported me and stayed with me in good and bad moments. Her love, fellowship and support was essential and I will be forever grateful for her patience during the development of this work.

To my parents, who always encouraged me to keep on studying. And my in-laws, for all the help with our life in Brazil during the course.

I wish to thank my advisor, Dr. Arnaud Mura, for all the dedication, patience and guidance through the years. His sense of organization and relentless dedication to contributing to and improving my overall academic expertise were invaluable and I bring with me not only the knowledge and skills acquired but the example to carry forward.

I would like to thank my co-advisor, Dr. Vincent Robin, for the means he put at my disposal to carry out this work, the enthusiasm and the advices.

Dra. Valéria Leite, my boss, tutor and friend at IEAv for her support and help with the administrative stuff there, and to have accepted to be part of the jury.

I want to thank professors Fabien Halter and Xue-Song Bai, who accepted to be reviewers this thesis and for their remarks which greatly helped me improve the quality of this manuscript. Also, Dr. Vladimir Sabelnikov and Dr. Véronique Fortuné, for accepting to be part of the jury.

My friends at the laboratory: Anthony Techer, Aimad Er-Raiy, Radouan Boukharfane and Song Zhao for many stimulating discussions on tricky technical issues. Jocelyne Bardeau, Marie Cannelle Eysseric and Audrey Veron for their support with all the administrative stuff. And also Zakaria Bouali, Nguyen Kha, Luis Carbajal, Marcos Onofre, Xiaodong Wang and Remy Dubois for their support and friendship.

Finally, I would like to acknowledge and thank the Brazilian Air Force and CNPq for the financial support. Also, this work was granted access to the HPC resources of CINES, IDRIS and TGCC under the allocations x20152b7456 and i20152b7251.

Table of contents

List of tables

List of figures

Symbols and Abbreviations

Latin letters

A^*	:	cross section area at the nozzle throat
A_e	:	cross section area at the nozzle exit
A_i	:	pre-exponential factor
BC	:	boundary condition
BP	:	boundary point
C_{c3}	:	Daly and Harlow model constant
C_I	:	Yoshizawa model constant
C_p	:	pressure coefficient
C_w	:	`WALE` model constant
c_p	:	specific heat at constant pressure of the mixture
$\hat{C}_{p\alpha}$	:	molar heat at constant pressure of species α
$c_{p\alpha}$	:	specific heat at constant pressure of species α
c_v	:	specific heat at constant volume of the mixture
D	:	cavity depth or molecular diffusivity
`Da`	:	Damköhler number
D_{inj}	:	fuel injection diameter
$\mathcal{D}_{sgs}$	:	turbulent diffusivity
$\widetilde{D}_{\alpha m}$	:	array of resolved flux diffusion coefficients of species α into the mixture
$D_{\alpha\beta}$	:	binary diffusion coefficient between species α and β
$\mathcal{D}$	:	distribution function
$\mathring{D}_{\alpha\beta}$	:	diffusion flux coefficient
$d_{\beta i}$	:	diffusion vector
E_{A_i}	:	activation energy
e	:	internal energy
e_{GP}	:	energy at the ghost point
e_{IP}	:	energy at the image point
e_t	:	total energy
$\mathcal{F}^L$	:	`IBM` forcing term (discrete forcing method)

F^L	:	Lagrangian force density
`Fo`	:	Fourier number
f	:	fraction of time the combustion is in jet-wake stabilized mode
$\langle f \rangle$	:	mean of the variable f
f^d	:	dominant frequency
f^L	:	`IBM` forcing term (continuous forcing method)
f_i^L	:	`IBM` forcing term over i-direction
GP	:	ghost point
h	:	mixture enthalpy
h^{in}	:	mixture enthalpy at the inlet
h_{GP}	:	enthalpy at the ghost point
h_{IP}	:	enthalpy at the image point
$\hat{H}_\alpha$	:	molar enthalpy of species α
h_t	:	total enthalpy
h_α	:	enthalpy of species α
$h^\theta_{\alpha,f}$	:	formation enthalpy of species α
h^*_α	:	enthalpy of species α of the fine-scale structure
h^0_α	:	enthalpy of species α of the surrounding zone
h^{in}_α	:	enthalpy of species α at the inlet
IP	:	image point
IQ_k	:	Pope quality index
IQ_η	:	Celik quality index
I_{sp}	:	specific impulse
$J_{\alpha i}$	:	molecular flux for species α
$\check{J}_{\alpha i}$	:	resolved molecular flux for species α
$J^{sgs}_{\varphi i}$	:	subgrid-scale mass flux of scalar quantity φ
`Ka`	:	Karlovitz number
`Kn`	:	Knudsen number
k	:	resolved turbulent kinetic energy
$k_{c,i}$	:	equilibrium constant
$k_{f,i}$	:	forward specific reaction rate
$k_{r,i}$	:	reverse specific reaction rate
k_{sgs}	:	subgrid-scale turbulent kinetic energy
L	:	cavity length or dimension
L/D	:	length-to-depth ratio
l_m	:	molecular mean free path
$\mathcal{L}_t$	:	turbulence integral length scale

$\mathcal{L}_\eta$	:	Kolmogorov length scale
$\mathtt{Le}$	:	Lewis number
$\mathtt{M}$	:	Mach number
$\mathtt{M}_{inj}$	:	fuel injection Mach number
$\mathbf{n}_F$	:	normal unity vector - fuel molecular diffusion flux
$\mathbf{n}_O$	:	normal unity vector - oxidizer molecular diffusion flux
NP_k	:	Eulerian point used for interpolation
NR	:	total number of elementary reactions
$\mathcal{N}_{int}$	:	total number of Eulerian points used to interpolate a Lagrangian point
$\mathcal{N}_{npt}$	:	total number of neighborhood points
$\mathcal{N}_{sp}$	:	total number of species in the mixture
$\mathcal{N}_{tr}$	:	total number of triangles in the `STL` file
P_{ign}	:	probability of ignition
p	:	pressure
p_0	:	pressure at the nozzle stagnation point
p_e	:	pressure at the nozzle exit
p_{GP}	:	pressure at the ghost point
p_{inj}	:	pressure of the fuel injection
p_{IP}	:	pressure at the image point
p_{NP_k}	:	pressure at node NP_k
$\mathtt{Pr}_{sgs}$	:	turbulent Prandtl number
q_i	:	molecular heat flux in the i-direction
$\breve{q}_i$	:	resolved heat flux
q_j^{sgs}	:	subgrid-scale heat flux
$\mathcal{R}$	:	ideal gas constant
r	:	radius
r_{inj}	:	fuel injection radius
$\mathtt{Re}$	:	Reynolds number
S_{ij}	:	strain rate tensor
$\widetilde{S}_{ij}$	:	filtered strain rate tensor
S_{ij}^d	:	traceless symmetric part (`WALE` model)
S_L^0	:	laminar flame velocity
$\mathtt{Sc}_{sgs}$	:	turbulent Schmidt number
SP	:	solid point
$S_{\bar{\rho}}$	:	numerical Schlieren
T	:	temperature
T_0	:	temperature at the nozzle stagnation point

T_0	:	vitiated air-stream temperature
T_O^{ox}	:	oxidizer injection temperature
T^*	:	temperature in the fine-scale structure
T^0	:	temperature in the surrounding zone
T^{in}	:	temperature at the inlet
T_F^{fuel}	:	fuel injection temperature
T_{GP}	:	temperature at the ghost point
T_{inj}	:	temperature of the fuel injection
T_{IP}	:	temperature at the image point
T_{NP_k}	:	temperature at node NP_k
T_w	:	temperature at the wall
t	:	time
t^*	:	normalized time
t_{ign}	:	auto-ignition time
t_{inj}	:	time required to develop the fuel injection flowfield
u_{GP}	:	velocity at the ghost point
u_{IP}	:	velocity at the image point
u_i	:	velocity in i-direction
u_{inj}	:	velocity of the fuel injection
u_{rms}	:	root-mean-square of velocity fluctuations
u_w	:	velocity at the wall
u_0	:	vitiated air-stream velocity
u_{τ_w}	:	friction velocity at the wall
V_e	:	exhaust gas velocity in the nozzle
$\mathbf{V}_F$	:	fuel molecular diffusion velocity
$\mathbf{V}_O$	:	oxidizer molecular diffusion velocity
$V_{\alpha i}$	:	component of diffusion velocity of species α in i-direction
v_k	:	Kolmogorov velocity scale
$\mathcal{W}$	:	molecular weight of the mixture
$\mathcal{W}_{NP_k}$	:	molecular weight of the mixture at node NP_k
$\mathcal{W}_\alpha$	:	molecular weigth of species α
X_α	:	molar fraction of species α
x^L	:	coordinates of the Lagrangian marker
$\mathring{\mathcal{X}}_\alpha$	:	normalized thermal diffusion ratio
Y_f	:	fuel mass fraction
$Y_{f,st}$	:	fuel stoichiometric mass fraction
Y_r	:	fuel mass fraction involved in the chemical reaction

Y_α	:	mass fraction of species α
Y_α^*	:	mass fraction of species α in the fine-scale structure
Y_α^0	:	mass fraction of species α in the surrounding zone
Y_α^{in}	:	mass fraction of species α at the inlet
$Y_{\alpha,GP}$	:	mass fraction of species α at the ghost point
$Y_{\alpha,IP}$	:	mass fraction of species α at the image point
Y_{α,NP_k}	:	mass fraction of species α at node NP_k

Greek letters

β_i	:	temperature exponent
Γ	:	solid/fluid interface
γ	:	specific heat ratio
γ^*	:	fine-scale structure volume fraction
Δ	:	characteristic mesh size
ΔA_{tr}^L	:	characteristic area of the elementary triangle T^L
$\Delta \hat{H}_{f\alpha}^0$	:	molecular formation enthalpy of species α
$\Delta h_{f\alpha}^0$	:	formation enthalpy of species α
ΔS_{tr}^L	:	characteristic length of the elementary triangle T^L
ΔV_{tr}^L	:	characteristic volume of the elementary triangle T^L
Δv_x	:	elementary volume of a computational cell
Δx_i	:	mesh concentration parameter in the i-direction
$\Delta x_{i,cur}$	:	characteristic mesh size in the i-direction
$\Delta x_{i,min}$	:	smallest mesh size in the i-direction
$\Delta x_{i,max}$	:	biggest mesh size in the i-direction
δ	:	boundary-layer thickness
$\delta(x - x_0)$	:	Dirac delta function at $x = x_0$
δ_{ij}	:	Kronecker (delta) tensor
δ_L^0	:	laminar flame thickness
ϵ	:	term used to avoid zero division
ε	:	Heaviside function
ε	:	turbulent kinetic energy dissipation rate
ζ	:	`IBM` solid/fluid marker
$\breve{\zeta}_p$	:	premixedness index
η	:	similarity variable
η_m	:	mixing efficiency

θ_j^{sgs} : subgrid-scale thermal flux
θ_α : thermal diffusion coefficient of species α
κ : bulk viscosity
λ : mixture thermal conductivity
λ_{sgs} : turbulent thermal conductivity
μ : dynamic viscosity
μ_{sgs} : subgrid-scale dynamic viscosity
ν : kinematic viscosity
ν_{sgs} : subgrid-scale kinematic viscosity
$\nu'_{\alpha,i}$: forward stoichiometric coefficient of species α in the i^{th} reaction
$\nu''_{\alpha,i}$: reverse stoichiometric coefficient of species α in the i^{th} reaction
ρ : density
ρ_{GP} : density at the ghost point
ρ_{IP} : density at the image point
ρ_{NP_k} : density at node NP_k
ρ_w : density at the wall
σ : shock sensor
σ_f^2 : variance of the variable f
τ : flame propagation timescale
τ_{ch} : chemical timescale
τ_{ij} : stress tensor
$\breve{\tau}_{ij}$: resolved stress tensor
τ_{ii}^{sgs} : subgrid-scale stress tensor
$\tau_{ii}^{sgs,d}$: deviatoric part of the subgrid-scale stress tensor
τ_k : Kolmogorov timescale
τ_{kk}^{sgs} : isotropic contribution to the subgrid-scale stress tensor
τ_m : subgrid mixing timescale
τ_{res} : residence time
τ_w : wall shear stress
τ_Δ : subgrid timescale
Φ : fuel-air equivalence ratio
Φ_k : interpolation weight of node NP_k
Φ_{mr} : most reactive equivalence ratio
φ : any scalar quantity
ξ : mixture fraction
ξ : `IBM` permeability function
ξ_{GZ} : `IBM` ghost zone marker function

ξ_T	:	transported mixture fraction
$\xi_{f,ox}$	:	reconstructed mixture fraction
ξ_{ign}^{-}	:	mixture fraction lean extinction limit
ξ_{ign}^{+}	:	mixture fraction rich extinction limit
ξ_{mr}	:	most reactive mixture fraction
ξ_{st}	:	stoichiometric mixture fraction
ξ_v^{res}	:	variance of the resolved mixture fraction
Ψ	:	domain of definition of the joint scalar PDF
ψ^*	:	scalar variable at the fine-scale structure
ψ^0	:	scalar variable at the surrounding zone
ψ_j	:	triple velocity correlation tensor
Ω	:	computational domain
Ω_{BP}	:	boundary points domain
Ω_F	:	fluid domain
Ω_{GP}	:	ghost points domain
Ω_{IP}	:	image points domain
Ω_p	:	*porous* medium domain
Ω_S	:	solid domain
ω	:	vorticity
$\dot{\omega}_T$	:	heat release rate
$\dot{\omega}_\alpha$	:	mass production rate of species α
$\dot{\omega}_{\alpha,i}$	:	mass production rate of species α in the i^{th} reaction

Abbreviations and acronyms

CDF	:	Cumulative Distribution Function
CFD	:	Computational Fluid Dynamics
CFL	:	Courant Friedrichs Lewy
CREAMS	:	Compressive REActive Multi-Species solver
DNS	:	Direct Numerical Simulation
EDC	:	Eddy Dissipation Concept
GP	:	Ghost point
GPM	:	Ghost-Point Method
HIT	:	Homogeneous Isotropic Turbulence
HRE	:	Hypersonic Research Engine
IBM	:	Immersed Boundary Method

IP	:	Image Point
JAXA	:	Japan Aerospace Exploration Agency
KEM	:	Kinetic Energy Missile
K-H	:	Kelvin-Helmholtz
LES	:	Large Eddy Simulation
LFL	:	Lower Flammability Limit
LHS	:	Left-hand side
NACA	:	National Advisory Committee for Aeronautics
NASA	:	National Aeronautics and Space Administration
NASP	:	National Space Program
NEO	:	Near Earth Orbit
ONERA	:	*Office National d'Études et de Recherches Aérospatiales*[1]
PaSR	:	Partially Stirred Reactor
PCST	:	Pre-combustion Shock Train
PDF	:	Probability Density Function
PREPHA	:	*Programme de Recherche et Technologie pour la Propulsion Hypersonique Avancée*[2]
PSR	:	Perfectly Stirred Reactor
PVM	:	Physical Virtual Model
RANS	:	Reynolds-averaged Navier-Stokes
RHS	:	Right-hand side
RT	:	Ray-tracing method
SOL	:	Shock-on-lip
SSTO	:	Single-Stage-to-Orbit
STL	:	Stereolithography
TCI	:	Turbulence-Chemistry Interaction
TSTO	:	Two-Stages-to-Orbit
TVD	:	Total Variation Diminishing
U-PaSR	:	Unsteady Partially Stirred Reactor
UFL	:	Upper Flammability Limit
VODE	:	Variable-coefficient Ordinary Differential Equation
WALE	:	Wall-Adapting Local Eddy
WENO	:	Weighted Essentially Non-Oscillatory

[1] National Office for Aerospace Studies and Research
[2] Advanced Hypersonic Propulsion Research and Technology Program

Chapter 1

Introduction

One of the challenges in the aerospace field of research is the determination of the thermodynamic effects taking place during a hypersonic flight in the atmosphere. Space launchers such as Saturn (USA), Soyuz (Russia), Ariane (France), ASLV (India) and VLS (Brazil), which travel in the Earth's atmosphere, have the purpose of placing objects in the space, starting from rest, crossing several atmospheric layers in an ascending flight, to finally reach the Earth orbit. Such systems have in common the fact that they carry both fuel and oxidizer for the propulsion system, which decreases the relation payload/weight and increases the costs of placing objects in space.

One of the main steps to develop these launchers is the propulsion system. Among the bipropellant chemical propulsion class, the most developed (and used) engines are solid propulsion and liquid propulsion rockets, with the last one requiring a more advanced technology than the first one [78]. Figure 1.1 presents the schematics of a solid (1.1a) and liquid (1.1b) propulsion system, respectively.

(a) Solid propulsion (b) Liquid propulsion

Figure 1.1 – (a) Solid [158] and (b) liquid [184] propulsion rocket schematics

The interest in hypersonic vehicles lies on the promise of an airbreathing reusable vehicle able to deploy a payload into the Earth orbit. Using airbreathing propulsion, they avoid the need to carry the oxidizer, which results in less weight and total volume of the vehicle, reduced costs, reduced complexity and smaller ground support [3, 77, 91, 159, 163].

The only airbreathing engine cycle capable to efficiently provide the thrust required for a hypersonic vehicle is the scramjet (supersonic combustion ramjet) engine, which is also part of the bipropellant chemical propulsion class. As a matter of fact, at hypersonic speeds, a typical value for the specific impulse of a H_2-O_2 rocket engine is about 400 s while for a H_2 fueled scramjet is between 2000 s and 3000 s [78].

Table 1.1 gives some typical values for the weight fraction in present missions, where one can see that more than half the weight of a rocket vehicle is due to the oxidizer. Also, comparing a rocket system with an aircraft capable to achieve Earth orbit with the same weight, the aircraft would be able to carry 11% additional payload weight.

Takeoff weight fraction	**Aircraft**	**Rocket**
Payload	15%	4%
Fuel	30%	24%
Oxygen	0%	65%
Rest	55%	7%

Table 1.1 – Typical takeoff weight fraction of current aircraft and multi-usage rocket systems [78]

Another way to improve the average installed specific impulse is combining the scramjet propulsion with a conventional rocket engine, thus increasing the launchers performance. A lot of studies have been devoted to such combined propulsion system but none of them were really conclusive about the practical gain that can be obtained [60].

A Single-Stage-to-Orbit (`SSTO`) launcher is the ultimate goal to reach a low-cost access to space. Studies performed in the `PREPHA` program [61] concluded that, if the air-breathing mode could be used efficiently at large flight Mach number, a combined propulsion could improve the feasibility of a `SSTO` [58]. However, due to the sensitivity of the payload mass in a `SSTO` launcher, the development of an operational vehicle with a new and very complex propulsion system would pose an unacceptable development risk level.

By contrast, it is relatively simple to develop a Two-Stages-to-Orbit (`TSTP`) launcher with an air-breathing engine as the first stage. It is also possible to combine the air-breathing engine with the rocket engine in the second stage, but that will pose the same difficulties found in the `SSTO`. Studies performed in France considering different kinds of combined propulsion systems as first stage showed that they are feasible, but they do not improve the overall performance. Other studies proposed the use of a scramjet operating up to Mach 10-12 as the first stage, easing the development of the second stage, but that corresponds to a very complex first stage vehicle. Complementary studies also showed that it can be interesting that the first stage operates at Mach numbers beyond the air-breathing engine limit [160], which corresponds to a more complex first stage vehicle.

According to Bertin and Cummings [19] there are at least three kinds of missions that require hypersonic vehicles:

1. Decisive strikes at the onset of enemy hostilities, decreasing its fighting capability.
2. Effective defense systems and weapons superiority if war cannot be avoided.
3. Cheap access to space.

These three missions are crucial to military forces, but this technology is also important for civilians, with possible applications in the following directions:

- Decreasing the energy necessary to reach orbit, allowing a higher payload and reducing the cost.
- Reducing considerably the duration of inter-continental flights.

The recent intensification of the efforts spent to develop air-breathing propulsion confirms that this is expected to be an efficient way to access space and the understanding of supersonic combustion will be crucial for aerospace industry, allowing to build supersonic vehicles capable to reach other continents in a few hours only and reach low orbit. Several concepts using scramjet engines are being developed in research centers, such as X-43 and X-51 (USA, figures 1.2a and 1.2b, respectively), HIFiRE (Australia/USA, figure 1.2c), LEA (France, figure 1.2d), SABRE (England, figure 1.2e) and 14-X (Brazil, figure 1.2f).

(a) X-43 [133]

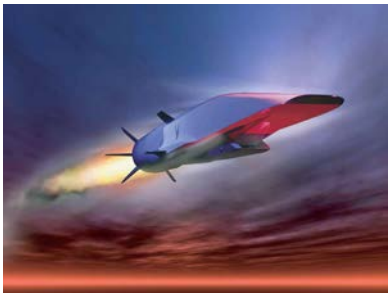

(b) X-51 [130]

(c) HIFiRE [178]

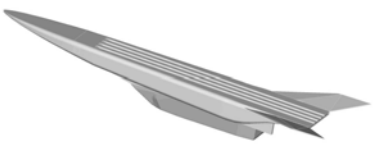

(d) LEA [62]

(e) SABRE [149]

(f) 14-X [68]

Figure 1.2 – Scramjet technology demonstrators

It is complicated to define precisely the propulsive balance in these kind of engines as the net thrust is the difference between thrust (momentum of the hot gases from the combustion chamber) and drag (due to air capture by the inlet). Falempin et al. [59] illustrated this fact as follows:

- At Mach 2, the nozzle produces a thrust of 2, which compensates an air capture drag of 1, resulting in a net thrust of 1.
- At Mach 8, for a net thrust of 1, the nozzle thrust must be 7, with a corresponding drag of 6.
- At Mach 12, a net thrust of 1 is obtained by a nozzle thrust of 12 and air capture drag of 11.

As the flight Mach number increases, the net thrust becomes more sensitive to parametric variations: an error of 5% on the nozzle performance, for example, can lead to a reduction of 60% in net thrust [59].

The optimization of the propulsion system integration into the vehicle airframe becomes mandatory as a small change in the flight parameters affects significantly the performance of the engine. Experimental tools such as wind tunnels and flight experiments are effective to work on this optimization, but they are often expensive and complex to implement and do not necessarily provide all the characteristic quantities of the flow, specially for large vehicles. Computational fluid dynamics studies is proven to be an alternative and complementary framework to conduct these studies, providing most of the required data with a lower cost when compared to experiments [122]. Moreover, it is the sole possible methodology before the development of a full scale model to be used in experimental studies [59, 122], taking into account finite Damköhler number effects for high Mach flow, where chemical and mixing timescale may have the same magnitude.

The corresponding turbulence-chemistry interaction (TCI) affects directly the flow structure in the combustion chamber, especially the mixing layers issued from the fuel injection, thus playing an important role in the mixture auto-ignition. For compressible flows, auto-ignition can be achieved by increasing the temperature through a shock wave. A good understanding of the physical phenomena at play in the stabilization zone is essential to ensure a robust and optimal operation of the propulsion system.

Nowadays it is possible to calculate ignition-stabilized flames using direct numerical simulation (DNS) only for moderate Reynolds numbers, but this is not feasible for scramjet flows for which only Reynolds-averaged Navier-Stokes (RANS) or large eddy simulation (LES) can be used. Figure 1.3a presents a H_2-Air jet flame studied by Yoo et al. [188] using

DNS and figure 1.3b displays the computation of the HiShot II supersonic combustion chamber by Fureby et al. [69].

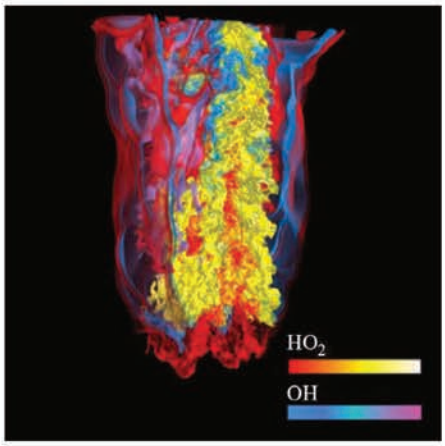

(a) Subsonic ignition-stabilized flame [188]

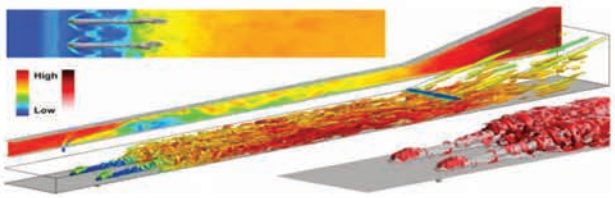

(b) LES of the HiShot II combustion chamber [69]

Figure 1.3 – DNS and LES examples

The filtered chemical terms (LES) or the averaged ones (RANS) need to be modeled because of the large non-linearity of their instantaneous values since the fluctuations of composition and temperature are used to describe the ignition and stabilization of a supersonic diffusion flame. For a scramjet, the quasi-laminar (QL) approach, not taking the TCI into account, has been widely used within the RANS framework because it can include ignition chemistry and features relatively low computational costs [49]. The statistical approach, taking into account detailed chemistry, as done in the studies of Gerlinger et al. [73], Baurle and Girimaji [14], and Möbus et al. [118, 119] is more general, but it is quite expensive. The flamelet approach has been used by Berglund and Fureby [18] within the LES framework, but there are not many studies using this approach with supersonic flow regimes [63, 185]. Finally, Sabelnikov and Fureby [156] proposed another approach based on turbulent mixing, with some encouraging results obtained [17].

The present work is devoted to the numerical simulation of ignition and turbulent combustion in a generic scramjet engine. The main objective is to study numerically the ignition and the combustion stabilization in the scramjet engine in order to contribute to its development.

The manuscript is organized as follows:

- §2 - Scramjet engines: This chapter presents the scramjet engine, its historical conception and some of the research programs that led it to the actual state of art. The technical overview presents the various parts of the engine and explain their characteristics and their roles in operation.

- §3 - Numerical methods: The general equations used in the simulation, the solver and its general characteristics (shock sensor, coupling with chemistry, etc.) and the numerical methods are presented in this chapter. It also includes the presentation of the `LES` filtered transport equations, the closure terms, and some test cases used to validate the implementation.

- §4 - Immersed Boundary Method: This chapter is dedicated to the presentation of the method, which can be used to model complex geometries in the computational domain, e.g. the combustion chamber of a scramjet engine. The `IBM` conception, some techniques used to achieve its purpose and the implementation of a hybrid approach (continuous forcing and discrete forcing methods) are also presented, as well as some test cases to verify and validate its implementation.

- §5 - Unsteady Partially Stirred Reactor: The reactor model used in the simulations is presented here together with its response in simple cases with special emphasis placed on the influence of the residence time, exchange time, etc.

- §6 - Non-reactive simulations: This chapter presents the non-reactive simulations. The numerical setup is presented, as well as the fuel and vitiated air inlet parameters. The computational resolution and statistical convergence of the simulation are also assessed in this chapter. Turbulent flow and mixing analysis are also performed.

- §7 - Reactive simulations: This chapter presents the reactive simulations performed. The results are compared considering the `U-PaSR` and the `PSR` approaches. Turbulent flow analysis and turbulent combustion development is also studied in this chapter, as well as the combustion stabilization mechanism and turbulence-chemistry interactions.

- §8 - Conclusions and Perspectives: The final chapter presents the main conclusions of the study and some perspectives for future works.

Chapter 2

Scramjet engines

2.1 Historical overview

In the beginning of the 20th century the idea of using an air-breathing propulsion system without moving parts for high-speed vehicles was born. René Lorin was one of the first to study the use of ram pressure and described the principles of a ramjet in several articles published in the journal *L'Aérophile* between 1908 and 1913. He presented the advantages of converting the energy from combustion products directly to a kinetic form (expansion of the combustion gases in a nozzle) instead of using a mechanical form as intermediate (mechanical shaft connected to a propeller) to be used as a propulsion system:

" *Il y aurait un grand avantage à pouvoir supprimer l'intermédiaire de la puissance mécanique. C'est ce que l'on obtient par l'emploi du propulseur à échappement* " (Lorin [106]) [1]

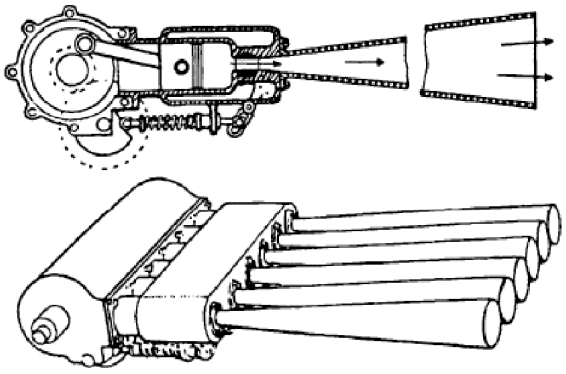

Figure 2.1 – Exhaust thruster as imagined by Lorin [106]

[1] There would be a great advantage being able to remove the intermediate part in a mechanical power system. This can be achieved by using an exhaust thruster.

The ramjet concept appeared for the first time under the name *exhaust thruster* (see figure 2.1) already consisting of the three elements of modern engines: air-compression system, energy supply to burn the air/fuel mixture and an expansion system for the burned hot gases. In 1913, he settled the ramjet concept by proposing the use of a supersonic flow as the inlet of the compression system. However, he concluded that this kind of engine would not be suitable for subsonic flights due to the low ram pressure because it relies on the pressure increase caused by the reduction of the velocity of the incoming flow, being incapable to generate thrust at low speeds [51, 78]. Figure 2.2 presents a schematic ramjet that is similar to the one studied by Lorin.

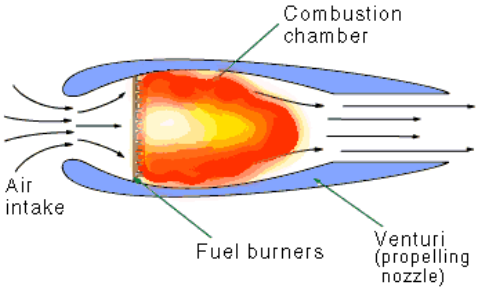

Figure 2.2 – Schematic of a ramjet engine [53]

Maxime Guillaume, in 1921, solved the low performance problem of the ramjet by suggesting the use of turbojet engines to increase the pressure up to the level required for its operation. In 1928, Albert Fono patented a propulsion system with all the elements of a modern ramjet for supersonic flight, as presented in figure 2.3, but there is no evidence that it was ever build.

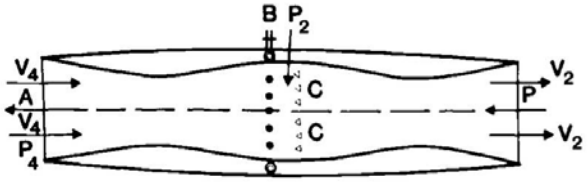

Figure 2.3 – Fono ramjet as reproduced from the original German patent [67]

Only in 1935, René Leduc got the patent of a ramjet propulsion aircraft that, later on, turned to be the experimental aircraft `Leduc 010`, see figure 2.4, which first powered flight took place on April 21, 1949, reaching Mach 0.84 while still climbing [103]. He subsequently improved his concept, leading to the `Leduc 016` and `Leduc 021`, which reached Mach 0.9.

During the Second World War several ramjet missiles models were studied, but their development was postponed due to the lack of materials available for the combustion chamber and due to the high initial velocity required for the ramjet to operate.

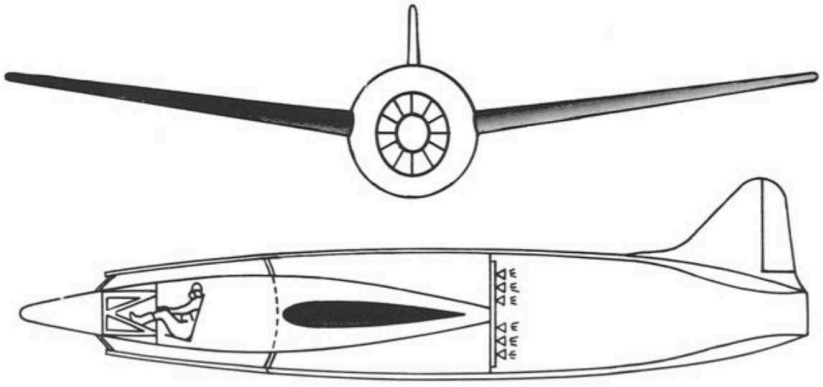

Figure 2.4 – Leduc ramjet aircraft as reproduced from the original French patent [102]

In 1953, based on the ramjet work of Leduc, the French enterprise Nord-Aviation began the development of an aircraft which could fly up to Mach 2, resulting in the aircraft known as `Griffon II`, shown by figure 2.5.

Figure 2.5 – Griffon II aircraft [127]

At the beginning of the 1990s studies related to the ramjet propulsion started again and actually there are missiles with advanced mixed propulsion systems (rocket/ramjet). Technologies such as intelligent flow control at the ramjet intake greatly contributed to increase the performance and reliability of the rockets using this propulsion system [126].

An important example of ramjet engine is the `Pratt & Whitney J58`, which was the propulsion system of the `SR-71 Blackbird` aircraft [98], shown in figure 2.6. This engine works as a turbojet from rest and at low speed, and it operates as a ramjet at high speed, reaching Mach 3.2.

As long as the flight Mach number remains between 3 and 6, ramjets are suitable because the ram pressure generated by decelerating the flow remains sufficient to generate thrust, but at higher Mach numbers it is no longer beneficial to decrease the flow to subsonic speeds due to O_2 dissociation inside the combustion chamber and the combustion must take place in supersonic conditions [78]. At hypersonic speeds the shear layer may

Figure 2.6 – SR-71 aircraft [128]

become chemically reactive because of the high temperatures caused by the air friction with the aircraft body [5].

The supersonic combustion ramjet (scramjet) engine is a variation of the ramjet air-breathing internal combustion engine designed for hypersonic speed and high altitude flight, where combustion takes place at supersonic speed. It was first studied in 1958 when Weber and MacKay [182] analyzed the combustion performance in supersonic flows, aiming to overcome the speed limit of ramjet engines. Ferri [66] and Swithenbank [172] also studied supersonic combustion and provided big contributions in this area, but it should be recognized that the early works of Weber and MacKay [182] still remain nowadays considered as the reference, without much changes.

In the early 60's more resources were oriented towards scramjet engine research. The NASA Hypersonic Research Engine (`HRE`) was build in 1964 aiming at the development of a scramjet technology demonstrator by installing a scramjet engine at the top of the `X-15 A-2` experimental aircraft, but they closed the program in 1974 without any launch but after 52 ground tests, see figure 2.7.

Figure 2.7 – HRE experimental engine [6]

The studies at that time were mostly focused on axisymmetric engines, but they did

not prove themselves compatible with an integration together with conventional engines [19]. This subsequently leads NASA to focus on rectangular engines to integrate them with the aircraft fuselage, see figure 2.8.

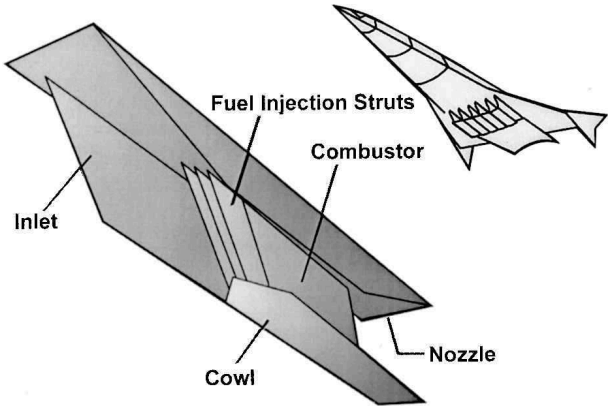

Figure 2.8 – NASA airframe-integrated engine configuration [44]

The most ambitious program involving scramjet engines was the National Space Program (NASP), whose aim was to develop the X-30 aircraft (see figure 2.9): a SSTO capable to takeoff and land from a conventional airport. Its propulsive chart includes several different cycles to accelerate up to hypersonic speeds. However, several difficulties were found during the development of the H_2 powered scramjet engine, which should be capable to operate at Mach numbers from 4 to 15 [44]. Its launch was not possible due to its high cost and the lack in technological expertise to develop its base engine and the program was finally canceled in 1995 leaving a great amount of data about ramjet and scramjet, which are used today in other programs.

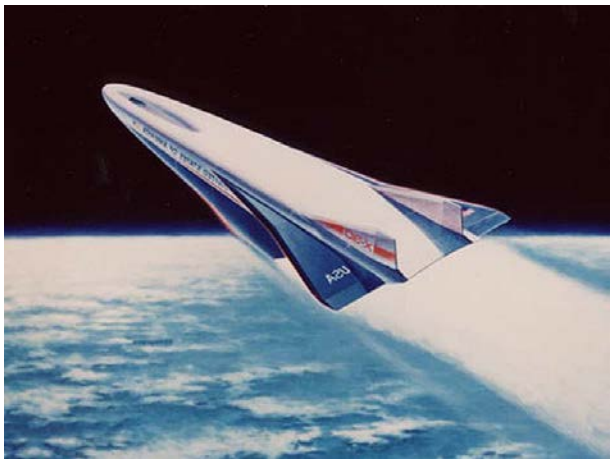

Figure 2.9 – X-30 aircraft concept [134]

In 1996 the Hyper X program was initiated aiming to explore the general performance of an airframe-integrated engine capable to operate as a ramjet at supersonic speeds and

as a scramjet in hypersonic speeds. This program resulted in the X-43 aircraft, shown in figure 2.10:

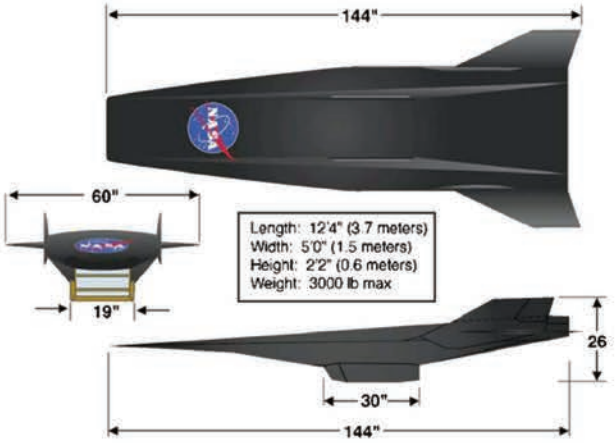

Figure 2.10 – X-43 design [121]

The first launch attempt was undertaken in June 2001 and failed because the rocket used to accelerate the X-43 lost control, forcing its self-destruction. In 2004 two other launch attempts were made, the first one reaching Mach 6.8 over 10 seconds and the other one reaching Mach 9.6 over the same duration of 10 seconds [121].

After the X-43 successful launch, still under the Hyper X program, the next step was the development of a hydrocarbon-powered scramjet engine: the X-51 aircraft. Several ground tests were performed in 2006 and 2007 focused on the study of the thrust generation between Mach numbers 4 and 6.

The first X-51 successful flight was reached in May 2010, where the scramjet engine operated during more than 200 seconds, reaching Mach 5 at 21 km of altitude [12]. The second launch was made in June 2011, however it ended earlier than expected due to an ignition problem after being accelerated up to Mach 5 [153]. In August 2012 the third test resulted in failure when the aircraft lost control after its separation from the rocket, before the scramjet ignition [109]. The last flight took place in 2013, when the aircraft was accelerated by a rocket engine up to Mach 4.8, then accelerated by the scramjet engine up to Mach 5.0 and flew over 240 seconds, before running out of fuel [154].

Like the ramjet engine, the scramjet contains no moving parts, relying on supersonic shock waves on its structure to compress and decelerate the air before combustion, but unlike a regular ramjet, which decelerates the airflow to subsonic speeds for combustion, the flow in a scramjet is supersonic through the whole engine, as in figure 2.11. By maintaining the flow supersonic through combustion, the scramjet engine avoids the terminal shock, associated with subsonic combustion, which leads to severe energy losses. Thus, it allows increased efficiency at higher speeds. The theoretical maximum speed for a

scramjet engine corresponds to Mach numbers between 12 and 24 [159].

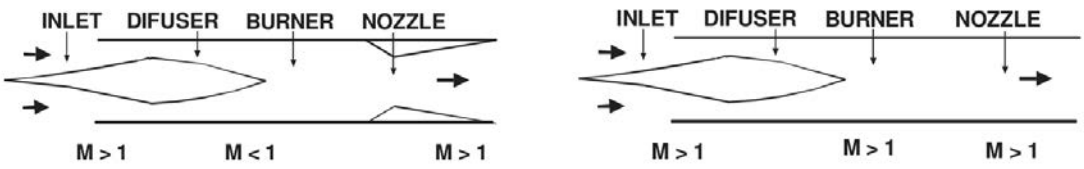

Figure 2.11 – Schematic of ramjet (left) and scramjet (right) engines [159]

As emphasized above, the scramjet engine and air-breathing engines in general have several advantages over rocket engines, like the weight proportion, as shown by figure 2.12, where more than half the mass of an aircraft with rocket engine is constituted by the oxygen to be used in the combustion chamber. Therefore an air-breathing aircraft can carry a heavier payload for the same take-off mass, thus reducing the associated costs [3, 77, 163].

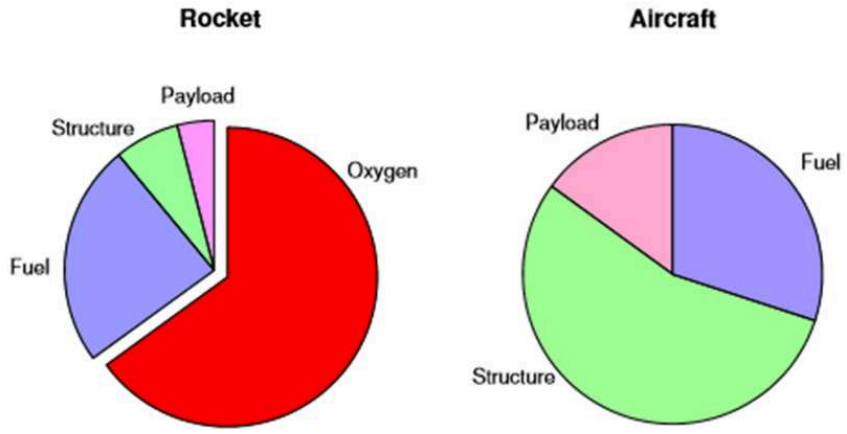

Figure 2.12 – Weight proportions for rocket and air-breathing engines [77]

Another advantage of air-breathing engines is the high specific impulse, which is higher than for rocket engines up to Mach number 15 for both hydrogen and hydrocarbon fuels, as shown in figure 2.13 [99, 137, 159], declining to the performance level of a rocket engine above Mach number 16 [163].

2.2 Technical overview

Even though it is conceptually simple, the scramjet engine faces complex technological challenges. The high speed flight inside the atmosphere presents several structural problems related to aerodynamic heating and vehicle drag, imposing the need for cooling of both the vehicle and the engine for prolonged operations. The high temperatures also

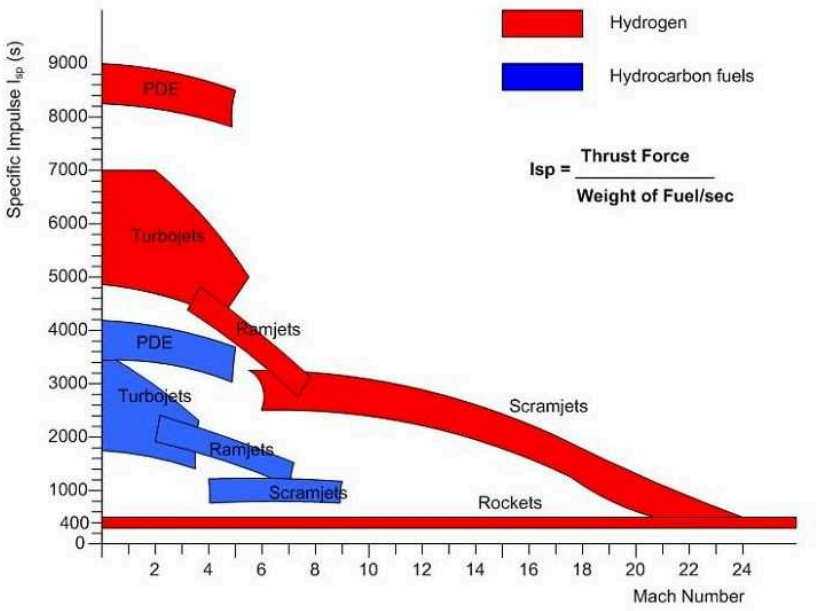

Figure 2.13 – Specific impulses of several air-breathing and rocket propulsion modes [179]

contribute to the dissociation of air molecules, as oxygen and nitrogen molecules decompose and recombine, and may eventually ionize at even higher speeds, as the temperature increase modifies the properties of the flow [159].

In a ramjet engine (see figure 2.14), the flow is compressed in several steps, passing through the oblique shock waves generated by the forebody of the vehicle, decelerating to subsonic speeds in a convergent-divergent duct. Once the flow is subsonic, fuel is injected in the combustion chamber, where it mixes and burns, causing temperature and pressure to increase. The flow is then accelerated back to supersonic speed in a convergent-divergent nozzle and, finally, exhausts into the atmosphere.

It is worth noting that this kind of engine has no moving parts, since the flow is compressed by the forebody of vehicle, which implies that it does not need to be axially symmetric along the centerline.

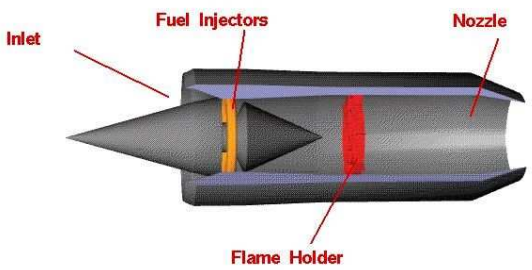

Figure 2.14 – Schematics of a ramjet engine [132]

When the flow is decelerated, the relative velocity and kinetic energy decrease, reap-

pearing as internal energy, which results in a significant increase of pressure, temperature and density. If the flight Mach number exceeds 6, the pressure is too high for practical burner structural design, there are excessive losses due to the normal shock wave system, excessive heat transfer through the wall and, because of high temperature levels, the chemical energy is lost through dissociation processes [78].

The logical solution to this problem is to only partially compress and decelerate the flow, avoiding the normal shock wave system, keeping it supersonic. The main difference of a scramjet from a ramjet engine is that the combustion now takes place at supersonic speeds: the flow is decelerated from hypersonic to supersonic speeds through conic or oblique shock waves generated by the forebody of the vehicle, and this supersonic flow with high pressure and temperature enters the combustion chamber where the fuel (either H_2 or a hydrocarbon fuel) is injected, mixed and burned right after the fuel injectors. Like the ramjet engine, the scramjet also has no moving parts, as can be seen in figure 2.15.

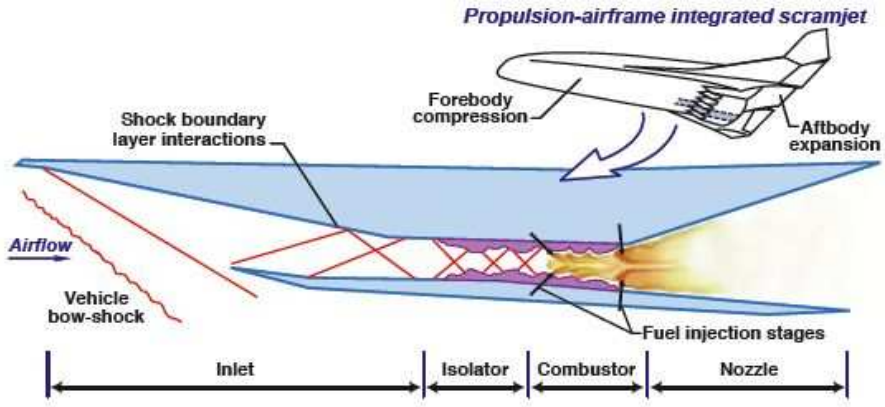

Figure 2.15 – Schematics of a scramjet engine [129]

As air resides for a very short time between engine capture and exit in the order of milliseconds, guaranteeing fuel mixture at molecular level becomes troublesome. This also imposes complications to flame stability, due to the intense gradients in composition and temperature in the flame region.

Since an aircraft fitted with a scramjet engine cannot take off by itself, this engine is only a part of a more complex system based on other thermodynamic cycles, where it must be able to take off with a turbojet engine, to accelerate to speeds which allow it to activate the scramjet to hypersonic speeds and then activate a rocket engine if operation beyond Earth's atmosphere is included in the mission [159].

2.2.1 Inlet

The integration with the propulsive system requires the aircraft forebody to compress the suctioned air in order to achieve adequate pressure and temperature for combustion and to maximize the pressure recovery. The inlet must be able to capture the exact amount of air required by the engine and decelerate it to the required speed without flow distortion and pressure loss and producing the least amount of drag [163, 180], while avoiding 3D flow because this would lead to the existence of cross flow and boundary layer increase. Also, it must be large enough so as to provide the necessary thrust even at high altitudes. Its design is crucial to the successful operation of the engine since it is the only provider of airflow and compression [108].

In a scramjet integrated to the airframe of the aircraft, compression can be achieved by both the vehicle forebody and the inlet. Several geometries for the inlet of a scramjet engine are available for use, with compression made internally, externally or with a mixed approach. Figure 2.16 presents two inlet models: the first one works oblique shock waves (see figure 2.16a) and the second one works with conic shock waves (see figure 2.16b).

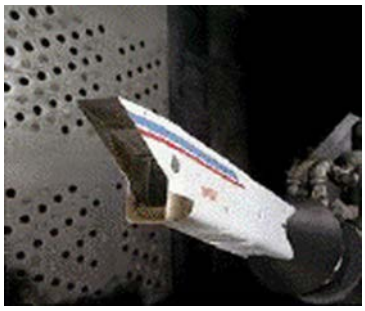

(a) Rectangular inlet

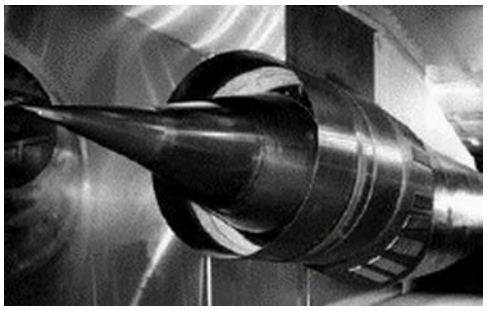

(b) Conic inlet

Figure 2.16 – Inlet type examples [131]

Some of the most common geometries are illustrated in figures 2.17 to 2.21 [78]. Figure 2.17 presents an external compression system, where one can notice that the shock waves are directed to the lip of the engine cowl and the internal flow is uniform and parallel. This condition is known as *shock-on-lip* (SOL) and it used to avoid spillage, which happens when part of the mass flow that should be available at the inlet *spills* under the cowl.

The compression device presented by figure 2.18 is similar to that of figure 2.17, but now the compression surface is curved. This curved surface generates a train of infinitesimal compression waves, which results in a finite pressure increase with no increase of entropy.

The mixed external and internal compression system is illustrated by figure 2.19 and makes use of multiple weaker shocks that are reflected internally in order to achieve the desired compression level. This system allows the cowl to be parallel to the freestream

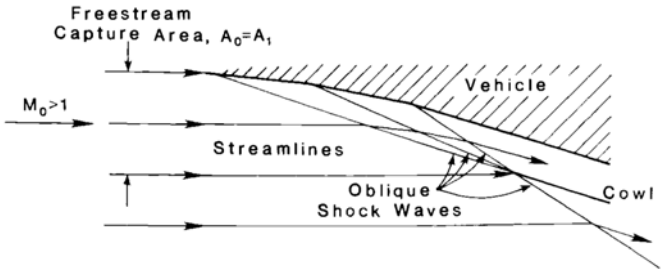

Figure 2.17 – External compression system

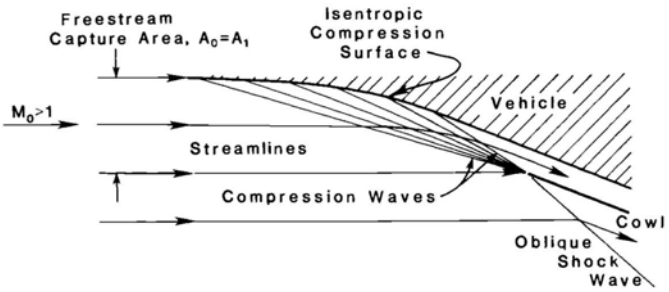

Figure 2.18 – Isentropic external compression system

flow because it does not need the engine cowl angle to follow the compressed flow, however the overall length of the system must be greater when compared to others.

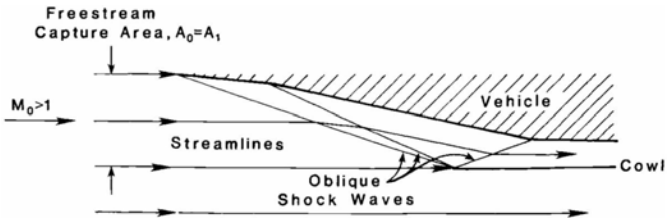

Figure 2.19 – Mixed compression system

The compression system shown in figure 2.20 is a symmetrical internal one, which uses an extra surface to generate a mirrored shock wave, producing an uniform and parallel internal flow. The use of the mirrored shock waves can produce complex flows when operating away from the design point. Such an inlet configuration is also known as *Busemann inlet* when configured in an axisymmetric version.

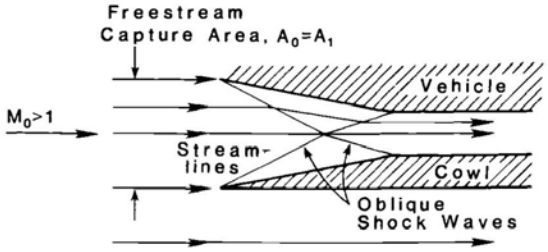

Figure 2.20 – Internal symmetrical compression system

Finally, figure 2.21 presents a system that combines external compression from the surfaces and internal compression generated within closed passages. The flow is separated in several identical streams, reducing the length required for compression. This system is known as lateral or sidewall mixed external and internal.

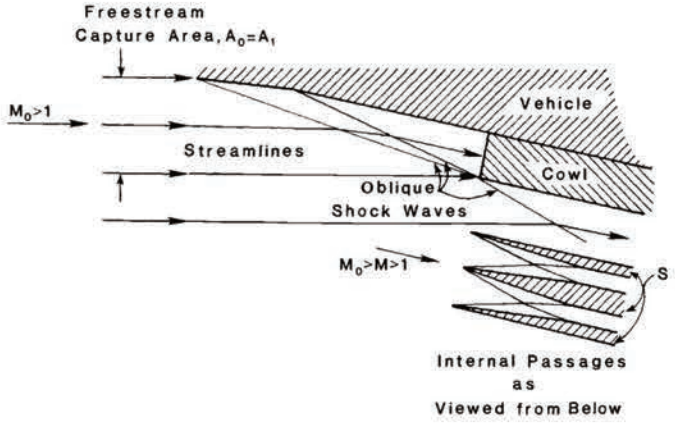

Figure 2.21 – Sidewall mixed compression system

A scramjet engine that operates in the lower hypersonic regime is called a dual-mode scramjet and the corresponding flow is characterized by the presence of subsonic and supersonic regions in the combustor [101, 164]. It can operate in three different ways, as depicted in figure 2.22.

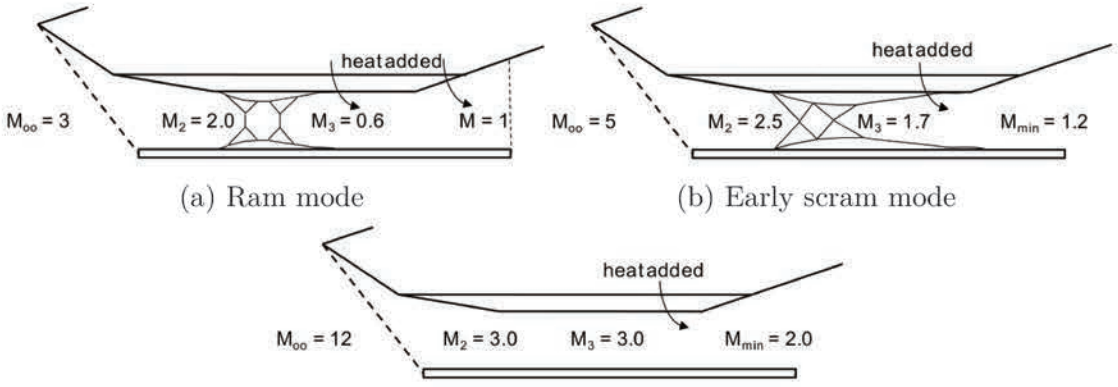

Figure 2.22 – Operation modes of a dual-mode scramjet engine [176]

2.2.2 Isolator

In the ram mode (see figure 2.22a), the engine operates as a ramjet: air is compressed and slowed by the inlet to a subsonic velocity at the entrance of the combustor and shock waves generate a pre-combustion shock train (PCST), which may lead to boundary layer separation from the surface of the combustor duct.

As the velocity is increased to a Mach number value between 5 and 7, the engine operates in the early scram mode (see figure 2.22b): the combustion is considered to be supersonic, but subsonic combustion may also occur in the vicinity of walls and within the flameholders. The shock train is weaker and the separated boundary layer is thinner, and combustion occurs at constant pressure because the separated boundary layer somehow leads to a new effective wall shape [176].

Finally, when the aircraft Mach number is larger than 7, only supersonic combustion occurs and the engine operates in what it is called the late scram mode (see figure 2.22c): there is no pre-combustion shock train since the flow is completely supersonic.

In order to contain these shock trains, a short length of duct is added to the scramjet flowpath upstream the combustion chamber section. This duct is called isolator and it avoids the shock trains to disrupt the inlet operation, helping to maintain a stable airflow to the combustion chamber. It should maximize the static pressure and the stagnation pressure recovery and minimize the flow distortion [10].

Figure 2.23 presents the flow structure inside such an isolator. If the boundary layer did not exist, there would be no shock train. However, the incoming boundary layers produces a series of oblique and normal shocks that spread the pressure rise along the duct. At some point in the isolator the flow reattaches to the wall and the shock train weakens, tending to disappear and improving the homogeneity of the flow inside the combustion chamber, allowing an efficient mixing and burning [151].

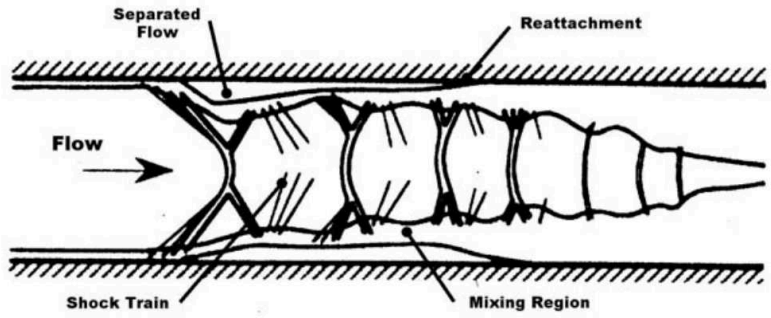

Figure 2.23 – Flow structure in the isolator [82]

As the combustion back pressure increases, the shock train length must increase in order to allow the combustor inlet pressure to rise sufficiently. However, if the shock train reaches the inlet, the mass of air captured will decrease, increasing the pressure and thermal loads, increasing drag and decreasing thrust, in a phenomena known as *engine unstart* [21, 42, 78].

2.2.3 Combustion chamber

Regardless of the compression system, the flow must be heated up in the combustion chamber and thrust is generated through the acceleration of the combustion products by the nozzle. The combustor is one of the most critical components of the scramjet, since it entails complicated phenomenon such as compressibility effects, heat release, residence time, shock interaction and turbulent mixing. The main challenges on its development are related to improving the mixing and burning efficient in a short residence time (of the order of one millisecond [84, 87, 95]) in order to stabilize the flame and minimizing the total pressure loss.

Over the years, several fuel injection techniques have been proposed, such as transverse fuel injection from a wall orifice [110], backward facing step with transverse injection [1, 96, 173], angled injection, cavity flame holder [16, 30, 83], aiming at favoring ignition and stabilization of the combustion processes [117]. A review of the combustion characteristics for different kinds of injectors can be found in the work of Deepu et al. [48].

Transverse injections is commonly used as a flame stabilization scheme as it provides flame stabilization by organizing an upstream recirculation zone and generating coherent structures favoring an efficient mixing between fuel and air [15], see figure 2.24.

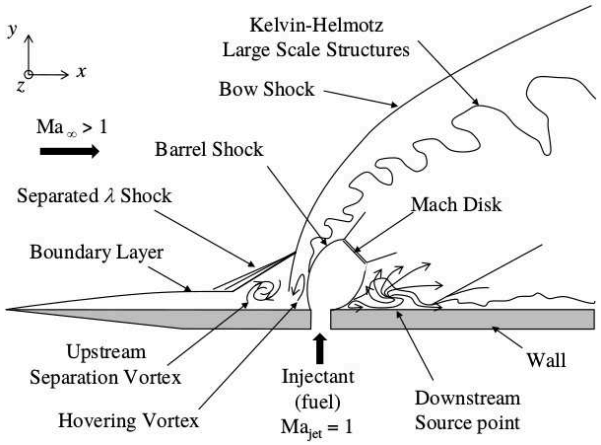

Figure 2.24 – Transverse fuel injection [174]

Figure 2.25 presents the schematics of a flow field over a backward face step, where a recirculation zone appear between the step and the reattachment zone. This happens because the boundary layer is separated at the leading edge of the step because of the sudden change in the geometric configuration, and it helps the ignition and stabilization of the flame because the velocity is this region is significantly decreased and the recirculation zone is associated to increased residence times.

According to Ben-Yakar and Hanson [16], which summarized the ongoing works on cavity flame holders, the magnitude of the length-to-depth ratio (L/D) can be used to

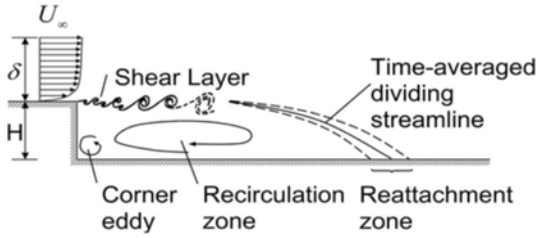

Figure 2.25 – Backward facing step flowfield [86]

characterize the cavity flow into two different regimes: open cavity ($L/D < 7-10$) when the upper shear layer reattaches to the downstream trailing edge (see figure 2.26a), and closed cavity ($L/D > 10-13$) when the upper shear layer reattaches to the floor face (see figure 2.26b). The critical length-to-depth ratio where transition between open and closed cavity occurs depends also on the Mach number, cavity width and the boundary layer thickness at the leading edge of the cavity. A characteristic of the cavity flame holder technique is that it can integrate the fuel injection and the flame holding capability together.

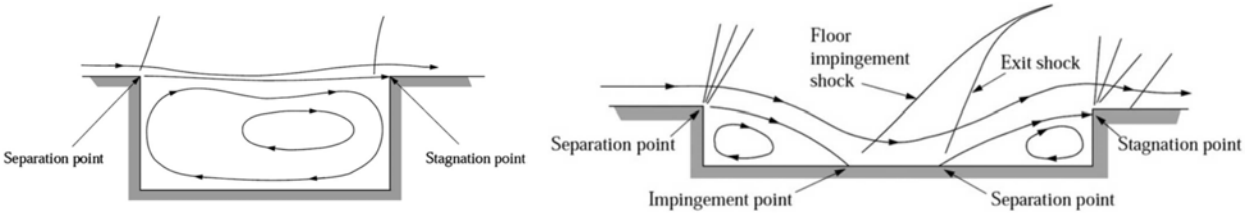

(a) Open cavity

(b) Closed cavity

Figure 2.26 – Cavity flow regimes [100]

The combination of different fuel injection techniques can be used to improve the fuel penetration and mixing efficiency, for example, combining a cavity flame holder and a backward facing step [191].

2.2.4 Exhaust nozzle

Finally, the nozzle design must accomodate with several issues like the composition of the combustion products, which involves the computations of the concentration of hundreds chemical species. Its objective is to direct and accelerate the combustion products in order to maximize the velocity at the exhaust, and this is done only with its geometry. In order to improve the aero-propulsive performance, the afterbody of the airframe can be used as part of the nozzle to further expand the exhaust jet stream [85].

A classical convergent-divergent nozzle, also called *Laval nozzle* is the most common one, consisting in a convergent section to accelerate the subsonic flow, a sonic throat

where $M = 1$ and a divergent section to accelerate the supersonic flow, as shown in figure 2.27.

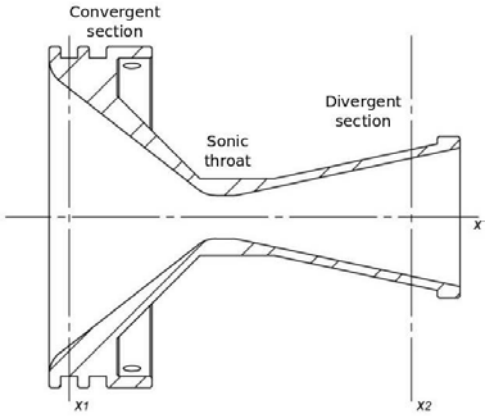

Figure 2.27 – Schematics of a Laval nozzle [146]

A theoretical isotropic nozzle is capable to eject the combustion products at maximum possible velocity. In this condition the flow properties depend only on the nozzle cross section area.

Equation 2.1 below summarizes the operation principle of a nozzle, indicating that the enthalpy decrease is equal to the kinetic energy increase [5], i.e. the flow is accelerated by its heat.

$$h_1 - h_2 = \frac{V_2^2 - V_1^2}{2} = c_p \left(T_1 - T_2\right) \tag{2.1}$$

The mass flow is limited by the sonic flow in the throat caused by an effect called clogging. When subsonic, the flow velocity increases in the convergent section up to $M = 1$ at the throat and it stops increasing even if the cross section area decreases. The velocity will only increase if the cross section area increases too, that is, in the divergent section.

Since the flow is supersonic in the scramjet engine, the exhaust nozzle is only divergent. The velocity of the expelled gases V_e [88] is given by equation 2.2:

$$V_e = \sqrt{2T_0 R \frac{\gamma}{\gamma - 1} \left[1 - \left(\frac{p_e}{p_0}\right)^{\frac{\gamma - 1}{\gamma}}\right]} \tag{2.2}$$

where T_0 is the stagnation temperature, $R = \mathcal{R}/\mathcal{W}$ is the specific gas constant, $\gamma = c_p/c_v$ is the specific heat ratio, pe is the pressure at the nozzle exit and p_0 is the pressure at the stagnation point.

From this equation, it can be concluded that:

- The maximum exhaust velocity is obtained in the vacuum, when the pressure ratio tends to infinity.
- Increasing the combustion chamber pressure does not increase significantly the exhaust gas velocity.
- A higher combustion temperature and a lower molecular weight may help to increase the velocity of the expelled gases.

The nozzle design is optimized in function of the temperature of the combustion chamber products and the expelled gas pressure. An optimal gas exhaust acceleration is obtained when the pressure at the nozzle exit is equal to ambient pressure, so the cross section area ration between the nozzle and its exit, also know as expansion ratio [88], is given by:

$$\frac{A^*}{A_e} = \left(\frac{\gamma+1}{2}\right)^{\frac{1}{\gamma-1}} \frac{p_e}{p_0} \sqrt{\frac{\gamma+1}{\gamma-1}\left[1-\left(\frac{p_e}{p_0}\right)^{\frac{\gamma-1}{\gamma}}\right]} \tag{2.3}$$

where A^* denotes the cross section area of the nozzle throat and A_e is the cross section area of the nozzle exit.

The nozzle looses its efficiency when the pressure at its exit (p_e) differs from the ambient one (p_0). If the flow is under expanded ($p_e > p_0$) the gas will keep expanding in the ambient, loosing energy. In the contrary, if it is over expanded ($p_e < p_0$), shock waves will decelerate the flow, losing efficiency. These phenomena are illustrated in figure 2.28:

Summary

Like ramjet engines, scramjets have no moving parts, but combustions takes place at supersonic speeds instead of subsonic ones. It makes use of ram pressure to generate thrust, being incapable to work at low speeds, so it needs another kind of propulsion to accelerate it to adequate velocities. Also it features several advantages when compared to rocket engines, such as being able to carry heavier payload since it does not need to carry its own oxidizer and having a high specific impulse.

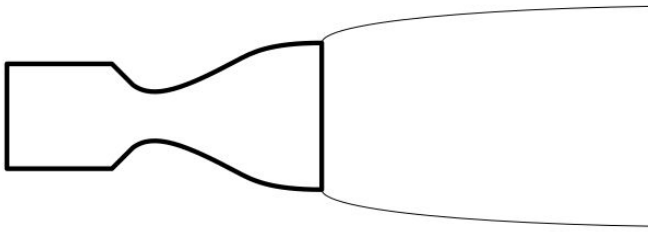

(a) Under expanded ($p_e > p_0$)

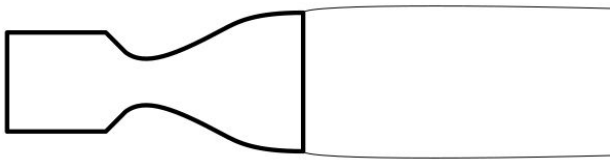

(b) Equilibrium ($p_e = p_0$)

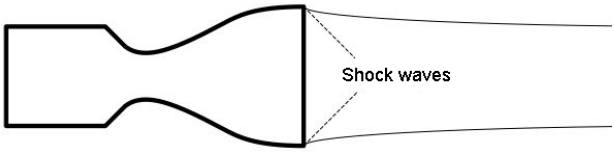

(c) Over expanded ($p_e < p_0$)

Figure 2.28 – Expansion ratio effects on the nozzle efficiency [71, 88]

Despite the working principles of scramjets being similar to ramjet and the fact that there are already some aircrafts and missiles that make use of ramjet engines, scramjets are still work-in-progress since there are only studies and concepts that makes use of this technology. One of the main problems found in scramjets is having enough time for fuel and oxidizer to mix and burn inside the combustion chamber, since the flow is supersonic, and also keep the flame stability. Some scramjet engines were already tested in flight, such as NASA's `X-43` and `X-51`.

This engine can be divided basically in 4 parts: inlet, isolator, combustion chamber and exhaust nozzle. The inlet is responsible to compress the suctioned air so as to achieve the necessary pressure and temperature for combustion. Its design is crucial to the successful operation of the engine since it is the only provider of airflow and compression. The main objective of the isolator is to contain the shock trains that are generated by the shock waves, which may disrupt the inlet operation.

One of the most critical components of the scramjet is the combustion chamber since it is responsible to mix the fuel and oxidizer and burn it efficiently in a short residence time in order to stabilize the flame. Several kinds of fuel injection techniques have been proposed to favor ignition and stabilization of the combustion process.

Finally, the exhaust nozzle, using only its own geometry, is responsible to direct and

accelerate the combustion products to maximize the velocity of the expelled gases.

The rest of the manuscript will be focused on the numerical simulation of a typical scramjet combustion chamber. First, the numerical methodology will be presented in the next chapter.

Chapter 3

Numerical methods

3.1 Governing equations

The equations below (3.1 to 3.4) describe a 3D, unsteady, compressible, turbulent and viscous flow, with $\mathcal{N}_{sp}$ reactive species, for a typical value of the Knudsen number `Kn` smaller than 0.01, which means that the molecular mean free path l_m is much smaller than the dimension L of domain in which the flow interacts, that is, the medium is not rarefied. This system of conservation laws is based on the following independent and conservative variables: density ρ, momentum ρu_i, total energy ρe_t and partial densities ρY_α.

$$\frac{\partial \rho}{\partial t} + \frac{\partial \rho u_i}{\partial x_i} = 0 \tag{3.1}$$

$$\frac{\partial \rho u_i}{\partial t} + \frac{\partial \rho u_i u_j}{\partial x_j} = -\frac{\partial p}{\partial x_i} + \frac{\partial \tau_{ij}}{\partial x_j} \tag{3.2}$$

$$\frac{\partial \rho e_t}{\partial t} + \frac{\partial \rho e_t u_i}{\partial x_i} = -\frac{\partial p u_i}{\partial x_i} - \frac{\partial q_i}{\partial x_i} + \frac{\partial u_i \tau_{ij}}{\partial x_j} \tag{3.3}$$

$$\frac{\partial \rho Y_\alpha}{\partial t} + \frac{\partial \rho Y_\alpha u_i}{\partial x_i} = -\frac{\partial J_{\alpha i}}{\partial x_i} + \rho \dot{\omega}_\alpha \quad , \quad \alpha = 1, \ldots, \mathcal{N}_{sp} \tag{3.4}$$

The first equation of the Navier-Stokes model (3.1) is the mass conservation. The following three equations (represented by 3.2) are the momentum conservation in x_1, x_2 and x_3-direction, as obtained from the fundamental principle of dynamics. The first law of thermodynamics, that is, the total energy variation of a physical system due to all the forces applied on it is presented in equation 3.3. Finally, the chemical species conservation is presented by $\mathcal{N}_{sp}$ equations, herein associated to equation 3.4. The closure of this system can be obtained considering the ideal gas law, presented by equation 3.5.

$$p = \frac{\rho \mathcal{R} T}{\mathcal{W}} \tag{3.5}$$

where $\mathcal{R} = 8.314\ \mathrm{J \cdot mol^{-1} \cdot K^{-1}}$ is the ideal gas constant and

$$\mathcal{W} = \sum_{\alpha=1}^{\mathcal{N}_{sp}} X_\alpha \mathcal{W}_\alpha = \left(\sum_{\alpha=1}^{\mathcal{N}_{sp}} \frac{Y_\alpha}{\mathcal{W}_\alpha} \right)^{-1} \tag{3.6}$$

is the molecular weight of the mixture, deduced from the molecular weight $\mathcal{W}_\alpha$ of each species α and their molar fraction X_α.

The stress tensor τ_{ij}, considering a Newtonian fluid, is given by

$$\tau_{ij} = \kappa S_{kk} \delta_{ij} + 2\mu \left(S_{ij} - \frac{1}{3} S_{kk} \delta_{ij} \right) \tag{3.7}$$

where κ is the volumetric viscosity (*bulk viscosity*) associated to the volume change caused by an imbalance of internal energy repartition, μ is the dynamic viscosity, $S_{ij} = \left({}^{\partial u_i}/_{\partial x_j} + {}^{\partial u_j}/_{\partial x_i} \right)/2$ is the strain rate tensor and δ_{ij} is the Kronecker delta.

Considering the external volumetric forces as zero, the molecular flux of each species α can be written as

$$J_{\alpha i} = \rho Y_\alpha V_{\alpha i} \tag{3.8a}$$

$$= -\sum_{\beta=1}^{\mathcal{N}_{sp}} \left(\rho \mathring{D}_{\alpha\beta} d_{\beta i} \right) - \rho Y_\alpha \theta_\alpha \frac{\partial \ln T}{\partial x_i} \tag{3.8b}$$

$$= -\sum_{\beta=1}^{\mathcal{N}_{sp}} \rho \mathring{D}_{\alpha\beta} \Bigg[\underbrace{\frac{\partial X_\beta}{\partial x_i}}_{(I)} + \underbrace{\left(X_\beta - Y_\beta \right) \frac{\partial \ln p}{\partial x_i}}_{(II)} \Bigg] - \underbrace{\rho Y_\alpha \theta_\alpha \frac{\partial \ln T}{\partial x_i}}_{(III)} \tag{3.8c}$$

where $V_{\alpha i}$ is the diffusion velocity of species α in i-direction, $d_{\beta i}$ is the diffusion vector, $\mathring{D}_{\alpha\beta} = Y_\alpha D_{\alpha\beta}$ is the diffusion flux coefficient, $D_{\alpha\beta} = {}^{\theta_\alpha}/_{(X_\beta \mathring{\chi}_\beta)}$ is the binary diffusion coefficient between species α and β which is such that $D_{\alpha\beta} = D_{\beta\alpha}$, $\mathring{\mathcal{X}}_\alpha = {}^{\mathcal{X}_\alpha}/_{X_\alpha}$ is normalized thermal diffusion ratio so as $\sum_{\alpha=1}^{\mathcal{N}_{sp}} \mathcal{X}_\alpha = 0$ and, finally, θ_α is the thermal diffusion coefficient of species α.

The identified terms of equation 3.8c represent mass diffusion through (I) concentration gradients (Fick Law), (II) pressure gradients, and (III) temperature gradient (Soret effect or thermodiffusion).

Finally, the molecular heat flux in the i-direction q_i writes

$$q_i = -\underbrace{\lambda \frac{\partial T}{\partial x_i}}_{(I)} + \sum_{\alpha=1}^{\mathcal{N}_{sp}} J_{\alpha i} \Bigg(\underbrace{h_\alpha}_{(II)} + \underbrace{\frac{RT \mathring{\mathcal{X}}_\alpha}{\mathcal{W}_\alpha}}_{(III)} \Bigg) \tag{3.9}$$

with λ being the thermal conductivity of the mixture.

The identified terms of equation 3.9 represent the heat diffusion through (I) conduction, temperature gradients (Fourier Law), (II) partial enthalpy flux, and (III) concentration gradients (Dufour effect).

The total energy e_t is expressed as the sum of the internal energy and the kinetic energy:

$$e_t = e + \frac{1}{2} u_i u_i \tag{3.10}$$

where, by definition, $e = h - p/\rho$.

Considering the mixture as an ideal gas, both internal energy and enthalpy are function only of temperature, that is, $e = e(T)$ and $h = h(T)$, so the specific heat at constant volume c_v and constant pressure c_p can be written as

$$c_v(T) = \frac{\partial e}{\partial T} \tag{3.11}$$

and

$$c_p(T) = \frac{\partial h}{\partial T} \tag{3.12}$$

The mixture enthalpy h, which is necessary to calculate the internal energy, is calculated from each species enthalpy h_α, as presented by equation 3.13.

$$h = \sum_{\alpha=1}^{\mathcal{N}_{sp}} Y_\alpha h_\alpha \tag{3.13}$$

where the species enthalpy can be calculated using the following expression:

$$h_\alpha = \Delta h^0_{f\alpha} + \int_{T_0}^{T} c_{p\alpha}(T)\, \mathrm{d}T \tag{3.14a}$$

$$= \frac{\mathcal{R}}{\mathcal{W}_\alpha} \left(a_{1\alpha} T + a_{2\alpha} \frac{T^2}{2} + a_{3\alpha} \frac{T^3}{3} + a_{4\alpha} \frac{T^4}{4} + a_{5\alpha} \frac{T^5}{5} + a_{6\alpha} \right) \tag{3.14b}$$

and the species specific heat at constant pressure $c_{p\alpha}$ is obtained from the polynomial function

$$c_{p\alpha}(T) = \frac{\mathcal{R}}{\mathcal{W}_\alpha} \left(a_{1\alpha} + a_{2\alpha} T + a_{3\alpha} T^2 + a_{4\alpha} T^3 + a_{5\alpha} T^4 \right) \tag{3.15}$$

where the coefficients $a_{l\alpha}$ ($l \in [\![1, 6]\!]$) are obtained from thermodynamic tables (cf. Appendix A), the characteristic of which were obtained empirically.

The specific heat of the mixture at constant pressure can be calculated in a way similar to the one given by equation 3.13:

$$c_p = \sum_{\alpha=1}^{\mathcal{N}_{sp}} Y_\alpha c_{p\alpha} \tag{3.16}$$

and the mixture specific heat at constant volume can be determined from the following relation:

$$c_v = c_p - \frac{\mathcal{R}}{\mathcal{W}} \tag{3.17}$$

The mass production rate of species α is the sum of all elementary reaction rates that involves this species, and it may be calculated from the following equation:

$$\dot{\omega}_\alpha = \sum_{i=1}^{NR} \dot{\omega}_{\alpha,i} = \sum_{i=1}^{NR} \left(\nu''_{\alpha,i} - \nu'_{\alpha,i}\right) q_i \tag{3.18}$$

where $\nu'_{\alpha,i}$ and $\nu''_{\alpha,i}$ are the forward (reactants to products) and reverse (products to reactants) stoichiometric coefficients, respectively, of species α in the i^{th} reaction.

The global reaction rate of the i^{th} reaction is the difference between the forward and reverse reaction rates:

$$q_i = k_{f,i} \prod_{\alpha=1}^{NR} [X_\alpha]^{\nu'_{\alpha,i}} - k_{r,i} \prod_{\alpha=1}^{NR} [X_\alpha]^{\nu''_{\alpha,i}} \tag{3.19}$$

where $k_{f,i}$ and $k_{r,i}$ are the forward and reverse specific reaction rates, respectively, and $[X_\alpha] = {}^{(\rho Y_\alpha)}/_{\mathcal{W}_\alpha}$ is the molar concentration of species α. The forward specific reaction rate is obtained from Arrhenius Law:

$$k_{f,i} = A_i T^{\beta_i} \exp\left(-\frac{E_{A_i}}{\mathcal{R}T}\right) \tag{3.20}$$

being A_i the pre-exponential factor, β_i the exponential factor for temperature and E_{A_i} the activation energy. These parameters depend on the considered reaction and they do not change with temperature. The forward and reverse specific reaction rates can be related with an equilibrium constant $k_{c,i} = k_{f,i}/k_{r,i}$.

Finally, the heat release rate can be calculated by summing all the production rates weighted with their formation enthalpy:

$$\dot{\omega}_T = -\sum_{\alpha=1}^{\mathcal{N}_{sp}} \Delta h^0_{f\alpha} \dot{\omega}_\alpha \tag{3.21}$$

3.2 Filtered Navier-Stokes equations

In order to separate the small turbulence scales from the bigger ones, a spatial filter must be used. Applying this filter to the set of compressible Navier-Stokes equations (3.1 - 3.4) requires the introduction of two important elements:

1. To deal with non-linear terms related to the volumetric mass, a Favre filter [64] must be used

$$\widetilde{\phi} = \frac{\overline{\rho\phi}}{\bar{\rho}} \tag{3.22}$$

so as to express the non-linear terms into a standard resolved (filtered) part plus a subgrid-scale (SGS) contribution.

2. An operator $\check{\bullet}$ defined as

$$\check{\phi}\left(\rho, T, u, Y, \dots\right) = \phi\left(\bar{\rho}, \widetilde{T}, \widetilde{u}, \widetilde{Y}, \dots\right) \tag{3.23}$$

is also introduced in order to discriminate the resolved terms from the filtered ones.

From this consideration, the filtered Navier-Stokes equations can be expressed in the following conservative form:

$$\frac{\partial \bar{\rho}}{\partial t} + \frac{\partial \bar{\rho}\widetilde{u}_i}{\partial x_i} = 0 \tag{3.24}$$

$$\frac{\partial \bar{\rho}\widetilde{u}_i}{\partial t} + \frac{\partial \bar{\rho}\widetilde{u}_i\widetilde{u}_j}{\partial x_j} = -\frac{\partial \bar{p}}{\partial x_i} + \frac{\partial \check{\tau}_{ij}}{\partial x_j} - \frac{\partial \tau_{ij}^{sgs}}{\partial x_j} + \frac{\partial}{\partial x_j}\left(\bar{\tau}_{ij} - \check{\tau}_{ij}\right) \tag{3.25}$$

$$\frac{\partial \bar{\rho}\widetilde{e}_t}{\partial t} + \frac{\partial \bar{\rho}\widetilde{e}_t\widetilde{u}_j}{\partial x_j} = -\frac{\partial \bar{p}\widetilde{u}_j}{\partial x_j} + \frac{\partial \check{\tau}_{ij}\widetilde{u}_i}{\partial x_j} - \frac{\partial \check{q}_j}{\partial x_j} - \frac{\partial \mathcal{L}_j^A}{\partial x_j} + B_6 - B_7 \tag{3.26}$$

$$\frac{\partial \bar{\rho}\widetilde{Y}_\alpha}{\partial t} + \frac{\partial \bar{\rho}\widetilde{Y}_\alpha\widetilde{u}_i}{\partial x_i} = -\frac{\partial \check{J}_{\alpha i}}{\partial x_i} - \frac{\partial J_{\alpha i}^{sgs}}{\partial x_i} - \frac{\partial}{\partial x_i}\left(\bar{J}_{\alpha i} - \check{J}_{\alpha i}\right) + \bar{\rho}\widetilde{\dot{\omega}}_\alpha \quad , \quad \alpha = 1, \dots, \mathcal{N}_{sp} \tag{3.27}$$

This set of equations is supplemented with the ideal gas law, but in its filtered form:

$$\bar{p} = \frac{\bar{\rho}\mathcal{R}\widetilde{T}}{\widetilde{\mathcal{W}}} \tag{3.28}$$

and with the molecular weight of the mixture determined from

$$\widetilde{\mathcal{W}} = \left(\sum_{\alpha=1}^{\mathcal{N}_{sp}} \frac{\widetilde{Y}_\alpha}{\mathcal{W}_\alpha}\right)^{-1} \tag{3.29}$$

The filtered energy equation (see equation 3.26) is the one provided by Ragab et al. [148], and the filtered total energy, calculated from the sum of the internal specific energy and the kinetic energy, is deduced from

$$\bar{\rho}\widetilde{e}_t = \bar{\rho}\widetilde{e} + \frac{1}{2}\bar{\rho}\widetilde{u}_i\widetilde{u}_i + \frac{1}{2}\tau_{ii}^{sgs} \tag{3.30}$$

with $\tau_{ii}^{sgs} = \overline{\rho u_i u_i} - \bar{\rho}\widetilde{u}_i\widetilde{u}_i$ the subgrid-scale (SGS) stress tensor.

From equation 3.26, we also have the following variables:

$$\mathcal{L}_j^A = \left[\overline{(\rho e_t + p)\, u_j} - (\bar{\rho}\widetilde{e}_t + \bar{p})\, \widetilde{u}_j\right] = q_j^{sgs} + \psi_j - \frac{1}{2}\tau_{ii}^{sgs}\widetilde{u}_j \tag{3.31}$$

$$B_6 = \frac{\partial \mathcal{L}_j^{sgs}}{\partial x_j} = \frac{\partial}{\partial x_j}\left(\overline{\tau_{ij}u_j} - \check{\tau}_{ij}\widetilde{u}_i\right) \tag{3.32}$$

and

$$B_7 = \frac{\partial}{\partial x_j}\left(\bar{q}_j - \check{q}_j\right) \tag{3.33}$$

where

- $q_j^{sgs} = \overline{\rho c_p T u_j} - \bar{\rho}\widetilde{c}_p\widetilde{T}\widetilde{u}_j = \overline{\rho h u_j} - \bar{\rho}\widetilde{h}\widetilde{u}_j \approx \widetilde{c}_p\theta_j^{sgs}$ is the SGS heat flux
- $\theta_j^{sgs} = \overline{\rho u_j T} - \bar{\rho}\widetilde{u}_j\widetilde{T}$ is the SGS thermal flux
- $\psi_j = {}^1\!/_2\left(\overline{\rho u_i u_i u_j} - \bar{\rho}\widetilde{u}_i\widetilde{u}_i\widetilde{u}_j\right)$ denotes the triple velocity correlation tensor
- $B_6 = \delta_j\mathcal{L}_j^{sgs} = \delta_j\left(\overline{\tau_{ij}u_j} - \check{\tau}_{ij}\widetilde{u}_i\right)$ is the SGS diffusive viscous flux
- $B_7 = \delta_j\left(\bar{q}_j - \check{q}_j\right)$ corresponds to the SGS molecular heat flux

The resolved stress tensor is calculated as

$$\check{\tau}_{ij} = \tau_{ij}\left(\widetilde{u}, \widetilde{T}\right) = 2\widetilde{\mu}\left(\widetilde{S}_{ij} - \frac{1}{3}\widetilde{S}_{kk}\delta_{ij}\right) \tag{3.34}$$

with the filtered strain rate tensor being

$$\widetilde{S}_{ij} = \check{S}_{ij} = \frac{1}{2}\left(\frac{\partial\widetilde{u}_i}{\partial x_j} + \frac{\partial\widetilde{u}_j}{\partial x_i}\right) \tag{3.35}$$

The resolved molecular flux of species α is evaluated from

$$\check{J}_{\alpha i} = J_{\alpha i}\left(\bar{\rho}, \widetilde{T}, \widetilde{Y}\right) = -\bar{\rho}\widetilde{D}_{\alpha m}\frac{\mathcal{W}_\alpha}{\widetilde{\mathcal{W}}}\frac{\partial\widetilde{X}_\alpha}{\partial x_i} + \bar{\rho}\widetilde{Y}_\alpha\underbrace{\sum_{\beta=1}^{\mathcal{N}_{sp}}\widetilde{D}_{\beta m}\frac{\mathcal{W}_\beta}{\widetilde{W}}\frac{\partial\widetilde{X}_\beta}{\partial x_i}}_{\check{V}_{ci}} \tag{3.36}$$

where $\widetilde{D}_{\alpha m}$ is the array of resolved flux diffusion coefficients of species α into the mixture and $\check{V}_{ci}$ is a corrective term used to ensure the total mass conservation. At each time step, the correction velocity $\check{V}_{ci}$ is evaluated and added to the velocity component $\widetilde{u}_i$ so as to enforce the compatibility between the discrete forms of species mass fractions and total mass conservation equations.

The resolved heat flux is given by

$$\check{q}_i = q_i\left(\bar{\rho}, \widetilde{T}, \widetilde{Y}\right) = -\widetilde{\lambda}\frac{\partial \widetilde{T}}{\partial x_i} + \sum_{\alpha=1}^{\mathcal{N}_{sp}} \check{J}_{\alpha i}\widetilde{h}_\alpha \tag{3.37}$$

Finally, the transport coefficients are estimated from their resolved counterparts:

$$\widetilde{\mu} \equiv \check{\mu} = \mu\left(\widetilde{Y}, \widetilde{T}\right) \tag{3.38}$$

$$\widetilde{D}_{\alpha m} \equiv \check{D}_{\alpha m} = D_{\alpha m}\left(\bar{\rho}, \widetilde{T}, \widetilde{Y}\right) \tag{3.39}$$

$$\widetilde{\lambda} \equiv \check{\lambda} = \lambda\left(\widetilde{T}, \widetilde{Y}\right) \tag{3.40}$$

These are the filtered Navier-Stokes equations, which were implemented, tested and studied by Techer [174] in his PhD thesis.

3.2.1 Subgrid-scale terms

The Boussinesq's framework is used to model the subgrid-scale stress tensor $\tau_{ij}^{sgs} = \overline{\rho u_i u_j} - \bar{\rho}\widetilde{u}_i\widetilde{u}_j$, with the deviatoric part being

$$\tau_{ij}^{sgs,d} = \tau_{ij}^{sgs} - \frac{1}{3}\tau_{kk}^{sgs}\delta_{ij} = -2\mu_{sgs}\left(\widetilde{S}_{ij} - \frac{1}{3}\widetilde{S}_{kk}\delta_{ij}\right) \tag{3.41}$$

where μ_{sgs} is the `SGS` eddy viscosity and τ_{kk}^{sgs} denotes the isotropic contribution of this tensor.

The `SGS` eddy viscosity μ_{sgs} is expressed by the `WALE` (Wall-Adapting Local Eddy) model of Nicoud and Ducros [135].

$$\mu_{sgs} = \bar{\rho}\left(C_w \Delta\right)^2 \frac{\left(S_{ij}^d S_{ij}^d\right)^{3/2}}{\left(\widetilde{S}_{ij}\widetilde{S}_{ij}\right)^{5/2} + \left(S_{ij}^d S_{ij}^d\right)^{5/4}} \tag{3.42}$$

where $C_w = C_s\sqrt{10.6}$ is the `WALE` model constant, $\Delta = \left(\Delta x_1 \Delta x_2 \Delta x_3\right)^{1/3}$ is the characteristic mesh size, and S_{ij}^d is the traceless symmetric part of the square of the resolved velocity gradient tensor:

$$S_{ij}^d = \frac{1}{2}\left(\frac{\partial \widetilde{u}_i}{\partial x_k}\frac{\partial \widetilde{u}_k}{\partial x_j} + \frac{\partial \widetilde{u}_j}{\partial x_k}\frac{\partial \widetilde{u}_k}{\partial x_i}\right) - \frac{1}{3}\frac{\partial \widetilde{u}_m}{\partial x_l}\frac{\partial \widetilde{u}_l}{\partial x_m}\delta_{ij} \tag{3.43}$$

This formulation was chosen because it recovers the right asymptotic behavior near walls, i.e. $\mu_{sgs} = \mathcal{O}\left(y^3\right)$ [72].

The Yoshizawa model [189] is one of the most standard models used to calculate the isotropic contribution of the subgrid-scale stress tensor. It is given by

$$\tau_{kk}^{sgs} = 2C_I\bar{\rho}\Delta^2\left\|\widetilde{S}\right\|^2 \tag{3.44}$$

where C_I is the Yoshizawa model constant, generally being equal to 0.066 according to Erlebacher et al. [54], and it does not depend on the flow Mach number.

The closure of the SGS mass flux relies on a standard turbulent diffusivity assumption, expressed in the following general form:

$$J_{\varphi,i}^{sgs} = \overline{\rho\varphi u_i} - \bar{\rho}\widetilde{\varphi}\widetilde{u}_i = \bar{\rho}\left(\widetilde{\varphi u_i} - \widetilde{\varphi}\widetilde{u}_i\right) = -\bar{\rho}\mathcal{D}_{sgs}\frac{\partial\widetilde{\varphi}}{\partial x_i} \tag{3.45}$$

where φ denotes any scalar quantity, $\mathcal{D}_{sgs} = \nu_{sgs}/\mathtt{Sc}_{sgs}$ is the turbulent diffusivity and $\mathtt{Sc}_{sgs}$ is the turbulent Schmidt number. Thus, the SGS mass flux for species α is given by

$$J_{\alpha i}^{sgs} = \overline{\rho Y_\alpha u_i} - \bar{\rho}\widetilde{Y_\alpha}\widetilde{u}_i = -\bar{\rho}\mathcal{D}_{sgs}\frac{\partial\widetilde{Y_\alpha}}{\partial x_i} \tag{3.46}$$

The SGS heat flux (from eq. 3.31) can be calculated from Eidson hypothesis [52]:

$$q_j^{sgs} = -\lambda_{sgs}\frac{\partial\widetilde{T}}{\partial x_j} \tag{3.47}$$

where $\lambda_{sgs} = {}^{(\mu_{sgs}\widetilde{c_p})}/_{\mathtt{Pr}_{sgs}}$ is the turbulent thermal conductivity and $\mathtt{Pr}_{sgs}$ is the turbulent Prandtl number (generally $0.5 \leq \mathtt{Pr}_{sgs} \leq 1.0$).

Finally, the triple velocity correlation tensor ψ_j (from eq. 3.31) can be calculated with Daly and Harlow [45] expression:

$$\psi_j = C_{c3}\nu_{sgs}\frac{\partial\tau_{kk}^{sgs}}{\partial x_j} \tag{3.48}$$

where $C_{c3} = 0.08$ is a model constant.

3.3 CREAMS solver

CREAMS (**C**ompressible **REA**ctive **M**ulti-**S**pecies) is a compressible, viscous, unsteady, multi-species, 3D and parallelized solver. It is coupled with CVODE [33, 79, 80] and EGLIB [55, 56, 57] libraries, which allow detailed chemistry and multicomponent transport effects to be taken into account. The coupling to CHEMKIN [92] library allows the solver to evaluate the transport coefficients by using JANAF tables [170]. Most of the developments of this solver have been conducted with the framework of the thesis of Martínez-Ferrer [111] and Buttay [35].

A mixture-average formulation based on a modified version of Hirschfelder and Curtiss [81] approximation has been retained, corresponding to a first-order approximation of the most detailed transport representation provided by the `EGLIB` library. The temporal integration is performed with an explicit third-order Total Variation Diminishing (`TVD`) scheme [76] (non-reactive contribution) which is compled to a `CVODE` (reactive contribution) using the Strang splitting method [169]. The treatment of the inviscid components of the conservative vector fluxes is achieved with a seventh-order accurate Weighted Essentially Non-Oscillatory (`WENO7`) reconstruction of the characteristic fluxes [11, 112]. In practice, the solver uses an optimal seventh-order accurate flux reconstruction and the application of the non-linear upwinding procedure is conditioned to a smoothness criterion based on a modified Adams and Shariff [2] shock sensor (cf. §3.3.2) [36]. The viscous and molecular diffusion fluxes are computed with an eighth-order centered difference scheme.

Given the non-linear dependence of the temperature with the thermochemical quantities, the mixture temperature cannot be calculated directly. Instead, from the total energy definition, it is calculated as the root of the following function, using the Newton-Raphson method [9]

$$f\left(T\right) = e_t + \frac{\mathcal{R}T}{\mathcal{W}} - h\left(T\right) - \frac{u_i u_i}{2} \tag{3.49}$$

The solver makes use of a Cartesian structured grid in order to facilitate de implementation of high-precision numerical schemes and the other walls that may be present in the domain are modeled with the Immersed Boundary Method (`IBM`) [27], combining direct-forcing and ghost-point-forcing algorithms (cf. §4).

3.3.1 Strang splitting method

A multi-species reactive flow is governed by several distinct time scales associated to different physical and chemical phenomena, which produces a stiff equation system. One of the difficulties related to this problem is how to solve the momentum and the chemical species equations considering the integration of the chemical source terms. An unsteady convective-diffusive problem with chemical source terms can be described by a partial differential equation

$$\frac{\partial Q}{\partial t} + \frac{\partial F_j}{\partial x_j} = \frac{\partial G_j}{\partial x_j} + S \tag{3.50}$$

with three distinct terms: a convective term F_j, a diffusive term G_j and a chemical source term S.

The reactive flow can display very stiff chemical source terms, and the chemical characteristic time can be very small compared to the convective and diffusive characteristic

times. To deal with this issue without too much loss of performance, the non-reactive parts of the equations are solved separately from the reactive parts using the Strang splitting method [169]. The solution after a time Δt calculated with the method is done by

$$Q^{n+1} = \left[L_r \left(\frac{\Delta t}{2} \right) L_i \left(\Delta t \right) L_r \left(\frac{\Delta t}{2} \right) \right] Q^n \tag{3.51}$$

with L_r and L_i corresponding to the reactive and non-reactive terms, respectively.

The non-reactive terms can be expressed as

$$\frac{\partial Q}{\partial t} = L_i \left(Q \left(t \right) \right) = -\frac{\partial F_j}{\partial x_j} + \frac{\partial G_j}{\partial x_j} \tag{3.52}$$

And the reactive terms are express as

$$\frac{\partial Q}{\partial t} = L_r \left(Q \left(t \right) \right) = S \tag{3.53}$$

The algorithm run to solve the system considering this method consists then in the following steps:

1. Solve the non-reactive part considering the initial conditions and timestep of $\Delta/2$.
2. Solve the reactive part considering the solution obtained in step 1 and a timestep of Δ.
3. Solve the non-reactive part considering the solution obtained in step 2 and a timestep of $\Delta/2$.

This strategy allows to reduce commutation errors and the same strategy is retained by several authors. The characteristics of such a symmetrized splitting scheme were analyzed by Sportisse [167].

3.3.2 Shock sensor

The presence of flow discontinuities causes an artificial increase in SGS viscosity and kinetic energy. In order to avoid that, it is necessary to weight these discontinuities through a relation like $f_{c,sk} = (1 - \sigma)$, with σ being a discontinuity sensor.

The modified shock sensor of Adams and Shariff [2] is rather simple, and it is based on the local values of the normalized spatial variations of both pressure and density.

$$\sigma = \begin{cases} 1 & \text{if } \dfrac{|\rho_{i+1} - \rho_i|}{\rho_i} \text{ and } \dfrac{|p_{i+1} - p_i|}{p_i} > \sigma_{set} \quad , \quad \forall i \in [1,3] \\ 0 & \text{else} \end{cases} \tag{3.54}$$

where σ_{set} is a user-defined value.

The Ducros et al. [50] shock sensor is used in shock/turbulence interaction problems comparing the dilatation field contribution with the vorticity one:

$$\sigma = \frac{\left(\vec{\nabla} \cdot \vec{u}\right)^2}{\left(\vec{\nabla} \cdot \vec{u}\right)^2 + \left\|\vec{\nabla} \wedge \vec{u}\right\|^2 + \epsilon} \quad , \quad \sigma \in [0,1] \tag{3.55}$$

with ϵ a tiny number used to avoid zero division. This way, the sensor is null in turbulent weakly-compressed or dilated regions ($\|\nabla \times \vec{u}\|^2 \gg (\nabla \cdot \vec{u})^2$ or $(\nabla \cdot \vec{u})^2 \approx 0$) and unity at shock locations ($(\nabla \cdot \vec{u})^2 \gg \|\nabla \times \vec{u}\|^2$).

3.3.3 Verification test cases

This section presents some academic test cases used to provide some additional verification of the `CREAMS` solver. It is noteworthy that the verification of the `IBM` will be presented in its corresponding chapter (cf. §4).

3.3.3.1 Non-reactive multi-species shock tube

This test case is a classical problem to verify the solver behavior in the presence of strong shocks, allowing for the verification of the coupling between the convective terms of Navier-Stokes equations and the multi-species thermodynamic libraries, as well as the robustness of `WENO7` scheme in the presence of strong discontinuities. It was proposed by Fedkiw et al. [65] and it is a modified version of the Sod shock tube [165].

This test case is performed by solving the Euler equations in its unidimensional form ($x \equiv x_1$ and $u \equiv u_1$), with a non-viscous compressible flow with a shock being propagated. It consists in a 10.0 cm long tube and the gas is composed of H_2, O_2, and Ar with mass fractions $(H_2, O_2, Ar) = (0.2, 0.1, 0.7)$ and conditions corresponding to the following Riemann problem:

$$\text{at } t = 0 \begin{cases} (T_L, p_L) = (400 \text{ K}, 8.0 \text{ kPa}) & \text{if } x < 5.0 \text{ cm} \\ (T_R, p_R) = (1200 \text{ K}, 80.0 \text{ kPa}) & \text{elsewhere} \end{cases} \tag{3.56}$$

The mesh is discretized with 400 points and the `CFL` value is set to 0.5.

Figure 3.1 presents the density, velocity, temperature and specific heat ratio at $t = 40.0\mu s$. The obtained results are in excellent agreement with those of Fedkiw et al. [65], indicating the same variation at the shock location ($x = 2.0$ cm), the contact discontinuity location ($x = 3.5$ cm) and the relaxation zone location (6.0 cm $\leq x \leq$ 8.0 cm) at the considered time. For the specific heat ratio profile, the difference between the reference results and the calculated ones remains below 0.1% which is quite acceptable.

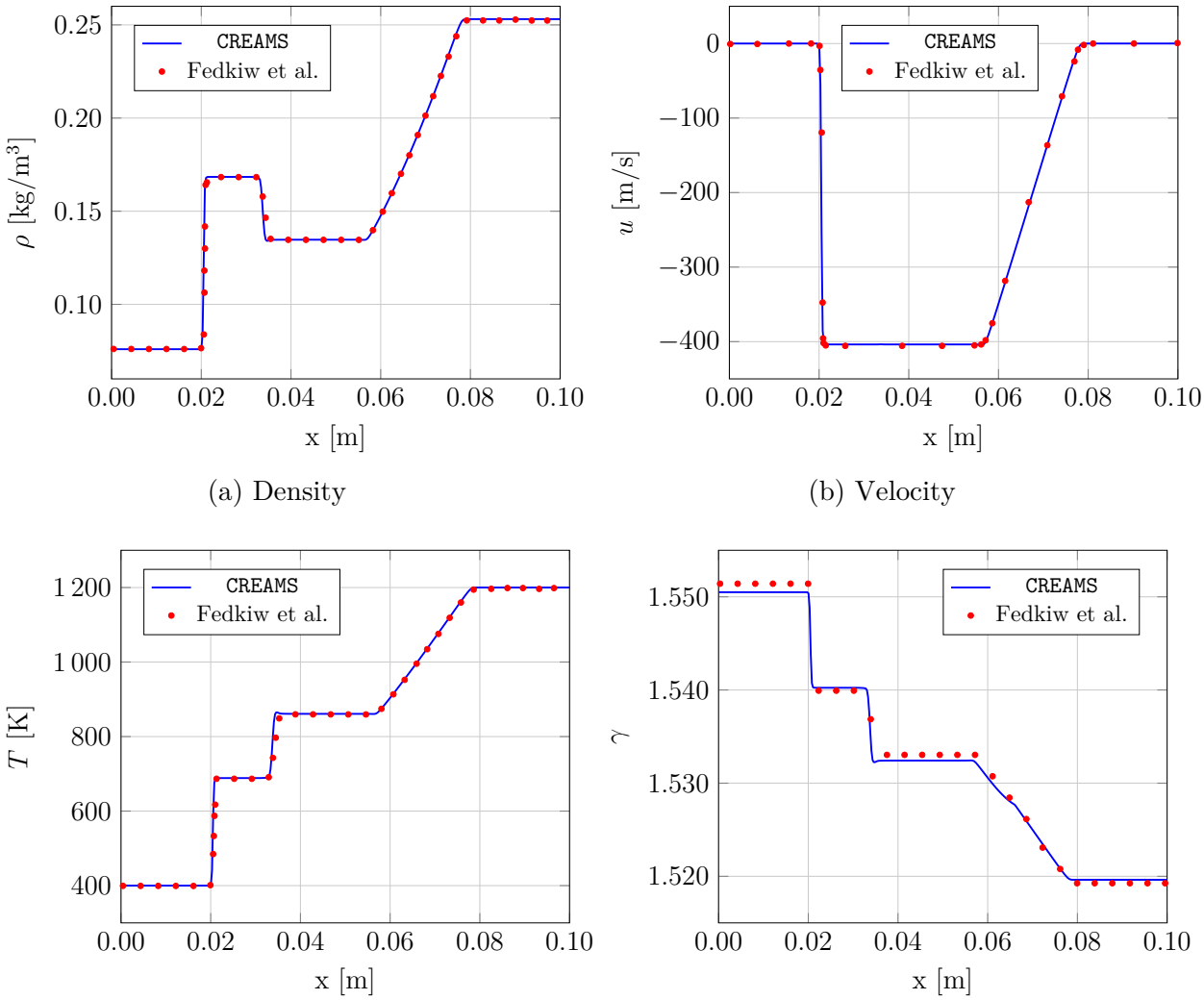

(a) Density

(b) Velocity

(c) Temperature

(d) Specific heat ratio

Figure 3.1 – Density, velocity, temperature and specific heat ratio profiles at $t = 40\mu s$

3.3.3.2 Blasius boundary layer

The objective of this test case is to verify the development of the boundary layer that is formed on a semi-infinite plate, which is held parallel to a constant unidirectional laminar flow. The similarity solution describes the formation of a boundary layer [183].

Blasius showed that the adimensional velocity profile for a laminar flat-plate flow should be similar for all streamwise positions x_1 when plotted against the non-dimensional distance from the wall [22]. The growth of the boundary layer of an incompressible flow requires some assumptions for continuity, momentum, and energy transport through the steady-state boundary layer, respectively:

$$\frac{\partial u_1}{\partial x_1} + \frac{\partial u_2}{\partial x_2} = 0 \tag{3.57}$$

$$u_1 \frac{\partial u_1}{\partial x_1} + u_2 \frac{\partial u_2}{\partial x_2} = U_\infty \frac{\partial p}{\partial x_1} + \nu \left(\frac{\partial^2 u_1}{\partial x_2^2} \right) \tag{3.58}$$

$$\rho c_p \left(u_1 \frac{\partial T}{\partial x_1} + u_2 \frac{\partial T}{\partial x_2} \right) = k \frac{\partial^2 T}{\partial x_2^2} \tag{3.59}$$

A similarity variable η is introduced in the x_1-direction:

$$\eta = x_2 \sqrt{\frac{U_\infty}{\nu x_1}} \tag{3.60}$$

with x_2 being the direction normal to the plate, U_∞ the free-stream flow velocity, ν the kinematic viscosity and x_1 the direction along the plate leading edge.

By integrating the velocity from the wall boundary, a stream function ψ can be defined:

$$\psi = \sqrt{2 \nu U_\infty x_1}\ f(\eta) \tag{3.61}$$

with $f(\eta)$ an unknown function.

The velocity components can be defined from the stream function ψ:

$$u_1 = \frac{\partial \psi}{\partial x_2} = U_\infty\ f'(\eta) \tag{3.62}$$

$$u_2 = -\frac{\partial \psi}{\partial x_1} = \sqrt{\frac{U_\infty \nu}{2 x_1}}\ \left(\eta f' - f \right) \tag{3.63}$$

where $'$ denotes differentiation with respect to η.

The velocity profile can be expressed in terms of $f'(\eta) = u_1 / U_\infty$ and η.

This test case was conducted considering ambient conditions ($T_{amb} = 300.0$ K and $p_{amb} = 1$ atm) for a bi-dimensional domain with dimensions $x_1 = 0.50$ m and $x_2 = 0.01$ m and mass fractions $(O_2, N_2) = (0.233, 0.767)$. The flow is parallel to the x_1-axis with velocity $U_\infty = 1.0$ m/s, and a slipwall boundary condition was considered in the upper part of the computational domain. The simulation was run over a relatively large time so that the boundary layer was fully developed, when the velocity profile is taken along

x_2-axis at $x_1 = 0.25$ m. The mesh contains 200 000 points (2 000 points along x_1-axis and 100 points along x_2-axis) and, along the x_2-direction, the cells are more refined near the flat plate.

Figure 3.2 presents the numerical results and the analytical Blasius solution [157] and one can notice that the simulation results are in good agreement with the reference solution. The growth of the boundary layer accelerates the fluid elsewhere to keep pace with fluid continuity and, as a result, the free-stream velocity becomes slightly higher than U_∞.

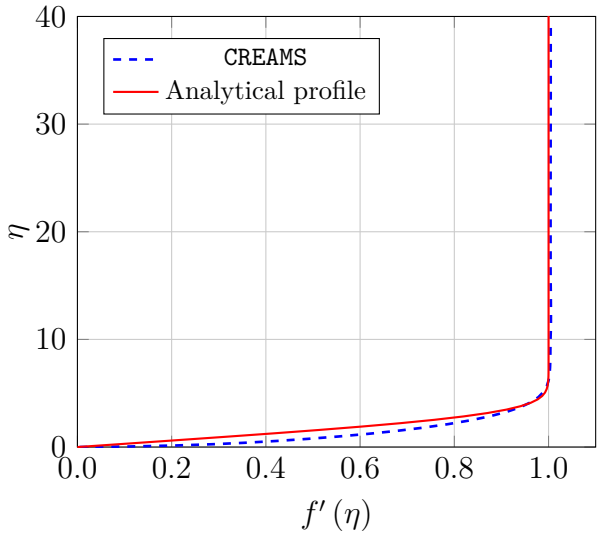

Figure 3.2 – Simulated and analytical Blasius profile results

3.3.3.3 Taylor-Green vortex

Since `CREAMS` deals with unsteady flow, the simulation is both space and time dependent. This test cases is aimed at verifying quantitatively the numerical accuracy of the solver when running a 2D problem. The same simulation was run with different mesh resolutions and timesteps and the ℓ^2-norm of the error is then verified.

The ℓ^2-norm basically minimizes the sum of the square of the differences (S) between the target (y_i) and estimated values ($f(x_i)$):

$$S = \sum_{i=1}^{n} \left(y_i - f(x_i)\right)^2 \tag{3.64}$$

The initial flow field is given by:

$$u_1 = V_0 \cos(x_1) \sin(x_2) \tag{3.65}$$

$$u_2 = -V_0 \sin(x_1) \cos(x_2) \tag{3.66}$$

$$p = p_0 + \frac{\rho_0 V_0^2}{16}\left(\cos\left(\frac{2x_1}{L}\right) + \cos\left(\frac{2x_2}{L}\right)\right) \tag{3.67}$$

$$T = T_0 \tag{3.68}$$

with the reference length (L), pressure (p_0) and temperature (T_0) being, respectively, 1 m, 10^5 Pa and 300 K. The flow velocity (V_0) and density (ρ_0) are calculated as the numerical simulation proceeds, with U_0 corresponding to $M = 0.1$, and the mass fractions are $(O_2, N_2) = (0.233, 0.767)$.

The low Mach number flow simulation is governed by the 2D compressible Navier-Stokes equations with constant physical properties. The Mach number must indeed be small enough so that the calculated solutions for pressure and vorticity fields are indeed very close to those obtained assuming an incompressible flow.

The Reynolds number is constant and defined as:

$$Re = \frac{\rho V_0 L}{\mu} = 20\,000 \tag{3.69}$$

with μ being the dynamic viscosity and it is calculated *on-the-fly*.

The considered domain is a square box, defined as $-\pi L \leq (x_1, x_2) \leq \pi L$ and no special boundary conditions are required since the domain is periodic.

At any point (i, j), and for a given level of numerical resolution, ψ^h is defined as the discrete value of any variable of interest, e.g. pressure or vorticity, and ψ^e the corresponding value of the reference solution. The ℓ^2-norm is used to calculate the error decay rate obtained when mesh resolution is increased, and it is defined below:

$$\ell^2\left(\psi^h_{(i,j)}\right) = \sqrt{\frac{1}{m}\frac{1}{n}\sum_{i=1}^{m}\sum_{j=1}^{n}\left(\psi^h_{(i,j)} - \psi^e_{(i,j)}\right)^2} \tag{3.70}$$

where $m = n$ being the total number of points in x_1 or x_2-axis.

Table 3.1 presents the meshes that were considered to proceed with this test case:

Mesh resolution	**Number of points**
16×16	256
32×32	1 024
64×64	4 096
128×128	16 384
256×256	65 536

Table 3.1 – Mesh resolutions and number of points

The timesteps considered are shown in table 3.2:

Timesteps (Δt)		
7.0×10^{-5}	7.0×10^{-6}	7.0×10^{-7}
6.0×10^{-5}	5.0×10^{-6}	5.0×10^{-7}
5.0×10^{-5}	4.5×10^{-6}	2.5×10^{-7}
4.0×10^{-5}	3.0×10^{-6}	1.6×10^{-7}
3.0×10^{-5}	2.0×10^{-6}	1.2×10^{-7}
2.0×10^{-5}	1.2×10^{-6}	1.0×10^{-7}
1.0×10^{-5}	1.0×10^{-6}	

Table 3.2 – Considered timesteps

Figure 3.3 presents the ℓ^2-norm of the numerical error based on the pressure field (fig. 3.3a) and vorticity field (fig. 3.3b) for different levels of spatial resolution ($N = 16, \ldots, 256$).

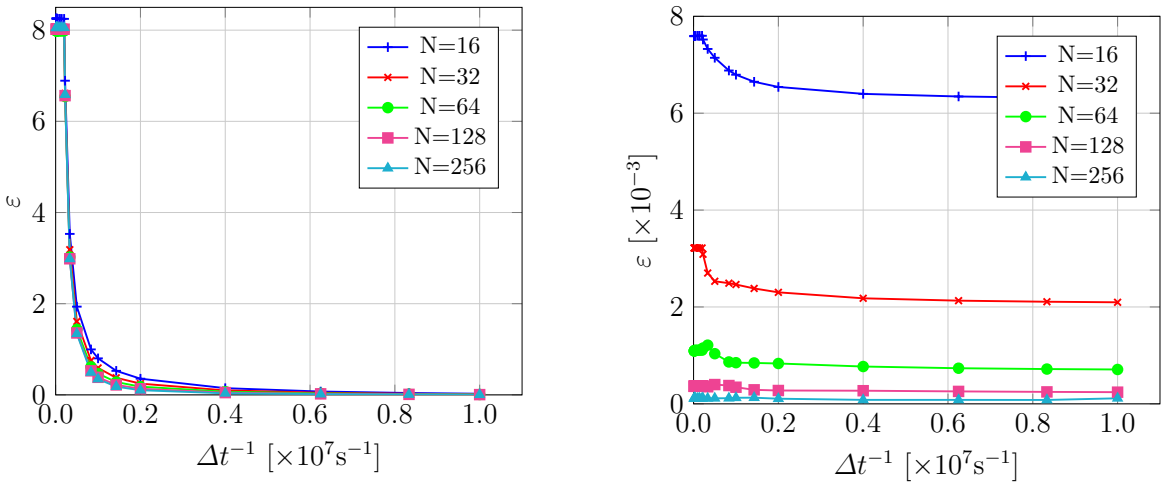

(a) Pressure

(b) Vorticity

Figure 3.3 – $\mathcal{L}^2$-norm of the error for different levels of spatial resolution

The verifications discussed above refer to an unsteady problem, which is both space and time dependent. However, as the timestep decreases, there will be one where we can consider that the solution no longer displays any dependence to time discretization: $\Delta t^{-1} = 4.0 \times 10^6 \text{ s}^{-1} \rightarrow \Delta t = 2.5 \times 10^{-7}$ s.

Figure 3.4 presents the ℓ^1, ℓ^2 and ℓ^∞-norm of the numerical error based on the pressure field (fig. 3.4a) and vorticity field (fig. 3.4b).

As expected, the error norm decreases by increasing the resolution level. The ℓ^2-norm evolution is also plotted for pressure and vorticity in figure 3.5 together with the 6^{th} order of convergence line.

The observed tendency show that the order of convergence of the ℓ^2-norm is around the 6^{th} order. It is a little bit less than 6 for values of N smaller than one hundred, and

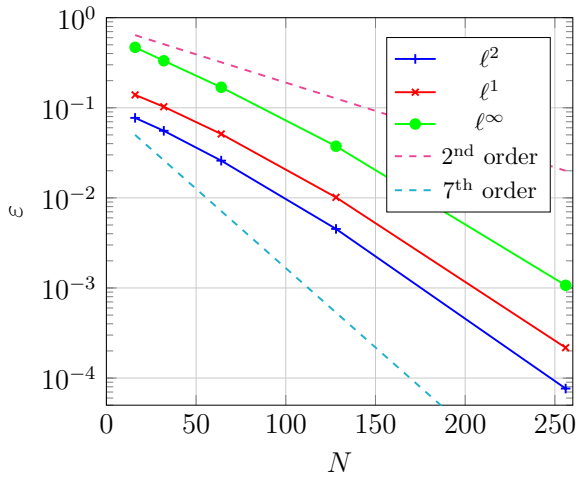

(a) Pressure

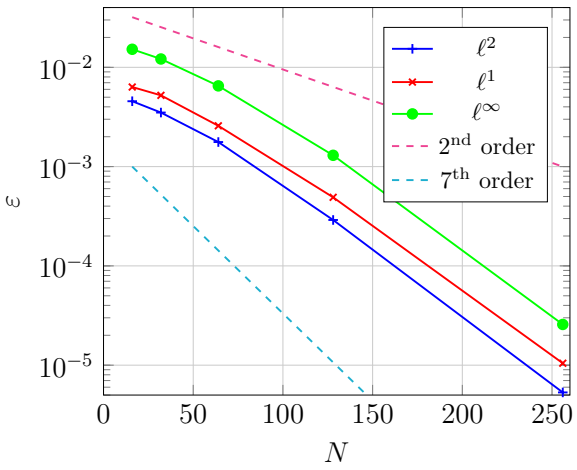

(b) Vorticity

Figure 3.4 – Analysis of the order of convergence of the error norm

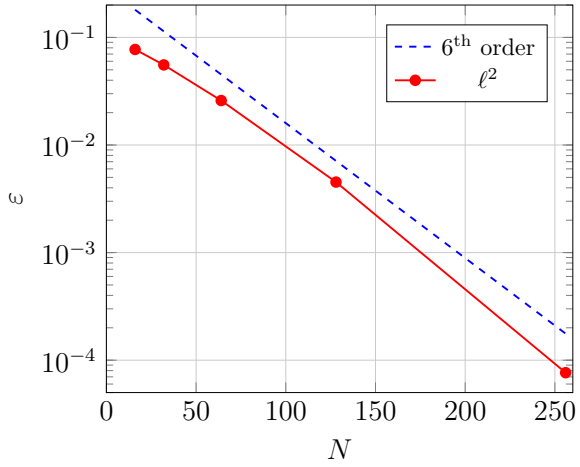

(a) Pressure

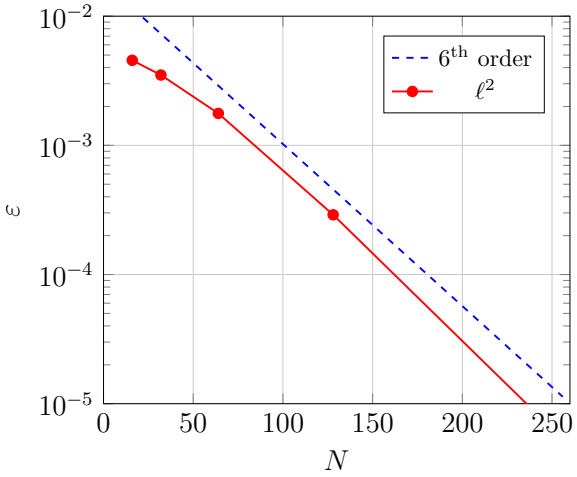

(b) Vorticity

Figure 3.5 – Order of convergence of the error norm

a little bit more than 6 for $N > 100$. These values can be considered as a convergence of order 6, which is a good value considering that `CREAMS` is 8^{th} order.

Summary

The main thermodynamic relations used to describe a perfect gas mixture and some theoretical elements concerning chemical reactions have been presented in this chapter. The Navier-Stokes equations and the molecular fluxes and associated transport coefficients have been introduced. `EGLIB` and `CHEMKIN` libraries are used to calculate the simplified transport properties and the chemical kinetics from the different reaction mechanisms.

Turbulence modelling is also presented in this chapter, Direct Numerical Simulation (DNS) indeed remains prohibitive for complex turbulent flows. The filtered Navier-Stokes equations are therefore presented together with the subgrid-scale closures retained for the velocity field and SGS transport.

CREAMS performs the temporal integration with a TVD scheme for the non-reactive terms and CVODE for the reactive terms. Both are coupled using the Strang splitting method. Two shock sensors can be used to avoid any artificial increase in the SGS viscosity due to discontinuities.

Some elementary test cases are run to validate the solver: non-reactive multi-species shock tube, Blasius boundary layer development and Taylor-Green vortex. They were chosen so as to verify its behavior in the presence of strong shocks, to verify the coupling between the convective terms of Navier-Stokes equations and the multi-species thermodynamic libraries, the boundary layer development and the solver accuracy.

The scramjet combustion chamber that will be considered as an application test case features a wall-mounted cavity, which must be modeled in the computational domain. This is achieved by making use of an IBM approach, which is described in the next chapter.

Chapter 4

Immersed Boundary Method

4.1 General introduction

This chapter is focused on the description and implementation of the immersed boundary method (IBM), which is used to model a solid obstacle (cavity) into the computational domain. Two approaches (continuous forcing and discrete forcing methods) and some verification test cases will be presented. A part of the corresponding results have been presented in reference [28].

The numerical investigation of fuel-air mixing and combustion in a scramjet combustion chamber must take into account its complex geometry. Since the flow Mach number is high, an adequate numerical treatment of shock waves must be achieved using high-resolution shock-capturing techniques in the discretization of the convective fluxes [11].

The combustion chamber geometry can be modeled using several techniques, such as coordinate transformations, body-fitted structured and unstructured grids, immersed boundaries or fictitious domain approaches. A very efficient strategy to simulate flows around obstacles or complex geometries in general is the use of body-fitted unstructured grids. In the presence of strong shocks, however, standard numerical schemes applied on unstructured grids may suffer from large dispersive and dissipative errors when compared to those resulting from the use of high-resolution schemes on structured grids.

In order to keep pace with the use of high-order finite difference schemes applied on Cartesian grid, the Immersed Boundary Method (IBM) is then chosen to be used in conjunction with the CREAMS solver. This method has some advantages over conventional body-fitted approaches when simulating flows with moving boundaries, complicated shapes or topological changes [187].

Peskin [138, 139] developed the principles of the immersed boundary framework in his

studies of blood flow in hearts, being followed by several proposed and developed strategies [74, 94]. The main idea is to use a regular Eulerian mesh for the fluid dynamics simulation coupled with a Lagrangian representation of the immersed boundary that exerts a singular force on the fluid. The mask methodology used to identify fluids and solids in the domain was proposed by Briscolini and Santangelo [32] and it is used to impose a zero velocity condition at the immersed boundary.

In order to describe this method, one can consider a calculation domain Ω with an immersed solid body in a viscous incompressible flow. This domain can be divided into a fluid part Ω_F, a solid part Ω_S, and a solid/fluid interface $\Gamma = \Omega_F \cap \Omega_S$, as shown by figure 4.1. For sake of simplicity, the discretization of the fluid space will be denoted as Eulerian and the discretization of the solid space will be denoted as Lagrangian.

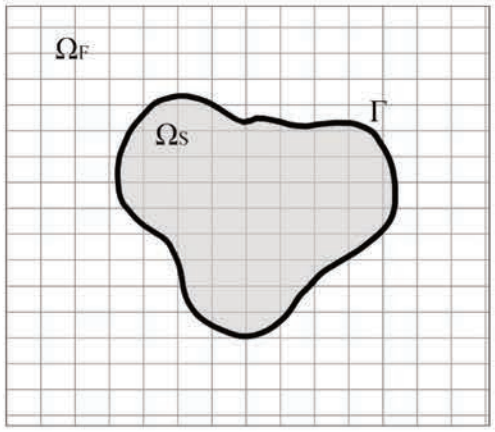

Figure 4.1 – Structured mesh with an immersed boundary and its decomposition

In an incompressible flow, the governing equations are done by the following system of equations:

$$\begin{cases} \dfrac{\partial u_i}{\partial t} + u_j \dfrac{\partial u_i}{\partial x_j} = -\dfrac{1}{\rho}\dfrac{\partial p}{\partial x_i} + \nu \dfrac{\partial^2 u_i}{\partial x_j^2} & \text{in } \Omega_F \quad (4.1a) \\ \dfrac{\partial u_i}{\partial x_i} = 0 & \text{in } \Omega_F \quad (4.1b) \\ u_i = u_{s,i} & \text{in } \Omega_S \quad (4.1c) \end{cases}$$

with $u_{s,i}$ being the solid velocity components.

The `IBM` method consists in the discretization of equations 4.1a and 4.1b over a Cartesian mesh considering the immersed body by imposing the boundary condition 4.1c. There are several methods to impose this boundary condition on the immersed body, but they can be divided in two main classes, according to Iaccarino and Verzicco [89]: continuous forcing method (cf. §4.2) and discrete forcing method (cf. §4.3). These two methods

differs on the way the forcing term is added to the Navier-Stokes equations.

4.2 Continuous forcing method (CFM)

This method was originally proposed by Peskin [138] and consists in adding a forcing function to equation 4.1a, which then becomes:

$$\frac{\partial u_i}{\partial t} + u_j \frac{\partial u_i}{\partial x_j} = -\frac{1}{\rho}\frac{\partial p}{\partial x_i} + \nu \frac{\partial^2 u_i}{\partial x_j^2} + f_i^L \qquad \text{in } \Omega_F \tag{4.2}$$

with $f^L = \left(f_1^L, f_2^L, f_3^L\right)$ being the forcing term.

The general form of the discretized equations then becomes:

$$\left[\mathcal{A}\left(u\right)\right]\left\{U\right\} = \left\{f^L\right\} \qquad \text{in } \Omega \tag{4.3}$$

with $\left[\mathcal{A}\left(u\right)\right]$ being the incompressible Navier-Stokes equations discrete operator, $\left\{U\right\} = \left\{u, p\right\}$ and $\left\{f^L\right\}$ the discrete forcing function.

Arquis and Caltagirone [8] developed a similar approach overcoming some disadvantages of the original method of Peskin, such as fluid-solid numerical leaks at the interfaces due to the non-conservation of the mass at the Lagrangian particles level. This new approach was subsequently improved by Angot et al. [7] and consists in the use of a porous medium to define the forcing terms. The whole domain Ω is considered as being composed of several different mediums: fluid medium Ω_F, porous medium Ω_p and solid medium Ω_S, each one having its own permeability constant.

$$\xi\left(x\right) = \begin{cases} \xi_f \to \infty & \text{in } \Omega_F \\ \xi_p & \text{in } \Omega_p \\ \xi_s \to 0^+ & \text{in } \Omega_S \end{cases} \tag{4.4}$$

A drag force term f^L is then added to the Navier-Stokes equation over the whole domain Ω:

$$\begin{cases} \dfrac{\partial u_i}{\partial t} + u_j \dfrac{\partial u_i}{\partial x_j} + \dfrac{1}{\rho}\dfrac{\partial p}{\partial x_i} - \nu \dfrac{\partial^2 u_i}{\partial x_j^2} = f_i^L & \text{(4.5a)} \\ \dfrac{\partial u_i}{\partial x_i} = 0 & \text{(4.5b)} \end{cases}$$

with f^L being defined as:

$$f^L = -\frac{\varepsilon}{\xi}(u - u_s) \tag{4.6}$$

and ε being the Heaviside function:

$$\varepsilon = \begin{cases} 0 & \text{in } \Omega_F \\ 1 & \text{in } \Omega_S \end{cases} \tag{4.7}$$

Equation 4.6 allows a non-slip condition over a solid body by penalizing the velocity. All volumes that contains a solid part must have a permeability constant ξ_p.

This method can be easily implemented since it only consists in adding an algebraic term in the momentum equations and it does not depend on the spatial discretization. It is also well suited to low Reynolds number flows. However, the smoothing of the forcing function results in a poor boundary modelling, restricting its use to low Reynolds number flows. Moreover, since the permeability function ξ must be very small in order to obtain a precise solution, the source term becomes very stiff as ξ becomes smaller, which can be troublesome. Finally, around the fictitious wall, the boundary layer thickness exhibits some dependency to the specification of f^L.

4.3 Discrete forcing method (DFM)

This method consists in the discretization of equation 4.1a without any modification in the fluid domain and the forcing term is applied implicitly or explicitly on the points near the solid/fluid interface Γ. The general form of the linear system to be solved is:

$$\left[\mathcal{A}'(u)\right]\{U\} = \{\mathcal{F}^L\} \qquad \text{in } \Omega \tag{4.8}$$

with $[\mathcal{A}'(u)]$ being the modified incompressible Navier-Stokes equations discrete operator, $\{U\} = \{u, p\}$ and $\{\mathcal{F}^L\}$ the terms that allows the imposition of the boundary conditions.

Mohd-Yusof [120] proposed the discrete forcing method in order to solve the restrictions related to the continuous forcing approach method, such as not being suitable to high Reynolds number flows. It consists in calculating the forcing term directly from the numerical solution. One of the main challenge of this method is to correctly model the boundary layer over immersed bodies.

Tseng and Ferziger [177] applied the forcing term on what they called the "ghost zone", located inside the immersed bodies. This "ghost zone" is composed of all the points of the mesh, called "ghost points", belonging to the solid domain.

The Navier-Stokes equations for incompressible flows with the corresponding forcing terms are illustrated below, considering the fluid domain Ω_F:

$$\begin{cases} \dfrac{\partial u_i}{\partial t} + u_j \dfrac{\partial u_i}{\partial x_j} + \dfrac{1}{\rho}\dfrac{\partial p}{\partial x_i} - \nu \dfrac{\partial^2 u_i}{\partial x_j^2} = f_i^L \xi_{GZ} & \text{(4.9a)} \\ \dfrac{\partial u_i}{\partial x_i} = 0 & \text{(4.9b)} \end{cases}$$

where $f^L = \left(f_1^L, f_2^L, f_3^L\right)$ is the forcing term and ξ_{GZ} is the ghost zone marker function. Considering an Euler-type temporal scheme, regardless of the spatial discretization scheme, and applying a Dirichlet condition $u = u_s$, it implies the imposition of the following forcing term at time $t = n + 1$:

$$f_i^{L,n+1} = \frac{u_{s,i} - u_i^n}{\Delta t} + u_j \frac{\partial u_i}{\partial x_j} + + \frac{1}{\rho}\frac{\partial p}{\partial x_i} - \nu \frac{\partial^2 u_i}{\partial x_j^2} \tag{4.10}$$

In order to calculate the velocity imposed to the ghost points it is necessary to extrapolate the data since the Dirichlet condition is not applied on a Cartesian mesh point. The procedure adopted to solve the momentum equations with this method consists in locating the fluid-solid interface, identifying the ghost points and extrapolating the data around them to impose the boundary conditions.

Figure 4.2 illustrates the ghost-point approach, where G is the ghost point, X_1 and X_2 are the two fluid points closer to the solid boundary and O is the image point, that is the node where the immersed boundary condition will be applied.

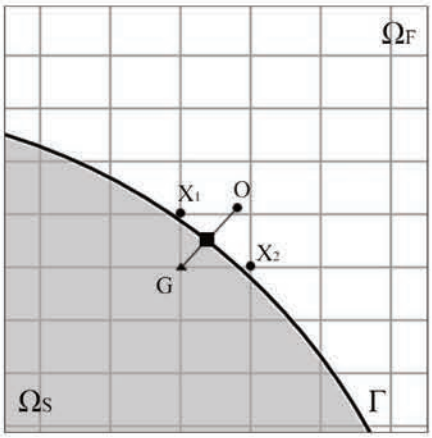

Figure 4.2 – Ghost points illustration

A 2D linear interpolation of any scalar quantity φ is expressed as $\varphi = a_0 + a_1 x_1 + a_2 x_2$, with the coefficients a_n ($n \in [\![0, 2]\!]$) being calculated from a linear interpolation in terms of $\{\varphi\} = (\varphi_1, \varphi_2, \varphi_3)$ over nodes O, X_1 and X_2, respectively.

$$\{\mathcal{A}\} = [\mathcal{B}]^{-1} \{\varphi\} \tag{4.11}$$

with

$$\{\mathcal{A}\} = (a_1, a_2, a_3) \tag{4.12}$$

and

$$[\mathcal{B}] = \begin{pmatrix} 1 & x_1|_O & x_2|_O \\ 1 & x_1|_{x_1} & x_2|_{x_1} \\ 1 & x_1|_{x_2} & x_2|_{x_2} \end{pmatrix} \tag{4.13}$$

Once the coefficients a_n are known, the value φ over the ghost point G can be calculated by extrapolation. There is however a drawback about extrapolating over the ghost point: numerical instabilities may appear when the point O is very close to a fluid point used for extrapolation because a_n tends to be very negative, leading to a very slow solution convergence. One way to avoid this problems consists in changing locally the solid/fluid interface location so that the point O is on the same fluid point location.

This method works very well with fluids at high Reynolds number, however since the forcing term is calculated from the numerical solution, it is very dependent on the numerical scheme used in the solver.

4.4 Implementation

The implementation of the continuous forcing method (`CFM`) is based on the works of Silva et al. [162], who considered an approach called *Physical Virtual Model* (herein called `PVM`). The discrete forcing method implementation is inspired from the works of Chaudhuri et al. [39], who developed the *Ghost-Point Method* (`GPM`).

For a successful implementation of these two methods into `CREAMS` code, some steps must be followed (more details can be found in the thesis of Boukharfane [26]):

- Identification of the Lagrangian points, in order to identify solid and fluid points in the Eulerian mesh.
- Identification of the interpolation points (`CFM`), ghost points and image points (`GPM`).
- Calculation of the forcing term (`CFM`) and treatment of the ghost points (`GPM`).
- Validation of the `CFM-GPM` coupling.

An important step to be taken before coding the `CFM` or the `GPM` methods is the identification of the immersed body: the stereolithography format (`STL`) was chosen to

describe the immersed body since it is widely used for rapid prototyping, 3D printing and computer-aided manufacturing [41], easing the process of importing the immersed body into the computational domain. This format describes the surface geometry of a 3D object using several triangles T^L with $L = 1, \ldots, \mathcal{N}_{tr}$, where $\mathcal{N}_{tr}$ is the total number of triangles. Each triangle is defined by the Cartesian coordinates of its vertices and a normal vector describing the orientation of its surface, as shown by figure 4.3.

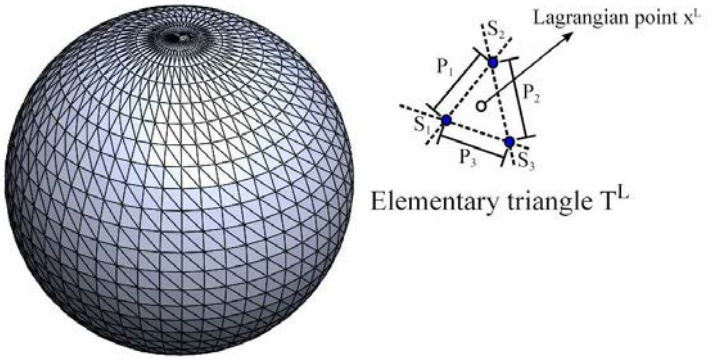

Figure 4.3 – Triangulated representation of the surface of an immersed body and definition of the Lagrangian point in the elementary triangle

The basic structure of a `STL` file is presented below:

```
solid name
  facet normal n_i n_j n_k
    outer loop
      vertex v1_x1 v1_x2 v1_x3
      vertex v2_x1 v2_x2 v2_x3
      vertex v3_x1 v3_x2 v3_x3
    endloop
  endfacet
endsolid name
```

It must start with the lowercase keyword **solid** and ends with **endsolid** with *name* being an optional parameter to identify the solid. Within these keywords are the individual triangles that describes the faces of a solid model consisting in a single normal vector directed away from the solid's surface, with coordinates n_i, n_j and n_k and inside the *loop* directives are the coordinates of the vertices of the triangle.

This format is specially interesting for the application of the `CFM` method since each triangle T^L defines, through its vertices, a single Lagrangian point located in its gravity center. However, in order to describe a smooth curve it requires a very refined mesh.

Once the STL file is read, the next step consists in flagging the Eulerian points as *solid* or *fluid*. This is specially important if the immersed body is moving, since the point flag may change during the execution of the code. A marker field ζ is then defined to identify these zones:

$$\zeta(x,t) = \begin{cases} 0 & \text{if } x = (x_1, x_2, x_3)^t \in \Omega_F \\ 1 & \text{if } x = (x_1, x_2, x_3)^t \in \Omega_S \end{cases} \tag{4.14}$$

where the whole computational domain is $\Omega = \Omega_F \cup \Omega_S$ and the solid/fluid interface is $\Gamma = \Omega_F \cap \Omega_S$.

The main issue in the flagging procedure is to determine if the Eulerian point P is inside or outside the solid body. There are several methods to address that, such as ray-casting, winding number and ray-tracing methods (RT), the last one being presently chosen since it is the most documented [23, 47].

The RT is based on Jordan theorem [166] and consists in tracing rays from an Eulerian point P to any point S far from the immersed body and calculating the number of intersections with the Lagrangian mesh, which are the immersed body edges. If the number of intersections is even then the point P is located in the fluid zone (outside the solid body, figure 4.4, point P_1), otherwise it is in the solid zone (inside the solid body, figure 4.4, point P_2). This algorithm may fail when used on complicated surface geometries, but it can be corrected by using additional random rays.

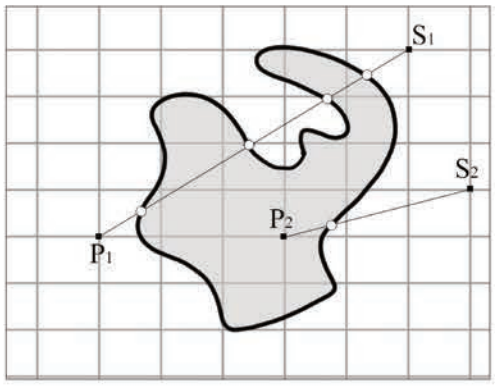

Figure 4.4 – Ray-tracing method

The efficiency of this procedure can be improved by defining a bounding box around the solid body, being the smallest one to contain all the vertices defining the surface of the immersed body. All points outside this box is thus considered to be in the fluid zone.

Once all the points are labeled as solid ($\zeta = 1$) or fluid ($\zeta = 0$), the CFM and the GPM methods can be applied.

4.4.1 Continuous forcing method

The continuous forcing method (CFM) consists of modelling the forcing term f^L of equation 4.2. The main idea is the reconstruction of the flow over the Lagrangian points using a forcing term or a transfer function in order to spread the immersed boundary effects over the Cartesian mesh. It is important to notice that this methods does not add any constant that needs to be adjusted to the flow equations. It does not require any interpolation scheme in the neighborhood of the Lagrangian points, and only adds a source term ρf_i^L in the scalar and energy conservation equation. For instance, the species mass fraction transport equation becomes:

$$\frac{\partial \rho Y_\alpha}{\partial t} + \frac{\partial \rho Y_\alpha u_i}{\partial x_i} = -\frac{\partial J_{\alpha i}}{\partial x_i} + \rho \dot{\omega}_\alpha + \rho f_i^L \quad , \quad \alpha = 1, \ldots, \mathcal{N}_{sp} \tag{4.15}$$

where the term f_i^L is calculated from the Lagrangian force field F_i^L, which is nothing more than the body force source term resulting from the influence of the immersed body over the fluid. This source term can be calculated with the following equation:

$$f^L(x) = \left(f_1^L, f_2^L, f_3^L\right)^t = \int_\Gamma F^L\left(x^L(s,t)\right)\, \delta\left(x - x^L(s,t)\right)\, \mathrm{d}s \tag{4.16}$$

with F^L being the Lagrangian force density, $x^L(s,t)$ the coordinates of the Lagrangian marker belonging to the immersed boundary, δ the Dirac delta function and $x \equiv (x_1, x_2, x_3)^t$ any Eulerian grid point. Each Lagrangian point x^L is located in the gravity center of the triangle T^L. It is worth recalling that $F^L\left(x^L(s,t)\right)\,\mathrm{d}s$ represents the force applied by the elementary surface of the immersed body $\mathrm{d}s$ to the fluid.

The discrete approximation of the Dirac delta function can be calculated from the expression suggested by Peskin [140]:

$$\delta\left(x - x^L(s,t)\right) \simeq \mathcal{D}\left(x, x^L\right) \tag{4.17a}$$

$$\mathcal{D}\left(x, x^L\right) = \mathcal{D}_1\left(\frac{x_1 - x_{l_1}}{\Delta x_1}\right)\mathcal{D}_1\left(\frac{x_2 - x_{l_2}}{\Delta x_2}\right)\mathcal{D}_1\left(\frac{x_3 - x_{l_3}}{\Delta x_3}\right)\Delta v_x^{-1} \tag{4.17b}$$

with $\Delta v_x = (\Delta x_1 \Delta x_2 \Delta x_3)$ being the elementary volume of the computational cell. Function $\mathcal{D}_1$ is defined as:

$$\mathcal{D}_1(\xi) = \begin{cases} \mathcal{D}_2(\xi) & \text{if } \|\xi\| \leq 1 \\ 0.5 - \mathcal{D}_2(2 - \|\xi\|) & \text{if } 1 < \|\xi\| \leq 2 \\ 0.0 & \text{if } 2 < \|\xi\| \end{cases} \tag{4.18}$$

with $\xi = x_i/\Delta x_i$ and $\mathcal{D}_2(\xi) = \left(3 - 2\|\xi\| + \sqrt{1 + 4\|\xi\| - 4\|\xi\|^2}\right)/8$.

Previous numerical simulations confirmed that the expression presented by 4.17 is associated to a good cost-benefit compromise between accuracy and computational cost [31]. Moreover, this is the most common delta function discretization applied to immersed boundary simulations. It is used to calculate the fluid velocity over a Lagrangian point ($u\left(x^L\right)$), which is then used to express the force density distribution $F^L\left(x^L\right)$, defined as:

$$F^L\left(x^L\right) = \frac{u^L - u\left(x^L\right)}{\Delta t} \tag{4.19}$$

where $u^L = \left(u_1^L, u_2^L, u_3^L\right)$ is the immersed body velocity (zero if motionless) and $u\left(u^L\right)$ is calculated with the following equation:

$$u\left(x^L\right) = \sum^{\mathcal{N}_{int}} \mathcal{D}\left(x, x^L\right) u\left(x\right) \Delta v_x \tag{4.20}$$

with $\mathcal{N}_{int}$ being the total number of Eulerian points used in the interpolation of the Lagrangian point x^L, which is determined by defining a sphere (or a circle in 2D cases) of radius r around x^L, as shown by figure 4.5. In order to guarantee a good numerical accuracy and low computational costs, the value of this radius is chosen such as $r \geq 3.5 \max\left(\Delta x_1, \Delta x_2, \Delta x_3\right)$. All points inside this sphere/circle are used in the interpolation process.

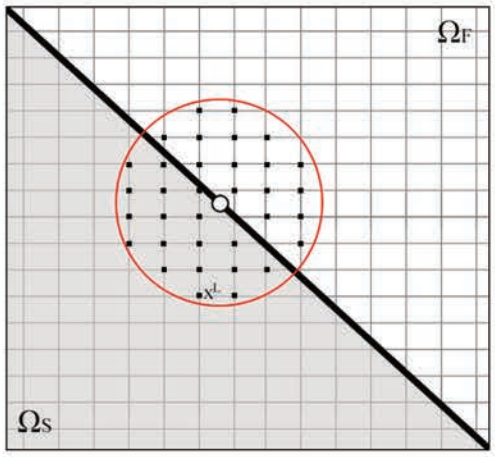

Figure 4.5 – Radius determining the number of Lagrangian points used to perform the interpolation

The Lagrangian forcing term is then calculated from the force density distribution F^L over Γ (eq. 4.19) by summing over all the elementary triangles T^L of the immersed body surface:

$$f^L\left(x\right) = \sum^{\mathcal{N}_{tr}} \mathcal{D}\left(x, x^L\right) F^L\left(x^L\right) \Delta V_{tr}^L \tag{4.21}$$

where ΔV_{tr}^L is the characteristic volume of the elementary triangle T^L associated to

the Lagrangian point x^L (fig. 4.3), defined as the product of the triangle characteristic length ΔS^L_{tr} and area ΔA^L_{tr}, i.e. $\Delta V^L_{tr} = \Delta S^L_{tr} \Delta A^L_{tr}$. The characteristic area ΔA^L_{tr} can be calculated using Heron's formula $\Delta A^L_{tr} = \sqrt{P\left(P-P_1\right)\left(P-P_2\right)\left(P-P_3\right)}$, where $P = {}^{(P_1+P_2+P_3)}/_2$, and the characteristic length is $\Delta S^L_{tr} = {}^{(P_1+P_2+P_3)}/_3$.

4.4.2 Ghost-point method

In subsonic flows the kinetic energy can be considered negligible with respect to thermal energy, which means that the energy budget is not affected by the immersed boundary procedure that is applied to the momentum equation. However, the treatment of energy equation requires further attention when dealing with supersonic flows. The ghost-point method is used to set the boundary conditions at the immersed body for scalar quantities, i.e. density, energy and mass fraction. The quantities at the ghost points are imposed based on the parameters of the points in the fluid zone.

Ghost points (GP) are the points in the solid domain Ω_S closer to the fluid domain Ω_F. In order to keep pace with the number of points required by the `CREAMS` stencils, the ghost points here consist in three layers of points near the immersed body wall, being defined as:

$$\Omega_{GP} = \{\left(x_{1,m}, x_{2,n}, x_{3,p}\right)^t \in \Omega_S \text{ if } \exists \left(x_{1,i}, x_{2,j}, x_{3,k}\right)^t \in \Omega_F, i \in I_m \vee j \in I_n \vee k \in I_p\} \quad (4.22)$$

where $I_m = [m-3, m+3]$, $I_n = [n-3, n+3]$ and $I_p = [p-3, p+3]$. If the immersed body is not moving, the ghost points zone Ω_{GP} is calculated only once, at the beginning of the simulation.

Each ghost point implies a vector normal to the nearest boundary triangle used to locate its corresponding image point (IP) in the fluid domain, defined as:

$$\Omega_{IP} = \{(x_1^*, x_2^*, x_3^*) \in \Omega_F, \exists!\, (x_1, x_2, x_3)^t \in \Omega_{GP} \wedge h\left[(x_1^*, x_2^*, x_3^*) \perp T^L\right] = h\left[(x_1, x_2, x_3) \perp T^L\right]\} \quad (4.23)$$

where $h\left[(x_1, x_2, x_3) \perp T^L\right]$ denotes the orthogonal distance from a given point (x_1, x_2, x_3) to its closest elementary triangle T^L. The `STL` format gives directly the normal vector for each triangle. Figure 4.6 presents the identification of an image points from its corresponding ghost point, where GP, BP, IP, NP_k and SP represent ghost point, boundary point, image point, Eulerian point used for interpolation and solid point, respectively.

One can notice that most of the time the image point will not be in the same position of a mesh node, so its flow field variable φ must be calculated by interpolating the flow field variables at the surrounding neighboring nodes NP_k (8 nodes for 3D, 4 nodes for

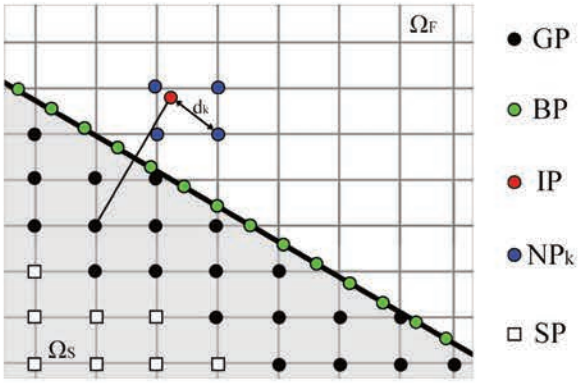

Figure 4.6 – Image point identification from its corresponding ghost point

2D). This can be done using an inverse distance weighting: defining $d_k = \|x_{IP} - x_k\|$ as the distance between the image point IP and each neighboring fluid point NP_k, the variable $\varphi(x_{IP})$ can be calculated as:

$$\varphi(x_{IP}) = \sum_{k=1}^{\mathcal{N}_{npt}} \varphi_{NP_k} \Phi_k \tag{4.24}$$

where $\mathcal{N}_{npt}$ is the total number of neighborhood points (8 for 3D, 4 for 2D) and $\Phi_k = d_k^{-2} / \sum_{i=1}^{\mathcal{N}_{npt}} d_i^{-2}$. When $d_k \to 0$ (fig. 4.7) the contribution of NP_l ($l \neq k$) can be neglected to enforce $\varphi_{IP} = \varphi_{NP_k}$.

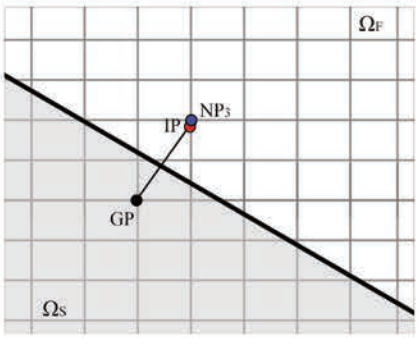

Figure 4.7 – Image point near a mesh node point

Moreover, points belonging to the solid domain ($NP_k \in \Omega_S$), as shown in figure 4.8, are not taken into account, being excluded from the interpolation procedure.

The flowfield variable at the image points IP are then evaluated from:

$$T_{IP} = \sum^{k} \Phi_k T_{NP_k} \tag{4.25a}$$

$$p_{IP} = \sum^{k} \Phi_k \frac{\rho_{NP_k} T_{NP_k} \mathcal{R}}{\mathcal{W}_{NP_k}} \tag{4.25b}$$

$$Y_{\alpha,IP} = \sum^{k} \Phi_k Y_{\alpha,NP_k} \tag{4.25c}$$

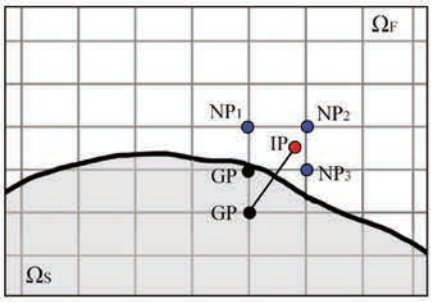

Figure 4.8 – Image point in the solid zone

where Φ_k is the interpolation weight of each node NP_k.

The total energy e_t could be calculated instead of the temperature T, however since it would require the subsequent calculation of the temperature from the total energy to be applied in the other equations, the direct (but approximate) evaluation of the temperature was therefore preferred for the sake of simplicity and efficiency. The density and the molecular weight at the image points are calculated with the following equations:

$$\rho_{IP} = \frac{p_{IP}\mathcal{W}_{IP}}{\mathcal{R}T_{IP}} \tag{4.26a}$$

$$\mathcal{W}_{IP} = \left(\sum_{\alpha=1}^{\mathcal{N}_{sp}} \frac{Y_{\alpha,IP}}{\mathcal{W}_\alpha}\right)^{-1} \tag{4.26b}$$

The ghost points GP are then reconstructed from the data calculated for their respective image points IP. The value of any conservative variable φ is the same as the one calculated at the corresponding image point considering the desired boundary condition for the immersed body.

The values at the ghost points, considering a Dirichlet boundary condition, are obtained from a first-order accurate approximation of the first-order derivative evaluated on both sides of the immersed boundary:

$$\varphi_{GP} = 2\varphi_{BP} - \varphi_{IP} \tag{4.27}$$

which means that $(\varphi_{BP}-\varphi_{GP})/h = (\varphi_{IP}-\varphi_{BP})/h$.

An isothermal wall with temperature T_w can be then imposed with the following expression:

$$T_{GP} = 2T_w - T_{IP} \tag{4.28}$$

For a Neumann boundary condition, the second-order approximation of the first-order derivative of a conservative variable φ normal to Γ can be writte as:

$$\left.\frac{\partial\varphi}{\partial n}\right|_{BP} = \frac{\varphi_{IP} - \varphi_{GP}}{2h} + \mathcal{O}\left(h^2\right) \tag{4.29}$$

where h is the distance between the ghost point (or image point) to the immersed boundary, i.e. $h = \|x_{IP} - x_{GP}\|^2$. As a consequence, the value of φ imposed at a ghost point is obtained from:

$$\varphi_{IP} = \varphi_{GP} + 2hc \tag{4.30}$$

with c being the desired boundary value $(\partial\varphi/\partial n)|_{BP}$.

An adiabatic wall can be imposed with the following expression:

$$\left.\frac{\partial T}{\partial n}\right|_{BP} = 0 \tag{4.31}$$

and a no species penetration condition with:

$$\left.\frac{\partial Y_\alpha}{\partial n}\right|_{BP} = 0 \tag{4.32}$$

which can be enforced by setting, respectively:

$$T_{GP} = T_{IP} \tag{4.33}$$

and

$$Y_{\alpha,GP} = Y_{\alpha,IP} \tag{4.34}$$

The other variables are imposed as follows:

$$p_{GP} = p_{IP} \tag{4.35}$$

$$\rho_{GP} = \rho_{IP} \tag{4.36}$$

$$\rho_{GP} Y_{\alpha,GP} = \rho_{IP} Y_{\alpha,IP} \quad , \quad \alpha = 1, \ldots, \mathcal{N}_{sp} \tag{4.37}$$

$$\rho_{GP} e_{GP} = \rho_{IP} h_{IP} - p_{IP} + \rho_{IP} \frac{u_{IP} u_{IP}}{2} \tag{4.38}$$

where h_{IP} is the enthalpy at the image point, calculated by using the mixture heat capacity $c_p = \sum_{\alpha=1}^{\mathcal{N}_{sp}} Y_{\alpha,IP} c_{p,\alpha}(T_{IP})$. Equations 4.35, 4.36, 4.37 and 4.38 represents no pressure gradient, mass conservation, no mass flux of any chemical species and zero temperature gradient, respectively.

4.4.3 Coupling procedure

The coupling of these two approaches (`CFM` and `GPM`) is obtained using the following algorithm:

1. Determine if the point is in the solid (Ω_S) or in the fluid (Ω_F) domain.
2. Determine the points that will be used in the interpolation procedure.
3. Generate the ghost (Ω_{GP}) and image (Ω_{IP}) points for the GPM.
4. Calculate the velocity at the Lagrangian points of the solid/fluid interface Γ.
5. Update the conservative variables with the forcing term $f^L(x)$.
6. Update the ghost point variables according to the boundary condition.

4.4.4 Corner treatment

Special attention is required when dealing with sharp angle corners since a ghost point can have more than one image point. The case of a right angle corner is presented by figure 4.9, considering a subset of 3×3 nodes.

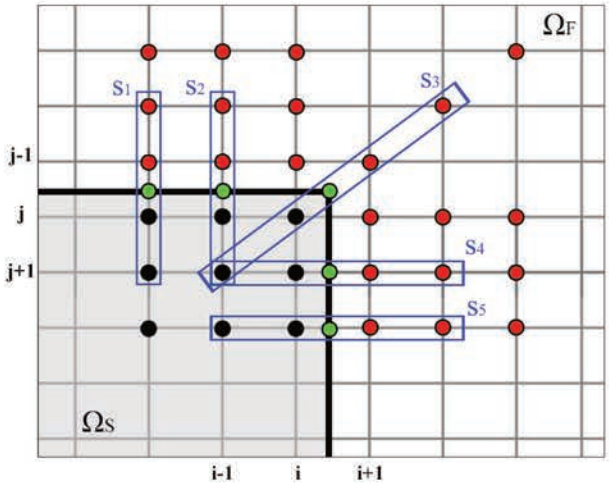

Figure 4.9 – Schematic of a corner region and definition of the stencils used in the interpolation procedure - part 1

Within the considered subset, in order to enforce the requested boundary condition, 9 equations are necessary to solve any unknown quantity φ at nodes (m, n), with $m = i-2, i-1, i$ and $n = j-2, j-1, j$.

The no-flux boundary condition on any quantity φ must be imposed at each stencil s_i $(i = 1, \ldots, 5)$, as shown in figure 4.9, using its third-order Lagrange polynomial $l_{i,3}$,

with $i = 0, \ldots, 3$, which interpolates 4 points of each stencil. For stencils s_1 and s_3, for example, one can write the following expressions, respectively:

$$\frac{\partial \varphi}{\partial n} = \sum_{l=0}^{3} \varphi \left(x_{1,i-2}, x_{2,j+l-1} \right) \frac{\partial l_{l,3}}{\partial n} \tag{4.39a}$$

$$\frac{\partial \varphi}{\partial n} = \sum_{l=0}^{3} \varphi \left(x_{1,i+l-1}, x_{2,j+l-1} \right) \frac{\partial l_{l,3}}{\partial n} \tag{4.39b}$$

The other 4 equations required to close the system are obtained using the Lagrange polynomial $l_{i,4}$, with $i = 1, ..., 4$, applied to stencils s_i $(i = 6, \ldots, 9)$, as shown in figure 4.10.

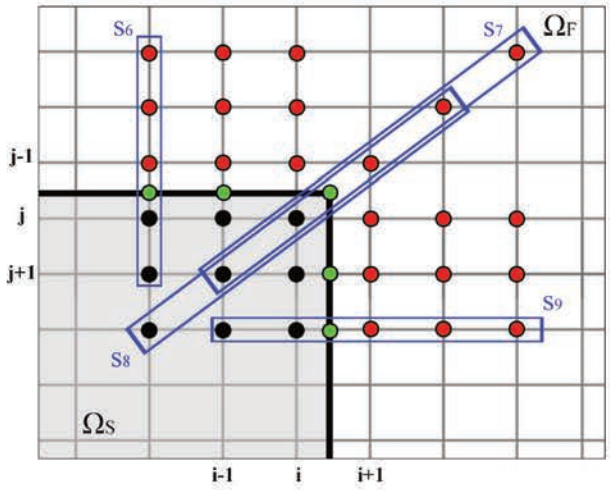

Figure 4.10 – Schematic of a corner region and definition of the stencils used in the interpolation procedure - part 2

Applying this procedure to stencil s_6 and s_7 leads, respectively, to:

$$\varphi \left(x_{1,i-2}, x_{2,j-1} \right) = \sum_{l=0}^{4} \varphi \left(x_{1,i-2}, x_{2,j+l-1} \right) l_{l,4} \left(x_{1,i-2}, x_{2,j-1} \right) \tag{4.40a}$$

$$\varphi \left(x_{1,i-1}, x_{2,j-1} \right) = \sum_{l=0}^{4} \varphi \left(x_{1,i+l-1}, x_{2,j+l-1} \right) l_{l,4} \left(x_{1,i-1}, x_{2,j-1} \right) \tag{4.40b}$$

Imposing a no-flux boundary condition, this system reduces to $AT = B$, where

$$A = \begin{bmatrix} 0 & 0 & 0 & 0 & 1 & -27 & 0 & 0 & 0 \\ 0 & 1 & -27 & 0 & 0 & 0 & 0 & 0 & 0 \\ 0 & 0 & 0 & 0 & 1 & 0 & 0 & 27 & 0 \\ 0 & 0 & 0 & 1 & 0 & 0 & -27 & 0 & 0 \\ 0 & 0 & 0 & 0 & 1 & 0 & 0 & 0 & 27 \\ 0 & 0 & 0 & 1 & 0 & 0 & -4 & 0 & 0 \\ 0 & 1 & -4 & 0 & 0 & 0 & 0 & 0 & 0 \\ 0 & 0 & 0 & 1 & 0 & 0 & 0 & 0 & -4 \\ 1 & 0 & 0 & 0 & -4 & 0 & 0 & 0 & 6 \end{bmatrix} \tag{4.41}$$

$$T = \begin{bmatrix} T_{i-2,j-2} \\ T_{i-2,j-1} \\ T_{i-2,j} \\ T_{i-1,j-3} \\ T_{i-1,j-2} \\ T_{i-1,j-1} \\ T_{i,j-2} \\ T_{i,j-1} \\ T_{i,j} \end{bmatrix} \tag{4.42}$$

and

$$B = \begin{bmatrix} -27T_{i-1,j+1} + T_{i-1,j+2} \\ -27T_{i-2,j+1} + T_{i-2,j+2} \\ -27T_{i+1,j-1} + T_{i+2,j-1} \\ -27T_{i+1,j-2} + T_{i+2,j-2} \\ -27T_{i+1,j+1} + T_{i+2,j+2} \\ -6T_{i+1,j-2} + 4T_{i+2,j-2} - T_{i+3,j-2} \\ -6T_{i-2,j+1} + 4T_{i-2,j+2} - T_{i-2,j+3} \\ -6T_{i+1,j+1} + 4T_{i+2,j+2} - T_{i+3,j+3} \\ 4T_{i+1,j+1} - T_{i+2,j+2} \end{bmatrix} \tag{4.43}$$

4.5 Verification and validation test cases

Some test cases based on the literature, therefore considered as reference data, are presented here in order to validate the `IBM` implementation and the `CFM-GPM` coupling into `CREAMS`.

4.5.1 Flow past a square cylinder

This test case aims at verifying the fluid-solid interaction of a supersonic flow characterized by $M_0 = 2.43$, $T_0 = 300$ K and $p_0 = 101\,325.0$ Pa with the fixed geometry of a square cylinder of size $a = 10.0$ mm. The computational domain has dimensions $L_a = 5.5\,a$, $L_{ch} = 50\,a$ and $H_{ch} = 10\,a$, as shown in figure 4.11. It features a cross-stream dimension that is sufficiently large in order to restrict the influence of the lateral boundary conditions. The squared cross-section of the object is modeled with 400 points, distributed according a cosine function in order to have more points gathered at the corners.

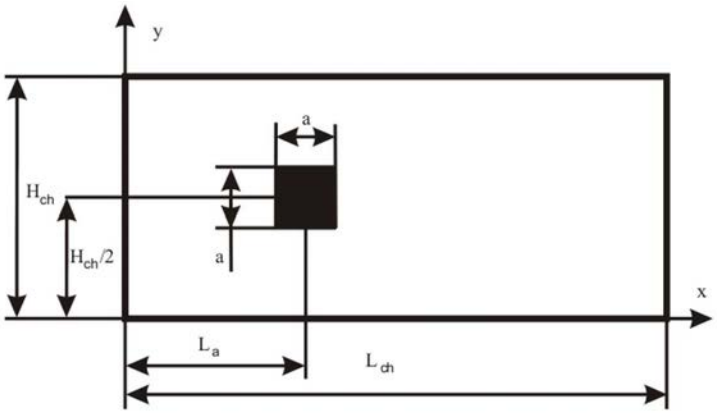

Figure 4.11 – Computational domain

The mesh size is $4\,000 \times 800$, with an uniform point distribution. The reference data are thos issued from the works of Shterev and Stefanov [161].

Figure 4.12 presents the Mach number contour with $\Delta M \approx 0.1$, colored by temperature.

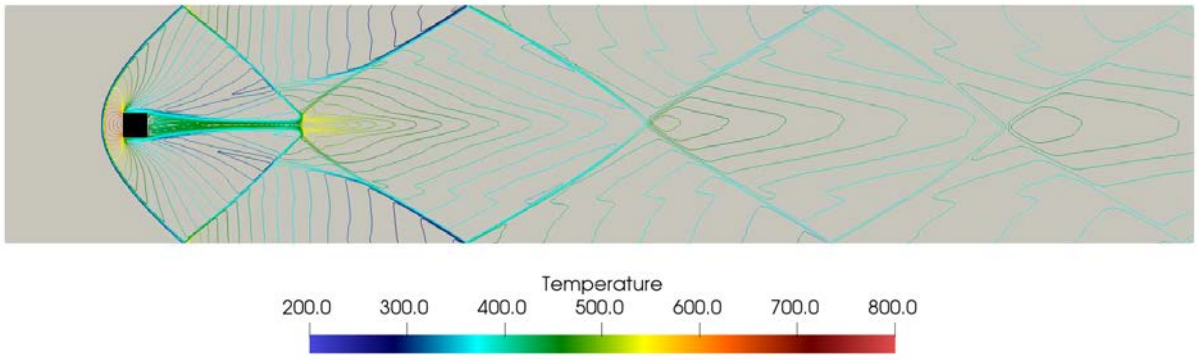

Figure 4.12 – Mach number contours

Figure 4.13 displays the pressure field (fig. 4.13a) and temperature (fig. 4.13b) distribution along x_2-axis in three distinct sections normal to the channel axis: in front of, in

the middle and behind the square cylinder. Reference data (Shterev and Stefanov [161]) are plotted with lines and `CREAMS` data are plotted with tick marks.

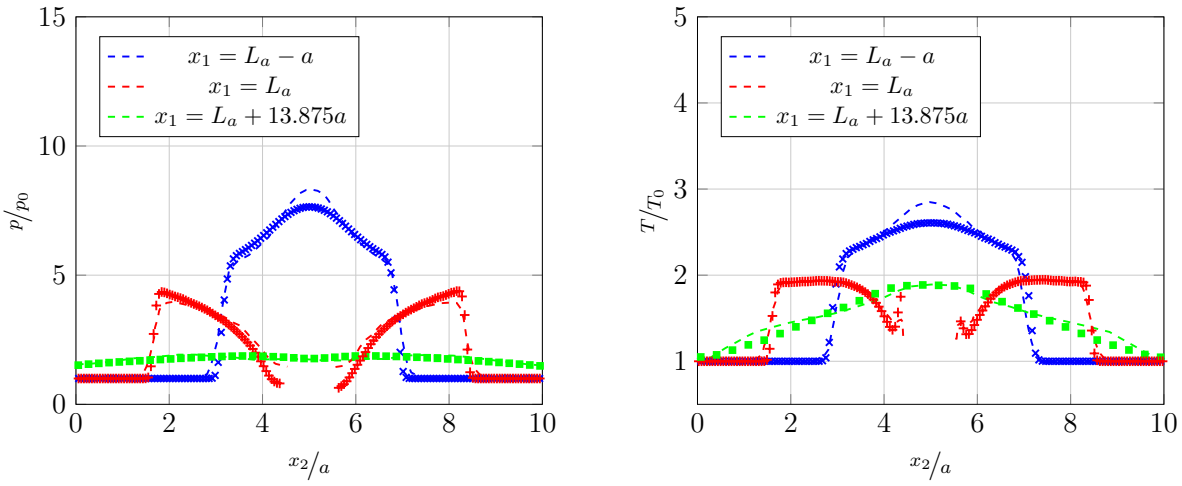

(a) Pressure (b) Temperature

Figure 4.13 – Pressure and temperature in sections normal to the channel axis

The obtained results are in satisfactorily agreement with those obtained by Shterev and Stefanov [161], indicating the same location for the shock. However, `CREAMS` results provided a slightly better shock detection, which can be verified with the more abrupt change of flow variables when compared to the reference curves.

4.5.2 Flow past a NACA 0012 profile

In order to verify the solver behavior for a viscous flow at high Mach numbers, a laminar supersonic flow past a NACA 0012 airfoil with chord-length $c = 0.1$ m, whose leading edge is located at the origin, is considered in this test case. The simulation parameters are $M_\infty = 2$, $\alpha = 10°$ and $Re_\infty = 1\,000$ and it is run with two meshes to discretize the computational domain $[-3\,c, 5\,c] \times [-2\,c, 2\,c]$: mesh M_1 with 125 000 points (500×250) and mesh M_2 with 500 000 points (1000×500).

The Mach number contours for mesh M_2 are shown by figure 4.14a. Qualitatively the results are similar to those issued from the reference, provided by De Palma et al. [46], shown by figure 4.14b.

The pressure coefficient distributions along the profile are presented by figure 4.15 together with the reference data.

By analyzing these images, one can notice that `CREAMS` results fit well with the data from De Palma et al. [46]. As expected, the more refined is the mesh, the better the results, as it can be verified with mesh M_2, which fits better with the reference solution. These

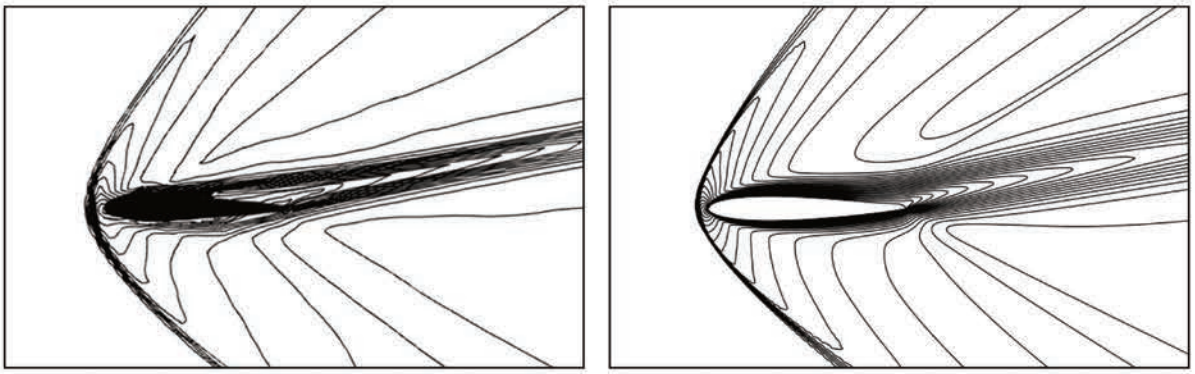

(a) CREAMS data (b) Reference data [46]

Figure 4.14 – Mach number contours and comparison with reference data

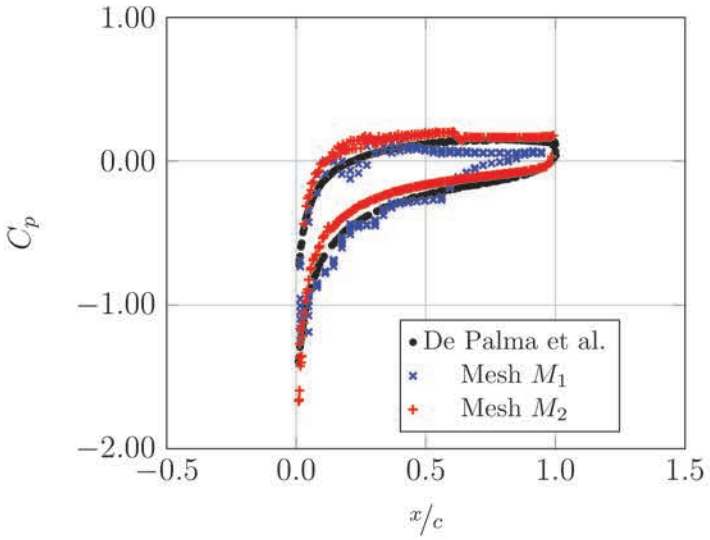

Figure 4.15 – Pressure coefficient distribution along the profile

differences are also caused by the fact that the IBM cannot perfectly reproduce curved bodies, as it works with the Cartesian grid used by CREAMS. This could be addressed by further refining the mesh near these curved zones, but that would be at the price of an increased computational cost.

4.5.3 Cavity flow

The flow over open cavities is characterized by a complex feedback process that causes a large-amplitude and self-sustained oscillations of the density, velocity and pressure fields around it. This test case consists in analyzing the flow behavior in the presence of several cavities featuring different length-to-depth ratio L/D and analyze its oscillation modes.

Figure 4.16 presents a schematic diagram of the computational domain with its dimen-

sions, as well as the boundary conditions and the cavity (in gray). The velocity profile at the inlet corresponds to a standard Blasius solution and the cavity walls are assumed to be adiabatic. Analytical hyperbolic tangent mappings were used to stretch the grid along x_2-direction, reaching a constant ratio $\Delta x_1/\Delta x_2$ of the order of unity around the cavity upper walls. The computational grid features 44 200 points (260×170) and the immersed boundary is represented with 383 points.

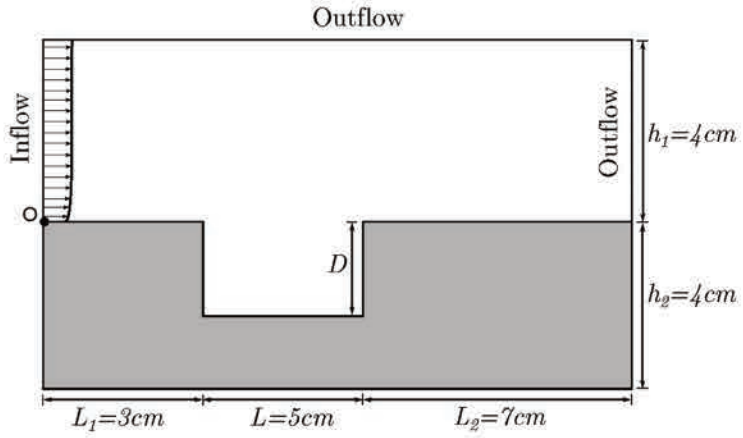

Figure 4.16 – Computational domain

Several cavities were numerically simulated with a length-to-depth ratio L/D varying from 1.25 to 2.75, thus allowing the analysis of the cavity depth effects. The Mach number, the initial temperature and the pressure are the same for all simulations, being, respectively, $M_\infty = 1.5$, $T_0 = 300$ K and $p_0 = 3.7 \times 10^5$ Pa.

Vorticity isocontours for some of the simulated cavities are presented by figure 4.17 at two different instants. Qualitatively they are representative of the shear layer mode of oscillation. Vortical disturbances are clearly evident and the visualizations are consistent with the results documented by Colonius et al. [43].

The flow obtained for $L/D = 1.25$ displays a typical shear layer mode, but the interaction of the vortexes with the end wall and its ejection becomes more violent as L/D increases, i.e. the cavity depth decreases. Moreover, the shed vortex increases to dimensions approximately equal to the cavity depth.

Figure 4.18 presents the amplitude of the acoustic oscillations that has been measured at several locations along the upper boundary conditions for some cavities. The amplitude of the dominant frequency (f_d) increases and reach a maximum at $x_1 = 70$ mm, decreasing and then increasing again at $x_1 = 100$ mm.

The values of the dominant frequencies f_d issued from the present set of simulations are plotted in figure 4.19, as well as the reference data obtained from the experimental study of Anavaradham et al. [4].

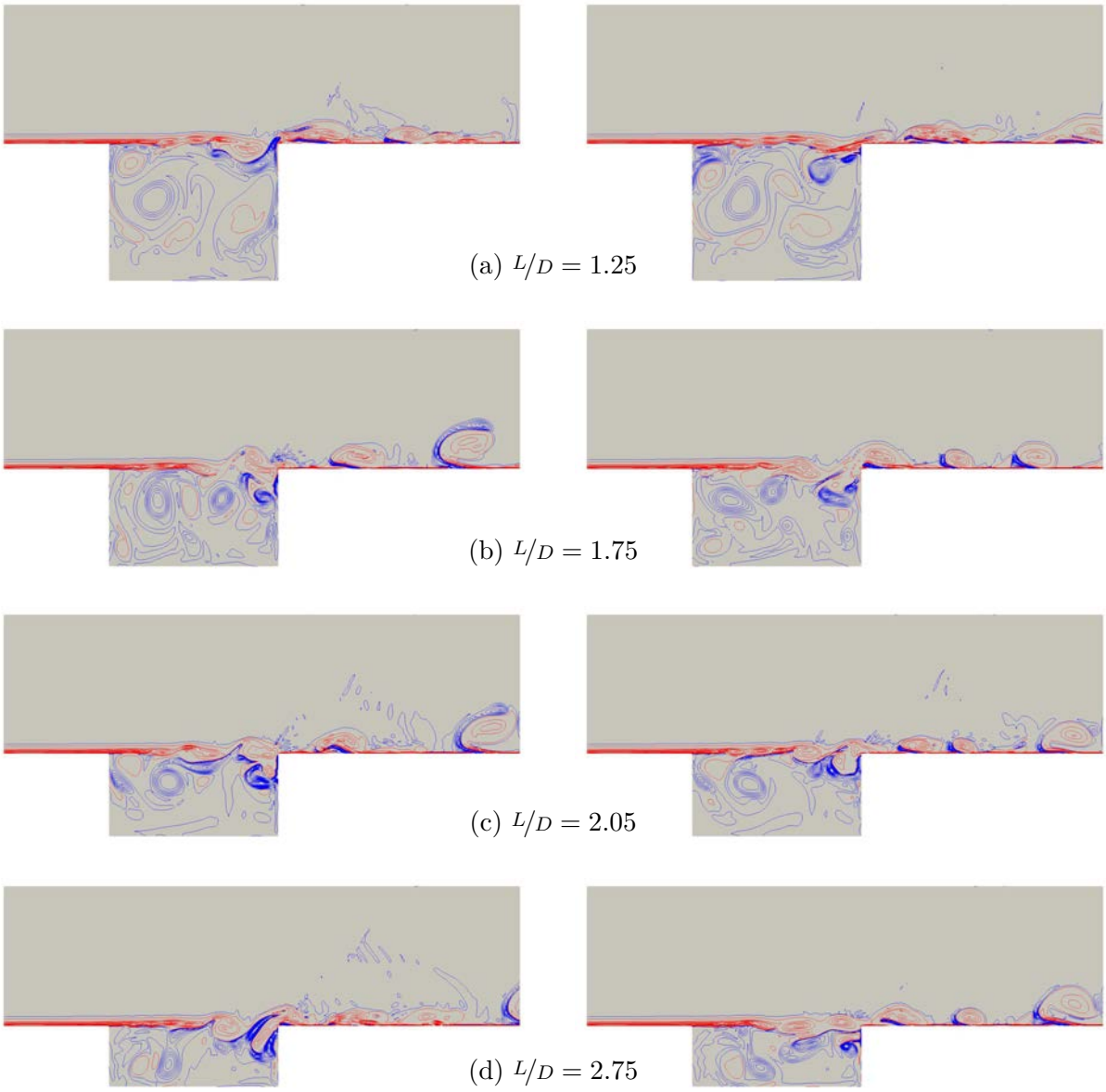

Figure 4.17 – Normalized vorticity isocontours at instants $(tU_\infty)/L = 559$ (left) and 565 (right). Blue lines: 15 contours between $-0.025 \leq (\omega D)/U_\infty \leq 1.000$. Red lines: 10 contours between $-6.000 \leq (\omega D)/U_\infty \leq -0.150$

From the images, it can be seen that the numerical predictions agree reasonably well with the experimental values, with differences being less than 5%, even with the abrupt shift of dominant frequency as the cavity depth is varied.

Summary

The main advantage of the `IBM` approach is that it works with a Cartesian mesh. It is not necessary to change the computational mesh to account for a solid object in

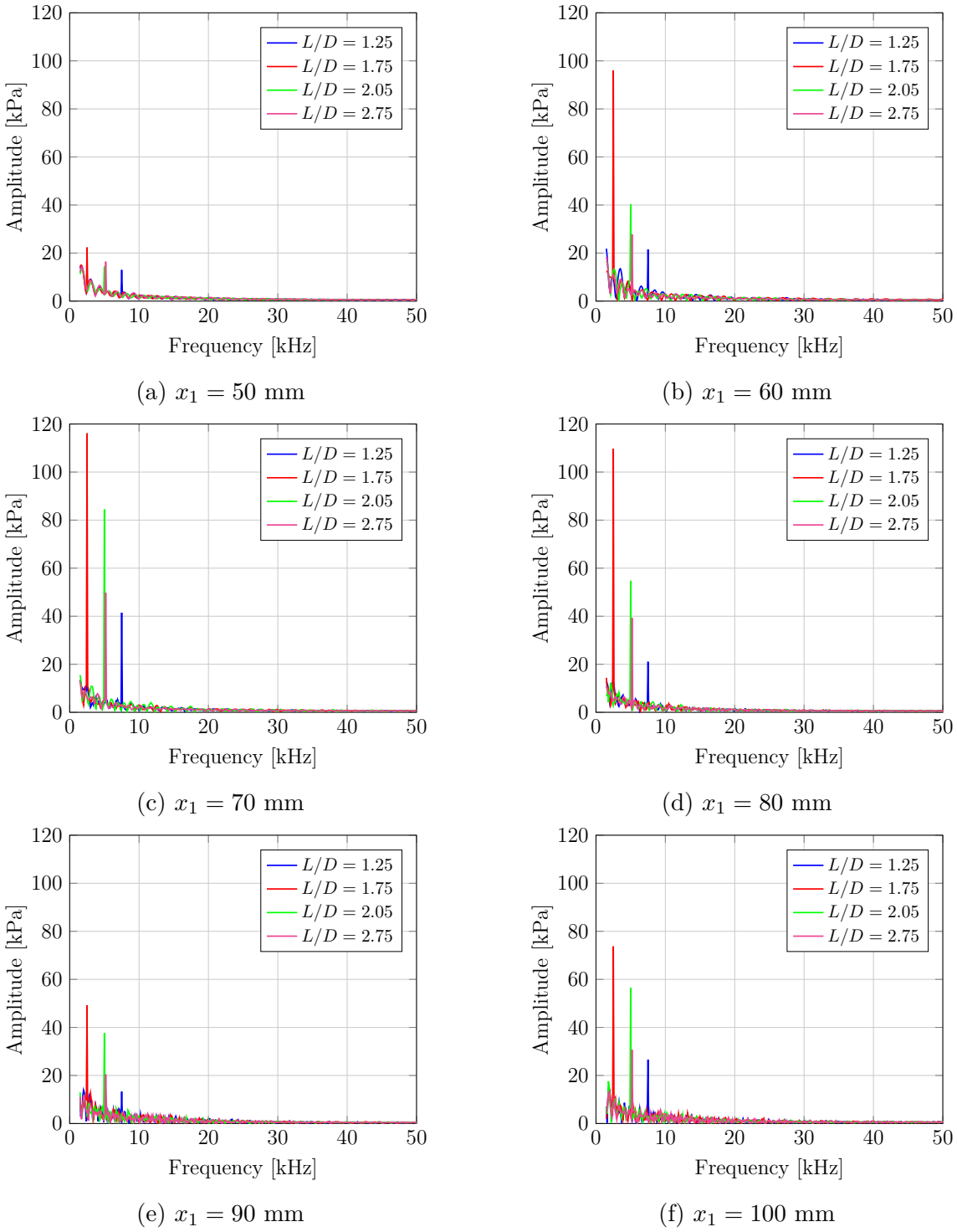

(a) $x_1 = 50$ mm

(b) $x_1 = 60$ mm

(c) $x_1 = 70$ mm

(d) $x_1 = 80$ mm

(e) $x_1 = 90$ mm

(f) $x_1 = 100$ mm

Figure 4.18 – Frequency spectrum at various locations along the upper boundary condition

the computational domain. The generated mesh must cover the entire domain, with the exception of the solid object, which must be identified so as to calculate its effects on the flow around it. Two `IBM` classes are presented in this chapter: continuous forcing and discrete forcing method, with the differences between them providing the way to add the

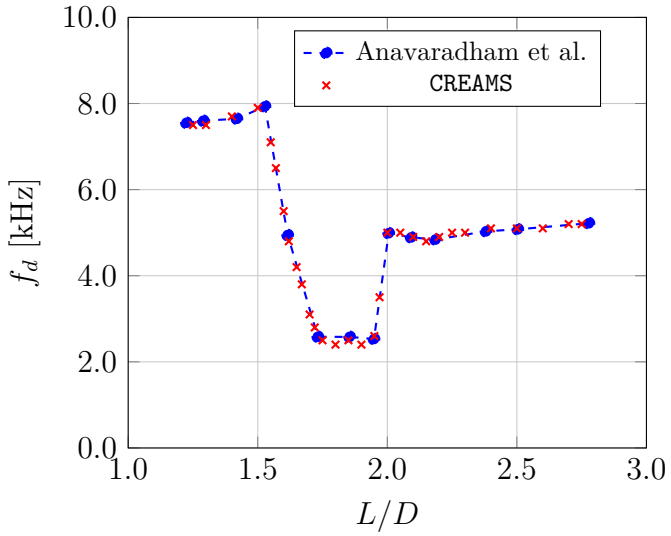

Figure 4.19 – Comparison between the simulation and experimental values of the dominant frequencies f_d for several length-to-depth ratio L/D

forcing term to the Navier-Stokes equations to simulate the solid wall.

The strategies considered to implements these two classes of `IBM` into `CREAMS`, so as to be able to simulate a compressible flow around complex geometries, are also presented. It consists in adding a forcing term into the moment equations and mirroring the ghost and image points in order to correct the energy and scalar equation.

The solid object geometry is modeled with a `STL` file, which is a triangulated representation of the surface of the object. Once the solid object is immersed into the solver Cartesian domain, the points are identified as solid, fluid, ghost, image or interpolation points, with the `IBM` working on the ghost, image and interpolation points. Special attention must be paid when dealing with corners, since the point mirroring along the axis may be superimposed.

Furthermore, some test cases were also run to verify this implementation: flow past a square cylinder, past a `NACA` profile and cavity flow. These simulations aim at verifying the fluid-solid interaction past different geometries, with different flow configurations.

The next step will be focused on the turbulence-chemistry interaction (`TCI`) modelling, which is especially critical for supersonic combustion since, under these conditions, chemical and turbulent time scales may have the same order of magnitude. This is the subject of the next chapter.

Chapter 5

Unsteady Partially Stirred Reactor

In a scramjet engine the compressed air flow from the inlet is kept supersonic throughout the whole flow path. The fast chemistry approach becomes less appropriate when dealing with supersonic combustion, as chemical reaction time scales tend to be of the same order of magnitude as turbulent time scales under these conditions, resulting in the Damköhler number tending to unity. A finite-rate chemistry-based approach is therefore expected to better describe this combustion regime, which is dominated by chemical processes including self-ignition phenomena.

The filtered species transport equation (eq. 3.27) includes the average source term $\bar{\dot{\omega}}_\alpha$, which is the averaged filtered species production rate. Due to its large non-linearity, the `PSR` approximation $\dot{\omega}_\alpha\left(\widetilde{T}, \widetilde{Y}_\alpha\right)$ may however be too restrictive, thus requiring it to be modeled taking into account the Turbulence-Chemistry Interaction (`TCI`).

Table 5.1 presents the several approaches to model the turbulent combustion, synthesized by Peters [141].

	Premixed	**Non-premixed (diffusive)**
Fast chemistry	Bray-Moss-Libby model	Conserved Scalar Equilibrium model
	Coherent flame model	
Finite-rate chemistry	Flamelet model (G-equation)	Flamelet model (mixture fraction)
		Conditional Moment Closure
	Transported `PDF` model	
	Eddy Dissipation Concept (`EDC`) model	

Table 5.1 – Turbulent combustion model classification

The `EDC` model is based on experimental and numerical observations and considers that chemical reactions take place only in small dissipative zones (worms), where molecular mixing processes are intense. Each fluid finite volume is treated as a Partially Stirred

Reactor (PaSR), composed of fine-scale structures with intense mixing at molecular level (zone *) and a surrounding non-reactive zone (zone ^{0}), as shown by figure 5.1. The fine-scale structure zone behaves as a Perfectly Stirred Reactor (PSR) and the surrounding zone is chemically inert thus, from a general point of view, the chemical source term can be written as:

$$\bar{\dot{\omega}}_\alpha = \int_\Psi \mathtt{PDF}\left(\psi\right) \dot{\omega}_\alpha\left(\psi\right) \mathrm{d}\psi \tag{5.1}$$

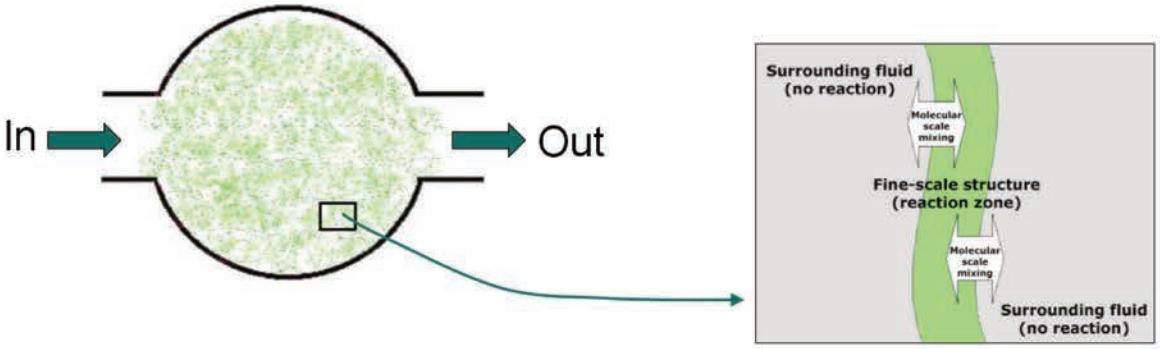

Figure 5.1 – Fluid finite volume featuring fine-scale structures and surrounding non-reactive zone

with Ψ being the associated domain of definition of the PDF and $\psi = \left[T, Y_\alpha\right]^T$. This PDF is bimodal with fine-scale structure (*) and surrounding zone (^{0}) contributions. It should be recalled that molecular mixing between fuel and oxidizer is a prerequisite before combustion takes place under non-premixed conditions [20, 168], therefore zone ^{0} is associated to non-burning states. The PDF is then decomposed into a fine-scale structure contribution (*) and a surroundings contribution (^{0}):

$$\mathtt{PDF}\left(\psi\right) = \gamma^* \delta\left(\psi - \psi^*\right) + \left(1 - \gamma^*\right) \delta\left(\psi - \psi^0\right) \tag{5.2}$$

in such a manner that the chemical source term can be written as bellow:

$$\bar{\dot{\omega}}_\alpha \approx \gamma^* \dot{\omega}_\alpha\left(\psi^*\right) + \left(1 - \gamma^*\right) \dot{\omega}_\alpha\left(\psi^0\right) \approx \gamma^* \dot{\omega}_\alpha\left(\psi^*\right) \tag{5.3}$$

with γ^* being the fine-scale structure volume fraction, i.e. the fraction of each calculation cell where the species are well mixed.

These two zones (* and ^{0}) are related through a quasi-equilibrium equation between chemical production and micro-mixing. For mass, it can be written as:

$$\bar{\rho}\left(Y_\alpha^* - Y_\alpha^0\right) = \tau_m \dot{\omega}_\alpha\left(T^*, Y_\alpha^*\right) \tag{5.4}$$

and for energy:

$$\bar{\rho} \sum_{\alpha=1}^{\mathcal{N}_{sp}} \left(Y_\alpha^* h_\alpha^* - Y_\alpha^0 h_\alpha^0 \right) = \tau_m \sum_{\alpha=1}^{\mathcal{N}_{sp}} h_{\alpha,f}^\theta \dot{\omega}_\alpha \left(T^*, Y_\alpha^* \right) \tag{5.5}$$

where h_α is the enthalpy of species α, τ_m is the micro-mixing time scale and $h_{\alpha,f}^\theta$ is the formation enthalpy of species α.

Such a modelling proposal relies on the early picture of turbulent flows provided by Batchelor and Townsend [13]. Chomiak [40] also indicated that the chemical reactions occur preferably in the fine-scale structure zones and proposed such premixed flame propagation mechanism at high Reynolds numbers. Figure 5.2 presents the shape of the fine-scale structures, obtained from numerical simulations performed by Woodward et al. [186], which confirmed that they are very small, with their volume decreasing with the increase of the Reynolds number, and concentrated in filaments immersed within the low vorticity zone.

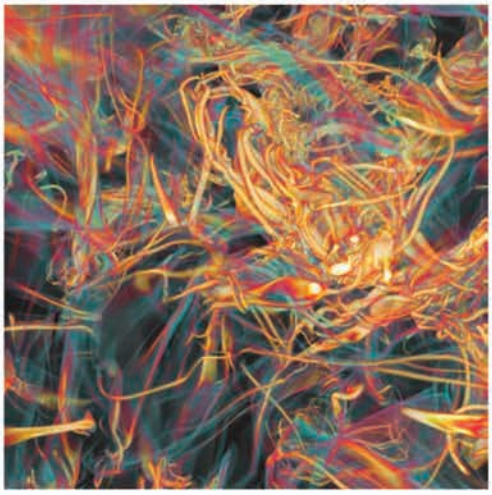

Figure 5.2 – Fine-scale structures shapes [186]

5.1 Description of the model

The Unsteady Partially Stirred Reactor (`U-PaSR`) is based on the `EDC` model and it takes into account the inhomogeneities of both composition and temperature inside the flame region, considering the effects of micro-mixing, finite-rate chemistry and the interactions between them. It implies that chemical reaction takes place in fine-scale structures where most of the viscous dissipation and molecular mixing processes take place.

Like the `EDC` model, the `U-PaSR` is a multiscale-based model with the fine-scale structure volume fraction and the mixing time scale being proportional to the Kolmogorov

velocity scale v_k and the Kolmogorov time scale τ_k, respectively. The mass and energy balance equations between the fine-scale and the surrounding regions are the same for both model (equations 5.4 and 5.5), with the main difference between them lying in the evaluation of the fine-scale structure volume fraction γ^*.

The fine-scale structure volume fraction γ^* is defined as the ratio between the volume of the reactive structures and the volume of the sum of both reactive and mixing structures, expressed as:

$$\gamma^* = \frac{\tau_{ch}}{\tau_{ch} + \tau_m} \tag{5.6}$$

with τ_{ch} being the chemical time scale and τ_m the subgrid mixing (micro-mixing) time scale.

The chemical time scale τ_{ch} can be evaluated by different ways. Here, for the sake of simplicity, and following the studies of Moule et al. [123, 124], it is evaluated by using the transit time obtained from a 1D laminar premixed flame calculated at stoichiometric conditions. The transit time is defined as the ratio of the premixed flame thickness δ_L^0 to its propagation velocity S_L^0:

$$\tau_{ch} = \frac{\delta_L^0}{S_L^0} \tag{5.7}$$

The present estimate is similar to the one obtained from a diffusion flame at the limit of extinction [104]. Since the objective of this time scale is to obtain an approximate value for the fine-scale structure volume fraction, only estimates are needed and it may therefore be relevant for both diffusion and premixed flames.

The subgrid mixing time scale τ_m is estimated as the harmonic mean of the Kolmogorov time scale τ_k and the subgrid time scale τ_Δ:

$$\tau_m = \sqrt{\tau_k \tau_\Delta} \tag{5.8}$$

with $\tau_k = \sqrt{\nu/\varepsilon}$ where $\varepsilon = k^{3/2}/\Delta$ and $k = \left(\nu_{sgs}/0.069\Delta\right)^2$, and $\tau_\Delta = \Delta/\nu'$ where $\nu' = \sqrt{2k/3}$ [17].

An important point about this `TCI` closure is that it satisfies the constraint that the `SGS` model should recover the `DNS` limit as the filter size tends to zero [145]. As $\Delta \to 0$, then $\gamma^* \to 1$ in such a manner that $[T^*, Y_\alpha^*]^T = \left[\widetilde{T}, \widetilde{Y}_\alpha\right]^T = [T, Y_\alpha]^T$, resulting in $\bar{\dot{\omega}}_\alpha = \gamma^* \dot{\omega}_\alpha\left(\psi^*\right) = \dot{\omega}_\alpha\left(\psi\right)$, with the `SGS` model degenerating to `DNS`.

The relevance of this closure has been investigated successfully by Moule et al. [123] through a `LES` of a `NASA` experiment. It has been also successively applied to the `RANS` simulation of a scramjet model investigated at Centre for Hypersonics of the University

of Queensland [125, 171]. The U-PaSR model is thus expected to offer an appropriate representation of combustion in supersonic flows, being suitable for applications with representative scramjet geometries.

5.2 Residence time influence

Considering, for the sake of simplicity, a constant specific heat and since $\bar{\psi} = \gamma^* \psi^* + (1 - \gamma^*)\,\psi^0$ for any variable ψ, the following equation can be deduced from equations 5.4 and 5.5:

$$\bar{\rho} \frac{T^* - T^{in}}{\tau_{res}} = \dot{\omega}_T \left(T^*, Y_\alpha^*\right) \tag{5.9}$$

which corresponds to a PSR associated to the fine-scale structure zone (*), being fed by molecular diffusion with the average composition and temperature, i.e. $T^{in} = \widetilde{T}$, with T^{in} the inlet temperature and the residence time being defined as $\tau_{res} = \tau_m\,(1 - \gamma^*)$.

The LHS of equation 5.9 corresponds to the heat transfer (curve HT in figure 5.3), which is a straight line proportional to $^1/_{\tau_{res}}$. The curve HR, in the same figure, is the reactor heat release and corresponds to the RHS of equation 5.9. It is negligible at low temperatures, increases up to a maximum, and then decreases again. The HR curve profile changes according to the inlet conditions. The intersection between HR and HT curves is the solution of a steady-state PSR problem, which behavior is different depending on the value of τ_{res}.

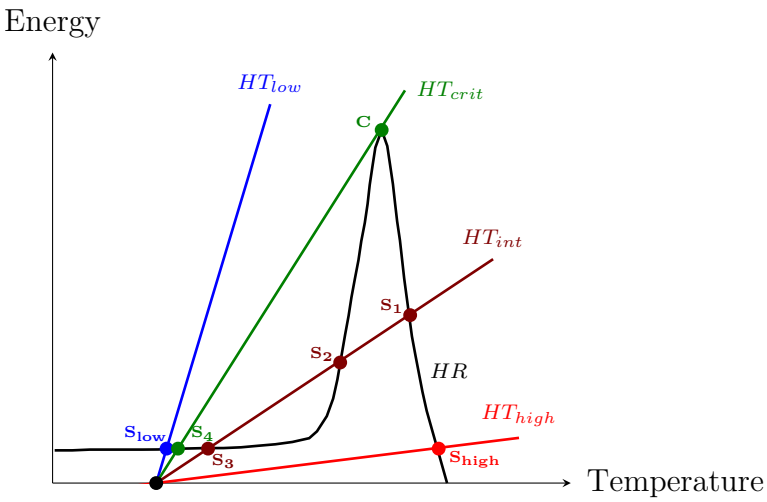

Figure 5.3 – PSR model steady-state solution

If the residence time is sufficiently small ($\tau_{res} \to 0$) there will be only one solution: the point S_{low}, which is the only intersection between HT_{low} and HR curves. This solution

is the so-called *cold* solution because there is not enough time for the mixture to burn in the reactor, with the solution being practically the same as the one associated to the inlet conditions. Under this condition and according to equation 5.6, $\gamma^* \to 1$, in such a manner that $Y_\alpha^* \sim \widetilde{Y}_\alpha$, meaning that the reactor behavior is limited by chemistry.

On the other side, for a sufficient long residence time ($\tau_{res} \to \infty$), there is also only one solution, which corresponds to the point S_{high}, being the intersection between HT_{high} and HR curves. The inlet mixture burns almost entirely inside the reactor and the solution is the so-called *hot* solution. The reactor behavior is limited by the mixing.

At an intermediate residence time there are three possible solutions: points S_1, S_2 and S_3, which correspond to the intersections between HT_{int} and HR curves. Solutions S_1 and S_3 are related to $\tau_{res} \to \infty$ and $\tau_{res} \to 0$, respectively, also being so-called *hot* and *cold* solutions. The third intermediate point (point S_2) is unstable due to the hysteresis effect, not being a valid final solution and falling back to points S_1 or S_3, depending on how stationary conditions have been reached.

Simulations with intermediate residence times are problematic since the average conditions ($\widetilde{\cdot}$) may be very different from fine-scale structure conditions (*), causing the resolution of equations 5.4 and 5.5 to be very sensible. The solution can converge, or not, depending on the initial conditions. This issue can be addressed by adding a non-stationary term to the system, resulting in the `U-PaSR` equations:

$$\begin{cases} \dfrac{\partial \bar{\rho} Y_\alpha^*}{\partial t} + \bar{\rho}\dfrac{\left(Y_\alpha^* - Y_\alpha^0\right)}{\tau_m} = \dot{\omega}_\alpha\left(T^*, Y_\alpha^*\right) & \text{(5.10a)} \\ \dfrac{\partial \bar{\rho} h^*}{\partial t} + \bar{\rho}\displaystyle\sum_{\alpha=1}^{\mathcal{N}_{sp}} \dfrac{\left(Y_\alpha^* h_\alpha^* - Y_\alpha^0 h_\alpha^0\right)}{\tau_m} = \sum_{\alpha=1}^{\mathcal{N}_{sp}} h_{\alpha,f}^\theta \dot{\omega}_\alpha\left(T^*, Y_\alpha^*\right) & \text{(5.10b)} \end{cases}$$

Fine-scale structures (*) and surroundings regions (^{0}) are inter-related since, for a variable ψ, $\widetilde{\psi} = \gamma^*\psi^* + (1-\gamma^*)\,\psi^0$, with γ^* given by equation 5.6. As in equation 5.9, this system can be written as function of average ($\widetilde{\cdot}$) and fine-scale structure (*) variables, resulting in

$$\begin{cases} \dfrac{\partial \bar{\rho} Y_\alpha^*}{\partial t} + \bar{\rho}\dfrac{\left(Y_\alpha^* - \widetilde{Y}_\alpha\right)}{\tau_m\left(1-\gamma^*\right)} = \dot{\omega}_\alpha\left(T^*, Y_\alpha^*\right) & \text{(5.11a)} \\ \dfrac{\partial \bar{\rho} h^*}{\partial t} + \bar{\rho}\displaystyle\sum_{\alpha=1}^{\mathcal{N}_{sp}} \dfrac{\left(Y_\alpha^* h_\alpha^* - \widetilde{Y}_\alpha \widetilde{h}_\alpha\right)}{\tau_m\left(1-\gamma^*\right)} = \sum_{\alpha=1}^{\mathcal{N}_{sp}} h_{\alpha,f}^\theta \dot{\omega}_\alpha\left(T^*, Y_\alpha^*\right) & \text{(5.11b)} \end{cases}$$

where the average filtered composition $\widetilde{\psi}$ is provided by the solver and the additional

variables ψ^* are evaluated from the above set of equations. Once both average filtered state $\widetilde{\psi}$ and fine-scale structure state $\psi^* = [T^*, Y_\alpha^*]^T$ are known, the two-fluid medium is fully determined since state $(^0)$ can be evaluated from

$$\psi^0 = \frac{\widetilde{\psi} - \gamma^* \psi^*}{1 - \gamma^*} \tag{5.12}$$

5.3 Sensitivity analysis of the steady-state solutions

The set of `U-PaSR` equations below describes the evolution of the fine-scale structure zone $(^*)$, the surroundings region $(^0)$ and the mean composition $(\widetilde{.})$. The equations considered are applied to a singles computational cell neglecting the possible influence of the the mean gradient of any quantity. The computational cell can be thought as a reactor being continuously fed by a stream of reactants at concentration (Y_α^{in}, T^{in}) and the residence time inside of the reactor is hereafter denoted by τ_{res}.

The evolution equation for the fine-scale structures is then given by

$$\begin{cases} \dfrac{\partial \bar{\rho} Y_\alpha^*}{\partial t} + \bar{\rho} \dfrac{\left(Y_\alpha^* - Y_\alpha^0\right)}{\tau_m} + \bar{\rho} \dfrac{\left(Y_\alpha^* - Y_\alpha^{in}\right)}{\tau_{res}} = \dot{\omega}_\alpha \left(T^*, Y_\alpha^*\right) & \text{(5.13a)} \\ \dfrac{\partial \bar{\rho} h^*}{\partial t} + \bar{\rho} \displaystyle\sum_{\alpha=1}^{\mathcal{N}_{sp}} \dfrac{\left(Y_\alpha^* h_\alpha^* - Y_\alpha^0 h_\alpha^0\right)}{\tau_m} + \bar{\rho} \sum_{\alpha=1}^{\mathcal{N}_{sp}} \dfrac{\left(Y_\alpha^* h_\alpha^* - Y_\alpha^{in} h_\alpha^{in}\right)}{\tau_{res}} = \displaystyle\sum_{\alpha=1}^{\mathcal{N}_{sp}} h_{\alpha,f}^\theta \dot{\omega}_\alpha \left(T^*, Y_\alpha^*\right) & \text{(5.13b)} \end{cases}$$

where $h_\alpha^{in}\left(T^{in}\right)$ is the enthalpy of species α at the inlet temperature T^{in} in such a manner that $h^{in} = \sum_\alpha Y_\alpha^{in} h_\alpha^{in}\left(T^{in}\right)$.

Equations 5.13a and 5.13b express the balance of mass (for each species α) and energy between the fine-scale structures $(^*)$ and the surrounding region $(^0)$. It is written in terms of mass and energy transfer between regions * and ^{0} so as to evidence the two-fluid framework that lies behind the present closure formulation. In practice, however, the set of equations that is evaluated in the `CFD` solver is written for $\widetilde{\psi}$ and ψ^*:

$$\begin{cases} \dfrac{\partial \bar{\rho} Y_\alpha^*}{\partial t} + \bar{\rho} \dfrac{\left(Y_\alpha^* - \widetilde{Y}_\alpha\right)}{\tau_m \left(1 - \gamma^*\right)} + \bar{\rho} \dfrac{\left(Y_\alpha^* - Y_\alpha^{in}\right)}{\tau_{res}} = \dot{\omega}_\alpha \left(T^*, Y_\alpha^*\right) & \text{(5.14a)} \\ \dfrac{\partial \bar{\rho} h^*}{\partial t} + \bar{\rho} \displaystyle\sum_{\alpha=1}^{\mathcal{N}_{sp}} \dfrac{\left(Y_\alpha^* h_\alpha^* - \widetilde{Y}_\alpha \widetilde{h}_\alpha\right)}{\tau_m \left(1 - \gamma^*\right)} + \bar{\rho} \sum_{\alpha=1}^{\mathcal{N}_{sp}} \dfrac{\left(Y_\alpha^* h_\alpha^* - Y_\alpha^{in} h_\alpha^{in}\right)}{\tau_{res}} = \displaystyle\sum_{\alpha=1}^{\mathcal{N}_{sp}} h_{\alpha,f}^\theta \dot{\omega}_\alpha \left(T^*, Y_\alpha^*\right) & \text{(5.14b)} \end{cases}$$

For the evolution of the average composition inside the reactor, considering an adiabatic chemical reactor, the following set of equations is considered:

$$\begin{cases} \dfrac{\partial \bar{\rho}\widetilde{Y}_\alpha}{\partial t} + \bar{\rho}\dfrac{\left(\widetilde{Y}_\alpha - Y_\alpha^{in}\right)}{\tau_{res}} = \gamma^* \dot{\omega}_\alpha \left(T^*, Y_\alpha^*\right) & \text{(5.15a)} \\ \dfrac{\partial \bar{\rho}\widetilde{h}}{\partial t} + \bar{\rho}\displaystyle\sum_{\alpha=1}^{\mathcal{N}_{sp}} \dfrac{\left(\widetilde{Y}_\alpha \widetilde{h}_\alpha - Y_\alpha^{in} h_\alpha^{in}\right)}{\tau_{res}} = \gamma^* \sum_{\alpha=1}^{\mathcal{N}_{sp}} h_{\alpha,f}^{\theta} \dot{\omega}_\alpha \left(T^*, Y_\alpha^*\right) & \text{(5.15b)} \end{cases}$$

Equations 5.15a and 5.15b show that the mean composition inside the reactor results from a balance between the inlet-outlet term and chemical reactions, weighted by the fine-scale structure volume fraction γ^*. The `U-PaSR` equations tend towards the `PSR` equations as $\gamma^* \to 1$.

The evolution equation for the surrounding region can be deduced from equations 5.13a and 5.15a for mass fraction and equations 5.13b and 5.15b for enthalpy:

$$\begin{cases} \dfrac{\partial \bar{\rho} Y_\alpha^0}{\partial t} + \bar{\rho}\dfrac{\left(Y_\alpha^0 - \widetilde{Y}_\alpha\right)}{\tau_m \left(1-\gamma^*\right)} + \bar{\rho}\dfrac{\left(Y_\alpha^0 - Y_\alpha^{in}\right)}{\tau_{res}} = 0 & \text{(5.16a)} \\ \dfrac{\partial \bar{\rho} h^0}{\partial t} + \bar{\rho}\displaystyle\sum_{\alpha=1}^{\mathcal{N}_{sp}} \dfrac{\left(Y_\alpha^0 h_\alpha^0 - \widetilde{Y}_\alpha \widetilde{h}_\alpha\right)}{\tau_m \left(1-\gamma^*\right)} + \bar{\rho}\sum_{\alpha=1}^{\mathcal{N}_{sp}} \dfrac{\left(Y_\alpha^0 h_\alpha^0 - Y_\alpha^{in} h_\alpha^{in}\right)}{\tau_{res}} = 0 & \text{(5.16b)} \end{cases}$$

Since there is no chemical reaction in the surrounding region, none of these equations contain any chemical contribution in the `RHS`.

The fine-scale volume fraction, approximated from equation 5.6, can be rewritten in terms of a Damköler number $\boldsymbol{\gamma} = {}^{\tau_m}/_{\tau_{ch}}$:

$$\gamma^* = \frac{1}{1+\boldsymbol{\gamma}} \tag{5.17}$$

The steady-state of the reactor is affected by the inlet feeding stream, the chemical reactions and the small-scale molecular mixing (exchange between fine-scale structure and surrounding zones).

5.3.1 Limiting behavior

`CREAMS` solves the set of dimensional equations for a detailed representation of chemistry. However, to make easier the analysis of the limiting behavior, we will consider the following set of equations:

$$
\begin{cases}
\dfrac{\partial \bar{\rho} Y_\alpha^*}{\partial \tau} + \boldsymbol{\alpha}\bar{\rho}\left(Y_\alpha^* - Y_\alpha^{in}\right) + \boldsymbol{\beta}\bar{\rho}\left(Y_\alpha^* - \widetilde{Y}_\alpha\right) = \boldsymbol{\gamma}\dot{\Omega}_\alpha\left(T^*, Y_\alpha^*\right) & \text{(5.18a)} \\
\dfrac{\partial \bar{\rho} h^*}{\partial \tau} + \boldsymbol{\alpha}\bar{\rho}\sum_{\alpha=1}^{\mathcal{N}_{sp}}\left(Y_\alpha^* h_\alpha^* - Y_\alpha^{in} h_\alpha^{in}\right) + \boldsymbol{\beta}\bar{\rho}\sum_{\alpha=1}^{\mathcal{N}_{sp}}\left(Y_\alpha^* h_\alpha^* - \widetilde{Y}_\alpha \widetilde{h}_\alpha\right) = \boldsymbol{\gamma}\sum_{\alpha=1}^{\mathcal{N}_{sp}} h_{\alpha,f}^\theta \dot{\Omega}_\alpha\left(T^*, Y_\alpha^*\right) & \text{(5.18b)} \\
\dfrac{\partial \bar{\rho} \widetilde{Y}_\alpha}{\partial \tau} + \boldsymbol{\alpha}\bar{\rho}\left(\widetilde{Y}_\alpha - Y_\alpha^{in}\right) = \boldsymbol{\gamma}\gamma^*\dot{\Omega}_\alpha\left(T^*, Y_\alpha^*\right) & \text{(5.18c)} \\
\dfrac{\partial \bar{\rho} \widetilde{h}}{\partial \tau} + \boldsymbol{\alpha}\bar{\rho}\sum_{\alpha=1}^{\mathcal{N}_{sp}}\left(\widetilde{Y}_\alpha \widetilde{h}_\alpha - Y_\alpha^{in} h_\alpha^{in}\right) = \boldsymbol{\gamma}\gamma^*\sum_{\alpha=1}^{\mathcal{N}_{sp}} h_{\alpha,f}^\theta \dot{\Omega}_\alpha\left(T^*, Y_\alpha^*\right) & \text{(5.18d)}
\end{cases}
$$

where $\tau = {}^{t}/_{\tau_{res}}$, $\boldsymbol{\alpha} = {}^{\tau_m}/_{\tau_{res}}$ is the mixing to residence time scale ratio, $\boldsymbol{\beta} = {}^{1}/_{(1-\gamma^*)}$ and $\boldsymbol{\gamma} = {}^{\tau_m}/_{\tau_{ch}}$ is the Damköhler number. The chemical rate is normalized with the chemical time scale τ_{ch}, i.e. $\dot{\Omega}_\alpha\left(T^*, Y_\alpha^*\right) = \tau_{ch}\dot{\omega}_\alpha\left(T^*, Y_\alpha^*\right)$.

Three independent non-dimensional parameters are used to analyze the limiting behavior of the `U-PaSR` reactor model: the mixing to residence time scale ratio ($\boldsymbol{\alpha}$), the Damköhler number ($\boldsymbol{\gamma}$) and a third one ($\boldsymbol{\beta}$) which can be deduced from them:

$$\boldsymbol{\alpha} = \frac{\tau_m}{\tau_{res}} \tag{5.19}$$

$$\boldsymbol{\gamma} = \frac{\tau_m}{\tau_{ch}} \tag{5.20}$$

$$\boldsymbol{\beta} = \frac{1+\boldsymbol{\gamma}}{\boldsymbol{\gamma}} \tag{5.21}$$

Setting the values of τ_m, τ_{res} and γ^* is equivalent to setting the values of the three non-dimensional numbers $\boldsymbol{\alpha}$, $\boldsymbol{\beta}$ and $\boldsymbol{\gamma}$ that appear in the above system of equations. To facilitate the analysis of the computational results, it is proposed to impose the value of the mixing time scale τ_m, the mixing to residence time scale ratio $\boldsymbol{\alpha}$ and the Damköhler number $\boldsymbol{\gamma}$, which allows to fix the values of τ_m, τ_{res} and γ^* that are required to solve the dimensional transport equations written for the fine-scale structure and average states ψ^* and $\widetilde{\psi}$, respectively. From the values of $\boldsymbol{\alpha}$ and $\boldsymbol{\gamma}$, one can indeed deduce $\tau_{res} = {}^{\tau_m}/_{\boldsymbol{\alpha}}$ and $\gamma^* = {}^{1}/_{(1+\boldsymbol{\gamma})}$.

It is necessary to define the initial values of the primitive variables Y_α^*, h^*, $\widetilde{Y}_\alpha$ and $\widetilde{h}$ as well as the inlet properties Y_α^{in} and h^{in}. The surrounding region $({}^0)$ is initialized the the inlet values Y_α^{in} and T^{in} and the fine-scale region $(^*)$ with the equilibrium values Y_α^{eq} and T^{eq}.

The pressure inside the reactor is fixed to 10^5 Pa and the mixing time scale τ_m is fixed to 10^{-3} s. The inlet enthalpy h^{in} is obtained from its temperature T^{in} and composition

(equivalence ratio Φ^{in}), being $T^{in} = 298.15$ K and $\Phi^{in} = 0.70$ (2.0% of H_2, 22.8% of O_2 and 75.2% of N_2).

Simulations are conducted for several values of $\boldsymbol{\alpha}$ and $\boldsymbol{\gamma}$, ranging from 10^{-5} to 10^{-1} and 10^{-1} to 10^{1}, respectively. Total simulation time is $t = 10^4$ s.

Figure 5.4 reports the average temporal evolution for several values of $\boldsymbol{\gamma}$ and $\boldsymbol{\alpha}$. The temperature reaches a steady-state value, which depends upon $\boldsymbol{\alpha}$ and $\boldsymbol{\gamma}$, whatever the values of $\boldsymbol{\alpha}$ and $\boldsymbol{\gamma}$. The smaller is $\boldsymbol{\alpha}$, the larger is the steady-state temperature. The homogeneity inside the reactor is increased: the `PaSR` tends towards a `PSR`. The larger is $\boldsymbol{\gamma}$, the smaller is the steady-state temperature value. Indeed, according to equation 5.17, the proportion of the fine-scale structure zone (i.e., the well-mixed zone, the reactive zone) is decreased. This may be rather perturbing to have a temperature that decreases with the Damköhler number, but this is nothing but an outcome of the retained definitions.

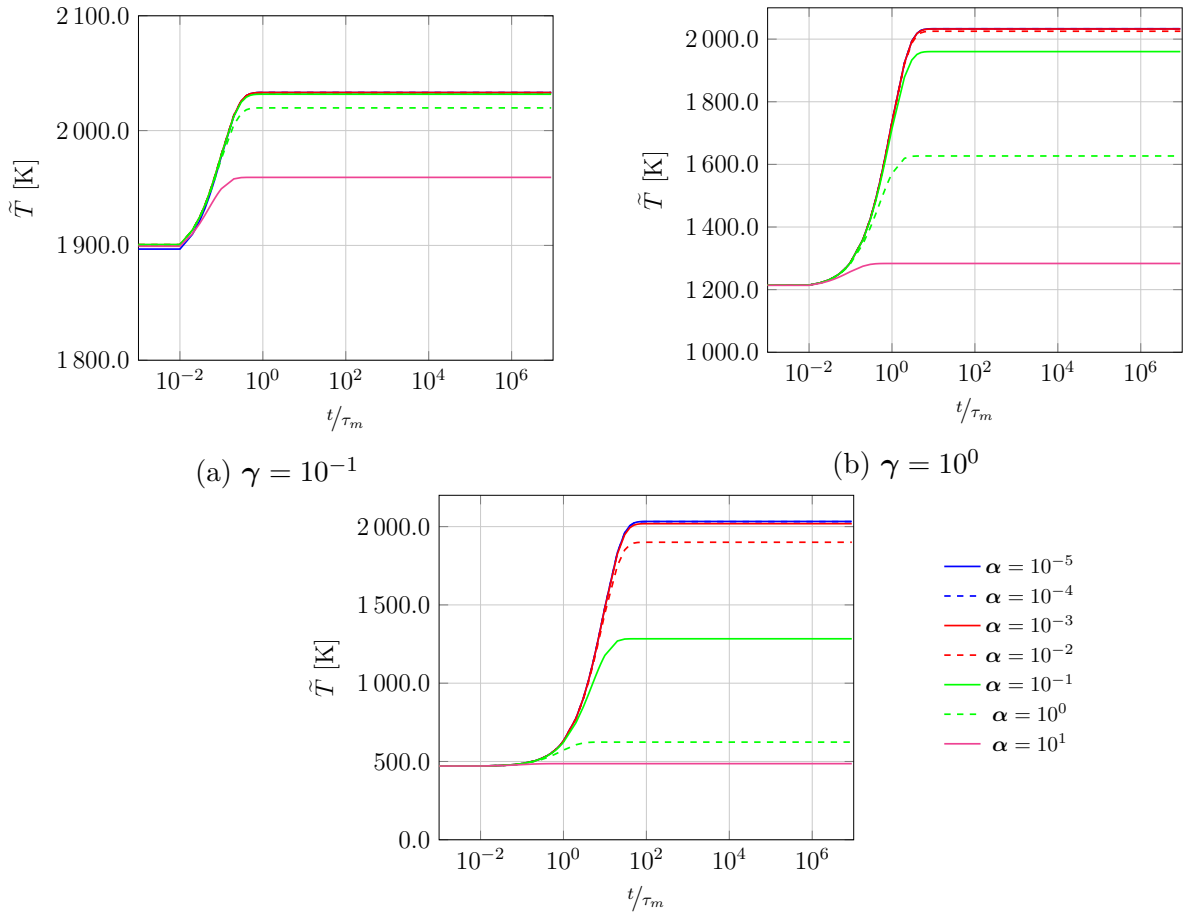

Figure 5.4 – Temperature temporal evolution

Figure 5.5 displays the steady-state value of the temperature as a function of $\boldsymbol{\alpha}$ (fig. 5.5a) and $\boldsymbol{\gamma}$ (fig. 5.5b). One can notice that, as $\boldsymbol{\alpha}$ decreases (i.e. the residence time

τ_{res} increases), the temperature tends to reach the same value whatever the value of $\boldsymbol{\gamma}$, which means that, as expected, the temperature is affected by both the residence time τ_{res} and the fine-scale structure volume fraction γ^*. However, provided that a sufficiently small value of $\boldsymbol{\alpha}$ is considered (i.e. large values of τ_{res}), the value retained for $\boldsymbol{\gamma}$ will not affect the mean temperature at steady-state: there will be enough time for the chemical processes to take place.

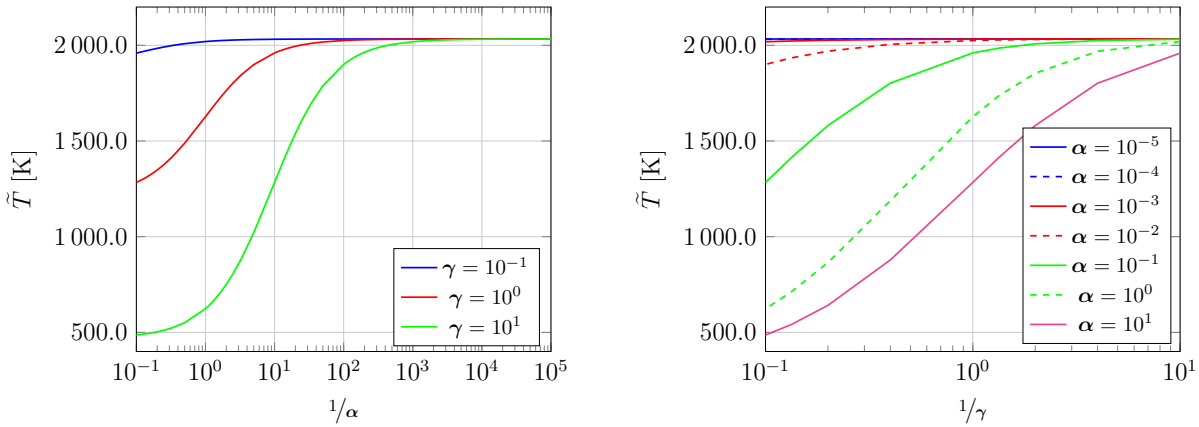

(a) Residence time variation

(b) Fine-scale structure fraction variation

Figure 5.5 – Steady-state mean temperature inside the reactor

Finally, since the quantities $\widetilde{\psi}$, ψ^* and ψ^0 are inter-related and since it is possible to solve the `U-PaSR` equations for $\widetilde{\psi}$, ψ^* and ψ^0, there exist several ways to calculate each quantity. For instance, ψ^0 can be evaluated by solving equations 5.16a and 5.16b or by deducing it from $\widetilde{\psi}$ and ψ^*.

Figure 5.6 presents the steady-state temperature of the surrounding zone (^{0}) as function of $\boldsymbol{\alpha}$ calculated from both equations 5.16a and 5.16b (represented by the lines) and from the relation with $\widetilde{\psi}$, ψ^* and ψ^0 (represented by the points).

One can notice that the two evaluations lead to the same value. This is quite a good verification of the `U-PaSR` equations programming (i.e., coding). This also confirms that the code can be handled with any couple of parameters $\left[\widetilde{\psi}, \psi^*\right]$, $\left[\widetilde{\psi}, \psi^0\right]$ or $\left[\psi^*, \psi^0\right]$, with the third composition easily deduced from the other two.

5.4 Preliminary comparison between the `PSR` and the `U-PaSR` models

Finally, this short chapter is ended by the simulation of a reactive flow over a rectangular cavity, which is used to compare the behavior of the `U-PaSR` and `PSR` models. The flow conditions for these reactive flow simulation are similar to those retained in §4.5.3

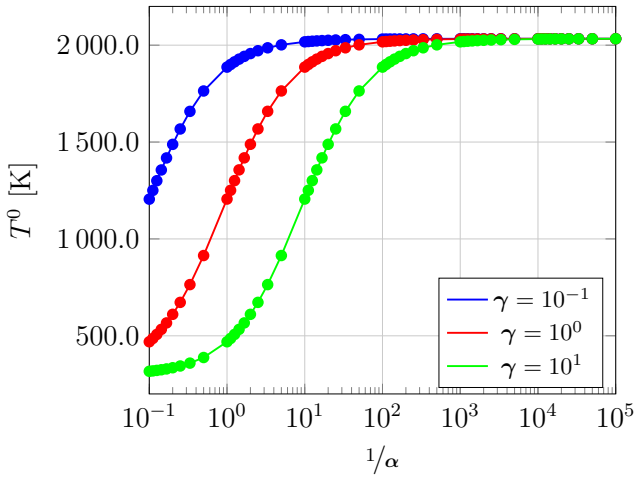

Figure 5.6 – Comparison between two possible evaluations of T^0 at steady-state

and the value of the length-to-depth ratio is $L/D = 2$. A mixture of hydrogen, oxygen and nitrogen is considered, with mass fractions $(H_2, O_2, N_2) = (0.01976, 0.95060, 0.02964)$ and the chemistry is represented with the detailed chemical scheme of O'Conaire et al. [136] (see appendix B for further details). Two distinct closures are considered to address Turbulence-Chemistry Interactions: one that ignores the influence of composition fluctuations and corresponds to the quasi laminar chemistry approximation (`PSR` hypothesis), and one that takes finite-rate chemistry and micro-mixing effects into account, dealing with the inhomogeneities of composition inside the flame region (`U-PaSR` hypothesis).

Figures 5.7 and 5.8 presents typical snapshots of the normalized temperature field (T/T_0) and the hydroperoxyl mass fraction (Y_{HO_2}), respectively. The hydroperoxyl is indeed considered as an excellent marker of autoignition for hydrogen combustion.

Figure 5.8 shows that the HO_2 production takes place in the vicinity of the shear layer. This radical is then depleted through OH radicals production and associated heat release resulting in accumulation of burned gases inside the cavity.

The comparison between `PSR` and `U-PaSR` results indicates, as expected, that the temperature levels issued from the `U-PaSR` model are slightly smaller than those issued from the `PSR` closure, which is explained by the fact that the `U-PaSR` model may take finite-rate chemistry and micro-mixing effects into account.

Summary

When dealing with supersonic combustion, chemical reaction time scales tend to be of the same order of magnitude as turbulent time scales. The Unsteady Partially Stirred Reactor (`U-PaSR`) is a multiscale-based model with fine-scale structure and mixing time scale

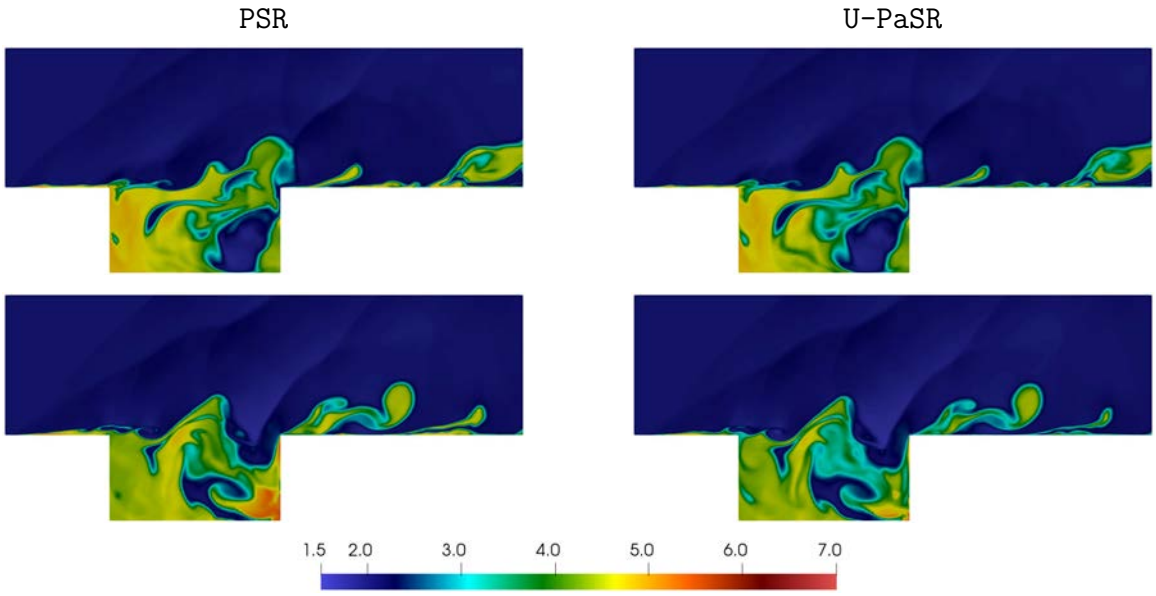

Figure 5.7 – Normalized temperature fields obtained at two given instants. Left: `PSR` model. Right: `U-PaSR` model.

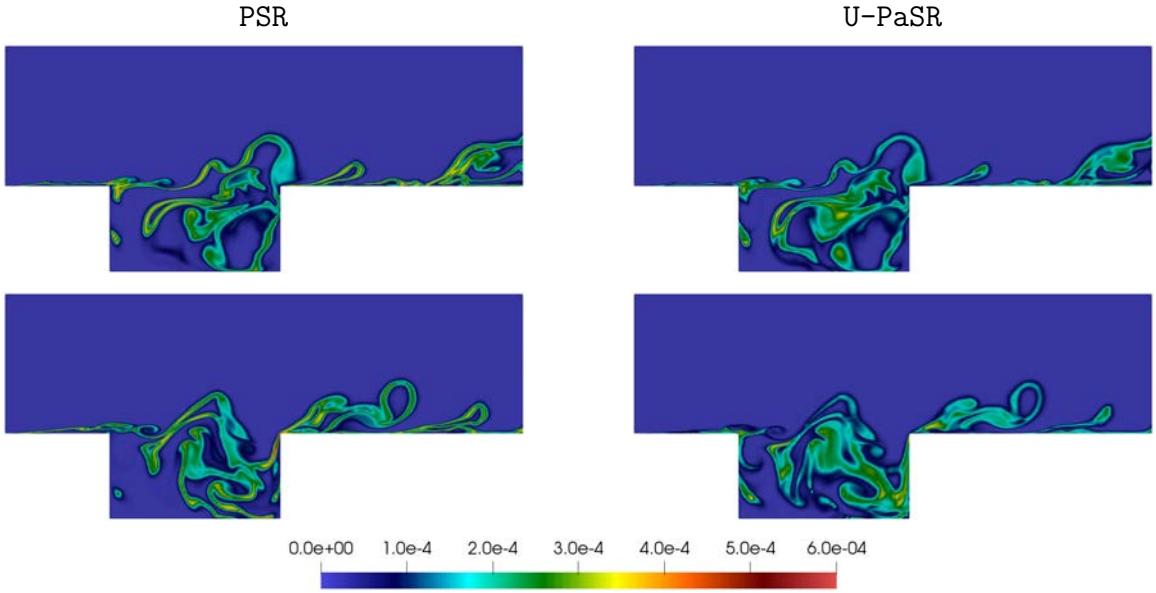

Figure 5.8 – Hydroperoxyl radical mass fraction fields obtained at two given instants. Left: `PSR` model. Right: `U-PaSR` model.

that takes into account the inhomogeneities of composition and temperature in the region where chemical reactions proceed. It is better suited to deal with supersonic combustion since it considers the effects of micro-mixing, finite chemistry and the interactions between them. Reaction takes place in fine-scale structure regions, that is well-mixed zones where most of the viscous dissipation and molecular mixing process take place.

The fine-scale volume fraction γ^* is defined as the ratio between the volume of the reactive structures and the volume of the sum of both reactive and mixing structures,

being function of both the chemical time scale and the subgrid mixing (micro-mixing) time scale. The chemical time scale τ_{ch} can be evaluated considering the transit time in a one-dimensional laminar premixed flame calculated at stoichiometric conditions, while the subgrid mixing time scale τ_m is estimated as the harmonic mean of the Kolmogorov time scale and the subgrid time scale. It is noteworthy that this closure satisfies the constraint that the `SGS` model should recover the `DNS` limit as the filter size tends to zero. Furthermore, the fine-scale volume fraction is used to relate the fine-scale structures ψ^*, the surrounding regions ψ^0 and the averaged state $\widetilde{\psi}$.

The particle residence time plays an important role in the model behavior. With a short residence time there is not enough time for the mixture to burn and the reactor behavior is limited by chemistry. The mixture burns almost entirely with a long residence time, with the reactor being limited by the mixing time. At intermediate residence times the reactor may be limited by chemistry of by the mixing time, depending on the conditions.

The limiting behavior of the `U-PaSR` is also verified. The homogeneity inside the reactor increases with the decrease of the subgrid mixing time scale, causing the `U-PaSR` model to tend towards a `PSR`. Temperature is affected by both the residence time and the fine-scale structure volume fraction. However, with a small subgrid mixing time scale, γ^* will not affect the mean temperature at steady-state since there will be enough time for the chemical processes to occur.

Moreover, since the averaged state ($\widetilde{\psi}$), the fine-scale structure region (ψ^*) and the surrounding region (ψ^0) are inter-related, the code was verified to confirm that it can handle any couple of parameters: $\left[\widetilde{\psi}, \psi^*\right]$, $\left[\widetilde{\psi}, \psi^0\right]$ or $\left[\psi^*, \psi^0\right]$, with the third one deduced from the others.

Finally, the `U-PaSR` and `PSR` models are both applied to the computation of a reactive flow over a rectangular cavity. The temperature levels obtained with the `U-PaSR` model are slightly smaller than those issued from the `PSR` due to the fact that it is capable to take into account finite-rate chemistry and micro-mixing effects. The next two chapters will be devoted to the computational study of a more representative geometry.

Chapter 6

Non-reactive simulations

This chapter focuses on the analysis of the non-reactive flow topology and structure in the scramjet engine model representative of the experiments performed by Micka and Driscoll [115, 116] at the University of Michigan.

6.1 Numerical setup

Figure 6.1 presents the experimental supersonic combustion facility consisting of a two dimensional Mach 2.2 nozzle, a constant area isolator that extends over 400.0 mm up to the leading edge of a rectangular cavity and a 349.0 mm long and 4° diverging section, dumping into a 152.0 mm diameter exhaust. The cavity is 50.8 mm long, 12.7 mm height and spans the entire width of the test section, which is equal to 38.1 mm.

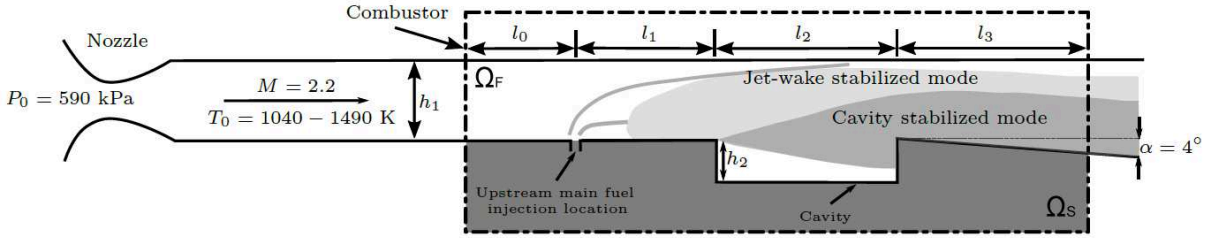

Figure 6.1 – Schematics of the combustion facility with the computational domain highlighted

The computational domain, highlighted in figure 6.1, can be decomposed into three distinct parts: a constant section channel s_1 with length $L_{x_1,s_1} = l_0 + l_1 = 94.5$ mm and height $L_{x_2,s_1} = h_1 = 39.4$ mm, a section s_2 with length $L_{x_1,s_2} = l_2 = 50.8$ mm featuring the wall-mounted cavity with depth $h_2 = 12.7$ mm, and a diverging section s_3 with length $L_{x_1,s_3} = l_3 = 76.2$ mm at 4° of inclination. The total length of the computational domain is then $L_{x_1} = 221.5$ mm and it is $L_{x_3} = 38.1$ mm in the spanwise direction. Section

s_1 features an injection port with diameter $D_{inj} = 2.5$ mm located along the combustor centerline at 44.5 mm upstream of the cavity leading edge.

The simulations are conducted within the `LES` framework with the subgrid-scale viscosity being treated using the `WALE` model (cf. §3). The parameters of the simulation are fixed as follows: $C_s = 0.18$, $C_I = 0.066$, $\texttt{Sc}_{sgs} = 0.7$ and $\texttt{Pr}_{sgs} = 0.7$, representing, respectively, the `WALE` model constant, the Yoshizawa model constant and the `SGS` Schmidt and Prandtl numbers. The `CFL` stability parameter was adjusted during the simulation between 0.3 and 0.7 and the Fourier number `Fo` was set at 0.9. The cavity geometry is modeled using `IBM` (cf. §4), detailed in appendix C and the corresponding boundary conditions are treated as a non-slip and adiabatic wall.

Time is normalized as $t^* = {}^{(t \cdot u_0)}/_{D_{inj}}$, with u_0 being the inlet flow velocity and D_{inj} the fuel injection orifice diameter. The simulation starts at $t^* = 0$ without any fuel injection and it is run without any chemical reactions. A fuel particle crosses the entire domain at $t^* = 300$ and the simulation runs up to $t^* = 750$. Data are saved at a frequency of 1.0 MHz from $t^* = 300$.

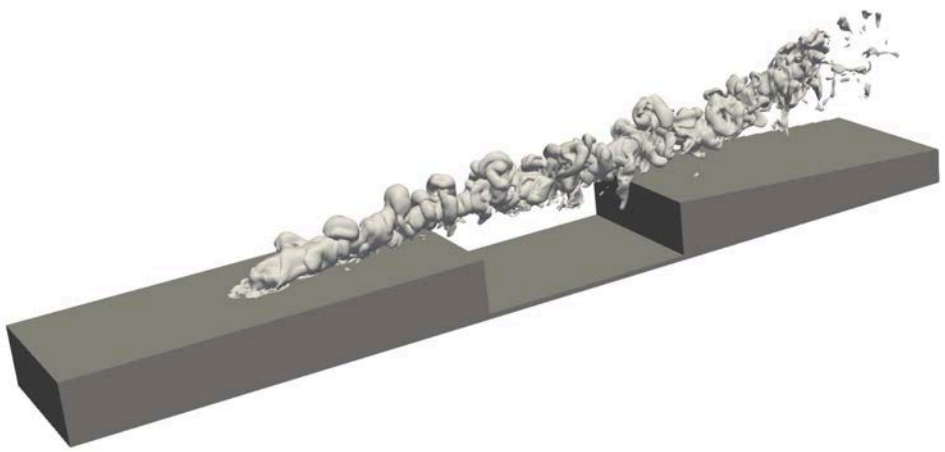

Figure 6.2 – Fully developed flowfield issued from the fuel injection at $t^* = 350$ (case `RFSC-LST`)

The computational grid is refined in the vicinity of the hydrogen jet exit, cavity walls and in the vicinity of the shear layer that develops above the cavity, gathering approximately $42,000,000$ points. The origin of the computational mesh is set at the center of the fuel injection orifice. A normalized mesh concentration parameter Δx_i, defined in equation 6.1, is used to determine the mesh size in relation to the biggest and the smallest mesh sizes, going from 0.0 (reduced concentration of points, i.e. larger mesh size) to 1.0 (high concentration of points, i.e. smaller mesh size).

$$\Delta x_i = 1 + \frac{\Delta x_{i,min} - \Delta x_{i,cur}}{\Delta x_{i,max} - \Delta x_{i,min}} \tag{6.1}$$

where Δx_i is the mesh concentration parameter, $\Delta x_{i,min}$ is the smallest mesh size, $\Delta x_{i,max}$ is the biggest mesh size and $\Delta x_{i,cur}$ is the current mesh size. All of these characteristic mesh sizes correspond to i-direction. Figure 6.3 presents the normalized mesh concentration Δx_1, Δx_2 and Δx_3:

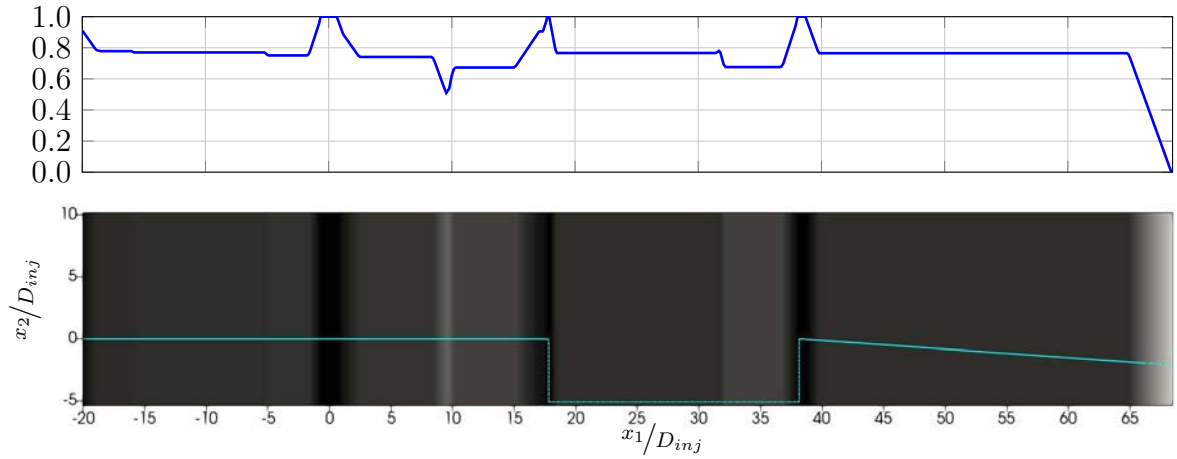

(a) Δx_1 (obtained at $x_3/D_{inj} = 0$)

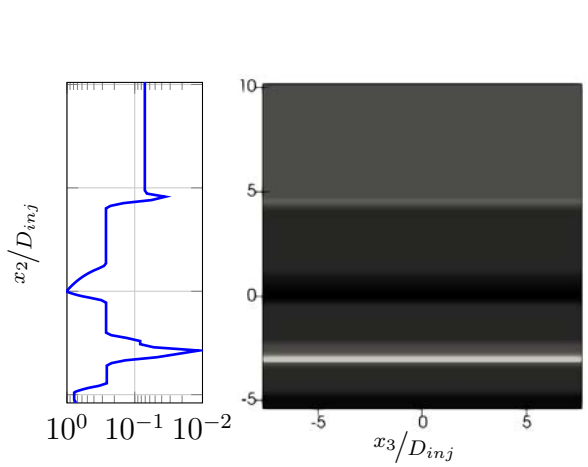

(b) Δx_2 (obtained at $x_1/D_{inj} = 0$)

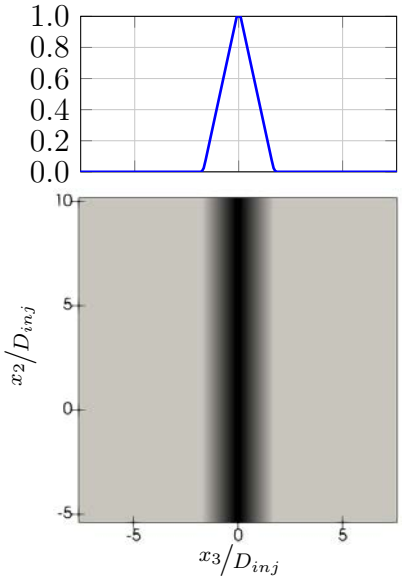

(c) Δx_3 (obtained at $x_1/D_{inj} = 0$)

Figure 6.3 – Normalized mesh size distribution with cavity geometry delineated with a colored line (cyan)

The initial air stagnation pressure is $p_0 = 590.0$ kPa and two distinct values of the vitiated air-stream temperature are considered: 1100.0 K (case `RFSC-LST`) and 1400.0 K (case `RFSC-HST`). Fuel is injected sonically at room temperature.

Table 6.1 gathers the main parameters that characterize the vitiated air and fuel inlet streams for both cases.

		Case RFSC-LST	Case RFSC-HST
Vitiated air inlet	T_0 (K)	1100.0	1400.0
	Y_{O_2}	0.244	0.251
	Y_{N_2}	0.671	0.607
	Y_{H_2O}	0.085	0.142
Fuel inlet	p_{inj} (kPa)	845.0	755.0
	T_{inj} (K)	288.0	288.0
	Y_{H_2}	1.0	1.0

Table 6.1 – Vitiated air and hydrogen inlet stream characteristics

6.1.1 Fuel inlet

In order to model the boundary layer in the fuel injector the following velocity profile is applied:

$$u\left(r,t\right) = \left[u_w - \left(u_{inj} - u_w\right) \operatorname{erf}\left(\frac{r - r_{inj}}{2\alpha r_{inj}}\right)\right] f\left(t\right) \tag{6.2}$$

where u_w is the flow velocity at the wall, u_{inj} is the nominal fuel injection velocity ($M_{inj} = 1.0$), r is the distance of the considered point to the center of the injection orifice, $r_{inj} = {}^{D_{inj}}/_2 = 1.25$ mm is the radius of the injection orifice, $\alpha = 0.05$ is a profile parameter for the velocity gradient. Finally, $f\left(t\right)$ is a temporal function that is used to avoid numerical instabilities that may arise when the fuel mass flow rate is applied directly. It is defined as:

$$f\left(t\right) = 1 - \exp\left(\frac{-5t}{t_{inj}}\right) \tag{6.3}$$

with t being the physical time and $t_{inj} = 0.2\mu$s the characteristic time required for the injection to be fully established. Figure 6.4 presents the normalized fuel injection velocity at steady-state.

Moreover, a passive scalar (mixture fraction or fuel inlet tracer ξ) is uniformly injected ($\xi = 1$) so as to follow the fuel presence in the computational domain.

6.1.2 Vitiated air inlet

The flow is accelerated by a Mach 2.2 nozzle and crosses through the isolator before entering the computational domain. In order to correctly impose the temperature and velocity profile at the inlet of the computational domain, some preliminary simulations of the isolator have been run. The corresponding results are presented in figure 6.5 for

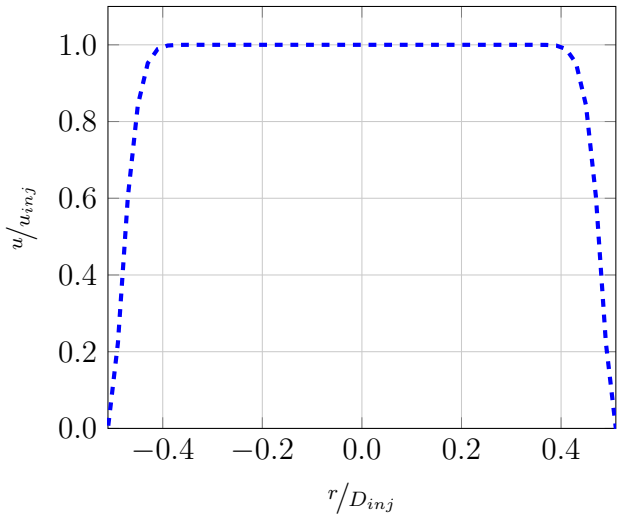

Figure 6.4 – Normalized fuel injection velocity at steady-state

cases `RFSC-LST` and `RFSC-HST`, where u_0 is the velocity corresponding to $M = 2.2$, while T_0 is 1100 K and 1400 K for cases `RFSC-LST` and `RFSC-HST`, respectively.

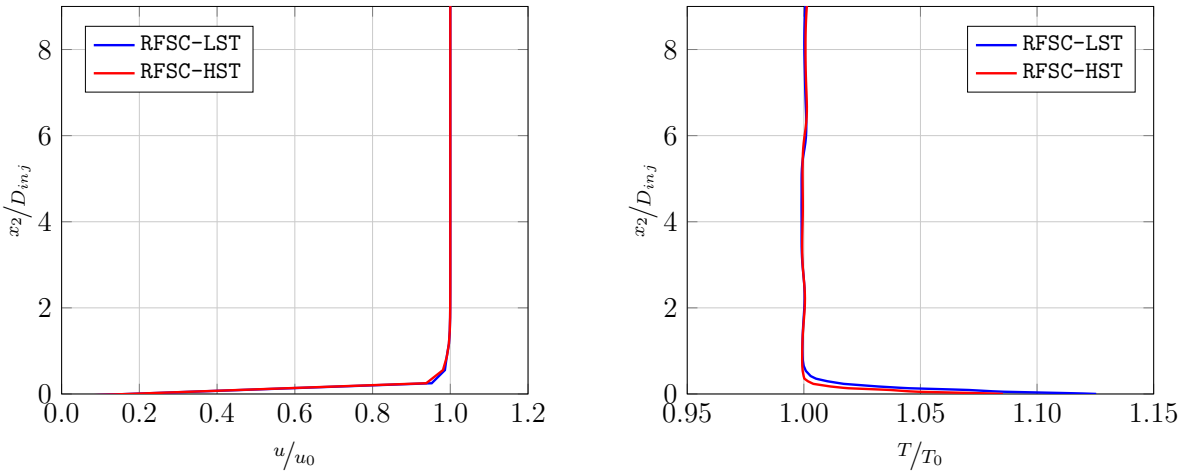

(a) Velocity (b) Temperature

Figure 6.5 – Velocity and temperature profile imposed in the vitiated air-stream

The pressure at the inlet of the computational domain is determined by considering the flow as isentropic:

$$\frac{p}{p_0} = \left(1 + \frac{\gamma - 1}{2} M_0^2\right)^{-\frac{\gamma}{\gamma - 1}} \tag{6.4}$$

with the value of the heat capacities γ being set to 1.313 and 1.287 for cases `RFSC-LST` and `RFSC-HST`, respectively, thus resulting in pressure values equal to 55.410 kPa and 55.426 kPa.

6.2 Computational resolution and statistical convergence

One of the main obstacle to the application of LES is the CPU time required to perform the simulations since the turbulent structures must be accurately resolved at all scales. In wall-bounded flows, the integral scale, away from walls, is proportional to the boundary-layer thickness δ. The resolution requirements are determined directly by the range of scales contributing to the desired statistics and indirectly by the accuracy of the model. Most of the turbulent kinetic energy production are associated to high speed streaks, which remain confined within a very small region in the vicinity of the wall [97], and the flow structures are extremely small when compared to the overall flow dimensions. These small structures, however, play an essential role in the turbulent boundary layer dynamics and therefore need to be well resolved. The choice of the mesh resolution therefore results from a compromise between what it should be and what one can afford computationally. There exist many criteria to asses the mesh resolution quality.

Table 6.2 presents the recommended order of magnitude for the computational mesh cell size, which, for a wall-resolved LES, must be small enough to correctly capture the boundary layer.

	DNS	**Wall-resolved LES**
Δx^+	$10-15$	$50-150$
Δy^+	1	<2
Δz^+	5	$10-40$

Table 6.2 – Recommended mesh size, expressed in wall units [142, 143, 152]

Figure 6.6 presents the mesh size distribution for case RFSC-LST, in wall units, over the IBM walls (fig. 6.6a), in a way similar to the one retained by Techer [174]. Considering only the zone where fuel and oxidizer are no longer separated, i.e. $\widetilde{\xi} \in [0.001, 0.999]$, shown in figure 6.6b, one can conclude that the mesh size satisfactorily satisfies the recommended criteria for a wall-resolved LES.

The same presentation is retained for case RFSC-HST, see figure 6.7, indicating that the mesh is also sufficiently resolved.

At this level, it is worth recalling that the non-dimensional velocity u^+ is expressed as the ratio between the mean longitudinal velocity u_1 and the friction velocity at the wall u_{τ_w}:

$$u^+ = \frac{u_1}{u_{\tau_w}} \tag{6.5}$$

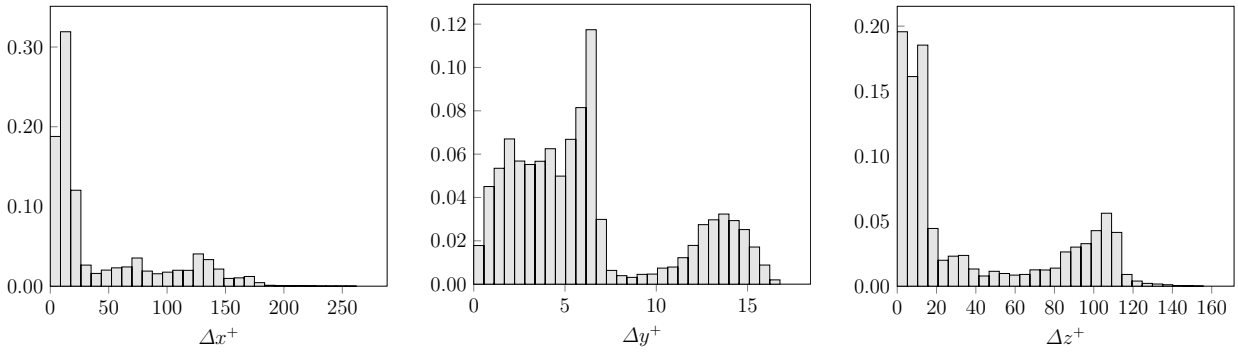

(a) Over all `IBM` walls

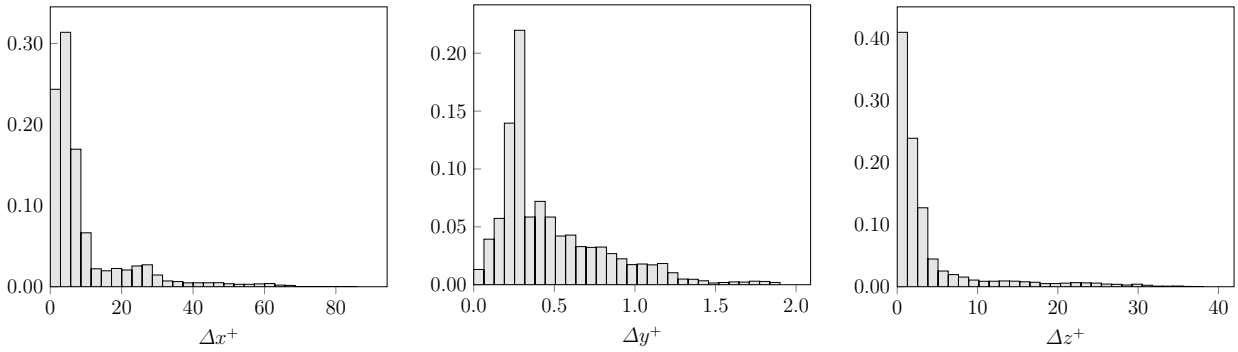

(b) Excluding regions associated to pure fuel and oxidizer

Figure 6.6 – Mesh size distribution histogram (case `RFSC-LST`)

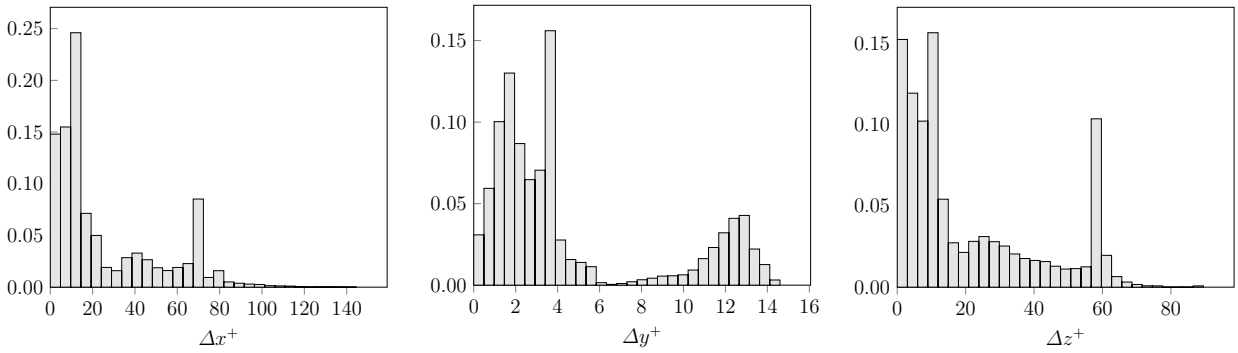

(a) Over all `IBM` walls

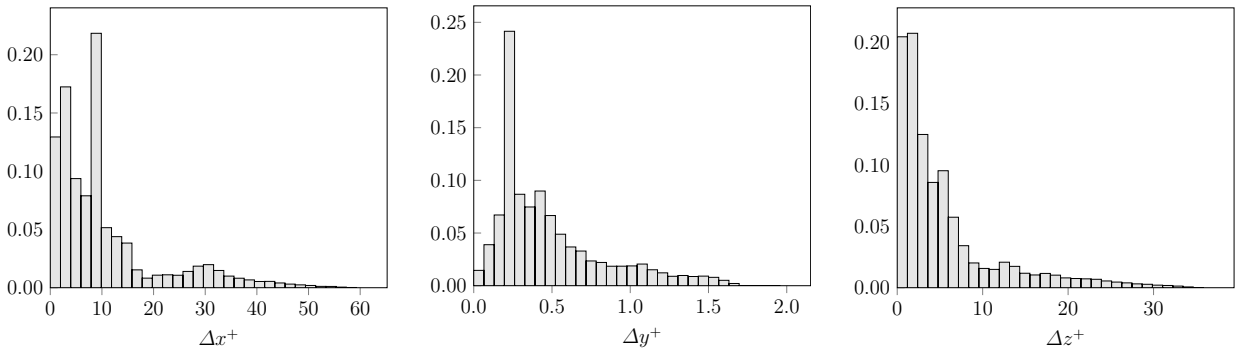

(b) Excluding regions associated to pure fuel and oxidizer

Figure 6.7 – Mesh size distribution histogram (case `RFSC-HST`)

and the wall distance y^+ is normalized by the ratio between the kinematic viscosity ν and the friction velocity at the wall u_{τ_w}, with x_2 being the distance perpendicular to the wall:

$$y^+ = \frac{x_2 u_{\tau_w}}{\nu} \tag{6.6}$$

with u_{τ_w} and τ_w expressed as:

$$u_{\tau_w} = \sqrt{\frac{|\tau_w|}{\rho_w}} \quad \text{and} \quad \tau_w = \mu \frac{\partial u}{\partial y}\bigg|_w$$

Figure 6.8 presents, respectively, the profiles of the normalized mean velocity u^+ plotted in wall units and the logarithm of the viscosity ratio $\log(\mu_{sgs}/\bar{\mu})$ at several locations in the median plane along the spanwise direction, i.e. $x_3/D_{inj} = 0$.

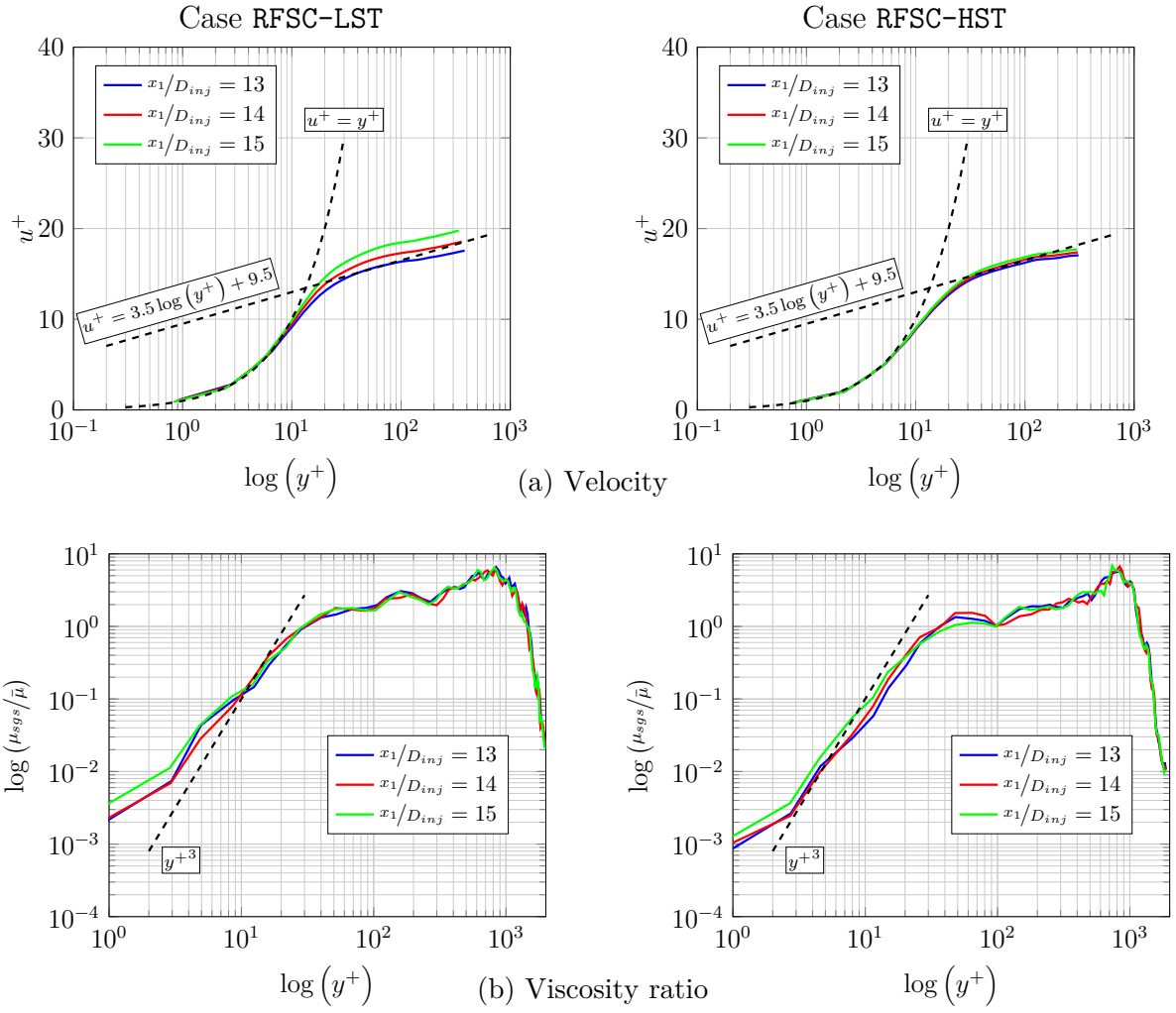

Figure 6.8 – Non dimensional velocity profile in wall units and viscosity ratio profile at several locations x_1/D_{inj} along $x_3/D_{inj} = 0$ for cases `RFSC-LST` (left) and `RFSC-HST` (right)

Despite the visible shift of the velocity in the logarithmic zone, these profiles confirm that the `WALE` model satisfactorily changes its behavior in the buffer layer that separates the logarithmic zone ($y^+ > 30.0$) from the viscous sublayer ($y^+ < 5.0$) [135, 175]. The viscosity ratio increases almost linearly, in logarithmic coordinates, especially in case `RFSC-HST`, which is consistent with the literature [135].

The assessment of the computational resolution is completed with a mesh quality analysis, allowing to verify its resolution in the flow. Two indexes were therefore considered, varying from zero (poor mesh resolution) to unity (good mesh resolution): the higher the value of the index, the better is the resolution.

The first quality index under consideration is the modified quality index IQ_k of Pope [145], defined as

$$IQ_k = \frac{k}{k + k_{sgs}} \tag{6.7}$$

where k is resolved turbulent kinetic energy k and k_{sgs} is its subgrid-scale unresolved counterpart, which is presently evaluated from the Yoshizawa closure [189]:

$$k_{sgs} = \frac{\nu_{sgs}}{(C_M \Delta)^2} \tag{6.8}$$

with $C_M = 0.069$. The mesh resolution is considered to be sufficient when $IQ_k \geq 0.8$, which means that at least eighty percent of the turbulent kinetic energy is captured at the resolved scale [145]. However, this quality index is sensitive to the subgrid-scale modelling, thus it is worthwhile to analyze its behavior together with other parameters.

The other quality index considered here is the one proposed by Celik et al. [37], which is expected to be less sensitive to the subgrid-scale modelling in comparison to IQ_k. It is based on a comparison between the computational grid characteristic size Δ and the Kolmogorov length scale $\mathcal{L}_\eta$, defined as:

$$IQ_\eta = \left[1 + \alpha_\eta \left(\frac{\Delta}{\mathcal{L}_\eta}\right)^m\right]^{-1} \tag{6.9}$$

with $\left(\alpha_\eta, m\right) = (0.05, 0.5)$. The value of $\mathcal{L}_\eta$ is evaluated from the following scaling rule:

$$\mathcal{L}_\eta = \left(\frac{\nu^3}{\varepsilon}\right)^{1/4} \tag{6.10}$$

with ε the turbulent kinetic energy dissipation rate.

Concerning the Celik quality index, it is worth recalling that a standard criterion for `DNS` computation is $k_{max}\mathcal{L}_\eta = 3/2$ in such a manner that, with a value of k_{max} of the order

of π/Δ, it leads to a value of $\Delta/\mathcal{L}_\eta$ approximately equal to 2.0, which once introduced in equation 6.9 gives $IQ_\eta = 0.93$. This means that in regions characterized by $IQ_\eta \geq 0.93$ the resolution is almost equivalent to the fulfillment of a standard DNS resolution criterion.

Figure 6.9 presents the PDF obtained with the two quality indexes, indicating that most of the values of the quality index IQ_k and IQ_η are higher than 0.80 and 0.93, respectively.

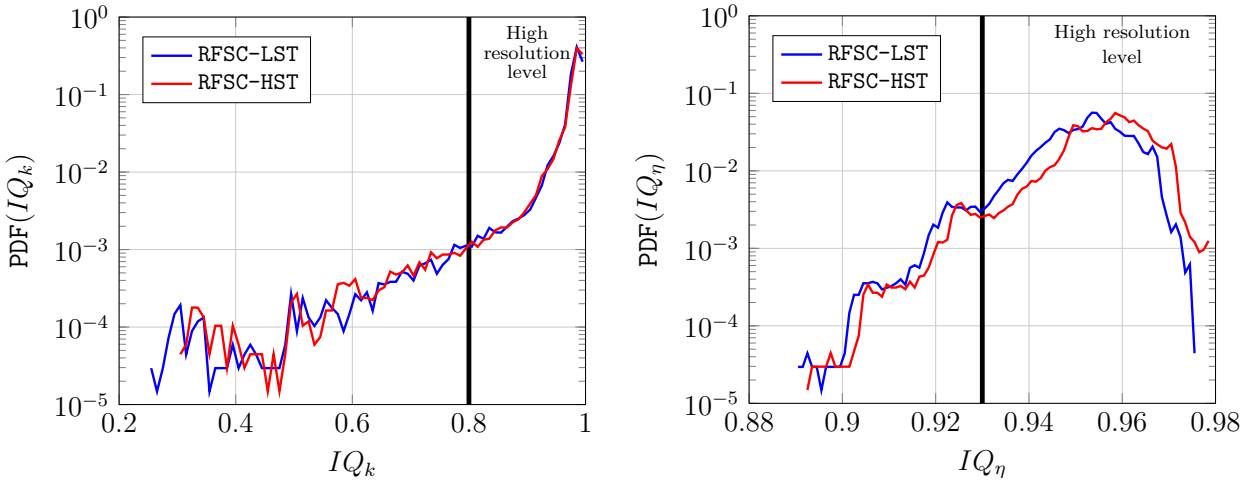

(a) Pope (b) Celik

Figure 6.9 – PDF of the quality index obtained in the median plane along the spanwise direction ($x_3/D_{inj} = 0$)

From the PDF, a Cumulative Distribution Function (CDF), may be expressed as

$$\mathbb{F}(x) = \int_0^x \mathtt{PDF}(IQ)\, \mathrm{d}IQ \tag{6.11}$$

and we consider also its complement to unity

$$1 - \mathbb{F}(x) = 1 - \int_0^x \mathtt{PDF}(IQ)\, \mathrm{d}IQ \tag{6.12}$$

The expression presented by equation 6.12 gives the probability of having an IQ value larger than a specified quantity. It is illustrated in figure 6.10, which shows that almost 98% of the obtained values of the Pope quality index IQ_k are larger than 0.80 and 95% of the obtained values of the Celik quality index IQ_η are larger than 0.93.

Finally, figures 6.11 and 6.12 presents the zones where the mesh is more resolved in the median plane along the spanwise direction ($x_3/D_{inj} = 0$) for Pope and Celik quality indexes, respectively. The vicinity of the fuel injection and the shear layer that develops above the wall-mounted cavity display quite acceptable levels of mesh resolution. The resolution

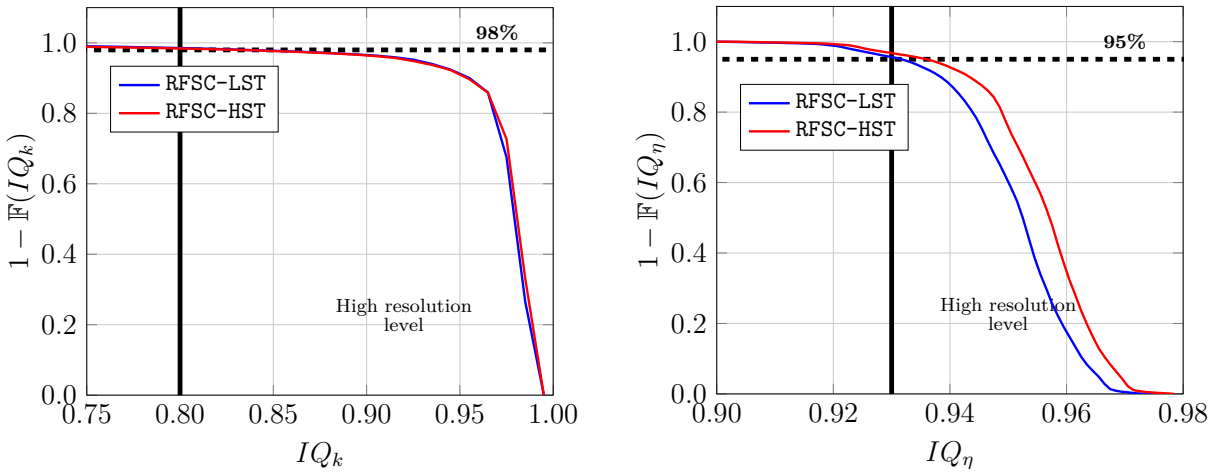

(a) Pope (b) Celik

Figure 6.10 – Probability to have a value of the quality index larger than 0.8 for IQ_k and larger than 0.93 for IQ_η

level is excellent upstream of the fuel inlet port and slightly decreases downstream of the hydrogen injection, especially for the Pope quality index. However, even in this region, the values remain quite satisfactory since they verify $IQ_k \geq 0.80$ and $IQ_\eta \geq 0.89$.

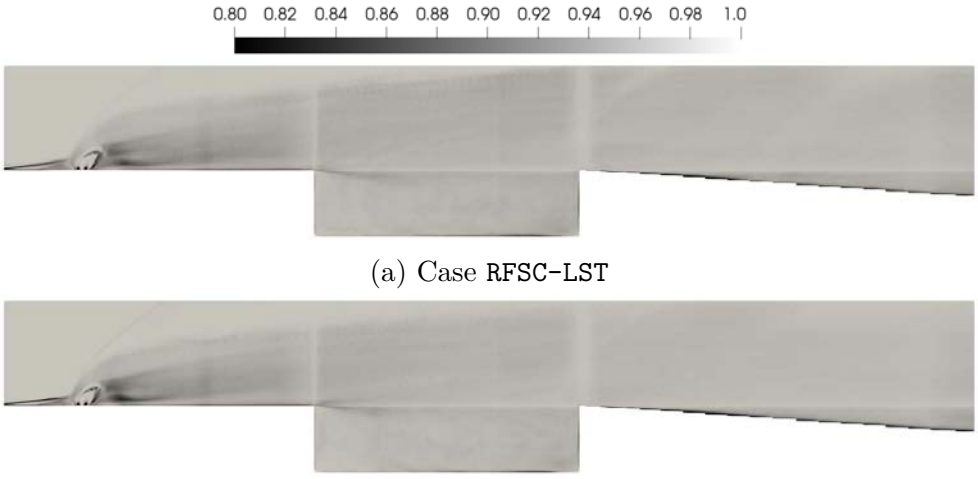

(a) Case `RFSC-LST`

(b) Case `RFSC-HST`

Figure 6.11 – Fields of Pope quality index IQ_k obtained in the median plane along the spanwise direction ($x_3/D_{inj} = 0$)

Then, we proceed with a statistical convergence analysis. Eight probes were placed in the computational domain, as shown in figure 6.13, so as to verify the convergence of the second-order moment. Table 6.3 summarizes the spatial filtering and temporal averaging operators.

Recalling that the temporal average (mean) of a variable f is expressed as

$$\langle f \rangle = \int_{\mathbb{R}} f \cdot \mathtt{PDF}\,(f)\ \mathrm{d}f \tag{6.13}$$

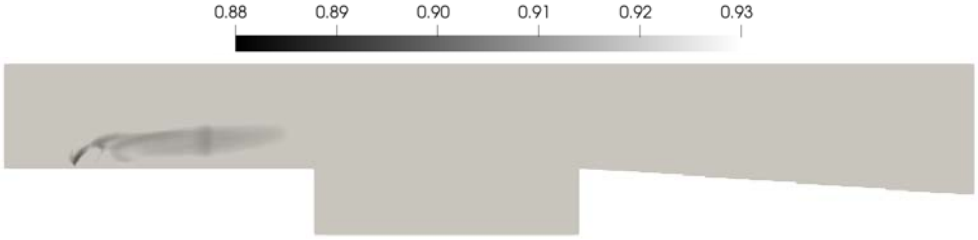

(a) Case `RFSC-LST`

(b) Case `RFSC-HST`

Figure 6.12 – Fields of Celik quality index IQ_η obtained in the median plane along the spanwise direction ($^{x_3}/_{D_{inj}} = 0$)

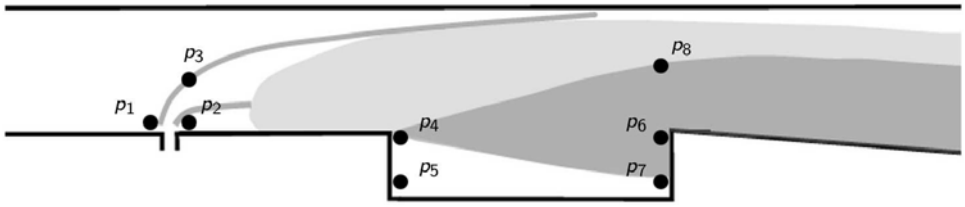

Figure 6.13 – Probes location for the second-order moment convergence analysis

Operator	Definition
$\bar{f}$	Spatial filter
$\widetilde{f} = {\overline{\rho f}}/{\bar{\rho}}$	Spatial filter weighted by density
$\langle f \rangle$	Temporal averaging (Reynolds average)
$\{f\} = {\langle \bar{\rho} f \rangle}/{\langle \bar{\rho} \rangle}$	Temporal averaging weighted by density (Favre average)

Table 6.3 – Expressions of spatial filtering and temporal averaging operators

The variance of a variable f corresponds to the expected value of the squared deviation from its mean, i.e

$$\sigma_f^2 = \int_{\mathbb{R}} (f - \langle f \rangle)^2 \cdot \mathtt{PDF}\,(f)\ \mathrm{d}f = \langle f^2 \rangle - \langle f \rangle^2 \tag{6.14}$$

Therefore, the second-order moment convergence of the filtered velocity $\bar{u}_i$ is checked by computing the following expression:

$$\langle \bar{u}_i \bar{u}_i \rangle - \langle \bar{u}_i \rangle \langle \bar{u}_i \rangle - \left(\bar{u}_i - \langle \bar{u}_i \rangle\right)^2 \tag{6.15}$$

Figure 6.14 presents the statistical convergence for velocities u_1 and u_2 for cases `RFSC-LST` and `RFSC-HST`, respectively. From these images, one can notice that the solu-

tion converges from $t^* \approx 450$ and $t^* \approx 500$ for cases `RFSC-LST` and `RFSC-HST`, respectively. Therefore, the statistical postprocessing of the computational results will take into account the snapshots obtained from these values up to the end of the simulation.

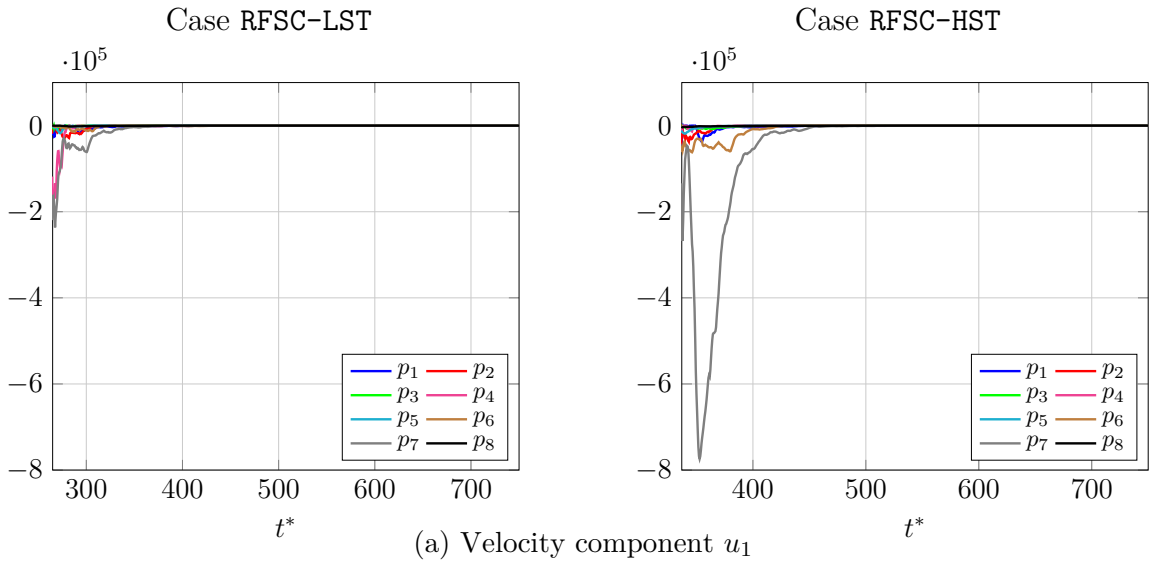

(a) Velocity component u_1

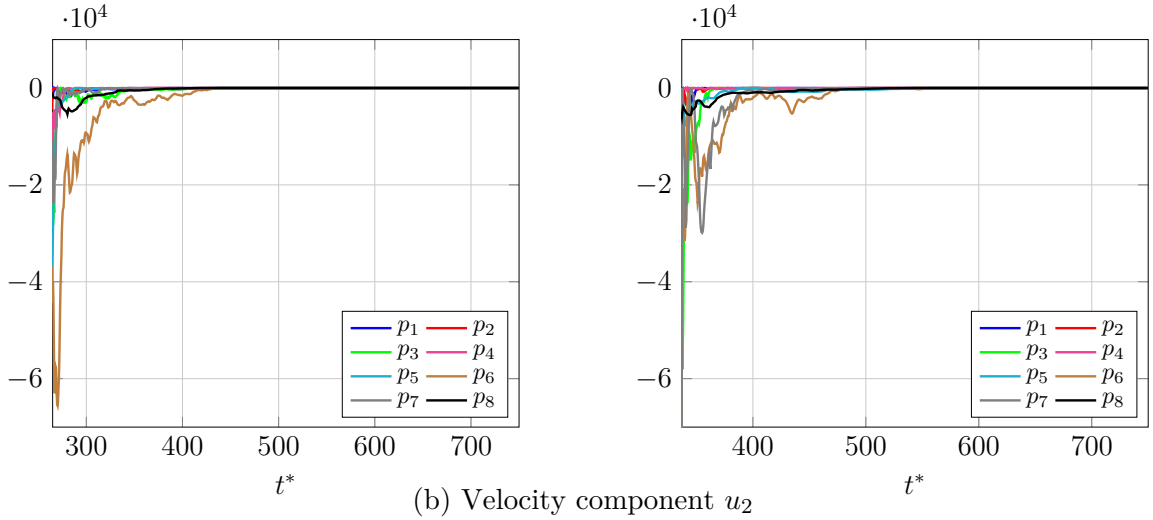

(b) Velocity component u_2

Figure 6.14 – Statistical convergence of the second-order moment

6.3 Computational results

6.3.1 Turbulent flow analysis

Figure 6.15 presents the instantaneous contours of numerical Schlieren $S_{\bar{\rho}}$ in the middle plane together with the iso-surface of fuel mass fraction Y_{H_2} colored by the normalized temperature $\widetilde{T}/T_0$ for cases `RFSC-LST` and `RFSC-HST`. The supersonic crossflow is blocked by a transverse jet, with the compression waves converging to a bow shock that wraps

the jet. The impact of the supersonic crossflow on the transverse jet generates large scale vortexes, which appear initially at the sides of the jet and slowly grow up in the near-field. These large scale coherent structures are generated by Kelvin-Helmholtz (K-H) instabilities induced by the velocity gradient [105]. This convection instability needs a continuous source of disturbance to be maintained. The turbulent boundary layer is separated in front of the bow shock, with a weak shock attached upon the separation region. Also, the large scale vortexes break into smaller ones during their transport further downstream.

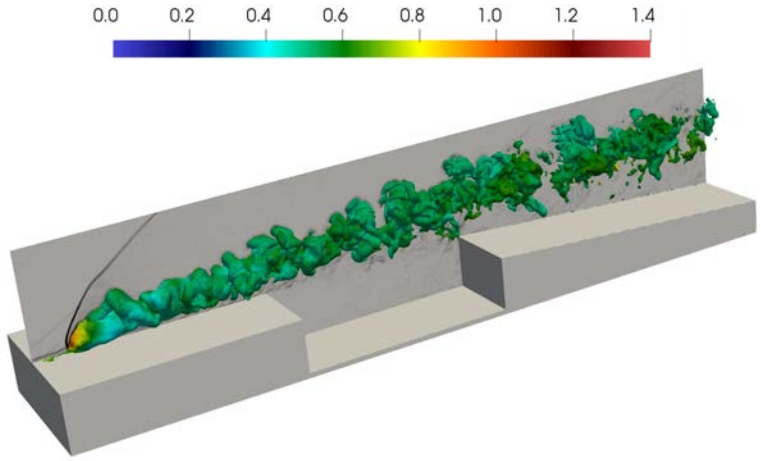

(a) Case RFSC-LST

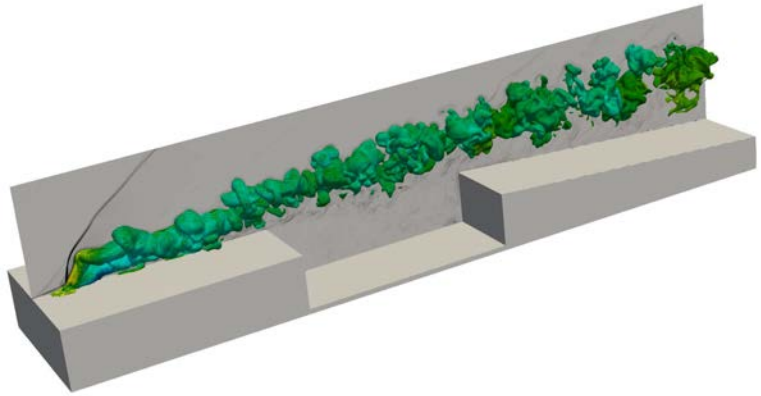

(b) Case RFSC-HST

Figure 6.15 – Instantaneous contours of numerical Schlieren $S_{\bar{\rho}}$ in the middle plane and iso-surface of fuel mass fraction Y_{H_2} colored by the normalized temperature $\widetilde{T}/T_0$

Instantaneous contours of fuel jet mass fractions in several spanwise planes are shown in figure 6.16 with sonic isolines in black. The initial mixing starts at the fuel jet injection and the jet is slightly teared up with the low-speed flow in the cavity. Most of the fuel is spread in the supersonic flow, with a small part flowing into the cavity, resulting in a mixing enhancement due to recirculation zones.

Figure 6.17 presents the flow streamlines for cases RFSC-LST and RFSC-HST, where

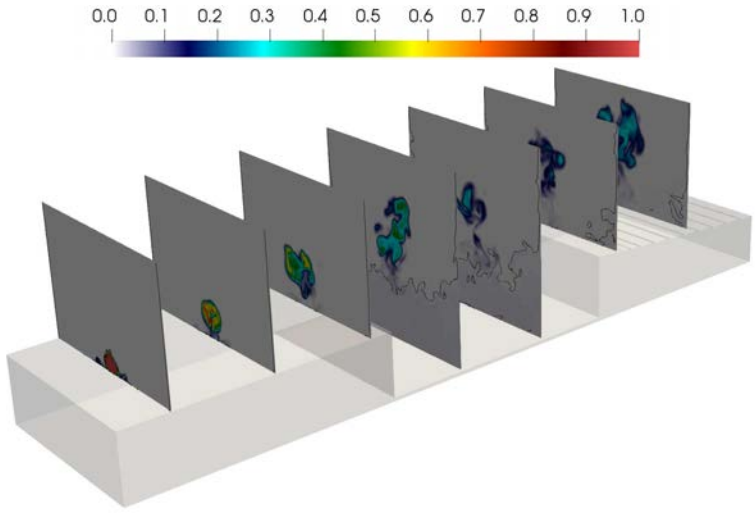

(a) Case `RFSC-LST`

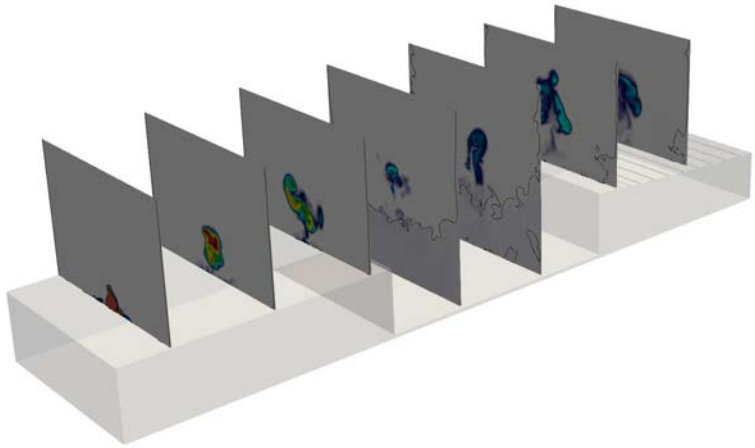

(b) Case `RFSC-HST`

Figure 6.16 – Instantaneous contours of fuel mass fraction at several spanwise planes: $x_1/D_{inj} = 0, 8, 16, 24, 32, 40, 48$

one can notice the presence of a large recirculation zone that covers up almost the entire cavity for case `RFSC-LST`, together with a smaller one located in the lower left corner. Case `RFSC-HST`, on the contrary, presents two large recirculation zones, each one occupying approximately half of the cavity, featuring also a small recirculation region at the lower left corner.

(a) Case `RFSC-LST`

(b) Case `RFSC-HST`

Figure 6.17 – Flow streamlines at $x_3/D_{inj} = 0$ showing the recirculation zones

Normalized average velocity can be calculated from the equation below:

$$\overline{U} = \frac{\sqrt{u_1u_1 + u_2u_2 + u_3u_3}}{U_\infty} \tag{6.16}$$

Figures 6.18 and 6.19 presents the normalized average velocity field zooming on the fuel injection and cavity. The supersonic crossflow is deflected away from the fuel jet when it crosses the bow shock and its velocity decreases. The turbulent boundary layer is separated due to the pressure gradient in front of the jet, forming a horseshoe vortex near the wall along the bow shock.

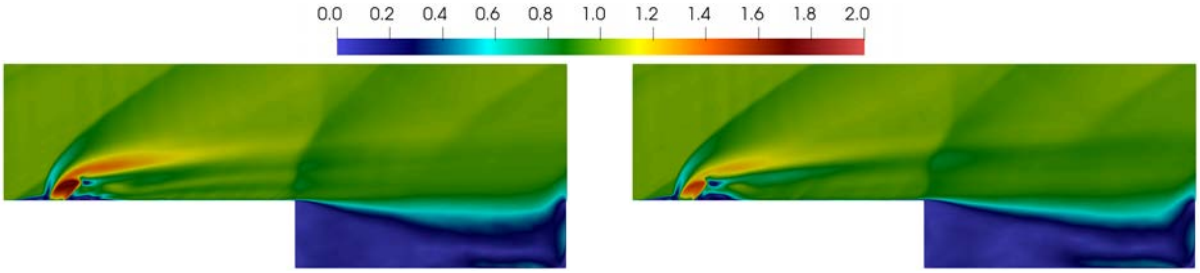

(a) Case `RFSC-LST` (b) Case `RFSC-HST`

Figure 6.18 – Normalized average velocity at $^{x_3}/_{D_{inj}} = 0$

6.3.2 Mixing efficiency analysis

The mixture fraction is nothing but an inlet tracer of the fuel feeding stream. Its value can be reconstructed from the ratio of the fuel to oxidizer mass fluxes

$$\xi_f = \xi_f\left(Y_f, Y_{ox}\right) = \frac{\phi\left(Y_f/Y_f^\infty\right) - \left(Y_{ox}/Y_{ox}^\infty\right) + 1}{1+\phi} \tag{6.17}$$

in such a manner that $\xi_f = 0$ in the oxidizer inlet stream and $\xi_f = 1$ in the fuel inlet stream. Considering the linearity of expression 6.17, we have $\widetilde{\xi}_f = \xi_f\left(\widetilde{Y}_f, \widetilde{Y}_{ox}\right)$.

Another way to calculate the mixture fraction is to solve its transport equation [75], assuming molecular diffusivity to be equal to thermal diffusivity ($\mathtt{Le} \approx 1$):

$$\frac{\partial}{\partial t}\left(\bar{\rho}\widetilde{\xi}\right) + \frac{\partial}{\partial x_i}\left(\bar{\rho}\widetilde{u}_i\widetilde{\xi}\right) + \frac{\partial}{\partial x_i}\left(\check{J}_{\xi i}\right) + \frac{\partial}{\partial x_i}\left(J_{\xi i}^{sgs}\right) - \frac{\partial}{\partial x_i}\left(\bar{J}_{\xi i} - \check{J}_{\xi i}\right) = 0 \tag{6.18}$$

where $\check{J}_{\xi i} = -\bar{\rho}\widetilde{D}\partial_i\widetilde{\xi}$ is the resolved molecular flux, $J_{\xi i}^{sgs} = -\overline{\rho\xi u_i} - \bar{\rho}\widetilde{\xi}\widetilde{u}_i$ is the subgrid scale mass flux, and $\left(\bar{J}_{\xi i} - \check{J}_{\xi i}\right)$ is the unresolved part of the molecular flux, which is assumed negligible [72, 174]. The boundary conditions are $\xi = 0$ at the oxidizer inlet and $\xi = 1$ at the fuel inlet.

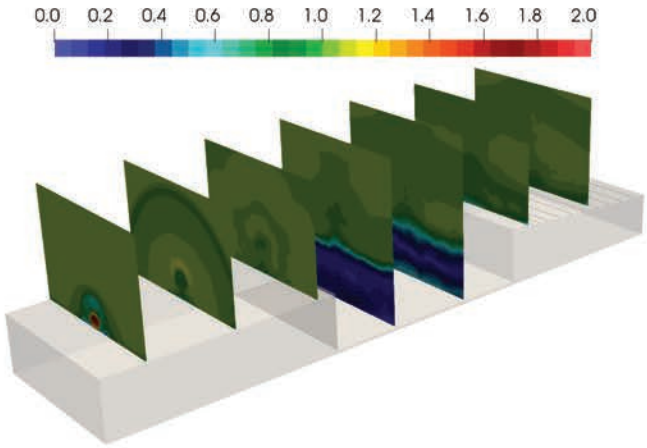

(a) Case RFSC-LST

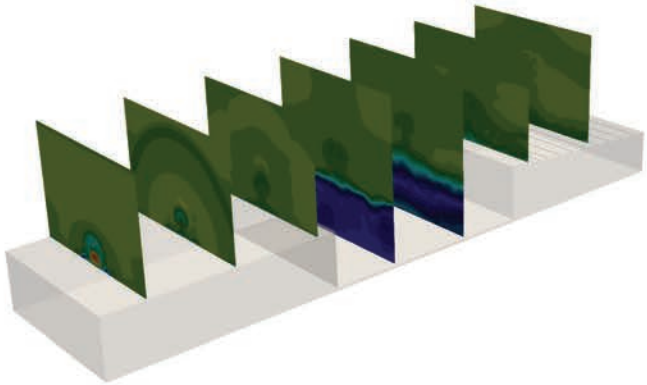

(b) Case RFSC-HST

Figure 6.19 – Normalized average velocity at several spanwise planes: $x_1/D_{inj} = 0, 8, 16, 24, 32, 40, 48$

These two quantities (ξ_f and ξ) must be similar if fuel and oxidizer inlets have the same boundary condition for both reconstructed (ξ_f) and transported (ξ) mixture fractions, and if the fuel and the oxidizer molecular diffusivity are approximately the same.

Within the LES framework, the variance of the mixture fraction may be calculated using the following decomposition [93, 144, 145]:

$$\sigma_\xi^2 = \widetilde{\xi''^2} = \langle \xi^2 \rangle - \langle \xi \rangle^2 = \frac{\langle \rho \xi^2 \rangle}{\langle \rho \rangle} - \frac{\langle \rho \xi \rangle^2}{\langle \rho \rangle^2} \tag{6.19a}$$

$$= \frac{1}{\langle \rho \rangle} \left[\left(\langle \bar{\rho} \widetilde{\xi^2} \rangle - \frac{\langle \bar{\rho} \widetilde{\xi} \rangle^2}{\langle \bar{\rho} \rangle} \right) + \left(\langle \rho \xi^2 \rangle - \langle \bar{\rho} \widetilde{\xi^2} \rangle \right) + \left(\frac{\langle \bar{\rho} \widetilde{\xi} \rangle^2}{\langle \bar{\rho} \rangle} - \frac{\langle \rho \xi \rangle^2}{\langle \rho \rangle} \right) \right] \tag{6.19b}$$

$$= \underbrace{\frac{\langle \bar{\rho} \widetilde{\xi^2} \rangle}{\langle \bar{\rho} \rangle} - \frac{\langle \bar{\rho} \widetilde{\xi} \rangle^2}{\langle \bar{\rho} \rangle^2}}_{(\mathbf{I}):\sigma^2_{\xi,res}} + \underbrace{\frac{\langle \bar{\rho} \left(\widetilde{\xi^2} - \widetilde{\xi}^2 \right) \rangle}{\langle \bar{\rho} \rangle}}_{(\mathbf{II}):\sigma^2_{\xi,sgs}} + \underbrace{\mathbf{R}_v}_{(\mathbf{III})} \tag{6.19c}$$

with

(I): $\sigma^2_{\xi,res}$, the resolved variance, calculated from the resolved field of the filtered variable.

(II): $\sigma^2_{\xi,sgs} = \langle \widetilde{V}_\xi \rangle$, the average value of the subgrid variance $\widetilde{V}_\xi \overset{\text{def}}{=} \widetilde{\xi^2} - \widetilde{\xi}^2$.

(III): $\mathbf{R}_v = \mathbf{R}_{\langle \rho\xi^2 \rangle} - \mathbf{R}_{\langle \rho\xi \rangle^2}$, a residual term such as

$$\mathbf{R}_{\langle \rho\xi^2 \rangle} = \frac{\langle \rho\xi^2 \rangle}{\langle \rho \rangle} - \frac{\langle \bar{\rho}\widetilde{\xi^2} \rangle}{\langle \bar{\rho} \rangle} \qquad \text{and} \qquad \mathbf{R}_{\langle \rho\xi \rangle^2} = \frac{\langle \rho\xi \rangle^2}{\langle \rho \rangle^2} - \frac{\langle \bar{\rho}\widetilde{\xi} \rangle^2}{\langle \bar{\rho} \rangle^2}$$

which can be neglected in a sufficiently well-resolved LES [181]. Further details can be found in the PhD thesis of Techer [174].

Figure 6.20 presents the longitudinal profile of the average reconstructed mixture fraction ($\widetilde{\xi}_f$) and the average transported one ($\widetilde{\xi}$), for cases RFSC-LST and RFSC-HST, at $(x_2/D_{inj}, x_3/D_{inj}) = (2, 0)$, focusing the injection and cavity region ($-4 \leq x_1/D_{inj} \leq 38$).

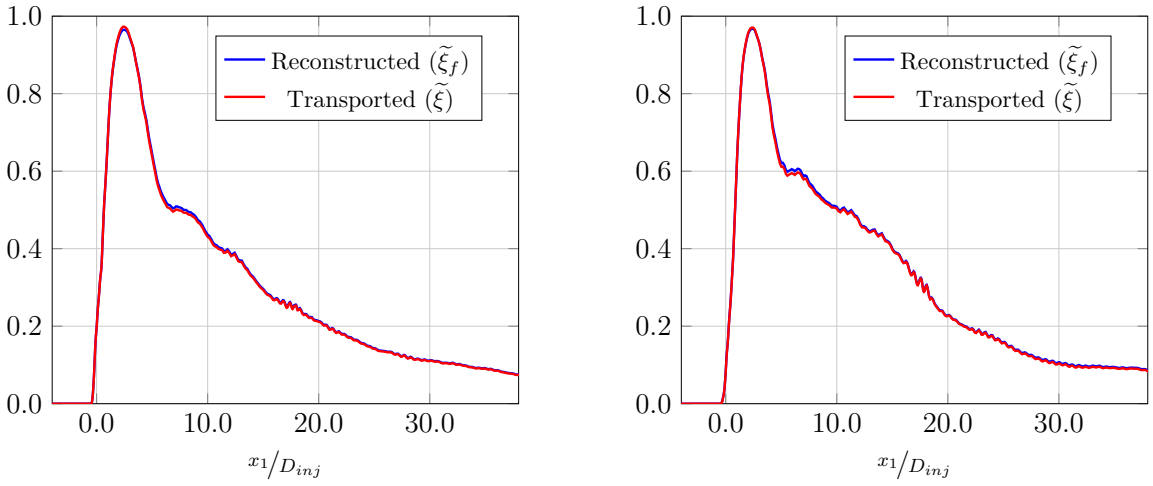

(a) Case RFSC-LST (b) Case RFSC-HST

Figure 6.20 – Longitudinal profile of the reconstructed (blue) and transported (red) mixture fraction, at $(x_2/D_{inj}, x_3/D_{inj}) = (2, 0)$

The same is done for the variance σ^2_ξ, displayed in figure 6.21.

Analyzing these results one can notice that, as expected, the reconstructed and the transported mixture fraction are similar, with only very small differences being obtained around $x_1/D_{inj} = 7$, but the overall results are quite satisfactory.

The mixing efficiency, i.e. the mixing degree of fuel and air, can be defined by the mass flow rate ratio of reactants that would react and the total mass flow rate of reactants:

$$\eta_m = \frac{\int Y_r \rho \, \mathrm{d}A}{\int Y_f \rho \, \mathrm{d}A} \tag{6.20}$$

where, following the analysis conducted in reference [105], the mass fraction of reactants that react Y_r is approximated as follows

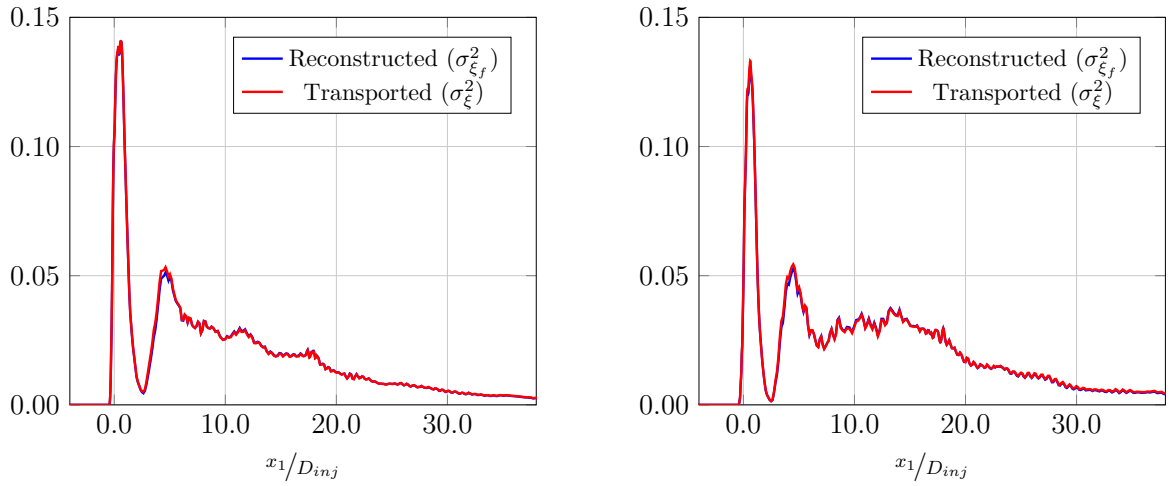

(a) Case `RFSC-LST` (b) Case `RFSC-HST`

Figure 6.21 – Longitudinal profile of the reconstructed (blue) and transported (red) mixture fraction (top) variance, at $\left(x_2/D_{inj}, x_3/D_{inj}\right) = (2, 0)$

$$Y_r = \begin{cases} Y_f & Y_f \leq Y_{f,st} \\ Y_{f,st}\left(\dfrac{1-Y_f}{1-Y_{f,st}}\right) & Y_f > Y_{f,st} \end{cases} \tag{6.21}$$

with Y_f being the fuel mass fraction, $Y_{f,st}$ the fuel stoichiometric mass fraction and Y_r the fuel mass fraction taking part in the reaction.

Figure 6.22 presents the mixing efficiency along the streamwise direction, zooming the fuel injection and the wall-mounted cavity, i.e., $-4 \leq x_1/D_{inj} \leq 38$. The obtained results display some similarities with those previously obtained by Liu et al. [105], who retained the same definition of the mixing efficiency. The mixing efficiency is close to 100% before the fuel injection because a small part of fuel propagates upstream along the turbulent boundary layer and is sufficiently mixed with air. A minimum point if found ahead of the fuel jet injection because the mixing is dominated by large scale vortexes in the jet shear layer. Moreover the mixing efficiency increases faster along the cavity, which means that mixing is enhanced, reaching almost 100% at the end of the cavity.

Summary

The conditions simulated in this chapter are relevant to experiments previously conducted at the University of Michigan [116, 117], but without chemical reactions.

The computations are performed with `CREAMS`, featuring the recently-implemented Immersed Boundary Method (`IBM`) algorithm. The simulations were conducted within the `LES` framework considering the Wall-Adapting Local Eddy (`WALE`) as the subgrid-scale

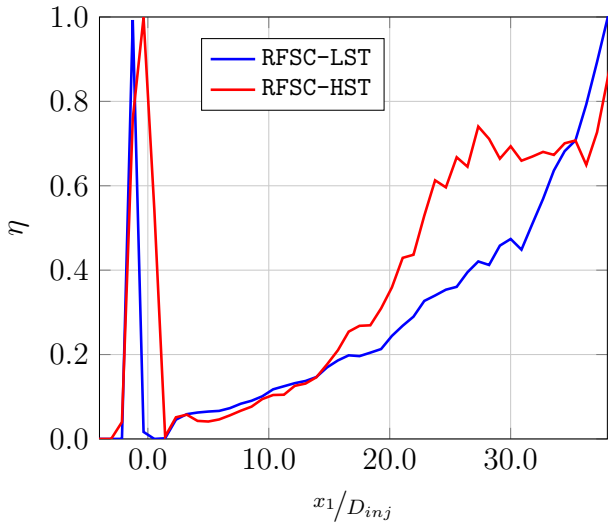

Figure 6.22 – Mixing efficiency along the streamwise direction

viscosity closure. Computational resolution was verified using several criteria and some efforts have been spent to capture the flow near the `IBM` walls as accurately as possible. Furthermore, the use of the `WALE` model allows to recover satisfactorily the behavior in the buffer layer that separates the logarithmic zone from the viscous sublayer.

Fuel mixing starts at the fuel jet injection, with the jet slightly tearing up with the low-speed flow inside the cavity, enhancing the mixing due to recirculation zones. Case `RFSC-LST` presents one large recirculation zone that covers the almost the entire cavity. Two large recirculation zones are found in case `RFSC-HST`, each one covering almost half of the cavity.

The supersonic crossflow is deflected away from the fuel jet when it crosses the bow shock and its velocity decreases. A horseshoe vortex is formed near the wall along the bow shock because of the pressure gradient in front of the jet.

Two different mixture fraction frameworks are compared: one reconstructed from fuel and oxidizer mass flux (ξ_f) and other calculated from the transport equation (ξ), with both providing similar results.

Finaly, mixing efficiency are evaluated between the fuel injection and the cavity region. The wall-mounted cavity provides a low-speed reflux region for the ignition and flame stability. Thus, the presence of the cavity increases significantly the mixing efficiency due to reflux effect inside it.

Chapter 7

Reactive simulations

The objective of the present chapter is to analyze the reactive flow topology and structure as well as combustion regimes, which are investigated on the basis of standard turbulent diagrams. The computational setup consists in a scramjet engine model representative of the experiments performed by Micka and Driscoll [115, 116] at the University of Michigan (cf. §6 - Non-reactive simulations). Combustion stabilization is studied for two different inlet vitiated air-stream temperature levels, denoted as `RFSC-LST` and `RFSC-HST` for low and high stagnation inlet temperatures, respectively. The results discussed in this chapter have been central to a paper published in the Proceedings of the International Conference on Computational Fluid Dynamics (`ICCFD`) [150].

7.1 Numerical setup

The computational setup is similar to the one presented in chapter §6 - Non-reactive simulations, consisting of a Mach 2.2 nozzle, a constant area isolator, a rectangular cavity and a diverging section (cf. figure 6.1). The computational domain and the parameters of the simulation are also the same.

Time is normalized in the same way ($t^* = {}^{(t \cdot u_0)}/_{D_{inj}}$) and the simulation starts at $t^* = 300$, from the non-reactive simulation, when the fuel injection is fully developed along the computational domain. Chemical reaction is activated and the simulation is run up to $t^* = 1200$. Data are saved at 1.0 MHz.

The two distinct values of the vitiated air-stream temperature considered in the non-reactive simulation (cases `RFSC-LST` and `RFSC-HST`) are considered to study the combustion stabilization process. The detailed mechanism of O'Conaire et al. [136], consisting of 9 chemical species (H_2, O_2, H_2O, H, O, OH, HO_2, H_2O_2 and N_2) and 21 elementary reaction steps, detailed in appendix B, is used to represent the H_2-air chemistry.

The main parameters that characterize the vitiated air and fuel inlet streams for both cases are the same as those presented in table 6.1.

Since the flow is now influenced by chemical reactions, statistical convergence analysis must be performed again. The same probes as those reported in figure 6.13 are used to check the second-order moment convergence of the filtered velocity, which are calculated from equation 6.15.

Figure 7.1 presents the statistical convergence for the first two velocity components for cases `RFSC-LST` and `RFSC-HST`, respectively, where one can notice that the solution converges from $t^* \approx 800$ and $t^* \approx 900$ for cases `RFSC-LST` and `RFSC-HST`, respectively. The statistical postprocessing of the computational results will take into account the snapshots obtained from these values up to the end of the simulation.

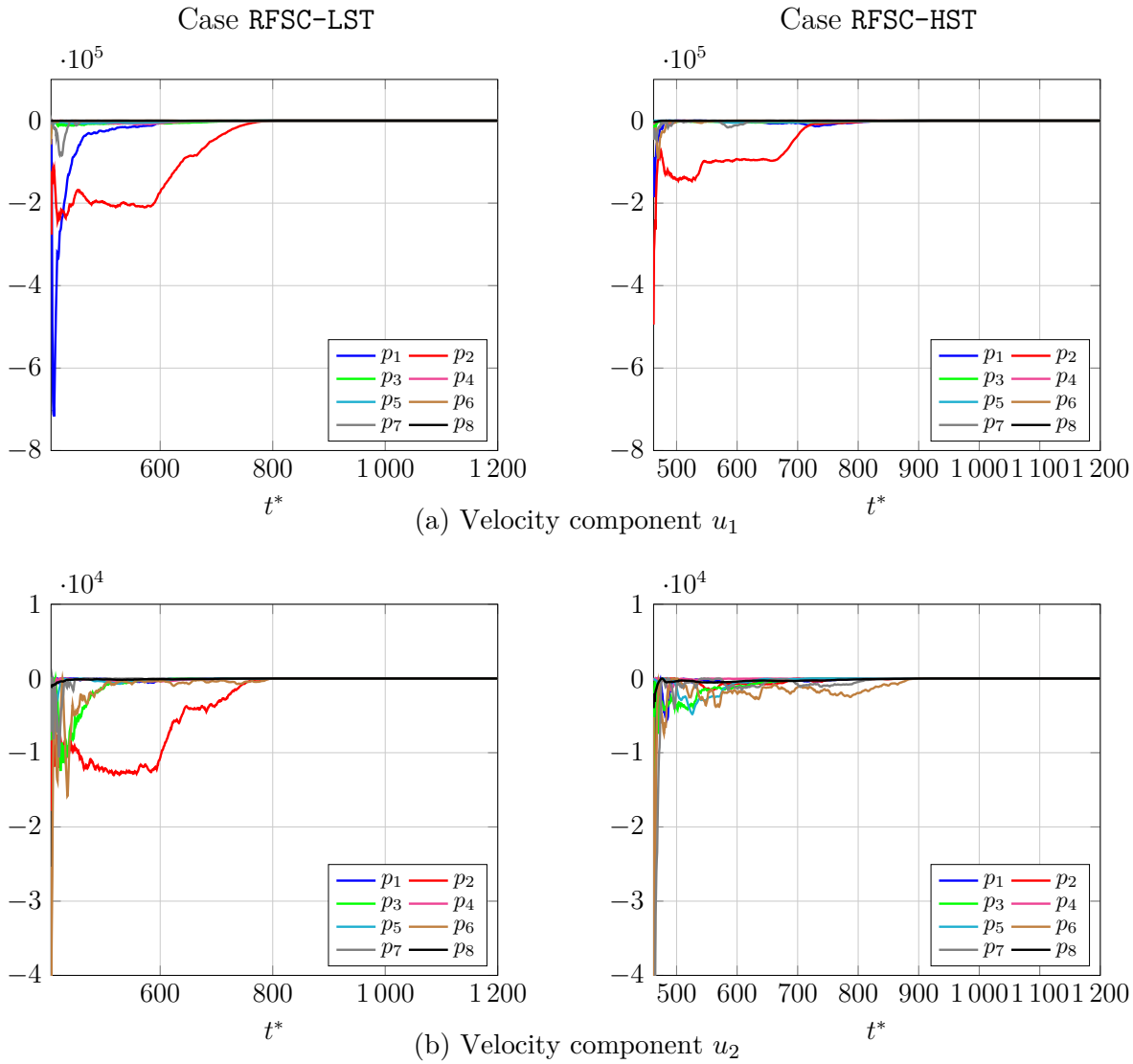

(a) Velocity component u_1

(b) Velocity component u_2

Figure 7.1 – Statistical convergence of the second-order moment

7.2 Temperature influence on the flame structure

According to the studies of Micka and Driscoll [115], for the range of conditions explored in Micka's thesis, the vitiated air-stream temperature T_0 plays an important role in determining the combustion stabilization mode. For inlet temperature such that $T_0 > 1350$ K the combustion is expected to be stabilized in jet-wake mode, whereas when $T_0 < 1150$ K it appears to be stabilized in cavity mode. In the intermediate range ($1150\text{ K} < T_0 < 1350\text{ K}$) combustion oscillates between the two stabilization modes. Equation 7.1 may be used to approximate the fraction of time f the combustion takes place in jet-wake stabilized mode:

$$f = \frac{1}{2} + \frac{1}{2}|T_0 - 1250\text{ K}|\,\mathrm{erf}\left(\frac{T_0 - 1250\text{ K}}{75\text{ K}}\right) \tag{7.1}$$

It is plotted in figure 7.2 together with the two conditions studied in the thesis.

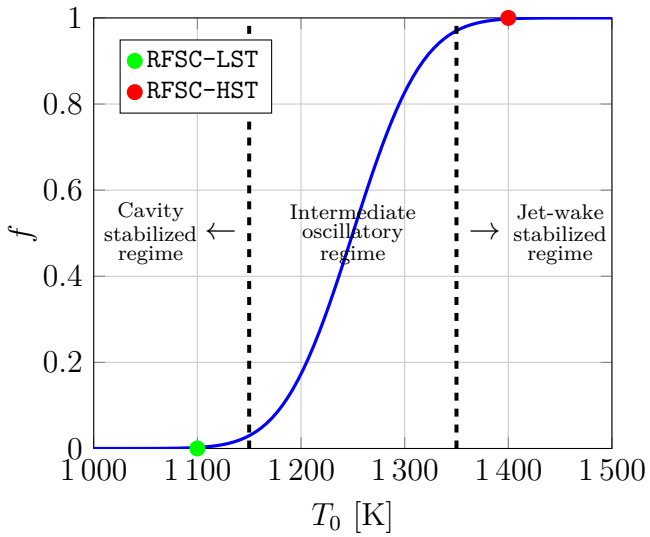

Figure 7.2 – Combustion stabilization mode vs. vitiated air-stream temperature

The flame remains in the cavity-stabilized mode at lower T_0 until a large enough fluctuation flashes it forward to a relatively stable location in the jet-wake mode. It will then remain in the jet-wake stabilized mode until it becomes unstable due to another fluctuation, forcing it to flash back to the cavity stabilized location. The magnitude of the fluctuations required for the flame to flash back and forth becomes smaller as T_0 increases. Alongside with that, as T_0 increases, the magnitude of the fluctuations that may cause the flame to flash back increases too. Thus, with the increase of the temperature T_0, the flame tends to remain more time in the jet-wake stabilized mode, until it reaches a high enough value where no fluctuations will be able to destabilize it.

7.3 Computational results

7.3.1 Comparison between PSR and U-PaSR models

Figures 7.3, 7.4 and 7.5 present, respectively, the average H_2, OH and HO_2 mass fraction profiles obtained at several locations x_1/D_{inj} in the median plane along the spanwise direction ($x_3/D_{inj} = 0$), considering the PSR (blue line) and the U-PaSR (red line) reactor model, for cases RFSC-LST (continuous line) and RFSC-HST (dashed line). Both PSR and U-PaSR approaches display quite similar results, with only very small differences seen in figure 7.5 at $x_1/D_{inj} = 6$, between $2 < x_2/D_{inj} < 4$, for case RFSC-LST. This similarity between PSR and U-PaSR may be explained by the fact that the mesh size is very small, causing $\gamma^* \to 1$, when the U-PaSR reactor behaves like a PSR one (cf. §5.1). Cases RFSC-LST and RFSC-HST present a similar behavior, but with different OH and HO_2 mass fractions due to different inlet temperatures in each case. Moreover, the presence of OH and HO_2 near the wall around the fuel injection indicates that combustion occurs in this region, which happens because of the presence of a small recirculation zone around it.

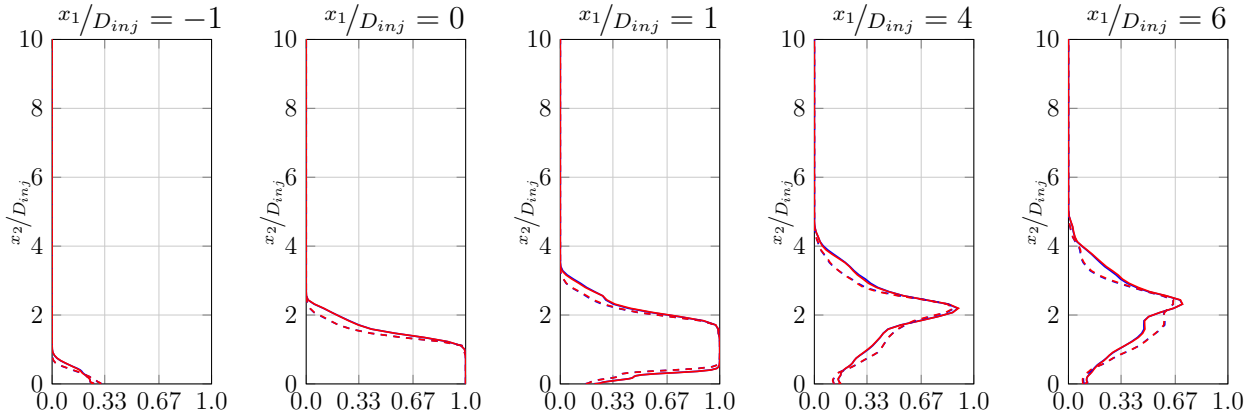

Figure 7.3 – PSR (blue) and U-PaSR (red) H_2 average mass fraction profile

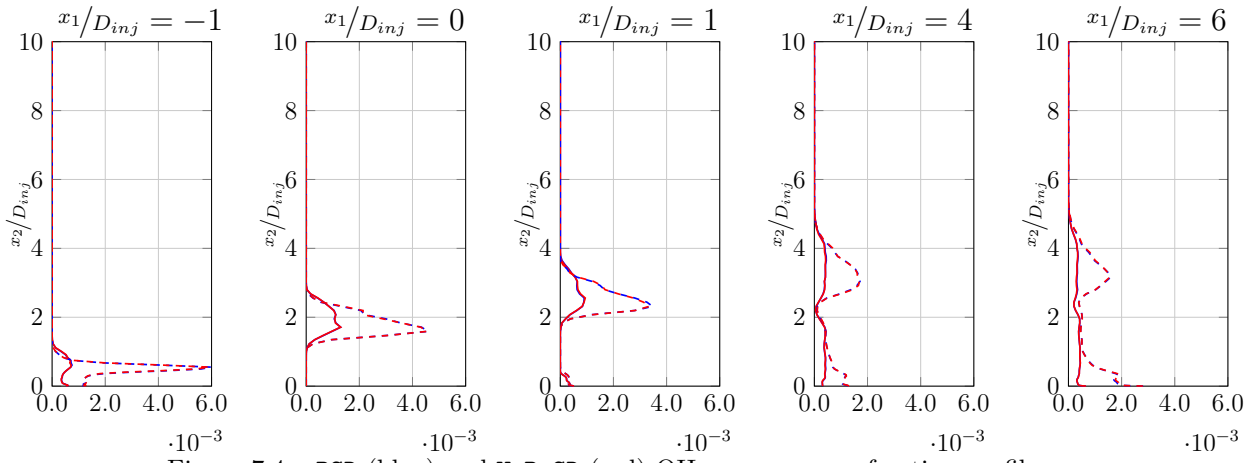

Figure 7.4 – PSR (blue) and U-PaSR (red) OH average mass fraction profile

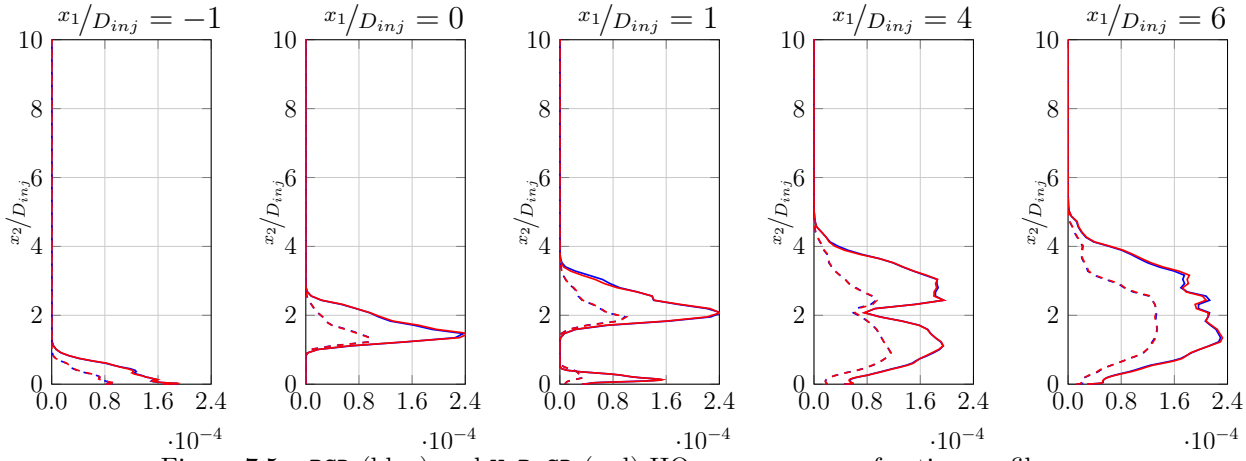

Figure 7.5 – PSR (blue) and U-PaSR (red) HO_2 average mass fraction profile

The resolved mass fraction variance $\widetilde{Y}_v^{res}$ is presented in figure 7.6 for OH (continuous line) and HO_2 (dashed line), considering PSR (blue line) and U-PaSR (red line) models, taken at $x_2/D_{inj} = 1$. The values obtained within the PSR modelling framework are very similar to those issued from the U-PaSR model. They are slightly large because of the micro-mixing effects that the U-PaSR model takes into account. The presence of the wall-mounted cavity causes the OH and HO_2 variances to decrease between $20 < x_1/D_{inj} < 40$ since the recirculation tends to keep the average properties more uniform inside it.

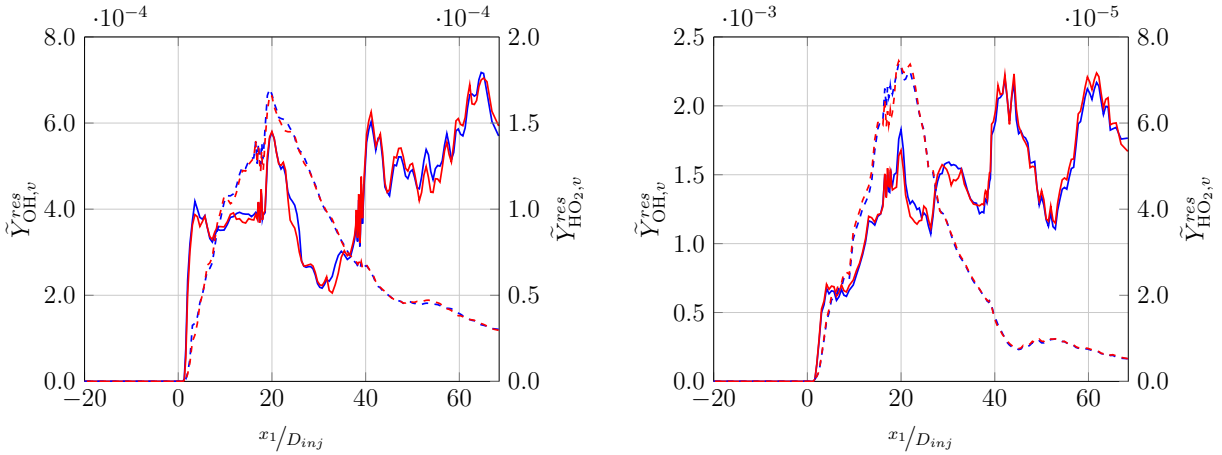

(a) Case RFSC-LST (b) Case RFSC-HST

Figure 7.6 – Resolved mass fraction variance $\widetilde{Y}_v^{res}$ for OH (continuous line) and HO_2 (dashed line), considering PSR (blue line) and U-PaSR (red line) approaches, at $x_2/D_{inj} = 1$

Figures 7.7, 7.8, 7.9, and 7.10 display a comparison between an average heat release, composed of 20 snapshots, considering PSR and U-PaSR approaches for cases RFSC-LST and RFSC-HST at $x_2/D_{inj} = 4$, 1, -3 and averaged along x_2-axis, respectively, focusing in the fuel injection and the cavity, i.e. $-4 \leq x_1/D_{inj} \leq 40$. The PSR approach presents a slightly higher heat release rate, especially when $x_1/D_{inj} > 20$, that is, inside the wall-

mounted cavity. Even if the PSR and U-PaSR averaged mass fractions are similar (cf. figures 7.3, 7.4 and 7.5), the small differences with the heat release rate can be explained by the fact that, for the U-PaSR approach, chemical reactions occur only within the fine-scale structures. On the x_2-axis averaged heat release field (figure 7.10), one can notice a significant increase of the heat release inside the cavity, which may be explained by the presence of the recirculation zone (cf. fig. 6.17).

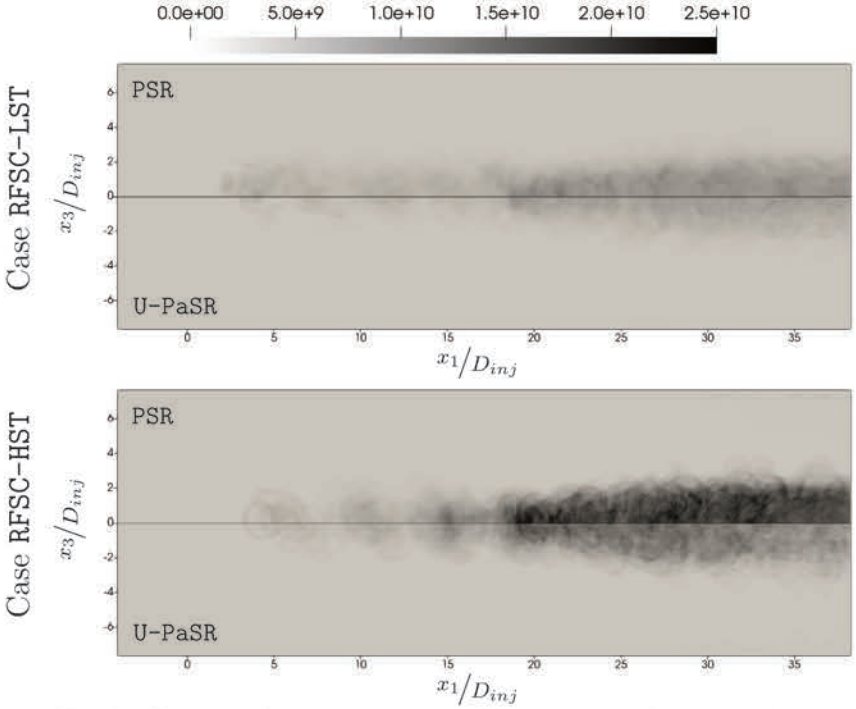

Figure 7.7 – Fields of average heat release rate obtained using the PSR and U-PaSR modelling frameworks. The top part of each image corresponds to PSR results and the bottom part to U-PaSR results ($x_2/D_{inj} = 4$)

Finally, the fine-scale structure volume fraction γ^* is reported in figure 7.11 for both cases at two different planes. It is noteworthy that γ^* is larger than 0.85 in almost the whole reactive zone, which explains the very small differences that are observed in the mass fraction profiles for the PSR and the U-PaSR reactor models. The U-PaSR approach does not affect significantly the combustion process in the present set of highly resolved simulations, which means that the PSR approach (Arrhenius Law) appears as a relevant representation.

7.3.2 Turbulent flow analysis

Figure 7.12 reports the instantaneous fields of some aerodynamic characteristics at $t^* = 950$ in the median plane along the spanwise direction ($x_3/D_{inj} = 0$) for cases RFSC-LST and RFSC-HST, respectively. The Prandtl-Meyer expansion can be clearly identified in

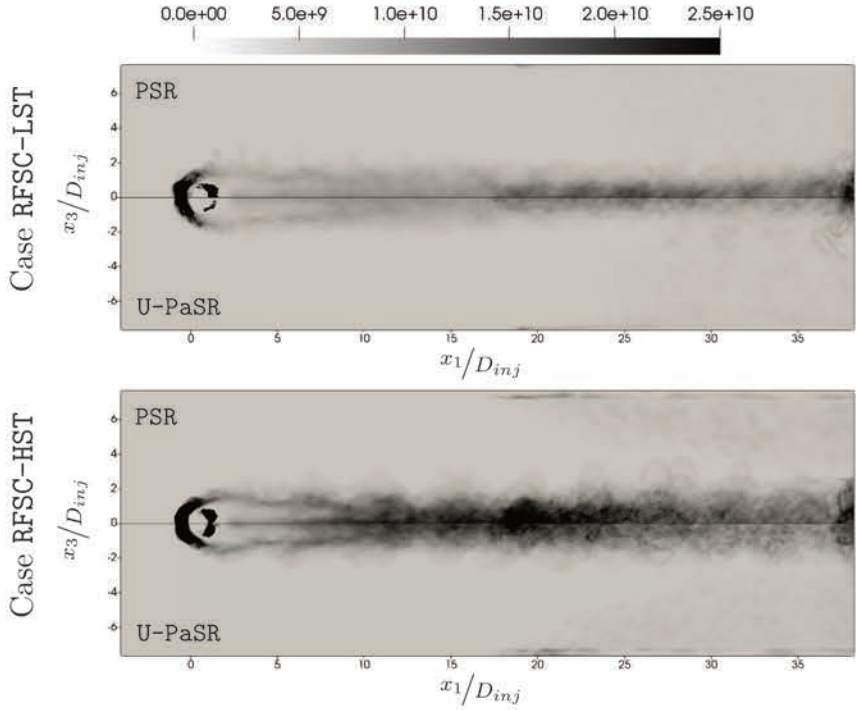

Figure 7.8 – Fields of average heat release rate obtained using the PSR and U-PaSR modelling frameworks. The top part of each image corresponds to PSR results and the bottom part to U-PaSR results ($x_2/D_{inj} = 1$)

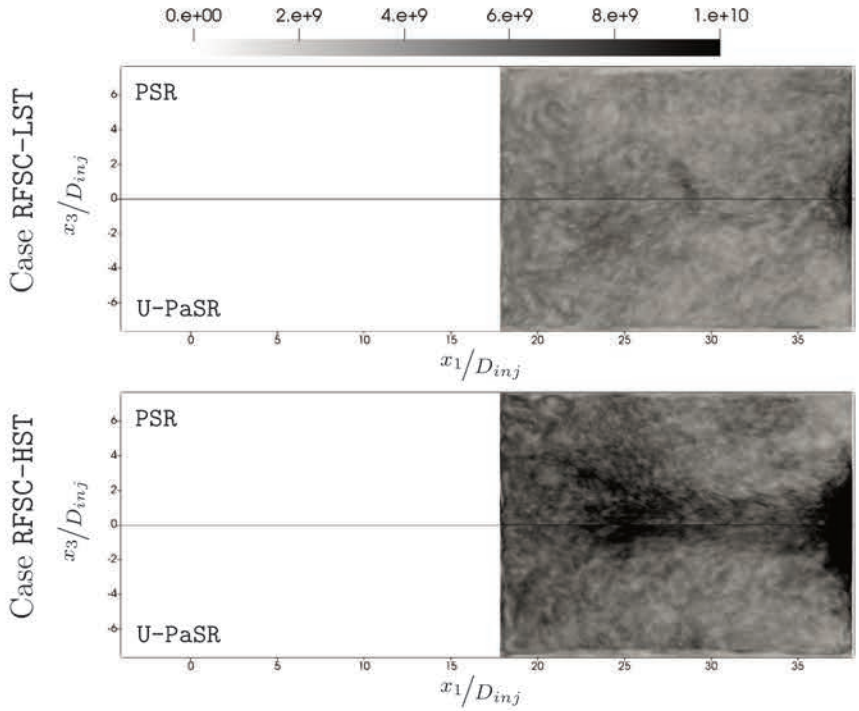

Figure 7.9 – Fields of average heat release rate obtained using the PSR and U-PaSR modelling frameworks. The top part of each image corresponds to PSR results and the bottom part to U-PaSR results ($x_2/D_{inj} = -3$)

figures 7.12a (Mach number) and 7.12b (temperature) where the temperature decreases abruptly and the fuel injection velocity increases. Moreover, from figures 7.12a, 7.12b,

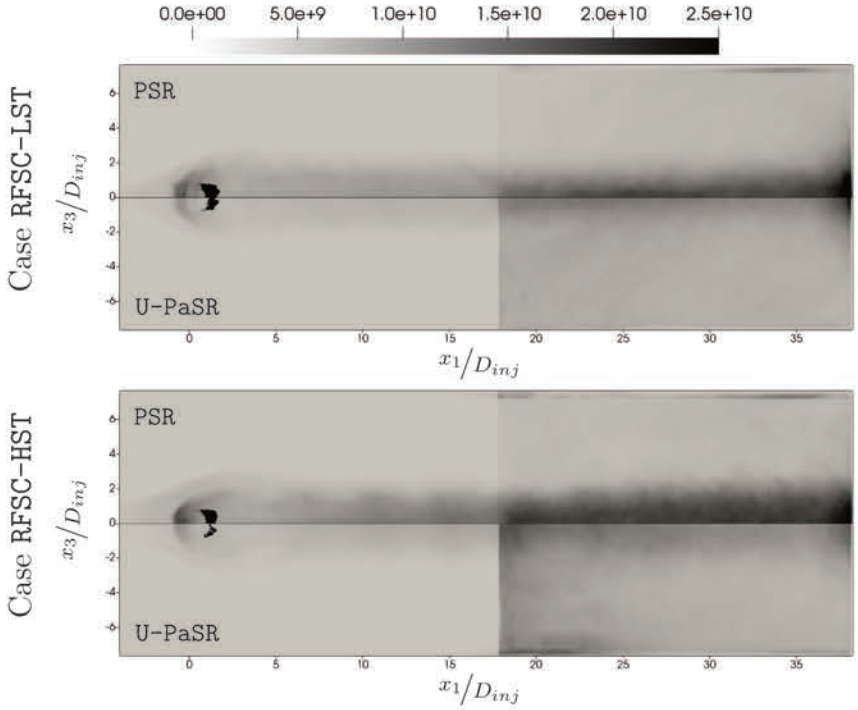

Figure 7.10 – Fields of heat release rate obtained using the PSR and U-PaSR modelling frameworks. The top part of each image corresponds to PSR results and the bottom part to U-PaSR results (averaged along x_2-axis)

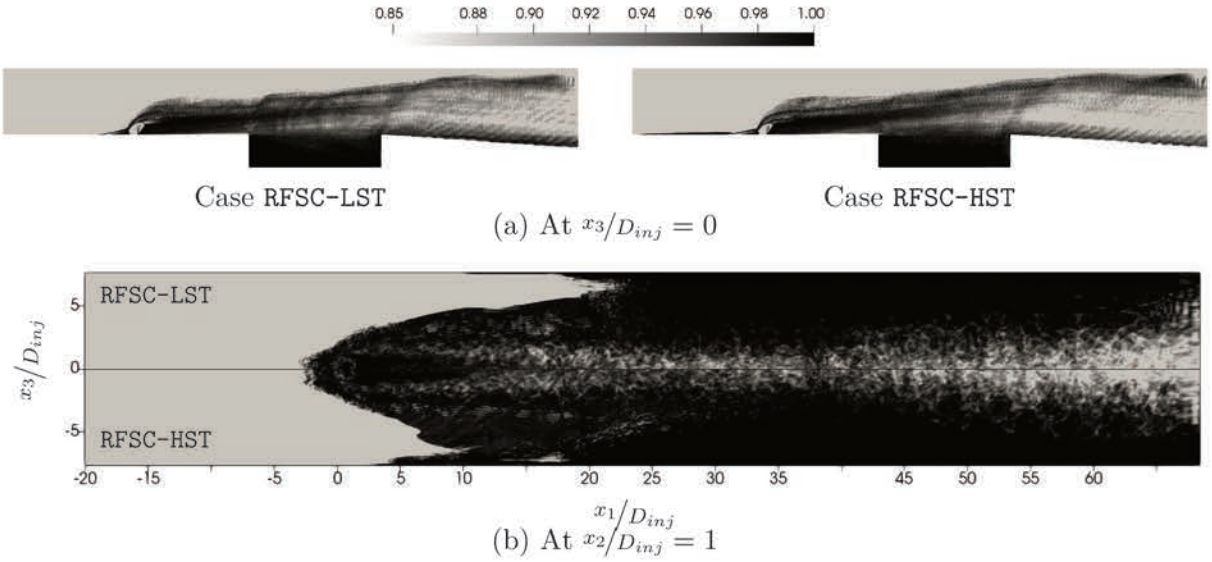

Figure 7.11 – Average fine-scale structure volume fraction γ^* at (a) $x_3/D_{inj} = 0$ and (b) $x_2/D_{inj} = 1$

7.12c and 7.12d, it is possible to verify that the flow recirculates inside the wall-mounted cavity, thus leading to an increase in the temperature in this region.

Vortex structures (fig. 7.12e) develop in the mixing layer above the fuel injection and rotate clockwise, i.e. $\omega_{x_3} > 0$. The velocity components $(\widetilde{u}_1, \widetilde{u}_2)$ (fig. 7.12c and 7.12d) highlight the interactions between the vortexes that develop in the wake of the fuel jet

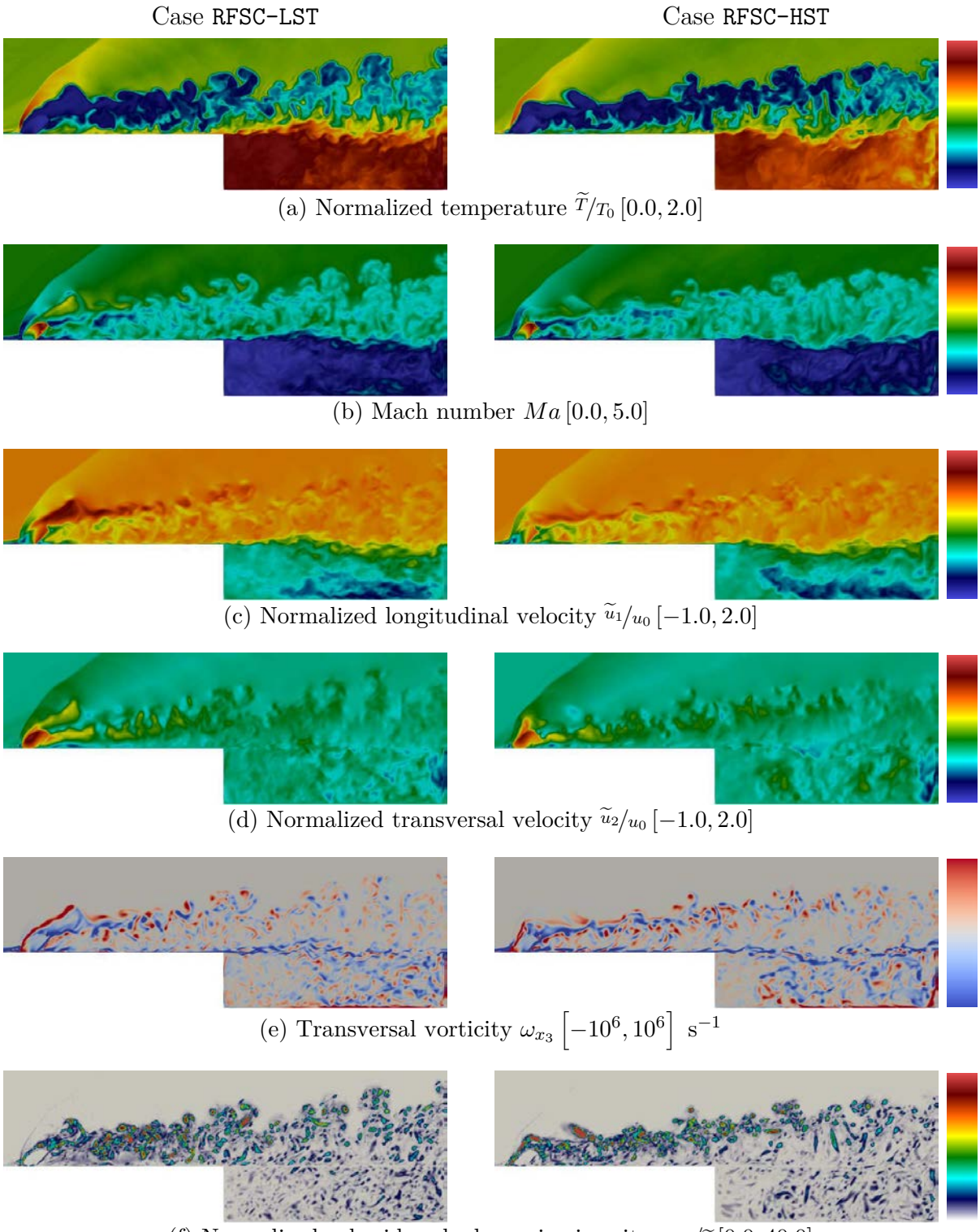

(a) Normalized temperature $\widetilde{T}/T_0\,[0.0, 2.0]$

(b) Mach number $Ma\,[0.0, 5.0]$

(c) Normalized longitudinal velocity $\widetilde{u}_1/u_0\,[-1.0, 2.0]$

(d) Normalized transversal velocity $\widetilde{u}_2/u_0\,[-1.0, 2.0]$

(e) Transversal vorticity $\omega_{x_3}\left[-10^6, 10^6\right]\ \mathrm{s}^{-1}$

(f) Normalized subgrid-scale dynamic viscosity $\mu_{sgs}/\widetilde{\mu}\,[0.0, 40.0]$

Figure 7.12 – Characterization of the instantaneous flowfield at $t^* = 950$ and $x_3/D_{inj} = 0$

injection ($\widetilde{u}_2 > 0$) and in the vicinity of the wall downstream of the barrel shock ($\widetilde{u}_2 < 0$), thus creating a low velocity region.

Finally, the subgrid-scale dynamic viscosity (fig. 7.12f) is very important in the regions where highly energetic turbulent structures are present, especially in the wake of the fuel injection and in the upper mixing layer (along the vitiated flow inlet). In order to minimize the total dissipation, the use of the shock sensor of Ducros et al. [50] (§3.3.2) cancels this viscosity at the shock locations where numerical dissipation is active. Figure 7.13 presents a zoom on the zones where the shock sensor is activated, which allows to satisfactorily detect these regions.

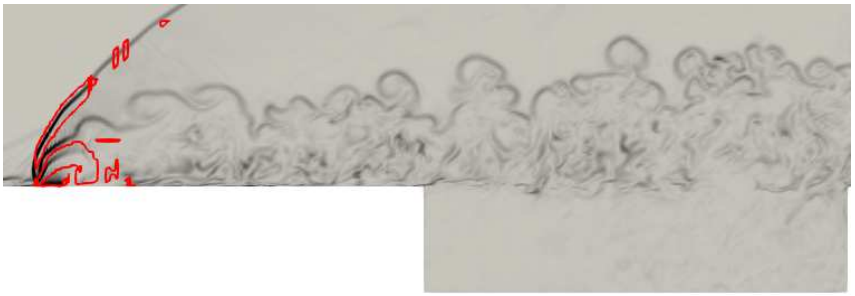

Figure 7.13 – Location of the activation of the shock sensor at $x_3/D_{inj} = 0$ (in red). Back side: numerical Schlieren field $S_{\bar{\rho}}$

Figure 7.14 presents the averaged fields of some aerodynamics characteristics also at $x_3/D_{inj} = 0$. Qualitatively, the fields are similar for both simulations, with only rather minor differences inside the cavity due to the combustion stabilization mode.

Figures 7.15, 7.16 and 7.17 compare the average longitudinal velocity $\widetilde{u}_1/u_0$, transversal velocity $\widetilde{u}_2/u_0$ and turbulent kinetic energy $\sqrt{k}/u_0$ in the median plane along spanwise direction ($x_3/D_{inj} = 0$) for cases `RFSC-LST` (in blue) and `RFSC-HST` (in red) at several locations x_1/D_{inj}. There is a significant increase of the longitudinal component of the velocity in the mixing layer above the fuel injection, reaching up to 1.4 times the vitiated air-stream velocity at $2 \leq x_1/D_{inj} \leq 6$. The field of the transversal component of the velocity reports a region with $\widetilde{u}_2 = 0$ between the vortexes in the wake of the fuel jet injection ($\widetilde{u}_2 > 0$) and at the wall downstream the barrel shock ($\widetilde{u}_2 < 0$), which favors the stabilization of the flow and the increase of a particle residence time. Moreover, the turbulent kinetic energy level is larger in the wake of the jet, its intensity decays in the vicinity of the mixing layer above the jet injection and significantly weakens as x_1/D_{inj} increases.

7.3.3 Turbulent combustion development

Two distinct combustion stabilization modes can be inferred from the analysis of the reactive flow field. Under moderate values of the air-stream temperature (case `RFSC-LST`) the cavity-stabilized mode is dominant, while for larger inlet temperatures

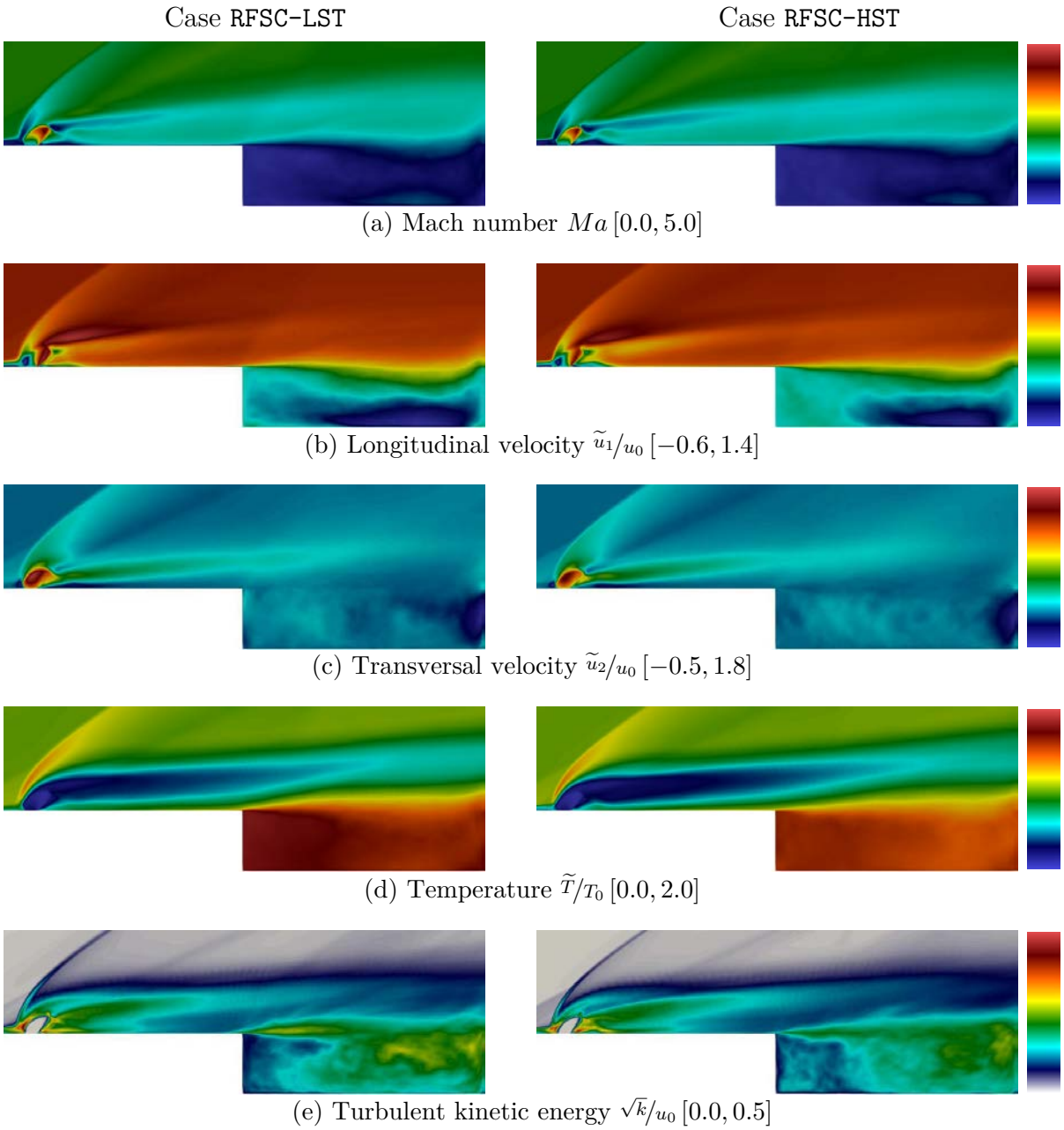

(a) Mach number $Ma\,[0.0, 5.0]$

(b) Longitudinal velocity $\widetilde{u}_1/u_0\,[-0.6, 1.4]$

(c) Transversal velocity $\widetilde{u}_2/u_0\,[-0.5, 1.8]$

(d) Temperature $\widetilde{T}/T_0\,[0.0, 2.0]$

(e) Turbulent kinetic energy $\sqrt{k}/u_0\,[0.0, 0.5]$

Figure 7.14 – Characterization of the mean flowfield at $x_3/D_{inj} = 0$

(case RFSC-HST), non-negligible water vapor dissociation and heat release occur in the vicinity of the fuel injection. Figure 7.18 presents an instantaneous snapshot at $t^* = 950$ of the iso-surface $\widetilde{\xi} = 0.5$ of the filtered fuel inlet tracer $\widetilde{\xi}$ (in light grey) as well as an iso-value of the OH filtered mass fraction $\widetilde{Y}_{\mathrm{OH}}$ colored by the normalized filtered temperature $\widetilde{T}/T_0$, for both simulated cases.

The temporal evolution of OH mass fraction and H_2O production rate at $x_3/D_{inj} = 0$ for cases RFSC-LST and RFSC-HST are presented in figures 7.19 and 7.20. The computational procedure retained to proceed with the ignition of the mixture, herein defined as the

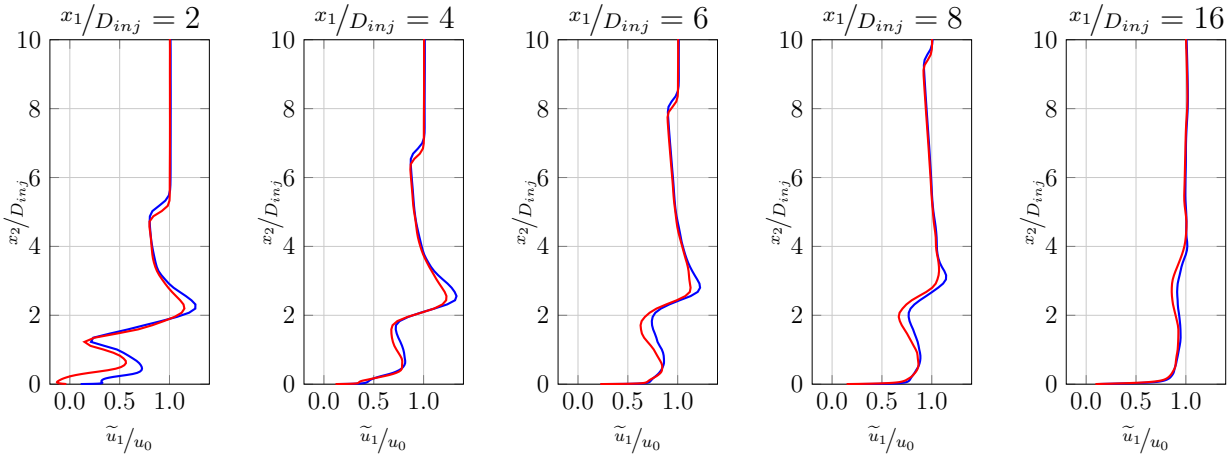

Figure 7.15 – Longitudinal velocity component profiles obtained at several locations x_1/D_{inj} for case `RFSC-LST` (blue) and `RFSC-HST` (red)

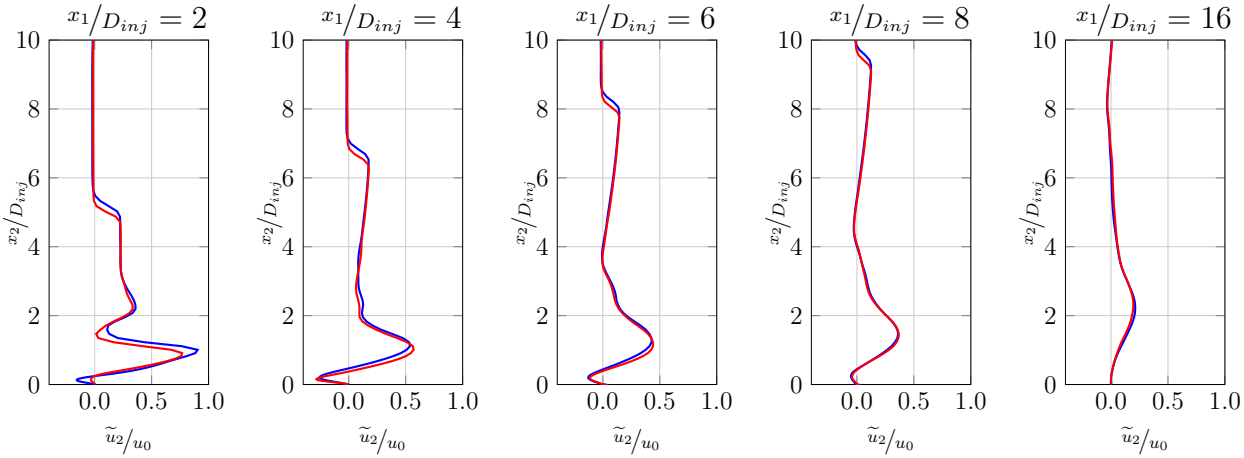

Figure 7.16 – Transversal velocity component profiles obtained at several locations x_1/D_{inj} for case `RFSC-LST` (blue) and `RFSC-HST` (red)

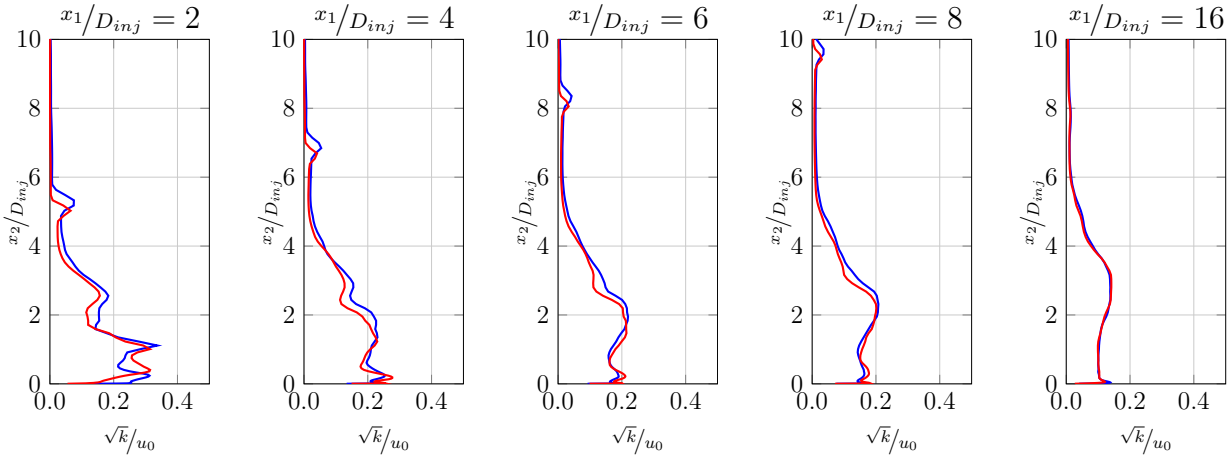

Figure 7.17 – Turbulent kinetic energy profiles obtained at several locations x_1/D_{inj} for case `RFSC-LST` (blue) and `RFSC-HST` (red)

condition where combustion first appear in the main flow, is similar to the one considered in the experiments. Although ignition may not start at the same physical time from the

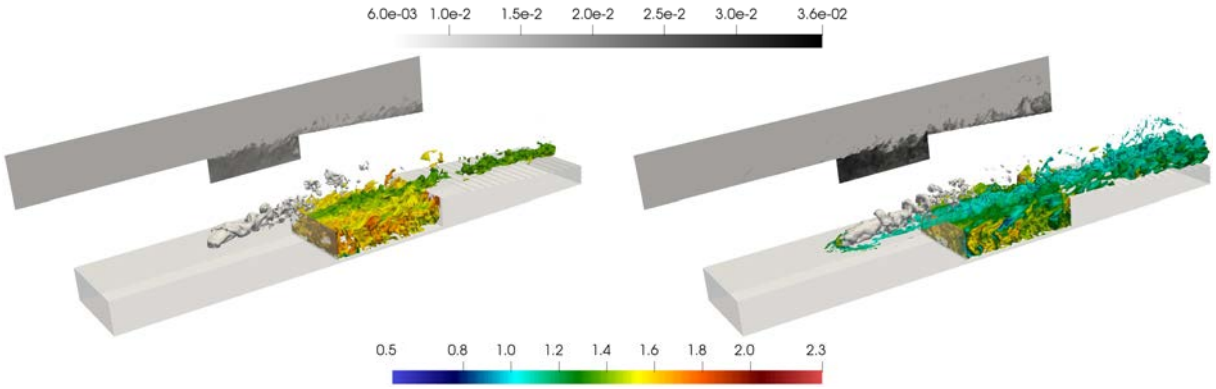

(a) Case `RFSC-LST` (b) Case `RFSC-HST`

Figure 7.18 – Isovalue surface of the filtered OH mass fraction colored by the normalized filtered temperature and fuel inlet tracer iso-surface $\widetilde{\xi} = 0.5$. Back side: OH mass fraction

experiments due to what is considered to be the initial time t_0, the temporal behavior and development of the combustion from ignition are similar to the one observed in the experiments performed by Micka and Driscoll [115]. Chemical reactions start at the bottom end of the cavity for case `RFSC-LST`: it first develops within the cavity, increasing the temperature and inducing a deflection of the shear layer due to the thermal expansion of the heat release. The conditions then become more favorable to the spreading of chemical reaction as the combustion process develops, thus increasing the temperature and allowing the reaction zone to extend over the whole cavity, up to a point where the heat release rate becomes sufficiently large to stabilize the combustion process. Depending on the operating conditions the combustion can spread upstream of the cavity, as it can be seen in case `RFSC-HST`.

It is noteworthy that, as expected (cf. §7.2), the vitiated air-stream temperature (T_0) significantly alters the combustion stabilization mode. Moreover, the combustion spreads significantly faster with a larger temperature and significant H_2O production takes place along the upper part of the cavity for case `RFSC-LST` (cavity stabilized mode), whereas for case `RFSC-HST` (jet-wake stabilized mode) it spreads downstream the fuel injection and within the cavity, as shown by figure 7.20.

The cavity-stabilized combustion mode is characterized by a reaction zone anchored at the leading edge of the cavity, spreading into the main flow at an approximately constant angle. In the jet-wake stabilized mode the reaction zone is stabilized upstream of the cavity and the leading edge is curved. Figure 7.21 compares the averaged heat release rate for cases `RFSC-LST` and `RFSC-HST` with the flame luminosity obtained experimentally and they appear to be similar to those obtained by Micka [116].

Figures 7.22 and 7.23 present the average mixture fraction field and profile in the median plane along the spanwise direction ($x_3/D_{inj} = 0$) for cases `RFSC-LST` and `RFSC-HST`.

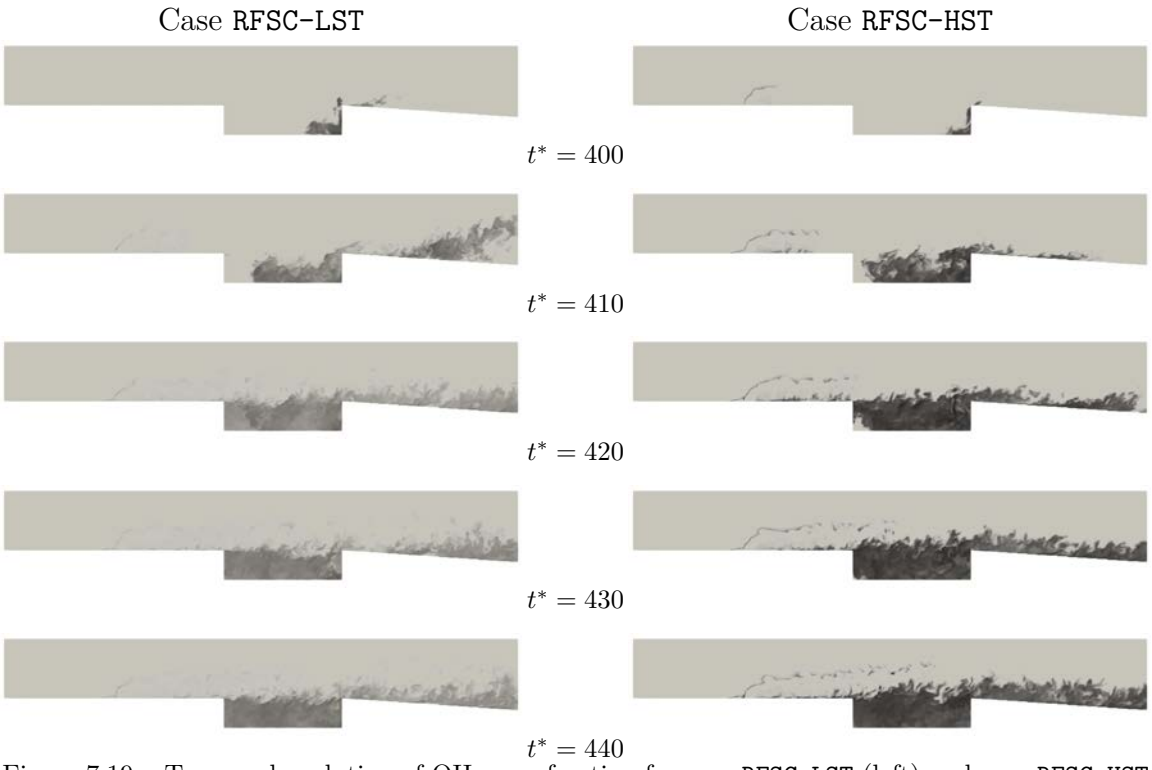

Figure 7.19 – Temporal evolution of OH mass fraction for case RFSC-LST (left) and case RFSC-HST (right), at $x_3/D_{inj} = 0$

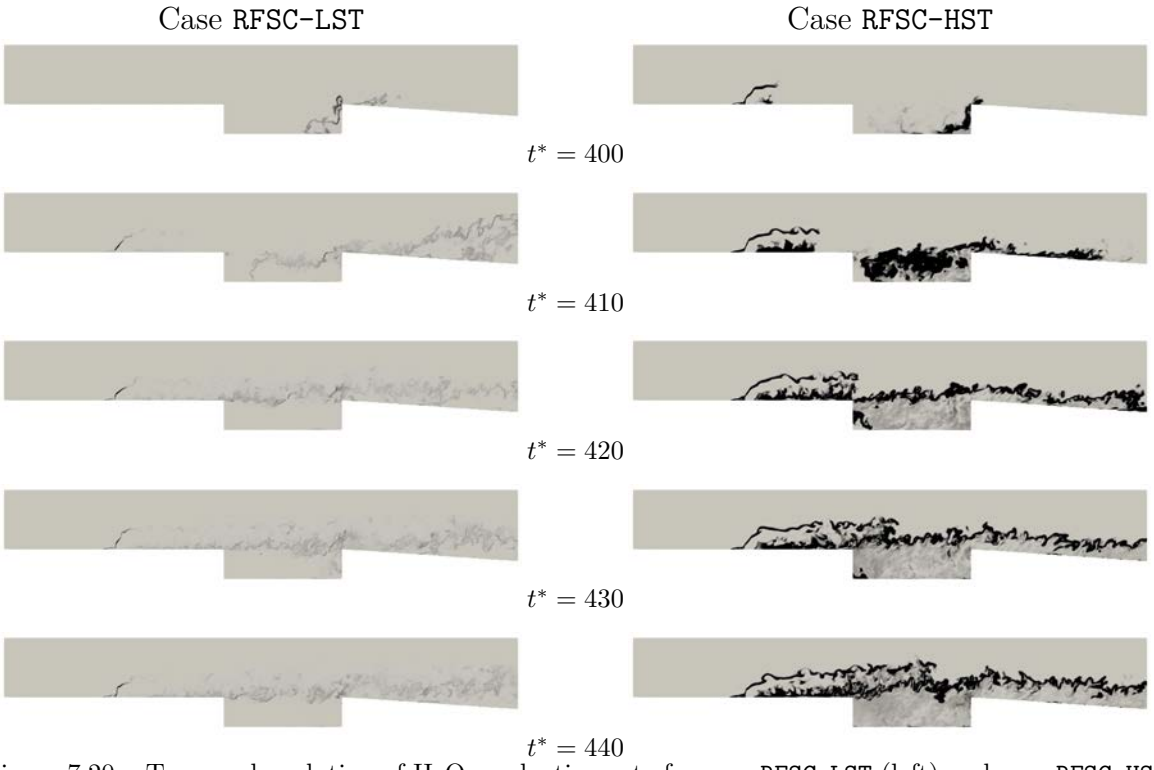

Figure 7.20 – Temporal evolution of H_2O production rate for case RFSC-LST (left) and case RFSC-HST (right), at $x_3/D_{inj} = 0$

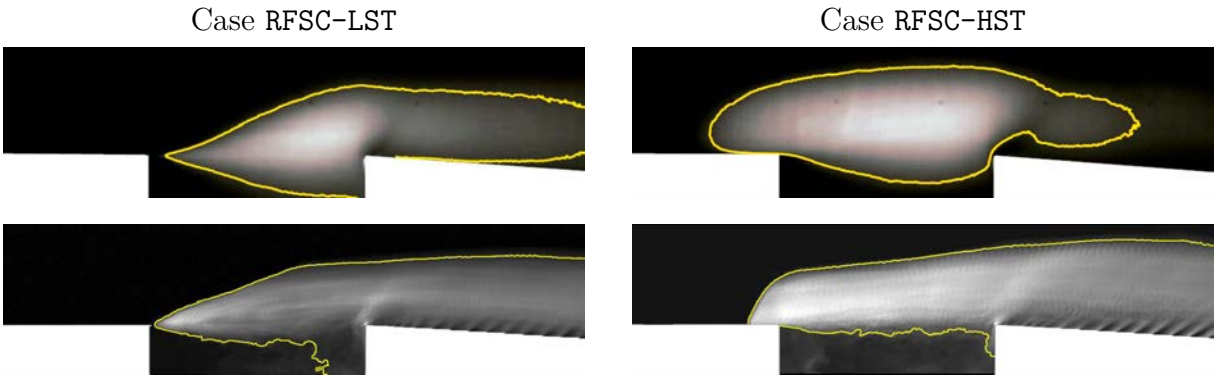

Figure 7.21 – Comparison with experimental data: flame luminosity adapted from Micka [116] (top) and average heat release rate (bottom)

As the normalized coordinate x_1/D_{inj} increases the mixture fraction decreases with the fuel being spread along the flow.

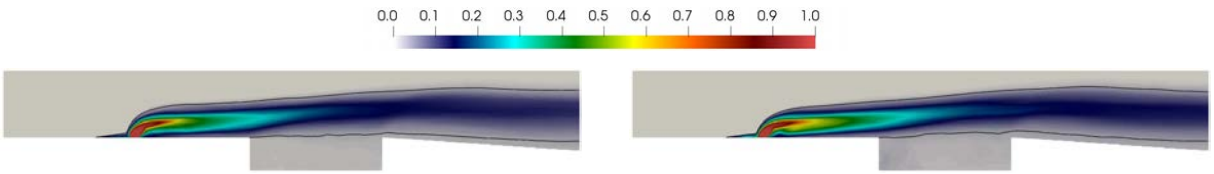

(a) Case RFSC-LST (b) Case RFSC-HST

Figure 7.22 – Average mixture fraction field $\widetilde{\xi}$ at $x_3/D_{inj} = 0$ with iso-line at stoichiometry

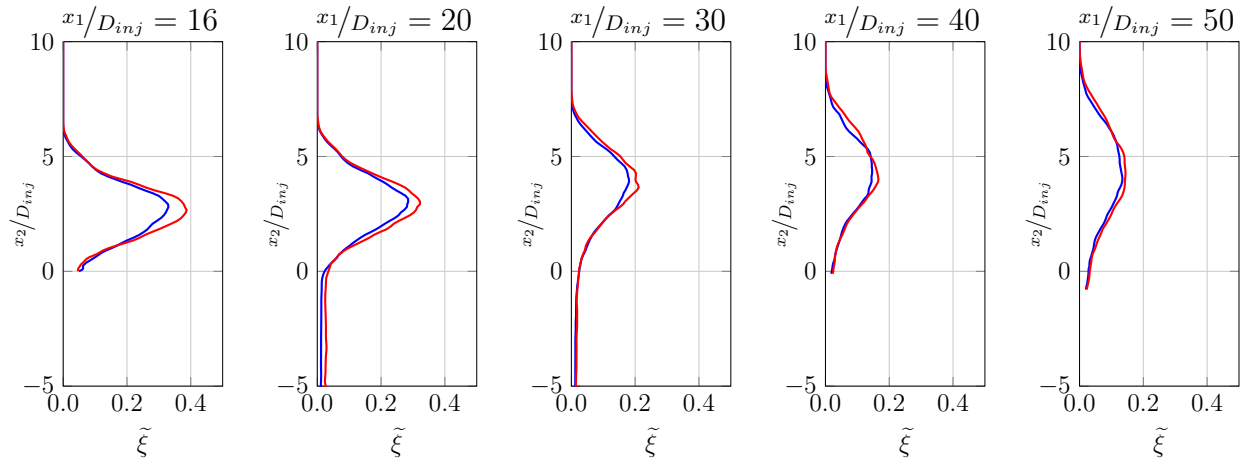

Figure 7.23 – Average mixture fraction profiles $\widetilde{\xi}$ at several x_1/D_{inj} locations for case RFSC-LST (blue) and RFSC-HST (red)

Figure 7.24 displays the PDF and the CDF (eq. 6.12) of the filtered mixture fraction $\widetilde{\xi}$, integrated over the whole computational domain. There is a probability of more than 65% and 77% that $\widetilde{\xi} \geq \widetilde{\xi}_{st}$ for cases RFSC-LST and RFSC-HST, respectively, with $\widetilde{\xi}_{st} = 0.030$.

Fuel/oxidizer mixtures are considered flammable if a flame may propagate into the corresponding mixture, which happens only under certain composition limits. The flamma-

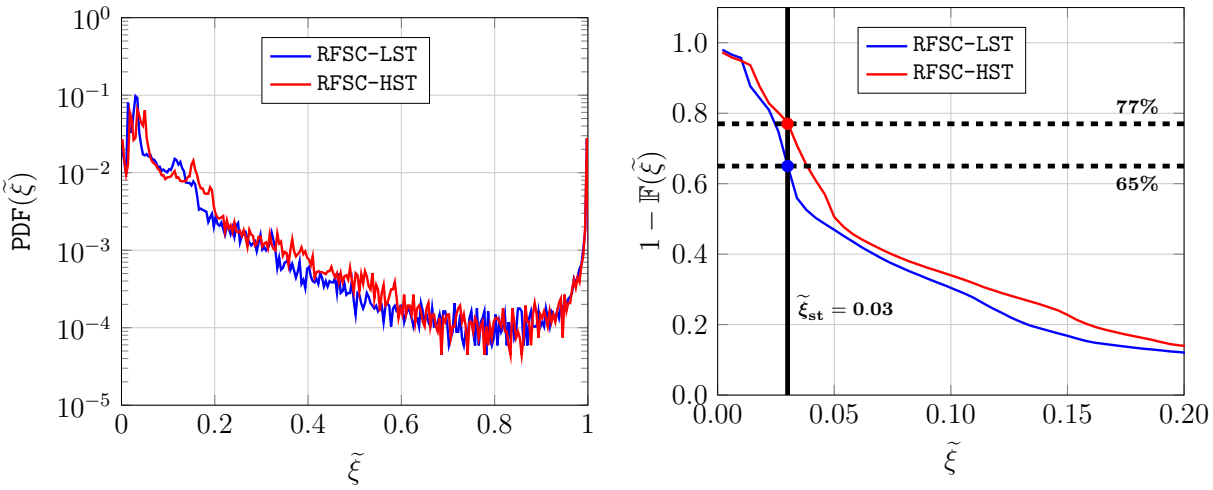

(a) PDF of the mixture fraction

(b) CDF of the mixture fraction

Figure 7.24 – PDF and CDF of the mixture fraction

bility limit of a mixture determines the lower and upper fuel concentration so that combustion can occur. It is obtained from experiments by varying the mixture composition and it may be altered by temperature, pressure, flame propagation direction under a gravitational field [190]. The lowest fuel concentration that is likely to lead to ignition in the presence of an energy source is called lower flammability limit (LFL). On the other hand, the highest concentration capable of ignite is called upper flammability limit (UFL). Both LFL and UFL are normally expressed in terms of volume percentage at 298 K and 1.0 atm. As an example, the LFL of a H_2-air mixture is 4% and the UFL is 75% [190], which corresponds to $\xi_{ign}^{-} = 0.003$ and $\xi_{ign}^{+} = 0.167$, respectively.

The probability that a flow ignites is based on the PDF of the fuel mass fraction, being defined as

$$P_{ign} = \int_{\xi_{ign}^{-}}^{\xi_{ign}^{+}} \mathrm{PDF}\left(\xi\right) \, \mathrm{d}\xi \tag{7.2}$$

where ξ_{ign}^{-} and ξ_{ign}^{+} are the minimum and maximum mixture fraction values where the mixture can burn. The field of P_{ign}, taken at $x_3/D_{inj} = 0$, is reported in figure 7.25, for cases RFSC-LST and RFSC-HST, zooming the fuel injection and the cavity, and considering the standard values of the flammability limits at 298 K. One can verify that, even at these temperature levels which remain rather far from the operating temperature of this device, the ignition probability field follows quite closely the cavity stabilization modes. It is however expected that more relevant results could be obtained by considering the flammability limits at the operating temperature levels of both fuel and oxidizer streams.

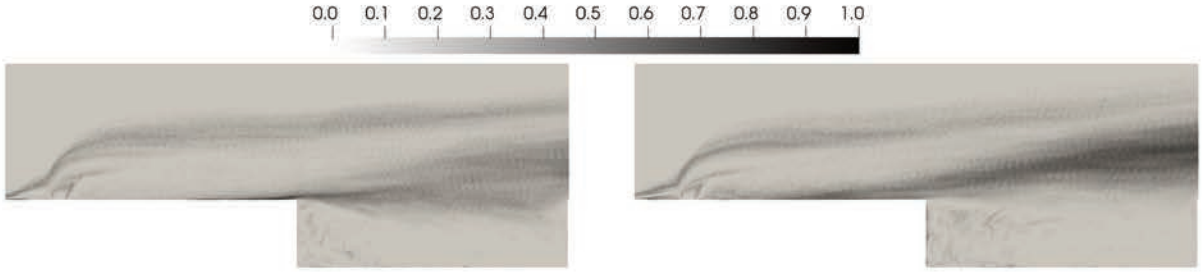

(a) Case RFSC-LST (b) Case RFSC-HST

Figure 7.25 – Ignition probability at $x_3/D_{inj} = 0$

Figure 7.26 presents the instantaneous H_2 mass fraction field between ξ_{ign}^- and ξ_{ign}^+, at $t^* = 900$ for cases RFSC-LST and RFSC-HST, taken at $x_2/D_{inj} = 1$ (top) and $x_3/D_{inj} = 0$ (bottom). The fuel-air mixture level is between the flammability limits in the mixing layer of the fuel jet and inside the cavity. Moreover, the cavity favors combustion to occur since the mixture temperature is higher inside it, as it can be verified in figure 7.26b.

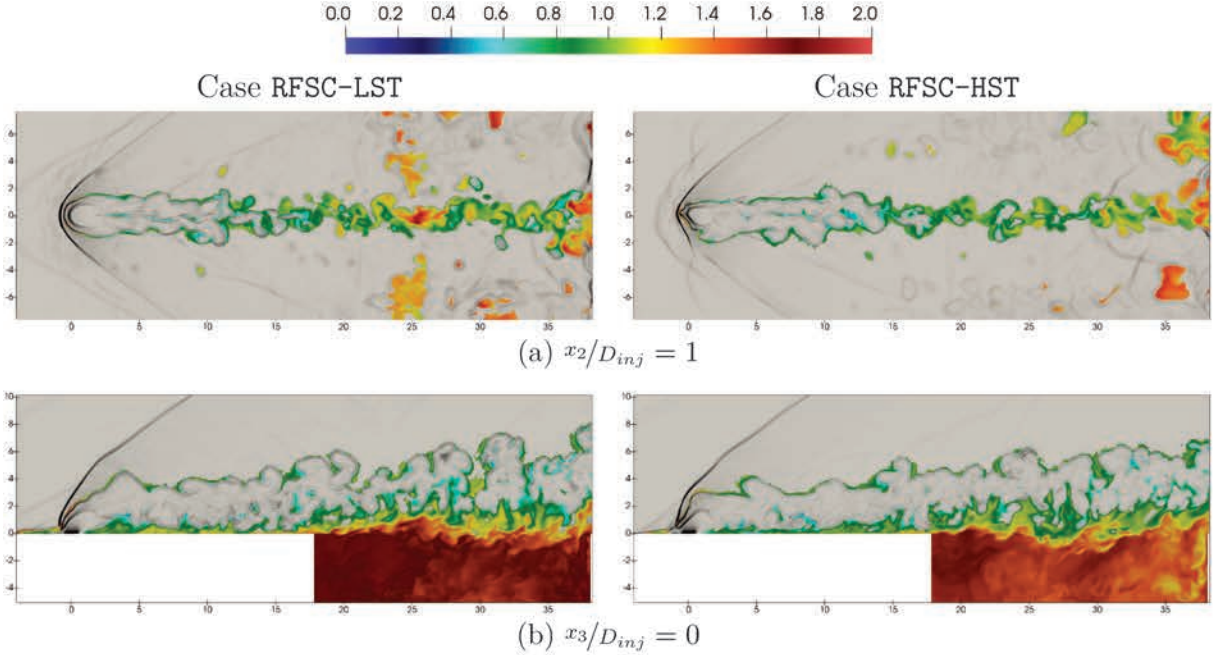

(a) $x_2/D_{inj} = 1$

(b) $x_3/D_{inj} = 0$

Figure 7.26 – Instantaneous H_2 mass fraction between ξ_{ign}^- and ξ_{ign}^+ colored by normalized temperature T/T_0 over a numerical Schlieren field, at $t^* = 900$

The temperature is a critical parameter to study self-ignition processes and the flame propagation phenomena. As emphasized by Gamba and Mungal [70], the reactive zone can be stabilized upstream or downstream of the fuel injection, in the mixing layer and near the walls. Figure 7.27 presents a scatterplot of the unburnt mixture temperature $\widetilde{T}$ as function of the mixture fraction $\widetilde{\xi}$ as well as a linear approximation (dashed line) and a polynomial approximation (continuous line). The linear approximation can be expressed

thanks to the following equation:

$$T^u_{mix}(\xi) = \xi T^{fuel}_F + (1-\xi)\, T^{ox}_O \tag{7.3}$$

with T^{fuel}_F being the fuel injection temperature and T^{ox}_O the vitiated air-stream temperature, whose values are provided in table 6.1.

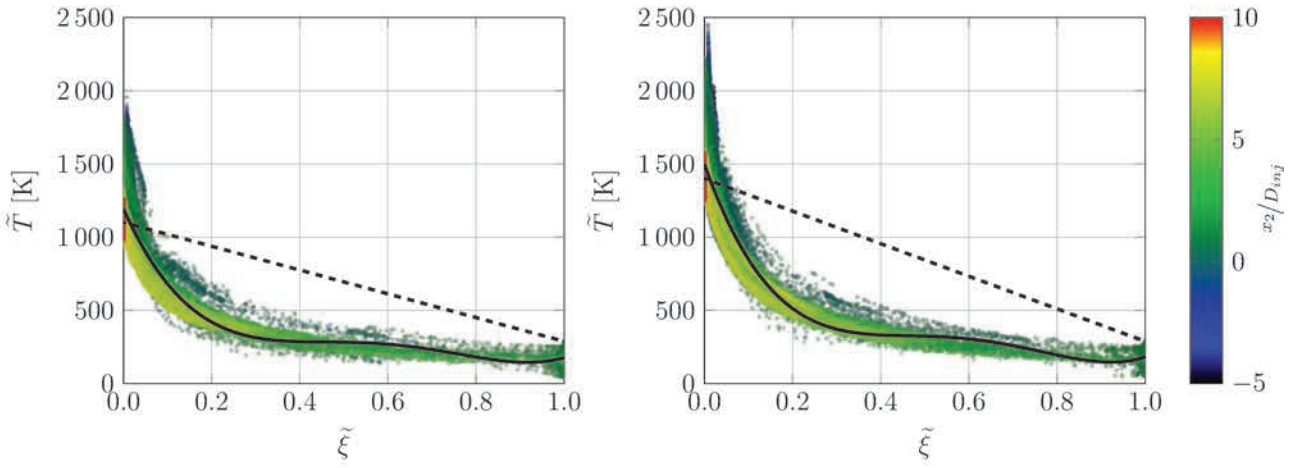

(a) Case `RFSC-LST` (b) Case `RFSC-HST`

Figure 7.27 – Scatterplot of the temperature at $t^* = 620$

It is worth recalling that in supersonic flow regimes, compressibility effects may play an important role, so the linear interpolation may not be adequate because of the presence of shocks and expansion waves. In the present simulation, the fuel jet ($\widetilde{\xi} = 1$) strongly expands, causing a significant temperature decrease. The temperature then increases with the Mach disk compression, whereas the oxidizer flow ($\widetilde{\xi} = 0$) is compressed by the curved shock and heated by the viscous friction at the wall before the cavity ($x_2/D_{inj} = 0$). Furthermore, since temperature is not an extensive quantity, the correct procedure would consist in considering the total enthalpy as a function of the mixture fraction. In this respect, a linear relationship may hold if the Lewis and Prandtl numbers are unity and the effects induced by temporal variations of pressure remains negligible, as emphasized by Izard [90], based on the previous works of Bray et al. [29] and Luo and Bray [107]:

$$h^u_t(\xi) = \xi h^{fuel}_t + (1-\xi)\, h^{ox}_t \tag{7.4}$$

The computation of T^u_{mix} from $h^u_t(\xi)$, however, raises another issue since $h_t(\xi) = h(\xi) + {}^{(u_i u_i)}/_2$ and the kinetic energy has no special relation with the mixture fraction. This specific issue has been discussed in details by Sabelnikov et al. [155]. Finally, the heat capacity of the fuel ($c^{fuel}_p \approx 14380$ $^{J}/_{kg\cdot K}$) and the oxidizer ($c^{ox}_p \approx 1100$ $^{J}/_{kg\cdot K}$ and $c^{ox}_p \approx 2570$ $^{J}/_{kg\cdot K}$, for cases `RFSC-LST` and `RFSC-HST`, respectively) are very different

and strongly non-linear functions of the temperature, which also explains the difference between the linear approximation and the simulation results.

Therefore, to represent this evolution, a 4^{th}-order polynomial approximation is considered to deduce the temperature from the mixture fraction:

$$T^u_{mix}(\xi) = a_{T_0} + a_{T_1}\xi + a_{T_2}\xi^2 + a_{T_3}\xi^3 + a_{T_4}\xi^4 \tag{7.5}$$

	a_{T_0}	a_{T_1}	a_{T_2}	a_{T_3}	a_{T_4}
Case `RFSC-LST`	1193.84	−6768.13	18435.84	−21496.39	8811.36
Case `RFSC-HST`	1498.32	−8551.71	22985.47	−26570.76	10819.60

Table 7.1 – Polynomial approximation coefficients

Since chemical reactions takes place far downstream the fuel injection, it is interesting to determine the premixed and non-premixed (i.e. diffusive) combustion mode contributions. A premixedness index $\check{\zeta}_p$ is considered for this purpose, it is defined as follows:

$$\check{\zeta}_p = \frac{1}{2}\left(1 + \mathbf{n}_F \cdot \mathbf{n}_O\right) \tag{7.6}$$

with $\mathbf{n}_F$ and $\mathbf{n}_O$ being normal unit vectors associated to the molecular diffusion flux of the fuel and oxidizer, respectively, evaluated as

$$\mathbf{n}_F = \frac{\widetilde{\mathbf{V}}_F}{\left\|\widetilde{\mathbf{V}}_F\right\|} \quad \text{and} \quad \mathbf{n}_O = \frac{\widetilde{\mathbf{V}}_O}{\left\|\widetilde{\mathbf{V}}_O\right\|}$$

This index is expected to approach zero for diffusive combustion and unity for premixed ones and it is largely used in preliminary inspections of partially-premixed combustion characteristics despite some special situations where its representativity can be questioned [113].

Figure 7.28 presents the `PDF` of this index at several times for cases `RFSC-LST` and `RFSC-HST`, for a volume restricted to $0.01 \leq \widetilde{\xi} \leq 0.99$ and heat release larger than 10^9 $W/_{\text{kg}}$, and confirms that the diffusive and premixed mode contributions are both significant, with a premixed flame structure developed in the vicinity of the cavity leading edge supporting the diffusive contribution, as it can be seen in figure 7.29. The recirculation zone around the fuel injection ($(-4, 0) \leq (x_1/D_{inj}, x_2/D_{inj}) \leq (8, 4)$) favors the increase of the premixedness level, as shown in 7.29b.

Since both combustion modes are significant, it is of utmost importance to identify the flame self-ignition conditions and its propagation. In order to identify these phenomena some calculations were performed with `CANTERA` software, considering the mixture at

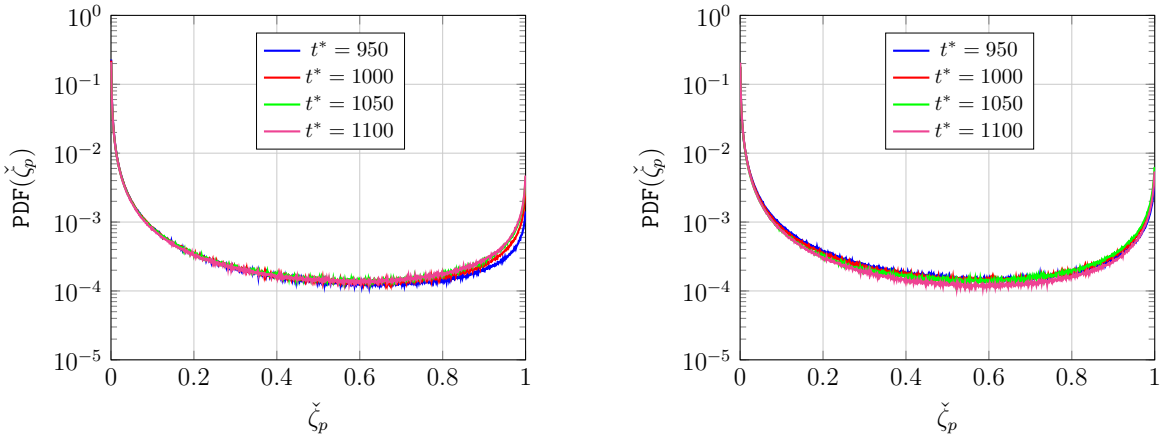

(a) Case `RFSC-LST` (b) Case `RFSC-HST`

Figure 7.28 – `PDF` of the premixedness index $\check{\zeta}_p$

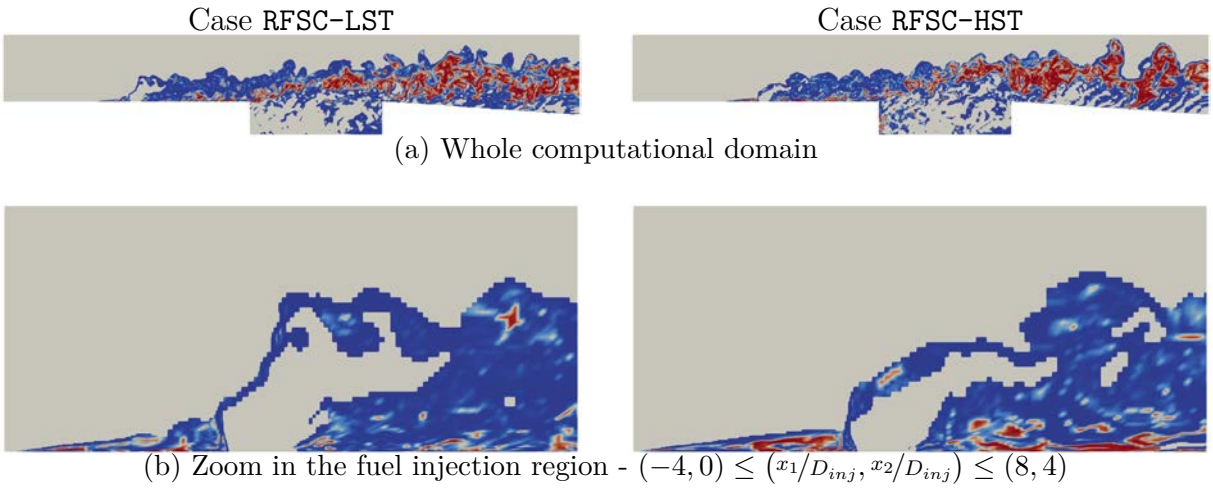

(a) Whole computational domain

(b) Zoom in the fuel injection region - $(-4, 0) \leq (x_1/D_{inj}, x_2/D_{inj}) \leq (8, 4)$

Figure 7.29 – Premixedness index distribution at $x_3/D_{inj} = 0$

constant pressure ($p_\infty = 55.4$ kPa, cf. §6.1.2) and with its temperature set as function of ξ, calculated from equation 7.5.

Figure 7.30 presents the self-ignition time evolution as function of the mixture fraction $\xi \in [0, 1]$ and equivalence ratio $\Phi \in [0, +\infty]$ for cases `RFSC-LST` and `RFSC-HST`, as well as the mixture temperature calculated from the polynomial approximation (eq. 7.5).

It is noteworthy that the ignition time does not change linearly with the mixture fraction ξ[1], being higher for lean mixtures ($\xi \to 0$), decreasing to a local minimum (most reactive state ξ_{mr} or Φ_{mr}) and then increasing again at rich mixtures ($\xi \to 1$ or $\Phi \to +\infty$). The most reactive state ξ_{mr}, i.e., the point where the self-ignition time is the smallest, differs from the stoichiometric point $\xi_{st} = 0.030$ ($\Phi = 1$), being $\xi_{mr} \approx 0.0120$ ($\Phi_{mr} \approx 0.39$) for case `RFSC-LST` and $\xi_{mr} \approx 0.0155$ ($\Phi_{mr} \approx 0.51$) for case `RFSC-HST`. This difference can

[1] As well as with the equivalence ratio $\Phi = \frac{\xi(1-\xi_{st})}{\xi_{st}(1-\xi)}$

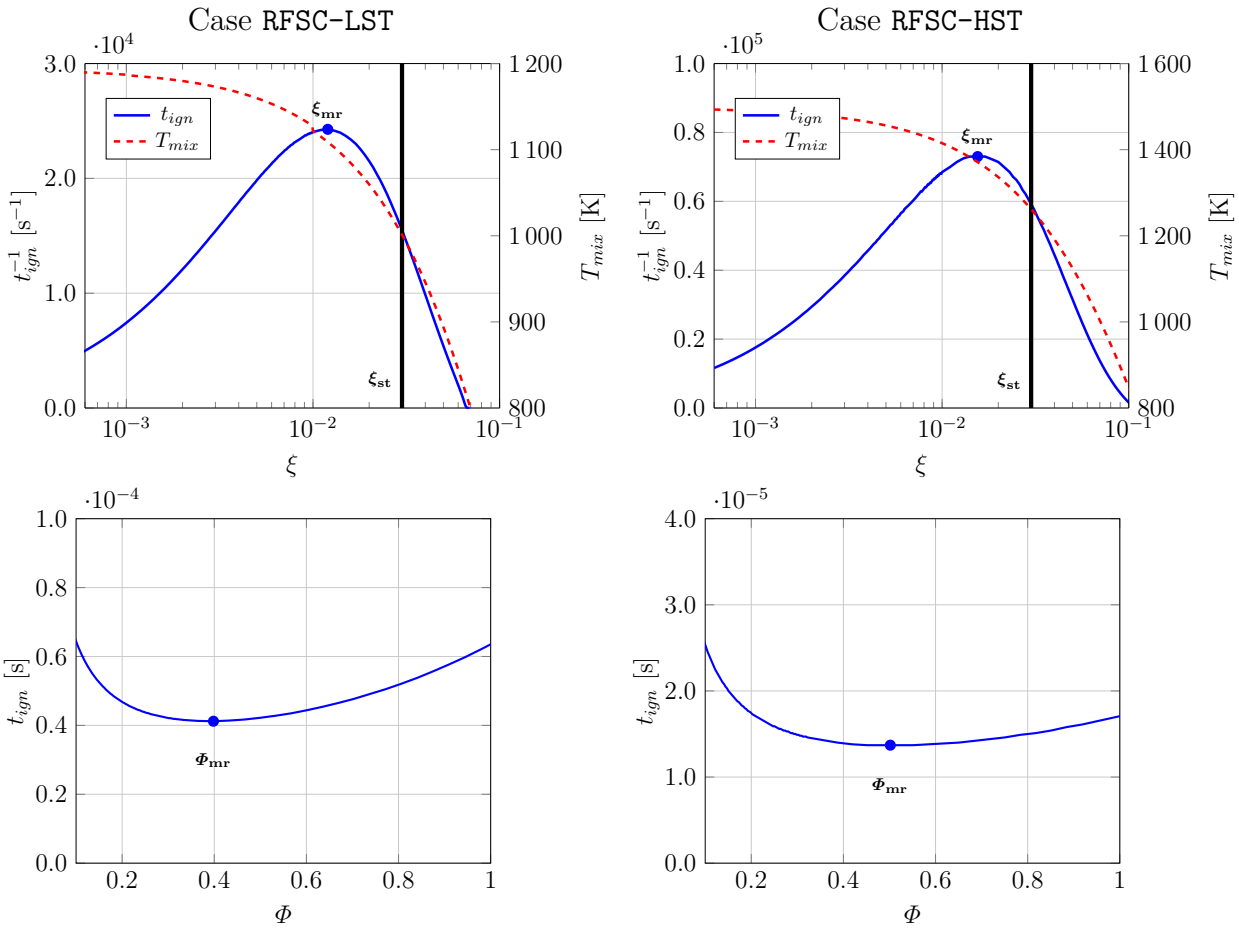

Figure 7.30 – Self-ignition time t_{ign} as function of the mixture fraction ξ (top) and equivalence ratio Φ (bottom)

be explained by temperature difference between the fuel and the oxydizer. When $\xi > \xi_{st}$ ($\Phi > 1$) the self-ignition time tends to infinity, meaning that it does not happen at rich mixtures, favoring the flame propagation regime. On the other side, when $\xi < \xi_{st}$ ($\Phi < 1$), only the auto-ignition regime is found since this condition is not suitable for propagation regime.

Figure 7.31 presents the evolution of the laminar flame velocity S_L^0 and its thickness δ_L^0 as function of the mixture fraction ξ, calculated with the detailed chemical mechanism of O'Conaire et al. [136], and it complements figure 7.30 in the mixture fraction domain $\xi \in [0, 1]$. When $\xi > 0.30$ (case `RFSC-LST`) or $\xi > 0.32$ (case `RFSC-HST`), the flame velocity S_L^0 tends to zero: the flammability limit is reached. The flame velocity is maximum at ξ_{st}, where the self-ignition mechanism is dominant, and decreases as ξ increases. Moreover, as S_L^0 decreases, the flame thickness δ_L^0 increases, up to the flammability limit.

The flame propagation timescale, defined as $\tau = {}^{\delta_L^0}/_{S_L^0}$, is shown in figure 7.32 as function of ξ and Φ where one can verify that $\tau \to 0$ when $\xi \to 0$ ($\Phi \to 0$) and $\tau \to +\infty$ when $\xi \to 1$ ($\Phi \to +\infty$).

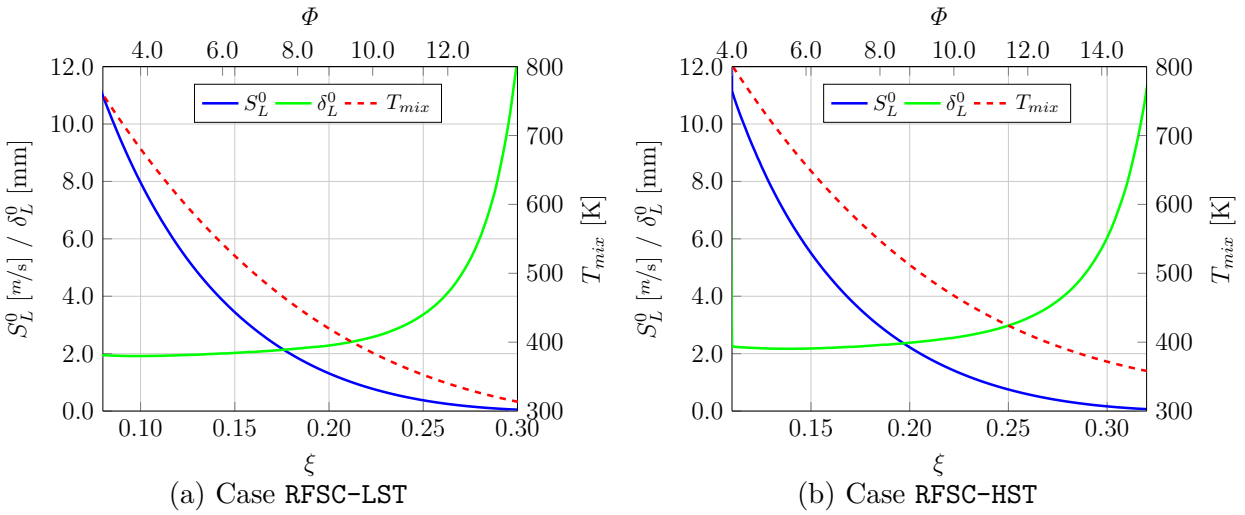

(a) Case `RFSC-LST` (b) Case `RFSC-HST`

Figure 7.31 – Laminar flame velocity S_L^0 and thickness δ_L^0 as function of the mixture fraction ξ

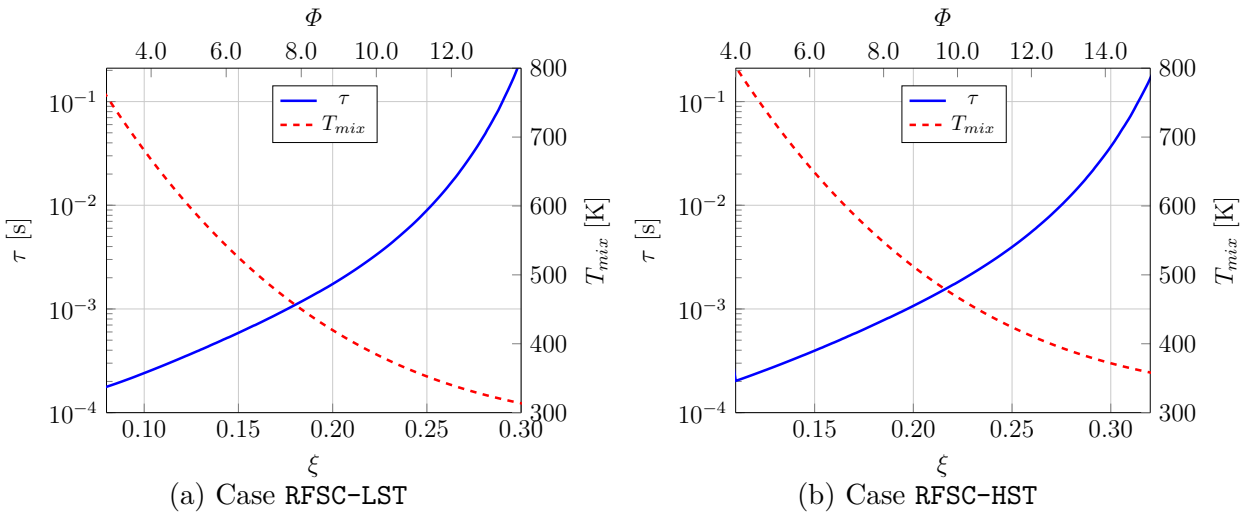

(a) Case `RFSC-LST` (b) Case `RFSC-HST`

Figure 7.32 – Flame propagation timescale τ as function of the mixture fraction ξ

Since a non-negligible amount of chemical reactions take place in a premixed combustion mode, the turbulent premixed combustion regimes are analyzed in the standard diagram of Barrère and Borghi [24, 25]. The data is plotted in figure 7.33 using a normalized length scale ratio $\mathcal{L}_t/\delta_L^0$ and velocity ratio u_{rms}/S_L^0 as the set of coordinates. Homogeneous Isotropic Turbulence (`HIT`) was considered in order to estimate the root-mean-square velocity fluctuation u_{rms} and turbulence integral length scale $\mathcal{L}_t$:

$$u_{rms} = \sqrt{\frac{2k}{3}} \quad \text{and} \quad \mathcal{L}_t = \frac{u_{rms}^3}{\varepsilon}$$

with k being the turbulent kinetic energy, calculated from the resolved contribution

$$k = \frac{\langle \bar{\rho}\widetilde{u}_i\widetilde{u}_i \rangle - \langle \bar{\rho} \rangle \langle \widetilde{u}_i \rangle \langle \widetilde{u}_i \rangle}{2\langle \bar{\rho} \rangle} \tag{7.7}$$

and ε its dissipation rate, given by:

$$\varepsilon = \frac{1}{\langle\rho\rangle}\left\langle \tau'_{ik}\frac{\partial u''_j}{\partial x_k} + \tau'_{jk}\frac{\partial u''_i}{\partial x_k}\right\rangle \tag{7.8}$$

The flame characteristics are estimated from the local conditions of the corresponding unburnt mixtures. Quantities S_L^0 and δ_L^0 are calculated at each point considering the following conditions:

- the mixture fraction ξ remains within the lean and rich flammability limits, i.e., in a range where the propagation of a premixed flame may occur.
- the point lies inside a zone where the probability to have a premixed flame structure remains larger than a given threshold value (40% here).

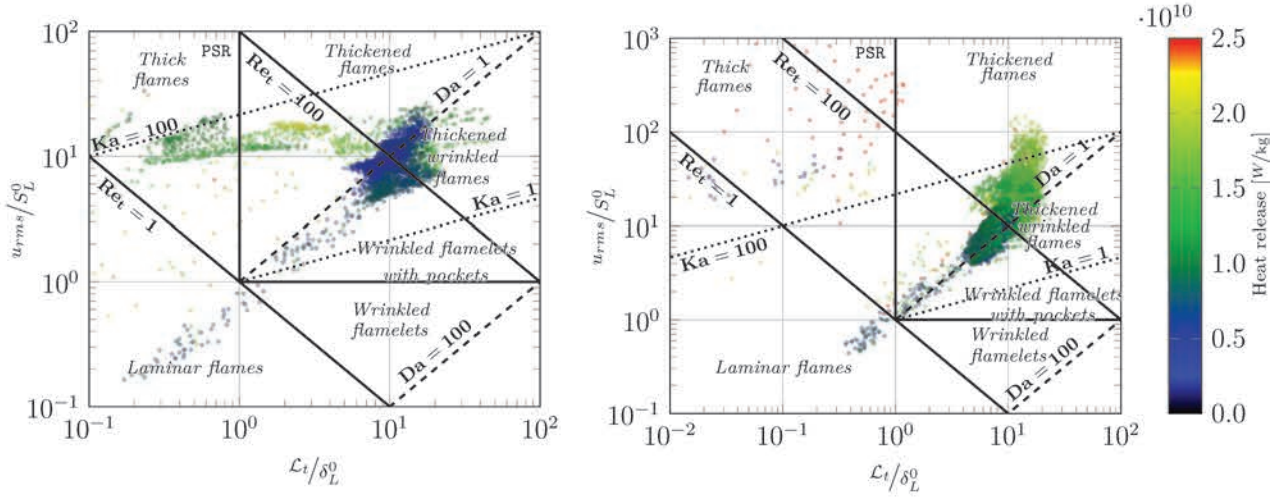

(a) Case `RFSC-LST` (b) Case `RFSC-HST`

Figure 7.33 – Premixed combustion diagram based on the Borghi-Barrère coordinates [25]

Several premixed combustion regimes are found in figure 7.33, such as so-called thick flames, thickened flames, thickened-wrinkled flames and even quasi-laminar ones. In case `RFSC-LST` most of the points are located in the vicinity of thickened-wrinkled flame regime, between the Klimov-Williams limit (`Ka` $= 1$) and the line corresponding to `Da` $= 1$, around the horizontal line corresponding to $^{u_{rms}}/_{S_L^0} = 10$, with some points featuring a non negligible heat release rate located in the thick flame region. Case `RFSC-HST` displays a significantly larger heat release rate, with a large set of points spread towards the thickened and thickened-wrinkled flame regimes, corresponding to a smaller Damköler number. Non-negligible finite-rate chemistry effects come into play.

Restricting the domain only to the fuel injection zone ($(-4, 0) \leq (^{x_1}/_{D_{inj}}, ^{x_2}/_{D_{inj}}) \leq (8, 4)$), still at $^{x_3}/_{D_{inj}} = 0$, one can verify that case `RFSC-LST` features a thick flame

regime, with smaller Damköler number and larger Karlovitz number values, whereas case `RFSC-HST` displays points located in the thickened flame and thick flame regimes, with lower and higher heat release rates, respectively, as shown in figure 7.34.

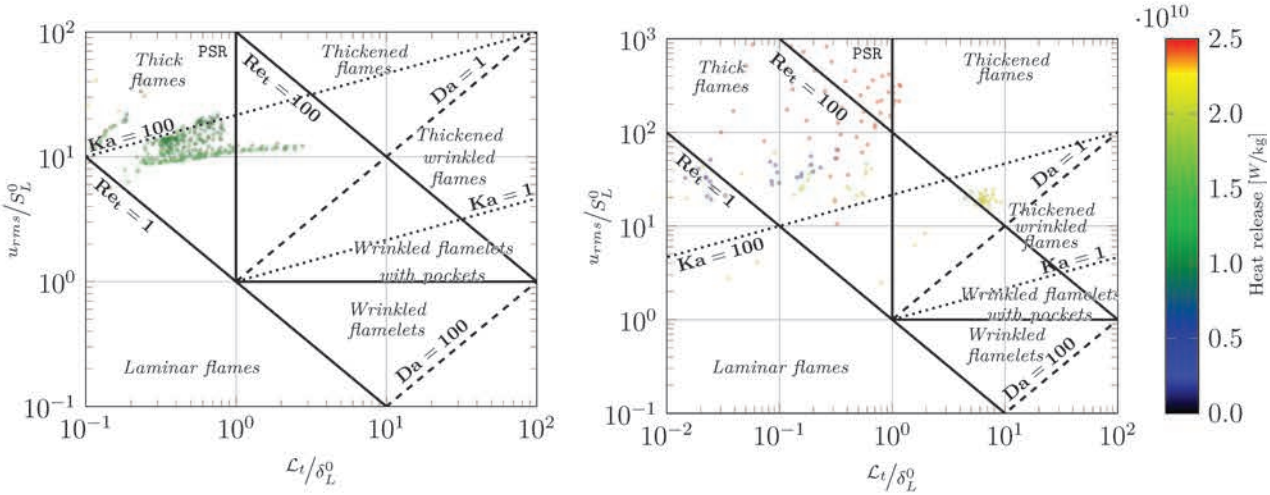

(a) Case `RFSC-LST` (b) Case `RFSC-HST`

Figure 7.34 – Premixed combustion diagram - focus on the fuel injection

Summary

The simulation conditions studied in this chapter are relevant to experiments previously conducted at the University of Michigan [116, 117]. Turbulence-chemistry interactions and flame stabilization mechanism are studied for a jet in a supersonic crossflow of vitiated air delivering hydrogen upstream of a squared cavity.

As in the previous chapter, the computations are performed with `CREAMS`, featuring the `IBM` algorithm. The simulations were conducted within the `LES` framework considering the Wall-Adapting Local Eddy (`WALE`) as the subgrid-scale viscosity closure. Two chemical reactor models were considered: Perfectly Stirred Reactor (`PSR`) and Unsteady Partially Stirred Reactor (`U-PaSR`), with both of them providing similar results, thus confirming the quality of the mesh resolution, since it can take into account micro-mixing effects.

Two combustion stabilization modes were recovered according the the inlet vitiated air stream temperature: cavity stabilized and jet-wake stabilized regimes. Combustion takes place in the cavity stabilization mode at low operative temperatures and in the jet-wake stabilization mode at higher operative temperatures, which is quite consistent with the experimental results of Micka and Driscoll [115]. Some oscillations between these two modes are expected at intermediate operative temperatures. In the cavity stabilized combustion mode, combustion is anchored at the leading edge of the cavity and spreads

into the main flow at an approximately constant angle, whereas in the jet-wake stabilized mode combustion takes place upstream the cavity.

The analysis of combustion regimes confirms the occurrence of highly turbulent premixed flame conditions. The corresponding distribution for case `RFSC-LST` is rather similar to the results obtained by Quinlan et al. [147] and Techer [174], with the points being shifted to a region with a larger Karlovitz number. These differences can be explained by a different configuration, especially pressure, temperature, mixture fraction and the fuel considered. For case `RFSC-HST`, however, the points distribution are more concentrated along the thickened and thickened-wrinkled flame region, with Damköler number values around unity, thus emphasizing that chemical reaction time scales are of the same order of magnitude as transport time scales.

Chapter 8

Conclusions and Perspectives

This thesis work has been undertaken at Institute Pprime and aims to contribute to the comprehension of supersonic turbulent combustion, focusing on scramjet engines applications.

At first, a brief description of the scramjet engine was reported, its conception and behavior, as well as some historical aspects in the technology development. Compared to rockets, which are actually the only kind of engine capable to reach hypersonic speeds, the scramjet has the advantage of being able to carry heavier payload since it does not need to carry its own oxidizer, using oxygen from the atmosphere. Like a ramjet, it has no moving parts and makes use of ram pressure to generate thrust, being unable to work at low speeds. The main difference lies in the fact that the flow is kept supersonic inside its combustion chamber, which poses as a challenge in its development since the time available to burn fuel with oxidizer is very short, making it more difficult to stabilize the flame. Basically, it can be divided in four distinct parts: inlet, responsible to compress and accelerate the flow so as to achieve the necessary pressure and temperature for combustion, isolator, which is responsible to contain the shock trains that may appear as the scramjet-equipped vehicle accelerates to operational velocity, the combustion chamber, where fuel and oxidizer are burn, and finally the exhaust nozzle, where thrust is generated by accelerating the combustion products. The combustion chamber is the most critical part of a scramjet engine since it must efficiently mix and burn the fuel and the oxidizer in a short residence time in order to stabilize the flame and minimize the total pressure loss.

As far as the numerical modelling is concerned, the main thermodynamic relations were presented: the Navier-Stokes equation in its compressible, reactive, multi-species form, as well as a perfect gas mixture relation. Simplified transport properties are calculated with `EGLIB` library and the chemical kinetics from the different reaction mechanisms are solved with `CHEMKIN` library. Turbulence modelling is also presented, including the filtered

Navier-Stokes equations and the subgrid-scale closing terms. CREAMS solver makes use of a Strang splitting method to couple the non-reactive terms with the reactive ones. It performs a temporal integration with a TVD scheme for the non-reactive terms and CVODE for the reactive terms. Moreover, two shock sensors, used to avoid the artificial increase in the SGS viscosity and kinetic energy due to discontinuities, are also presented. Finally, some test cases are presented to validate the solver.

The wall-mounted cavity is modeled using a recently implemented Immersed Boundary Method (IBM), which works with a Cartesian mesh and allows to insert a solid object in the computational domain without changing the topology of the mesh. Two different classes of IBM are presented, whose differences lie in the way to add the forcing term to the Navier-Stokes equations to simulate the solid wall: continuous forcing and discrete forcing method. The CFM method, which works with the continuous forcing formalism, add the forcing term to the momentum equations. The GPM method, working with the discrete forcing formalism, is coupled to the CFM method so as to correct the energy equation and generalize the application of the IBM. The solid object is modeled with a STL file, which makes use of several triangles to represent the immersed boundary, and the points are then identified as solid, fluid, ghost point, image point or interpolation point. Furthermore, a special treatment of the corners is also presented. Some test cases are also considered to verify the implementation of the method into the solver.

Since the flow is kept supersonic inside the scramjet combustion chamber, chemical reaction time scales tend to be of the same order of magnitude as turbulent time scales, which causes the fast chemistry approach to be less appropriate. The unsteady partially stirred reactor (U-PaSR) is a multiscale-based model with fine-scale structure and mixing timescale being related to the Kolmogorov velocity scale and Kolmogorov timescale, respectively, taking into account inhomogeneities of composition and temperature in the flame region and considering the effects of micro-mixing, finite chemistry and interactions between them. Within this modelling framework, chemical reaction takes place in fine-scale structure regions, where most of the viscous dissipation and molecular mixing processes take place, and the SGS model recovers the DNS limit as the filter size tends to zero, which means that, with a very well resolved mesh, this model behaves like a well-stirred reactor. Moreover, since it makes use of a finite-rate chemistry-based approach, the particle residence time plays an important role in the reactor behavior. A short residence time provides not enough time for the mixture to burn, with the solution being practically the same of the inlet conditions: the reactor behavior is limited by chemistry. A long residence time allows the mixture to burn almost entirely, with the reactor behavior being limited by the mixing and chemical time. At intermediate residence time the reactor behavior may be limited by chemistry or by the mixing time, depending on the

conditions (temperature, mass fraction). A verification of the U-PaSR model is performed and compared with the PSR one.

Finally, two simulations with conditions relevant to experiments performed at the University of Michigan are performed: one featuring a lower inlet stream temperature (case RFSC-LST) and another with a higher inlet stream temperature (case RFSC-HST). Several criteria are used to verify the computational resolution and some efforts were spent to capture the flow near the IBM walls as accurately as possible. The computations performed gather everything that was presented in the initial chapters: it makes use of the LES framework and the IBM algorithm, with the U-PaSR being used only in the reactive simulations that are performed next. The WALE model is considered as the subgrid-scale viscosity closure, since it was capable to satisfactorily recover the behavior in the buffer layer that separates the logarithmic zone from the viscous sublayer. Fuel mixing starts at the fuel jet injection, with the hydrogen jet slightly tearing up with the fluid present inside the cavity, which enhances the mixing. Cases RFSC-LST and RFSC-HST feature two different recirculation behaviors inside the cavity: the first one with only one large recirculation zone that covers the cavity almost entirely and the last one associated with two big recirculation zones covering each one approximately half of the cavity. Mixing efficiency are evaluated for both cases between the fuel injection and the cavity region. It is verified that the presence of the cavity increases significantly the mixing efficiency.

At the end, chemical reactions are activated so as to study turbulence-chemistry interactions and flame stabilization mechanism on the same configuration. Two reactor models were considered: perfectly stirred reactor (PSR) and unsteady partially stirred reactor (U-PaSR). Both reactor models provided similar results, which confirms that the simulations are very well resolved, being able to take into account micro-mixing effects at the resolved scale. Two combustion stabilization modes were recovered: cavity-stabilized mode for case RFSC-LST and jet-wake stabilized mode for case RFSC-HST, being consistent with the experimental results of Micka and Driscoll [115]. Cavity-stabilized combustion mode features the combustion zone anchored at the leading edge of the cavity and spreading into the main flow at an approximately constant angle. Combustion takes place upstream the cavity in the jet-wake combustion stabilization mode. Highly turbulent premixed flame conditions are obtained in both cases. The distribution of combustion regimes associated to case RFSC-LST is similar to the results obtained by Quinlan et al. [147] and Techer [174], but with some points being shifted to a larger Karlovitz number region, which may be explained different pressure, temperature, mixture fraction and the fuel considered in the simulation. Case RFSC-HST, however, reflects thickened and thickened-wrinkled flames, with the reaction processes intensity being the same order of magnitude as the transport phenomena ($\mathrm{Da} \approx 1$).

Perspectives and future works related to the present study may consist in the use of a less-refined mesh in order to discriminate the behavior of the `U-PaSR` model without recovering the `DNS` limit. The corresponding set of computations will be faster with a less-refined mesh. Complementary simulations may be run at intermediate values of the vitiated air inlet operative temperature so as to understand how the oscillations between cavity-stabilized and jet-wake stabilized combustion mode may happen and how long each one is active. Furthermore, since the analysis of combustion regimes confirms the occurrence of highly turbulent premixed flame conditions, it may be interesting to work on the representation of turbulence-chemistry interactions and propose models that are suited to such conditions.

Appendix A

Thermodynamic tables

Thermodynamic tables gives the polynomial interpolation coefficients used calculate molecular enthalpy, specific heat at constant pressure and molecular entropy of species α using the following interpolation functions:

$$\frac{\hat{C}_{p\alpha}(T)}{\mathcal{R}} = a_{1\alpha} + a_{2\alpha}T + a_{3\alpha}T^2 + a_{4\alpha}T^3 + a_{5\alpha}T^4 \tag{A.1}$$

$$\frac{\hat{H}_{\alpha}(T)}{\mathcal{R}} = a_{1\alpha}T + a_{2\alpha}\frac{T^2}{2} + a_{3\alpha}\frac{T^3}{3} + a_{4\alpha}\frac{T^4}{4} + a_{5\alpha}\frac{T^5}{5} + a_{6\alpha} \tag{A.2}$$

$$\frac{\hat{S}_{\alpha}(T, p_{std})}{\mathcal{R}} = a_{1\alpha}\ln T + a_{2\alpha}T + a_{3\alpha}\frac{T^2}{2} + a_{4\alpha}\frac{T^3}{3} + a_{5\alpha}\frac{T^4}{4} + a_{7\alpha} \tag{A.3}$$

with $\mathcal{R}$ being the ideal gas constant. These data are obtained from experimental measures at standard pressure $p_{std} = 1\text{atm}$[1].

Normally the temperature interval is between 300K and 5000K, but sometimes a lower (or a higher) temperature is needed. In this case some authors recommend to extrapolate the function linearly.

Finally, the enthalpies and specific heat for each species α are calculated with the following equations:

$$h_{\alpha}(T) = \Delta h^0_{f\alpha} + \int_{T_0}^{T} c_{p\alpha}(\theta)\ \mathrm{d}\theta = \frac{\hat{H}_{\alpha}(T)}{\mathcal{W}_{\alpha}} \tag{A.4}$$

$$c_{p\alpha}(T) = \frac{\hat{C}_{p\alpha}(T)}{\mathcal{W}_{\alpha}} \tag{A.5}$$

The main thermodynamic tables are given by:

[1]The ideal gas hypothesis implies that the internal energy and the enthalpy are only temperature-dependent.

- NASA Glenn [114], generated by Gordon and McBride from NASA Lewis Research Center.
- `JANAF` [38, 170], used by `CHEMKIN` software from SANDIA.
- Burcat [34], generated, updated and distributed by Professor Burcat.

and they are presented with the following structure:

$$\begin{array}{cccccc} M_\alpha & & T_{min} & T_{max} & T_{int} \\ a_{1\alpha}^+ & a_{2\alpha}^+ & a_{3\alpha}^+ & a_{4\alpha}^+ & a_{5\alpha}^+ \\ a_{6\alpha}^+ & a_{7\alpha}^+ & a_{1\alpha}^- & a_{2\alpha}^- & a_{3\alpha}^- \\ a_{4\alpha}^- & a_{5\alpha}^- & a_{6\alpha}^- & a_{7\alpha}^- & \mathcal{A} \end{array}$$

The first line is composed by the chemical species M_α and the temperature intervals where the interpolation function can be used. There are two temperature intervals: a higher one with temperatures between T_{int} and T_{max} associated to coefficients $a_{l\alpha}^+ \in [\![1, 7]\!]$, and a lower one with temperatures between T_{min} and T_{int} associated to coefficients $a_{l\alpha}^- \in [\![1, 7]\!]$. For NASA Gleen thermodynamic table, T_{int} is always 1000K, so T_{int} is replaced by the molecular weight $\mathcal{W}_\alpha$. Also, for NASA Glenn and Burcat, $\mathcal{A}$ is the ratio between the molecular formation enthalpy and the ideal gas constant:

$$\mathcal{A} = \frac{\Delta \hat{H}_{f,\alpha}^0}{\mathcal{R}} \tag{A.6}$$

Appendix B

O'Conaire chemical mechanism

```
!
! Conaire
! 21-steps mechanism
!
ELEMENTS
   H  O  N
END

SPECIES
   H2  O2  H2O  H  O  OH  HO2  H2O2  N2
END

REACTIONS                                          CAL/MOLE
   H+O2=O+OH              1.915E+14    0.00      1.644E+04    ! 01
      REV                / 5.481E+11    0.39     -2.930E+02 /
   O+H2=H+OH              5.080E+04    2.67      6.292E+03    ! 02
      REV                / 2.667E+04    2.65      4.880E+03 /
   OH+H2=H+H2O            2.160E+08    1.51      3.430E+03    ! 03
      REV                / 2.298E+09    1.40      1.832E+04 /
   O+H2O=OH+OH            2.970E+06    2.02      1.340E+04    ! 04
      REV                / 1.465E+05    2.11     -2.904E+03 /
   H2+M=H+H+M             4.577E+19   -1.40      1.044E+05    ! 05
      REV                / 1.146E+20   -1.68      8.200E+02 /
      H2/2.5/  H2O/12.0/
   O2+M=O+O+M             4.515E+17   -0.64      1.189E+05    ! 06
      REV                / 6.165E+15   -0.50      0.000E+00 /
   H2/2.5/ H2O/12.0/
   OH+M=O+H+M             9.880E+17   -0.74      1.021E+05    ! 07
      REV                / 4.714E+18   -1.00      0.000E+00 /
      H2/2.5/  H2O/12.0/
   H2O+M=H+OH+M           1.912E+23   -1.83      1.185E+05    ! 08
      REV                / 4.500E+22   -2.00      0.000E+00 /
      H2/0.73/  H2O/12.0/
   H+O2(+M)=HO2(+M)       1.475E+12    0.60      0.000E+00    ! 09
!      REV                / 3.090E+12    0.53      4.887E+04 /
      LOW                / 3.482E+16   -4.11E-01 -1.115E+03 /
      TROE / 0.5  1.0000E-30  1.0000E+30  1.0000E+100 /
   H2/1.3/ H2O/14.0/
   HO2+H=H2+O2            1.660E+13    0.00      8.230E+02    ! 10
```

```
40        REV                / 3.164E+12    0.35       5.551E+04 /
41     HO2+H=OH+OH             7.079E+13    0.00       2.950E+02    ! 11
42        REV                / 2.027E+10    0.72       3.684E+04 /
43     HO2+O=OH+O2             3.250E+13    0.00       0.000E+00    ! 12
44        REV                / 3.252E+12    0.33       5.328E+04 /
45     HO2+OH=H2O+O2           2.890E+13    0.00      -4.970E+02    ! 13
46        REV                / 5.861E+13    0.24       6.908E+04 /
47     H2O2+O2=HO2+HO2         4.634E+16   -0.35       5.067E+04    ! 14
48        REV                / 4.200E+14    0.00       1.198E+04 /
49        DUPLICATE
50     H2O2+O2=HO2+HO2         1.434E+13   -0.35       3.706E+04    ! 15
51        REV                / 1.300E+11    0.00      -1.629E+03 /
52        DUPLICATE
53     H2O2(+M)=OH+OH(+M)      2.951E+14    0.00       4.843E+04    ! 16
54  !      REV                / 3.656E+08    1.14      -2.584E+03 /
55        LOW                / 1.202E+17    0.00       45500.000 /
56        TROE / 0.5  1.0000E-30  1.0000E+30  1.0000E+100 /
57        H2/2.5/  H2O/12.0/
58     H2O2+H=H2O+OH           2.410E+13    0.00       3.970E+03    ! 17
59        REV                / 1.269E+08    1.31       7.141E+04 /
60     H2O2+H=H2+HO2           6.025E+13    0.00       7.950E+03    ! 18
61        REV                / 1.041E+11    0.70       2.395E+04 /
62     H2O2+O=OH+HO2           9.550E+06    2.00       3.970E+03    ! 19
63        REV                / 8.660E+03    2.68       1.856E+04 /
64     H2O2+OH=H2O+HO2         1.000E+12    0.00       0.000E+00    ! 20
65        REV                / 1.838E+10    0.59       3.089E+04 /
66        DUPLICATE
67     H2O2+OH=H2O+HO2         5.800E+14    0.00       9.557E+03    ! 21
68        REV                / 1.066E+13    0.59       4.045E+04 /
69        DUPLICATE
70  END
```

Appendix C

GMSH cavity geometry

```
// Cavity generator (ibm1.geo)

//============================================================
// CAVITY MODEL

//      (l1)                      (l5)     (l6)
//  +-----------+             +-----------+----+
//  0           |             |
//         (l2) |             | (l4)
//              |    (l3)     |
//              +-------------+

//============================================================
// Model generation data

// Model type (2: 2D / 3: 3D)
modeldim = 3;

// What to plot (1: full / 2: cavity only / 3: isolator only)
whatplot = 2;

//============================================================
// Cavity data

// Isolator length
isolfull = 358.0e-3;
isolpart = 50.0e-3;

// Length between the injection and the cavity
cavbefore = 44.5e-3;

// Cavity length and height
cavlength = 50.8e-3;
cavheight = 12.7e-3;

// Exhaustor length
exhaustfull = 349.0e-3;
exhaustpart = cavlength * 1.5e+0;

```

```
40 //============================================================
41
42 // Dimension of the IBM model
43 If(whatplot == 1) // Full geometry
44   ntl1orig = 750;
45   isol     = isolfull;
46   exhaust  = exhaustpart;
47 EndIf
48 If(whatplot == 2) // Cavity only
49   ntl1orig = 180;
50   isol     = isolpart;
51   exhaust  = exhaustpart;
52 EndIf
53 If(whatplot == 3) // Isolator only
54   ntl1orig  = 750;
55   isol      = isolfull;
56   cavlength = +0.0e+0;
57   cavheight = +0.0e+0;
58   exhaust   = +0.0e+0;
59 EndIf
60 l1 = isol + cavbefore;
61 l2 = cavheight;
62 l3 = cavlength;
63 l4 = cavheight;
64 l5 = exhaust;
65 l6 = +0.0e+0;
66 If(l5 > 0)
67   l6 = +3.5e-3;
68 EndIf
69
70 // Angles of each curve (in degrees)
71 alphal1 = +0.0000;
72 alphal2 = -90.0000;
73 alphal3 = +0.0000;
74 alphal4 = +90.0000;
75 alphal5 = -4.0000;
76 alphal6 = +0.0000;
77
78 // Number of points for each curve (0 for automatic calculation)
79 ntl1 = ntl1orig;
80 ntl2 = 20;
81 ntl3 = 70;
82 ntl4 = ntl2;
83 ntl5 = 150;
84 ntl6 = 9;
85
86 // Angle of the whole model (in degrees)
87 alphatot = +0.0000;
88
89 // Thickness of the model
90 dimz = +1.00e-5;
91 If(modeldim == 3)
92   dimz = +38.1e-3;
93 EndIf
94
```

```
95  // Starting point coordinates (point 0)
96  startx = -isol;
97  starty = +0.00e+0;
98  startz = +0.00e+0;
99  If(modeldim == 3)
100   startz = -dimz / 2;
101 EndIf
102
103 // Number of points in Z-direction (0 for automatic calculation)
104 ntz = 2;
105 If(modeldim == 3)
106   ntz = 50;
107 EndIf
108
109 // Offset
110 tx = +0.00e+0;
111 ty = +0.00e+0;
112
113
114 // Total number of surfaces
115 totsurf = 1;
116 If(l2 > 0.0)
117   totsurf = totsurf + 1;
118 EndIf
119 If(l3 > 0.0)
120   totsurf = totsurf + 1;
121 EndIf
122 If(l4 > 0.0)
123   totsurf = totsurf + 1;
124 EndIf
125 If(l5 > 0.0)
126   totsurf = totsurf + 1;
127 EndIf
128 If(l6 > 0.0)
129   totsurf = totsurf + 1;
130 EndIf
131
132 // Other parameters
133 cosspac     = 0;        // Points spacing (0: don't use cosine
       spacing / 1: use cosine spacing)
134 ptfactor    = +1.00e+4; // Multiplication factor to calculate the
       number of points
135 scalefactor = 1.0;      // Scaling factor (not applied to Z-axis)
136
137 //============================================================
138
139 // Adjust variables
140 alphatot = -alphatot * (Pi / 180);
141 alphal1  = alphal1  * (Pi / 180);
142 alphal2  = alphal2  * (Pi / 180);
143 alphal3  = alphal3  * (Pi / 180);
144 alphal4  = alphal4  * (Pi / 180);
145 alphal5  = alphal5  * (Pi / 180);
146 alphal6  = alphal6  * (Pi / 180);
147
```

```
148 // Specific variable adjustments
149 l4 = l4 / Sin(alphal4);
150 l5 = l5 / Cos(alphal5);
151
152 // Scale some variables
153 scalefactor = Fabs(scalefactor);
154 l1 = l1 * scalefactor;
155 l2 = l2 * scalefactor;
156 l3 = l3 * scalefactor;
157 l4 = l4 * scalefactor;
158 l5 = l5 * scalefactor;
159 l6 = l6 * scalefactor;
160
161 // Calculate number of points for each curve
162 If(ntl1 == 0)
163   ntl1 = Ceil((l1 * ptfactor) - 1);
164 EndIf
165 If(ntl2 == 0)
166   ntl2 = Ceil((l2 * ptfactor) - 1);
167 EndIf
168 If(ntl3 == 0)
169   ntl3 = Ceil((l3 * ptfactor) - 1);
170 EndIf
171 If(ntl4 == 0)
172   ntl4 = Ceil((l4 * ptfactor) - 1);
173 EndIf
174 If(ntl5 == 0)
175   ntl5 = Ceil((l5 * ptfactor) - 1);
176 EndIf
177 If(ntl6 == 0)
178   ntl6 = Ceil((l6 * ptfactor) - 1);
179 EndIf
180 If(ntz == 0)
181   ntz = Ceil((z * ptfactor) - 1);
182 EndIf
183 If(ntz < 2)
184   ntz = 2;
185 EndIf
186
187 // Other variables
188 el = 1.0;
189 contpts = 1;
190 contlin = 1;
191 contplan = 1;
192
193
194 // Draw points
195 stepz = dimz / (ntz - 1);
196 For z In {0:dimz:stepz}
197
198 // First point
199   nl[0] = 0;
200   dx = 0;
201   dy = 0;
202   dz = z;
```

```
203   contpts = newp; Point(contpts) = {startx+dx, starty+dy,
          startz+dz, el};
204
205 // Points for l1
206   nl[1] = ntl1;
207   x0 = dx;
208   y0 = dy;
209   For k In {1:nl[1]:1}
210     dl = k * (l1 / nl[1]);
211     If(cosspac == 1)
212       dl = ((1 - Cos(k * (Pi / nl[1]))) / 2) * l1;
213     EndIf
214     x = dl * Cos(alphal1);
215     y = dl * Sin(alphal1);
216     x = tx + x0 + x;
217     y = ty + y0 + y;
218     dx = (x * Cos(alphatot)) + (y * Sin(alphatot));
219     dy = (-x * Sin(alphatot)) + (y * Cos(alphatot));
220     dz = z;
221     contpts = newp; Point(contpts) = {startx+dx, starty+dy,
            startz+dz, el};
222   EndFor
223
224 // Points for l2
225   nl[2] = 0;
226   If(l2 > 0.0)
227     nl[2] = ntl2;
228     x0 = x0 + l1 * Cos(alphal1);
229     y0 = y0 + l1 * Sin(alphal1);
230     For k In {1:nl[2]:1}
231       dl = k * (l2 / nl[2]);
232       If(cosspac == 1)
233         dl = ((1 - Cos(k * (Pi / nl[2]))) / 2) * l2;
234       EndIf
235       x = dl * Cos(alphal2);
236       y = dl * Sin(alphal2);
237       x = tx + x0 + x;
238       y = ty + y0 + y;
239       dx = (x * Cos(alphatot)) + (y * Sin(alphatot));
240       dy = (-x * Sin(alphatot)) + (y * Cos(alphatot));
241       dz = z;
242       contpts = newp; Point(contpts) = {startx+dx, starty+dy,
              startz+dz, el};
243     EndFor
244   EndIf
245
246 // Points for l3
247   nl[3] = 0;
248   If(l3 > 0.0)
249     nl[3] = ntl3;
250     x0 = x0 + l2 * Cos(alphal2);
251     y0 = y0 + l2 * Sin(alphal2);
252     For k In {1:nl[3]:1}
253       dl = k * (l3 / nl[3]);
254       If(cosspac == 1)
```

```
255         dl = ((1 - Cos(k * (Pi / nl[3]))) / 2) * l3;
256       EndIf
257       x = dl * Cos(alphal3);
258       y = dl * Sin(alphal3);
259       x = tx + x0 + x;
260       y = ty + y0 + y;
261       dx = (x * Cos(alphatot)) + (y * Sin(alphatot));
262       dy = (-x * Sin(alphatot)) + (y * Cos(alphatot));
263       dz = z;
264       contpts = newp; Point(contpts) = {startx+dx, starty+dy,
             startz+dz, el};
265     EndFor
266   EndIf
267
268 // Points for l4
269   nl[4] = 0;
270   If(l4 > 0.0)
271     nl[4] = ntl4;
272     x0 = x0 + l3 * Cos(alphal3);
273     y0 = y0 + l3 * Sin(alphal3);
274     For k In {1:nl[4]:1}
275       dl = k * (l4 / nl[4]);
276       If(cosspac == 1)
277         dl = ((1 - Cos(k * (Pi / nl[4]))) / 2) * l4;
278       EndIf
279       x = dl * Cos(alphal4);
280       y = dl * Sin(alphal4);
281       x = tx + x0 + x;
282       y = ty + y0 + y;
283       dx = (x * Cos(alphatot)) + (y * Sin(alphatot));
284       dy = (-x * Sin(alphatot)) + (y * Cos(alphatot));
285       dz = z;
286       contpts = newp; Point(contpts) = {startx+dx, starty+dy,
             startz+dz, el};
287     EndFor
288   EndIf
289
290 // Points for l5
291   nl[5] = 0;
292   If(l5 > 0.0)
293     nl[5] = ntl5;
294     x0 = x0 + l4 * Cos(alphal4);
295     y0 = y0 + l4 * Sin(alphal4);
296     For k In {1:nl[5]:1}
297       dl = k * (l5 / nl[5]);
298       If(cosspac == 1)
299         dl = ((1 - Cos(k * (Pi / nl[5]))) / 2) * l5;
300       EndIf
301       x = dl * Cos(alphal5);
302       y = dl * Sin(alphal5);
303       x = tx + x0 + x;
304       y = ty + y0 + y;
305       dx = (x * Cos(alphatot)) + (y * Sin(alphatot));
306       dy = (-x * Sin(alphatot)) + (y * Cos(alphatot));
307       dz = z;
```

```
308         contpts = newp; Point(contpts) = {startx+dx, starty+dy,
                startz+dz, el};
309       EndFor
310     EndIf
311
312   // Points for l6
313     nl[6] = 0;
314     If(l6 > 0.0)
315       nl[6] = ntl6;
316       x0 = x0 + l5 * Cos(alphal5);
317       y0 = y0 + l5 * Sin(alphal5);
318       For k In {1:nl[6]:1}
319         dl = k * (l6 / nl[6]);
320         If(cosspac == 1)
321           dl = ((1 - Cos(k * (Pi / nl[6]))) / 2) * l6;
322         EndIf
323         x = dl * Cos(alphal6);
324         y = dl * Sin(alphal6);
325         x = tx + x0 + x;
326         y = ty + y0 + y;
327         dx = (x * Cos(alphatot)) + (y * Sin(alphatot));
328         dy = (-x * Sin(alphatot)) + (y * Cos(alphatot));
329         dz = z;
330         contpts = newp; Point(contpts) = {startx+dx, starty+dy,
                startz+dz, el};
331       EndFor
332     EndIf
333
334     nl[7] = 0;
335
336   EndFor
337   contpts = Ceil(contpts / ntz);
338
339
340   // Draw lines
341
342   // Draw lines in the X-Y domain
343   For z In {1:ntz:1}
344     zaxis = contpts * (z - 1);
345     For k In {1:contpts-1:1}
346       l1 = zaxis + k;
347       l2 = l1 + 1;
348       contlin = newl; Line(contlin) = {l1, l2};
349       Transfinite Line {contlin} = 2 Using Progression 1;
350     EndFor
351   EndFor
352
353   // Draw lines along Z-axis (edges)
354   For z In {1:ntz-1:1}
355     acum = contpts * (z - 1);
356     For k In {0:totsurf:1}
357       acum = acum + nl[k];
358       l1 = acum + 1;
359       l2 = l1 + contpts;
360       contlin = newl; Line(contlin) = {l1, l2};
```

```
361     Transfinite Line {contlin} = 2 Using Progression 1;
362   EndFor
363 EndFor
364
365 // Draw lines along Z-axis (other lines)
366 For z In {1:ntz-1:1}
367   acum = contpts * (z - 1);
368   For k In {1:contpts-1:1}
369     l1 = acum + k;
370     l2 = l1 + 1 + contpts;
371     contlin = newl; Line(contlin) = {l1, l2};
372     Transfinite Line {contlin} = 3 Using Progression 1;
373   EndFor
374 EndFor
375 contlin = contpts -1;
376
377 // Create surfaces
378 For z In {1:ntz-1:1}
379   zaxis1 = contlin * (z - 1);
380   zaxis2 = (totsurf + 1) * (z - 1);
381
382 // Create squares
383   acum = contlin * (z - 1);
384   For l In {1:totsurf:1}
385     ini = acum + nl[l-1] + 1;
386     fim = ini + nl[l] - 2;
387     For k In {ini:fim:1}
388       l1 = k;
389       l2 = (contlin * ntz) + ((totsurf+1) * (ntz-1)) + 1 + k;
390       l3 = contlin + 1 + k;
391       l4 = l2 - 1;
392       contplan = news; Line Loop(contplan) = {l1, l2, -l3, -l4};
393       Surface(contplan) = {contplan};
394     EndFor
395     acum = acum + nl[l-1];
396   EndFor
397
398 // Create triangles
399   acum1 = 0;
400   acum2 = 0;
401   acum3 = 0;
402   For k In {1:totsurf:1}
403
404     l1 = (contlin * ntz) + ((totsurf + 1) * (ntz - 1)) + 1 + acum1
          + zaxis1;
405     l2 = contlin + 1 + acum1 + zaxis1;
406     l3 = (contlin * ntz) + 1 + acum2 + zaxis2;
407     contplan = news; Line Loop(contplan) = {-l1, l2, l3};
408     Surface(contplan) = {contplan};
409
410     l1 = (contlin * ntz) + 2 + acum2 + zaxis2;
411     l2 = (contlin * ntz) + ((totsurf + 1) * (ntz - 1)) + nl[1] +
          acum3 + zaxis1;
412     l3 = nl[1] + acum3 + zaxis1;
413     contplan = news; Line Loop(contplan) = {l1, -l2, l3};
```

```
414       Surface(contplan) = {contplan};
415
416       acum1 = acum1 + nl[k];
417       acum2 = acum2 + 1;
418       acum3 = acum3 + nl[k+1];
419
420     EndFor
421   EndFor
```

Bibliography

[1] Abbitt III, J. D., Segal, C., McDaniel, J. C., Krauss, R. H., and Whitehurst, R. B. (1993). Experimental supersonic hydrogen combustion employing staged injection behind a rearward-facing step. *Journal of Propulsion and Power*, 9(3):472–478.

[2] Adams, N. A. and Shariff, K. (1996). A high-resolution hybrid compact-ENO scheme for shock-turbulence interaction problems. *Journal of Computational Physics*, 127(1):27–51.

[3] Alcaide, R. L. M. (2009). Investigação da combustão supersônica em túnel de choque hipersônico. Master's thesis, Instituto Tecnológico de Aeronáutica, São José dos Campos, SP, Brazil.

[4] Anavaradham, T. G., Chandra, B. U., Babu, V., Chakravarthy, S., and Panneerselvam, S. (2004). Experimental and numerical investigation of confined unsteady supersonic flow over cavities. *The Aeronautical Journal*, 108(1081):135–144.

[5] Anderson, J. D. (1990). *Modern compressible flow: with historical perspective*, volume 12. McGraw-Hill New York.

[6] Andrews, E. (2001). Scramjet development and testing in the United States. In *10th AIAA/NAL-NASDA-ISAS International Space Planes and Hypersonic Systems and Technologies Conference*. AIAA Paper 2001–1927.

[7] Angot, P., Bruneau, C.-H., and Fabrie, P. (1999). A penalization method to take into account obstacles in incompressible viscous flows. *Numerische Mathematik*, 81(4):497–520.

[8] Arquis, E. and Caltagirone, J. (1984). Sur les conditions hydrodynamiques au voisinage d'une interface milieu fluide-milieu poreux: application à la convection naturelle. *CR Acad. Sci. Paris II*, 299:1–4.

[9] Atkinson, K. E. (2008). *An introduction to numerical analysis*. John Wiley & Sons.

[10] Bagaveyev, N., Bhagwandin, V., and Engblom, W. (2010). Parametric investigation of racetrack-to-circular cross-section transition of a dual-mode ramjet isolator. In *48th AIAA Aerospace Sciences Meeting Including. The New Horizons Forum and Aerospace Exposition*, page 942.

[11] Balsara, D. S. and Shu, C.-W. (2000). Monotonicity preserving weighted essentially non-oscillatory schemes with increasingly high order of accuracy. *Journal of Computational Physics*, 160(2):405–452.

[12] Barnstorff, K. (2010). *X-51A makes longest scramjet flight*. NASA Langley Research Center. Available at: `https://www.nasa.gov/topics/aeronautics/features/X-51A.html`.

[13] Batchelor, G. K. and Townsend, A. A. (1949). The nature of turbulent motion at large wave-numbers. *Proc. R. Soc. Lond. A*, 199(1057):238–255.

[14] Baurle, R. and Girimaji, S. (2003). Assumed PDF turbulence-chemistry closure with temperature-composition correlations. *Combustion and Flame*, 134(1-2):131–148.

[15] Ben-Yakar, A. (2000). *Experimental investigation of mixing and ignition of transverse jets in supersonic crossflows*. PhD thesis, Stanford University.

[16] Ben-Yakar, A. and Hanson, R. K. (2001). Cavity flame-holders for ignition and flame stabilization in scramjets: an overview. *Journal of propulsion and power*, 17(4):869–877.

[17] Berglund, M., Fedina, E., Fureby, C., Tegnér, J., and Sabelnikov, V. (2010). Finite rate chemistry large-eddy simulation of self-ignition in supersonic combustion ramjet. *AIAA journal*, 48(3):540–550.

[18] Berglund, M. and Fureby, C. (2007). LES of supersonic combustion in a scramjet engine model. *Proceedings of the Combustion Institute*, 31(2):2497–2504.

[19] Bertin, J. J. and Cummings, R. M. (2003). Fifty years of hypersonics: where we've been, where we're going. *Progress in Aerospace Sciences*, 39(6-7):511–536.

[20] Bilger, R. (2004). Some aspects of scalar dissipation. *Flow, turbulence and combustion*, 72(2-4):93–114.

[21] Billig, F. S. (1993). Research on supersonic combustion. *Journal of Propulsion and Power*, 9(4):499–514.

[22] Blasius, H. (1950). The boundary layers in fluids with little friction. Technical report, NACA TM–1256, Whasington, DC.

[23] Borazjani, I., Ge, L., and Sotiropoulos, F. (2008). Curvilinear immersed boundary method for simulating fluid structure interaction with complex 3D rigid bodies. *Journal of Computational physics*, 227(16):7587–7620.

[24] Borghi, R. (1984). Sur la structure des flammes turbulentes. *Journal de chimie physique*, 81:361–370.

[25] Borghi, R. (1985). On the structure and morphology of turbulent premixed flames. In *Recent advances in the Aerospace Sciences*, pages 117–138. Springer.

[26] Boukharfane, R. (2018). *Contribution à la simulation numérique d'écoulements turbulents compressibles canoniques*. PhD thesis, ISAE-ENSMA Ecole Nationale Supérieure de Mécanique et d'Aérotechique-Poitiers.

[27] Boukharfane, R., Bouvelle, B., Bouali, Z., and Mura, A. (2015). An immersed boundary method to simulate compressible reactive flows featuring shock-wave interactions with three-dimensional solid obstacles. *Proceedings of the 25th International Colloquium on the Dynamic of Explosions and Reactive Systems, Leeds, UK*.

[28] Boukharfane, R., Ribeiro, F. H. E., Bouali, Z., and Mura, A. (2018). A combined ghost-point-forcing/direct-forcing immersed boundary method (IBM) for compressible flow simulations. *Computers & Fluids*, 162:91–112.

[29] Bray, K., Libby, P., and Williams, F. (1980). High speed turbulent combustion. In *Turbulent reacting flows*, pages 609–638. Springer.

[30] Brès, G. and Colonius, T. (2007). Direct numerical simulations of three–dimensional cavity flows. In *13th AIAA/CEAS Aeroacoustics Conference (28th AIAA Aeroacoustics Conference)*, page 3405. AIAA.

[31] Bringley, T. T. and Peskin, C. S. (2008). Validation of a simple method for representing spheres and slender bodies in an immersed boundary method for stokes flow on an unbounded domain. *Journal of Computational Physics*, 227(11):5397–5425.

[32] Briscolini, M. and Santangelo, P. (1989). Development of the mask method for incompressible unsteady flows. *Journal of Computational Physics*, 84(1):57–75.

[33] Brown, P. N., Byrne, G. D., and Hindmarsh, A. C. (1989). VODE: A variable-coefficient ODE solver. *SIAM journal on scientific and statistical computing*, 10(5):1038–1051.

[34] Burcat, A. (2006). *Prof. Burcat Thermodynamic Data*. Institute of Chemistry Eötvös University. Available at: `https://garfield.chem.elte.hu/Burcat/burcat.html`.

[35] Buttay, R. (2015). *Etude de l'interaction choc/turbulence/combustion en écoulement cisaillé réactif: analyse des jets réactifs fortement sous-détendus*. PhD thesis, ISAE-ENSMA Ecole Nationale Supérieure de Mécanique et d'Aérotechique-Poitiers.

[36] Buttay, R., Lehnasch, G., and Mura, A. (2016). Analysis of small-scale scalar mixing processes in highly under-expanded jets. *Shock Waves*, 26(2):193–212.

[37] Celik, I., Cehreli, Z., and Yavuz, I. (2005). Index of resolution quality for large eddy simulations. *Journal of fluids engineering*, 127(5):949–958.

[38] Chase Jr, M., Davies, C., Downey Jr, J., Frurip, D., McDonald, R., and Syverud, A. (2013). *NIST-JANAF thermochemical tables*. National Institute of Standards and Technology. Available at: `https://janaf.nist.gov`.

[39] Chaudhuri, A., Hadjadj, A., and Chinnayya, A. (2011). On the use of immersed boundary methods for shock/obstacle interactions. *Journal of Computational Physics*, 230(5):1731–1748.

[40] Chomiak, J. (1970). A possible propagation mechanism of turbulent flames at high reynolds numbers. *Combustion and Flame*, 15(3):319–321.

[41] Chua, C. K., Leong, K. F., and Lim, C. S. (2003). *Rapid prototyping: principles and applications*, volume 1. World Scientific.

[42] Cockrell, C., Auslender, A., Guy, R., McClinton, C., and Welch, S. (2002). Technology roadmap for dual-mode scramjet propulsion to support space-access vision vehicle development. In *AIAA/AAAF 11th International Space Planes and Hypersonic Systems and Technologies Conference*. AIAA Paper 2002–5188.

[43] Colonius, T., Basu, A., and Rowley, C. (1999). Numerical investigation of the flow past a cavity. In *5th AIAA/CEAS Aeroacoustics Conference and Exhibit*. AIAA Paper 1999–1912.

[44] Curran, E. T. (2001). Scramjet engines: the first forty years. *Journal of Propulsion and Power*, 17(6):1138–1148.

[45] Daly, B. and Harlow, F. (1970). Transport equations in turbulence. *The Physics of Fluids*, 13(11):2634–2649.

[46] De Palma, P., De Tullio, M., Pascazio, G., and Napolitano, M. (2006). An immersed-boundary method for compressible viscous flows. *Computers & Fluids*, 35(7):693–702.

[47] De Tullio, M. D., De Palma, P., Iaccarino, G., Pascazio, G., and Napolitano, M. (2007). An immersed boundary method for compressible flows using local grid refinement. *Journal of Computational Physics*, 225(2):2098–2117.

[48] Deepu, M., Gokhale, S., and Jayaraj, S. (2007). Recent advances in experimental and numerical analysis of scramjet combustor flow fields. *Institute of Engineering of India*, 88:13–23.

[49] Dessornes, O. and Scherrer, D. (2005). Tests of the JAPHAR dual mode ramjet engine. *Aerospace Science and Technology*, 9(3):211–221.

[50] Ducros, F., Ferrand, V., Nicoud, F., Weber, C., Darracq, D., Gacherieu, C., and Poinsot, T. (1999). Large-eddy simulation of the shock/turbulence interaction. *Journal of Computational Physics*, 152(2):517–549.

[51] Dugger, G. (1969). AIAA selected reprints/vol VI, ramjets. *The American Institute of Aeronautics and Astronautics*.

[52] Eidson, T. M. (1985). Numerical simulation of the turbulent rayleigh–bénard problem using subgrid modelling. *Journal of Fluid Mechanics*, 158:245–268.

[53] Encyclopedia of Science (2017). *Ramjet*. Available at: `https://www.daviddarling.info/encyclopedia/R/ramjet.html`.

[54] Erlebacher, G., Hussaini, M. Y., Speziale, C. G., and Zang, T. A. (1992). Toward the large-eddy simulation of compressible turbulent flows. *Journal of Fluid Mechanics*, 238:155–185.

[55] Ern, A. and Giovangigli, V. (1994). *Multicomponent transport algorithms*, volume 24. Springer Science & Business Media.

[56] Ern, A. and Giovangigli, V. (1995). Fast and accurate multicomponent transport property evaluation. *Journal of Computational Physics*, 120(1):105–116.

[57] Ern, A. and Giovangigli, V. (2004). Eglib: A general-purpose fortran library for multicomponent transport property evaluation. *Manual of EGlib version*, 3:12.

[58] Falempin, F. (1997). French hypersonic program PREPHA-system studies synthesis. *XIII ISABE-1997*.

[59] Falempin, F., Bouchez, M., and Calabro, M. (2009). The microspace launcher: first step to the fully air-breathing space launcher. *Progress in Propulsion Physics*, 1:569–592.

[60] Falempin, F., Novelli, P., Hendrick, P., and Souchier, A. (2002). Airbreathing/rocket combined cycle propulsion efforts in europe. Technical report, AAAF–2002–268–Versailles.

[61] Falempin, F., Scherrer, D., Laruelle, G., Rostand, P., Fratacci, G., and Schultz, J. (1998). French hypersonic propulsion program prepha-results, lessons and perspectives. In *8th AIAA International Space Planes and Hypersonic Systems and Technologies Conference*, page 1565.

[62] Falempin, F. and Serre, L. (2010). French flight test program LEA status. Technical report, MBDA Le Plessis Robinson (France).

[63] Fan, Z., Liu, W., Sun, M., Wang, Z., Zhuang, F., and Luo, W. (2012). Theoretical analysis of flamelet model for supersonic turbulent combustion. *Science China Technological Sciences*, 55(1):193–205.

[64] Favre, A. (1983). Turbulence: Space-time statistical properties and behavior in supersonic flows. *The Physics of fluids*, 26(10):2851–2863.

[65] Fedkiw, R. P., Merriman, B., and Osher, S. (1996). *Numerical methods for a mixture of thermally perfect and/or calorically perfect gaseous species with chemical reactions.* Department of Mathematics, University of California, Los Angeles.

[66] Ferri, A. (1968). Review of scramjet propulsion technology. *Journal of Aircraft*, 5(1):3–10.

[67] Fono, A. (1928). German patent no. 554,906.

[68] Força Aérea Brasileira (2017). *Brasil quer testar nos próximos anos velocidade hipersônica em voo.* Available at: `https://www.fab.mil.br/noticias/mostra/29437/LAAD%202017%20%E2%80%93%20Brasil%20quer%20testar%20nos%20pr%C3%B3ximos%20anos%20velocidade%20hipers%C3%B4nica%20em%20voo`.

[69] Fureby, C., Chapuis, M., Fedina, E., and Karl, S. (2011). CFD analysis of the HyShot II scramjet combustor. *Proceedings of the Combustion Institute*, 33(2):2399–2405.

[70] Gamba, M. and Mungal, M. G. (2015). Ignition, flame structure and near-wall burning in transverse hydrogen jets in supersonic crossflow. *Journal of Fluid Mechanics*, 780:226–273.

[71] Gamble, E., Terrell, D., and DeFrancesco, R. (2004). Nozzle selection and design criteria. In *40th AIAA/ASME/SAE/ASEE Joint Propulsion Conference and Exhibit*, page 3923.

[72] Garnier, E., Adams, N., and Sagaut, P. (2009). *Large eddy simulation for compressible flows*. Springer Science & Business Media.

[73] Gerlinger, P., Nold, K., and Aigner, M. (2010). Influence of reaction mechanisms, grid spacing, and inflow conditions on the numerical simulation of lifted supersonic flames. *International Journal for Numerical Methods in Fluids*, 62(12):1357–1380.

[74] Glowinski, R., Pan, T., Wells Jr, R. O., and Zhou, X. (1996). Wavelet and finite element solutions for the Neumann problem using fictitious domains. *Journal of Computational Physics*, 126(1):40–51.

[75] Gomet, L., Robin, V., and Mura, A. (2015). A multiple-inlet mixture fraction model for nonpremixed combustion. *Combustion and Flame*, 162(3):668–687.

[76] Gottlieb, S. and Shu, C. (1998). Total variation diminishing Runge-Kutta schemes. *Mathematics of computation of the American Mathematical Society*, 67(221):73–85.

[77] Griffiths, A. D. (2005). *Development and demonstration of a diode laser sensor for a scramjet combustor*. PhD thesis, The Australian National University.

[78] Heiser, W. H. and Pratt, D. T. (1994). *Hypersonic airbreathing propulsion*. AIAA.

[79] Hindmarsh, A. C., Brown, P. N., Grant, K. E., Lee, S. L., Serban, R., Shumaker, D. E., and Woodward, C. S. (2005). Sundials: Suite of nonlinear and differential/algebraic equation solvers. *ACM Transactions on Mathematical Software (TOMS)*, 31(3):363–396.

[80] Hindmarsh, A. C. and Serban, R. (2002). User documentation for cvodes, an ode solver with sensitivity analysis capabilities. *Livermore (California): Lawrence Livermore National Laboratory*, 189.

[81] Hirschfelder, J. and Curtiss, C. (1949). The theory of flame propagation. *The Journal of Chemical Physics*, 17(11):1076–1081.

[82] Hoeger, T. C. (2012). *CFD transient simulation of an isolator shock train in a scramjet engine*. PhD thesis, Air Force Institute of Technology Wright-Patterson AFB OH School of Engineering and Management.

[83] Huang, W., Luo, S.-B., Pourkashanian, M., Ma, L., Ingham, D. B., Liu, J., and Wang, Z.-G. (2010a). Numerical simulations of a typical hydrogen fueled scramjet combustor with a cavity flameholder. In *2010 International Conference of Mechanical Engineering, London, UK*.

[84] Huang, W., Qin, H., Luo, S.-B., and Wang, Z.-G. (2010b). Research status of key techniques for shock-induced combustion ramjet (scramjet) engine. *Science in China Series E: Technological Sciences*, 53(1):220–226.

[85] Huang, W. and Wang, Z.-G. (2009). Numerical study of attack angle characteristics for integrated hypersonic vehicle. *Applied Mathematics and Mechanics*, 30(6):779–786.

[86] Huang, W., Wang, Z.-G., Luo, S.-B., Liu, J., Xia, Z.-X., Lei, J., Jin, L., Wang, Z.-W., Pourkashanian, M., Ma, L., et al. (2011). Overview of fuel injection techniques for scramjet engines. In *ASME 2011 Turbo Expo: Turbine Technical Conference and Exposition*, pages 17–24. American Society of Mechanical Engineers.

[87] Huang, W., Wang, Z.-G., Pourkashanian, M., Ma, L., Ingham, D. B., Luo, S.-b., and Liu, J. (2010c). Hydrogen fueled scramjet combustor - the impact of fuel injection. In *Fuel Injection*. InTech.

[88] Huzel, D. K. and Huang, D. H. (1971). Design of liquid propellant rocket engines. NASA SP-125. *NASA Special Publication*, 125.

[89] Iaccarino, G. and Verzicco, R. (2003). Immersed boundary technique for turbulent flow simulations. *Applied Mechanics Reviews*, 56(3):331–347.

[90] Izard, J.-F. (2009). *Contribution à la modélisation de la combustion non-prémélangée turbulente dans les écoulements rapides*. PhD thesis, ISAE-ENSMA Ecole Nationale Supérieure de Mécanique et d'Aérotechique-Poitiers.

[91] Javaid, K. H. and Serghides, V. C. (2005). Airframe-propulsion integration methodology for waverider-derived hypersonic cruise aircraft design concepts. *Journal of Spacecraft and Rockets*, 42(4):663–671.

[92] Kee, R. J., Dixon-Lewis, G., Warnatz, J., Coltrin, M. E., and Miller, J. A. (1986). A fortran computer code package for the evaluation of gas-phase multicomponent transport properties. *Sandia National Laboratories Report SAND86-8246*, 13:80401–1887.

[93] Kemenov, K. A., Wang, H., and Pope, S. B. (2012). Modelling effects of subgrid-scale mixture fraction variance in LES of a piloted diffusion flame. *Combustion Theory and Modelling*, 16(4):611–638.

[94] Khadra, K., Angot, P., Parneix, S., and Caltagirone, J.-P. (2000). Fictitious domain approach for numerical modelling of navier–stokes equations. *International Journal for Numerical Methods in Fluids*, 34(8):651–684.

[95] Kim, K. M., Baek, S. W., and Han, C. Y. (2004). Numerical study on supersonic combustion with cavity-based fuel injection. *International Journal of Heat and Mass Transfer*, 47(2):271–286.

[96] Kim, S. D., Seo, J. I., and Song, D. J. (2007). A computational analysis of unsteady transonic/supersonic flows over backward facing step in air jet nozzle. *Journal of Mechanical Science and Technology*, 21(2):336–347.

[97] Kline, S. J., Reynolds, W. C., Schraub, F., and Runstadler, P. (1967). The structure of turbulent boundary layers. *Journal of Fluid Mechanics*, 30(4):741–773.

[98] Kloesel, K. J., Ratnayake, N. A., and Clark, C. M. (2011). A technology pathway for airbreathing, combined-cycle, horizontal space launch through SR–71 based trajectory modeling. In *17th AIAA International Space Planes and Hypersonic Systems and Technologies Conference, San Francisco, CA*. AIAA Paper 2011–2229.

[99] Kuentzmann, P. and Falempin, F. (2002). *Ramjet, Scramjet & PDE - An Introduction*. Available at: `https://www.onera.fr/sites/default/files/ressources_documentaires/cours-exposes-conf/ramjet-scramjet-and-pde-an-introduction.pdf`.

[100] Lawson, S. and Barakos, G. (2011). Review of numerical simulations for high-speed, turbulent cavity flows. *Progress in Aerospace Sciences*, 47(3):186–216.

[101] Le, D. B. (2005). Scramjet isolator flow studies. 2005 Virginia Space Grant Consortium (VSGC) Student Research Conference, Newport News - VA.

[102] Leduc, R. (1935). French patent no. 439,805.

[103] Leduc, R. (1957). Early work and latest realizations with ramjet engines. *Journal of Jet Propulsion*, 27(1):65–67.

[104] Liñán, A. (1974). The asymptotic structure of counterflow diffusion flames for large activation energies. *Acta Astronautica*, 1(7-8):1007–1039.

[105] Liu, C., Zhao, Y., Wang, Z., Wang, H., and Sun, M. (2017). Dynamics and mixing mechanism of transverse jet injection into a supersonic combustor with cavity flameholder. *Acta Astronautica*, 136:90–100.

[106] Lorin, R. (1908). Le propulseur à échappement et l'aéroplane à grande vitesse. *L'Aérophile*, pages 332–336.

[107] Luo, K. and Bray, K. (1998). Combustion-induced pressure effects in supersonic diffusion flames. In *Symposium (International) on Combustion*, volume 27(2), pages 2165–2171. Elsevier.

[108] Mahoney, J. J. (1990). *Inlets for supersonic missiles*. The American Institute of Aeronautics and Astronautics.

[109] Majumdar, D. (2012). *X-51A waverider test flight ends in failure*. Flight Global. Available at: `https://www.flightglobal.com/news/articles/x-51a-waverider-test-flight-ends-in-failure-375529`.

[110] Manna, P. and Chakraborty, D. (2005). Numerical investigation of transverse sonic injection in a non-reacting supersonic combustor. *Proceedings of the Institution of Mechanical Engineers, Part G: Journal of Aerospace Engineering*, 219(3):205–215.

[111] Martínez-Ferrer, P. J. (2013). *Etude par simulation numérique de l'auto-allumage en écoulement turbulent cisaillé supersonique*. PhD thesis, ISAE-ENSMA École Nationale Supérieure de Mécanique et d'Aérotechique - Poitiers.

[112] Martínez-Ferrer, P. J., Buttay, R., Lehnasch, G., and Mura, A. (2014). A detailed verification procedure for compressible reactive multicomponent Navier–Stokes solvers. *Computers & Fluids*, 89:88–110.

[113] Martínez-Ferrer, P. J., Lehnasch, G., and Mura, A. (2017). Compressibility and heat release effects in high-speed reactive mixing layers II: Structure of the stabilization zone and modeling issues relevant to turbulent combustion in supersonic flows. *Combustion and Flame*, 180:304–320.

[114] McBride, B. J., Zehe, M. J., and Gordon, S. (2002). *NASA Glenn coefficients for calculating thermodynamic properties of individual species*. NASA Glenn Research Center. Available at: `https://www.grc.nasa.gov/WWW/CEAWeb/TP-2002-21556.htm`.

[115] Micka, D. and Driscoll, J. (2008). Dual-mode combustion of a jet in cross-flow with cavity flameholder. In *46th AIAA Aerospace Sciences Meeting and Exhibit*, page 1062.

[116] Micka, D. J. (2010). *Combustion stabilization, structure, and spreading in a laboratory dual-mode scramjet combustor*. PhD thesis, University of Michigan.

[117] Micka, D. J. and Driscoll, J. F. (2009). Combustion characteristics of a dual-mode scramjet combustor with cavity flameholder. *Proceedings of the Combustion Institute*, 32(2):2397–2404.

[118] Möbus, H., Gerlinger, P., and Brüggemann, D. (2001). Comparison of Eulerian and Lagrangian Monte Carlo PDF methods for turbulent diffusion flames. *Combustion and Flame*, 124(3):519–534.

[119] Möbus, H., Gerlinger, P., and Brüggemann, D. (2003). Scalar and joint scalar-velocity-frequency Monte Carlo PDF simulation of supersonic combustion. *Combustion and Flame*, 132(1-2):3–24.

[120] Mohd-Yusof, J. (1997). Combined immersed-boundary/B–spline methods for simulations of flow in complex geometries. *Annual Research Briefs*, 317.

[121] Moses, P. L., Rausch, V. L., Nguyen, L. T., and Hill, J. R. (2004). Nasa hypersonic flight demonstratorsoverview, status, and future plans. *Acta Astronautica*, 55(3-9):619–630.

[122] Moule, Y. (2013). *Modélisation et Simulation de la Combustion dans les Écoulements Rapides: Applications aux Superstatoréacteurs*. PhD thesis, ISAE-ENSMA Ecole Nationale Supérieure de Mécanique et d'Aérotechique-Poitiers.

[123] Moule, Y., Sabelnikov, V., and Mura, A. (2014a). Highly resolved numerical simulation of combustion in supersonic hydrogen–air coflowing jets. *Combustion and Flame*, 161(10):2647–2668.

[124] Moule, Y., Sabelnikov, V., Mura, A., and Smart, M. (2014b). Computational fluid dynamics investigation of a Mach 12 scramjet engine. *Journal of Propulsion and Power*, 30(2):461–473.

[125] Moule, Y. and Smart, M. (2013). Performance analysis of a Mach 12 scramjet at off-design conditions. *Journal of Propulsion and Power*, 29(1):282–285.

[126] Moura, G. S. (2007). Análise teórica e experimental do desempenho de um estatoreator a combustível sólido utilizando polibutadieno hidroxilado. Master's thesis, Instituto Nacional de Pesquisas Espaciais, São José dos Campos, SP, Brazil.

[127] Musée Air + Espace - Paris Le Bourget (2018). *Griffon II aircraft*. Available at: `https://www.museeairespace.fr/wp-content/uploads/sites/2/cache/2015/06/H_griffon2_1_/1175681215.jpg`.

[128] NASA (1990). *Armstrong Flight Research Center: NASA Dryden SR-71 Photo Collection*. Available at: https://www.dfrc.nasa.gov/Gallery/Photo/SR-71/HTML/EC90-0096-2.html.

[129] NASA (2008). *Langley Research Center: How scramjets work*. Available at: https://www.nasa.gov/centers/langley/news/factsheets/X43A_2006_5.html.

[130] NASA (2010). *X-51A makes longest scramjet flight*. Available at: https://www.nasa.gov/topics/aeronautics/features/X-51A.html.

[131] NASA (2014). *Glenn Learning Technologies Project: Inlets*. Available at: https://www.grc.nasa.gov/www/k-12/BGP/inlet.html.

[132] NASA (2015). *Glenn Learning Technologies Project: Ramjet engines*. Available at: https://www.grc.nasa.gov/www/K-12/airplane/rampart.html.

[133] NASA (2016). *X-43A (Hyper-X)*. Available at: https://www.nasa.gov/centers/armstrong/history/experimental_aircraft/X-43A.html.

[134] NASA (2017). *Rockwall X-30*. Available at: https://www.nasa.gov/centers/armstrong/history/experimental_aircraft/X-30.html.

[135] Nicoud, F. and Ducros, F. (1999). Subgrid-scale stress modelling based on the square of the velocity gradient tensor. *Flow, Turbulence and Combustion*, 62(3):183–200.

[136] O'Conaire, M., Curran, H. J., Simmie, J. M., Pitz, W. J., and Westbrook, C. K. (2004). A comprehensive modeling study of hydrogen oxidation. *International Journal of Chemical Kinetics*, 36(11):603–622.

[137] Orloff, B. S. (2006). A comparative analysis of single-stage-to-orbit rocket and air-breathing vehicles. Master's thesis, Air Force Institute of Technology Wright-Patterson AFB OH Department of Aeronautics and Astronautics.

[138] Peskin, C. S. (1972). Flow patterns around heart valves: a numerical method. *Journal of Computational Physics*, 10(2):252–271.

[139] Peskin, C. S. (1977). Numerical analysis of blood flow in the heart. *Journal of Computational Physics*, 25(3):220–252.

[140] Peskin, C. S. (2002). The immersed boundary method. *Acta Numerica*, 11:479–517.

[141] Peters, N. (2000). *Turbulent Combustion*. Cambridge University Press.

[142] Piomelli, U. and Balaras, E. (2002). Wall-layer models for large-eddy simulations. *Annual Review of Fluid Mechanics*, 34(1):349–374.

[143] Piomelli, U. and Chasnov, J. R. (1996). Large-eddy simulations: Theory and applications. In *Turbulence and Transition Modelling*, pages 269–336. Springer.

[144] Poinsot, T. and Veynante, D. (2005). *Theoretical and numerical combustion*. RT Edwards, Inc.

[145] Pope, S. B. (2004). Ten questions concerning the large-eddy simulation of turbulent flows. *New Journal of Physics*, 6(1). p. 35.

[146] Porto, B. F. (2007). Teoria, metodologia de projeto e desenvolvimento de motores foguete a propelente sólido e foguetes experimentais. Bacherlor's thesis, Pontifícia Universidade Católica do Paraná, Curitiba, PR, Brazil.

[147] Quinlan, J., McDaniel, J. C., Drozda, T. G., Lacaze, G., and Oefelein, J. C. (2014). A priori analysis of flamelet-based modeling for a dual-mode scramjet combustor. In *50th AIAA/ASME/SAE/ASEE Joint Propulsion Conference*. AIAA Paper 2014–3743.

[148] Ragab, S., Sheen, S.-C., and Sreedhar, M. (1992). An investigation of finite-difference methods for large-eddy simulation of a mixing layer. In *30th Aerospace Sciences Meeting and Exhibit*. AIAA Paper 1992–554.

[149] Reaction Engines (2018). *Synergetic Air-Breathing Rocket Engine*. Available at: `https://www.reactionengines.co.uk/sabre`.

[150] Ribeiro, F. H., Boukharfane, R., Robin, V., and Mura, A. (2018). Numerical study of combustion stabilization in a scramjet engine model with cavity flameholder. *Proceedings of the 10th International Conference on Computational Fluid Dynamics, Barcelona*.

[151] Rice, T. and Cybyk, B. (2003). High aspect ratio isolator performance for access-to-space vehicles. *12th AIAA International Space Planes and Hypersonic Systems and Technologies*, page 7041. AIAA Paper 2003–7041.

[152] Rogallo, R. S. and Moin, P. (1984). Numerical simulation of turbulent flows. *Annual Review of Fluid Mechanics*, 16(1):99–137.

[153] Rosenberg, Z. (2012). *August failure of Boeing X-51 likely due to fin, resonance*. Flight Global. Available at: `https://www.flightglobal.com/news/articles/august-failure-of-boeing-x-51-likely-due-to-fin-resonance-378080`.

[154] Rosenberg, Z. (2013). *Hypersonic X-51 programme ends in success*. Flight Global. Available at: `https://www.flightglobal.com/news/articles/hypersonic-x-51-programme-ends-in-success-385481`.

[155] Sabelnikov, V., Deshaies, B., and da Silva, L. F. F. (1998). Revisited flamelet model for nonpremixed combustion in supersonic turbulent flows. *Combustion and Flame*, 114(3-4):577–584.

[156] Sabelnikov, V. and Fureby, C. (2013). LES combustion modeling for high Re flames using a multi-phase analogy. *Combustion and Flame*, 160(1):83–96.

[157] Schlichting, H. and Gersten, K. (2016). *Boundary-layer theory*. Springer.

[158] Science Learning Hub (2015). *Ramjet operation*. Available at: `https://www.sciencelearn.org.nz/resources/393-types-of-chemical-rocket-engines`.

[159] Segal, C. (2009). *The scramjet engine: processes and characteristics*, volume 25. Cambridge University Press.

[160] Serre, L. (1999). Towards a low risk airbreathing ssto program-a continuous robust prepha based tsto. In *9th International Space Planes and Hypersonic Systems and Technologies Conference*. AIAA Paper 1999–4946.

[161] Shterev, K. and Stefanov, S. (2008). Finite volume calculations of gaseous slip flow past a confined square in a two-dimensional microchannel. In *Proceedings of the 1st European Conference on Microfluidics, La Societé Hydrotechnique de France*.

[162] Silva, A. L. E., Silveira-Neto, A., and Damasceno, J. (2003). Numerical simulation of two-dimensional flows over a circular cylinder using the immersed boundary method. *Journal of Computational Physics*, 189(2):351–370.

[163] Smart, M. (2008). Scramjets. Technical report, RTO-EN-AVT-150-09.

[164] Smart, M. K. (2010). Scramjet isolators. Technical report, RTO-EN-AVT-185-10.

[165] Sod, G. A. (1978). A survey of several finite difference methods for systems of nonlinear hyperbolic conservation laws. *Journal of Computational Physics*, 27(1):1–31.

[166] Spanier, E. H. (1989). *Algebraic topology*, volume 55(1). Springer Science & Business Media.

[167] Sportisse, B. (2000). An analysis of operator splitting techniques in the stiff case. *Journal of Computational Physics*, 161(1):140–168.

[168] Sreenivasan, K. (2004). Possible effects of small-scale intermittency in turbulent reacting flows. *Flow, Turbulence and Combustion*, 72(2-4):115–131.

[169] Strikwerda, J. C. (2004). *Finite difference schemes and partial differential equations*, volume 88. Society for Industrial and Applied Mathematics.

[170] Stull, D. and Prophet, H. (1971). JANAF thermodynamic tables. *National Standard Reference Data Series, National Bureau of Standards, Washington, DC*.

[171] Suraweera, M. V. and Smart, M. K. (2009). Shock-tunnel experiments with a Mach 12 rectangular-to-elliptical shape-transition scramjet at offdesign conditions. *Journal of Propulsion and Power*, 25(3):555–564.

[172] Swithenbank, J. (1967). Hypersonic air-breathing propulsion. *Progress in Aerospace Sciences*, 8:229–294.

[173] Takahashi, S., Yamano, G., Wakai, K., Tsue, M., and Kono, M. (2000). Self-ignition and transition to flame-holding in a rectangular scramjet combustor with a backward step. *Proceedings of the Combustion Institute*, 28(1):705–712.

[174] Techer, A. (2017). *Simulation aux grandes échelles implicite et explicite de la combustion supersonique*. PhD thesis, ISAE-ENSMA Ecole Nationale Supérieure de Mécanique et d'Aérotechique-Poitiers.

[175] Techer, A., Moule, Y., Lehnasch, G., and Mura, A. (2018). Mixing of fuel jet in supersonic crossflow: Estimation of subgrid-scale scalar fluctuations. *AIAA Journal*, pages 465–481.

[176] Torrez, S., Scholten, N., Micka, D., Driscoll, J., Bolender, M., Doman, D., and Oppenheimer, M. (2008). A scramjet engine model including effects of precombustion shocks and dissociation. In *44th AIAA/ASME/SAE/ASEE Joint Propulsion Conference & Exhibit*, page 4619. AIAA Paper 2008-4619.

[177] Tseng, Y.-H. and Ferziger, J. H. (2003). A ghost-cell immersed boundary method for flow in complex geometry. *Journal of Computational Physics*, 192(2):593–623.

[178] University of Queensland (2016). *Hypersonic flight on the horizon*. Available at: `https://www.eait.uq.edu.au/hypersonic-flight-horizon`.

[179] University of Texas at Arlington (2014). *Specific impulse for various propulsion systems*. Available at: `https://arc.uta.edu/research/pde_files/IspvsM.jpg`.

[180] Van Wie, D. M. (2000). Scramjet inlets. *Scramjet propulsion*, 189:447–511.

[181] Veynante, D. and Knikker, R. (2006). Comparison between les results and experimental data in reacting flows. *Journal of turbulence*, 7:N35.

[182] Weber, R. J. and MacKay, J. S. (1958). An analysis of ramjet engines using supersonic combustion. Technical report, NACA TN 4386.

[183] White, F. M. and Corfield, I. (2006). *Viscous fluid flow*, volume 3. McGraw-Hill New York.

[184] Wikimedia Commons (2013). *Liquid fuel rocket schematic*. Available at: `https://commons.wikimedia.org/wiki/File:LiquidFuelRocketSchematic.jpg`.

[185] Williams, F. (2000). Progress in knowledge of flamelet structure and extinction. *Progress in Energy and Combustion Science*, 26(4-6):657–682.

[186] Woodward, P. R., Porter, D. H., Sytine, I., Anderson, S., Mirin, A. A., Curtis, B., Cohen, R. H., Dannevik, W. P., Dimits, A. M., Eliason, D. E., Winkler, K.-H., and Hodson, S. W. (2001). Very high resolution simulations of compressible, turbulent flows. In *Computational Fluid Dynamics*, pages 3–15. World Scientific.

[187] Ye, T., Mittal, R., Udaykumar, H., and Shyy, W. (1999). An accurate cartesian grid method for viscous incompressible flows with complex immersed boundaries. *Journal of Computational Physics*, 156(2):209–240.

[188] Yoo, C. S., Sankaran, R., and Chen, J. (2009). Three-dimensional direct numerical simulation of a turbulent lifted hydrogen jet flame in heated coflow: flame stabilization and structure. *Journal of Fluid Mechanics*, 640:453–481.

[189] Yoshizawa, A. (1986). Statistical theory for compressible turbulent shear flows, with the application to subgrid modeling. *Physics of Fluids*, 29:2152–2164.

[190] Zabetakis, M. G. (1965). Flammability characteristics of combustible gases and vapors. Technical report, Bureau of Mines, Washington DC.

[191] Zhao, Z., Song, W., YL, X., and JL, L. (2009). An experimental investigation of the cold flowfield in a model scramjet combustor. *Proceedings of the Institution of Mechanical Engineers, Part G: Journal of Aerospace Engineering*, 223(4):425–431.

Simulation numérique de la combustion turbulente dans des situations génériques représentatives de la propulsion d'un super-statoréacteur (scramjet)

Fábio Henrique Eugênio Ribeiro

1 Introduction

L'évolution des moyens de transport à très grandes vitesses dépend fortement du développement d'une composante essentielle : la chambre de combustion. Au sein de la classe de propulsion chimique bipropellante, les moteurs qui suscitent le plus de développement et qui sont les plus utilisés sont les fusées à propulsion solide et à propulsion liquide. Ce dernier mode de propulsion nécessite une technologie plus avancée que dans le cas de la propulsion solide [21].

L'intérêt pour les véhicules hypersoniques réside dans la promesse d'un type de véhicule doté de moteurs aérobies (*airbreathing*) capable de déployer une charge utile en orbite terrestre et qui puisse être réutilisable. Les super-statoréacteurs à combustion supersonique (scramjet) font actuellement partie des moteurs aérobies les plus prometteurs pour la propulsion de ce type de véhicule. La chambre de combustion est traversée par un écoulement supersonique qui réduit considérablement le temps de séjour disponible afin de : (i) réaliser l'injection du carburant, (ii) mélanger le combustible et l'air, et (iii) procéder à l'allumage puis à la combustion du mélange.

Plus de la moitié de la masse d'un véhicule-fusée est associée à l'oxydant, tandis qu'un véhicule avec moteur aérobie peut supporter une charge utile supplémentaire de 11%, comme indiqué dans le tableau 1.

Fraction de masse au décollage	**Avion**	**Fusée**
Charge utile	15%	4%
Carburant	30%	24%
Oxyène	0%	65%
Autre	55%	7%

Tableau 1 – Répartion typique de la fraction de masse au décollage des aéronefs actuels et des systèmes de transport de fusée multi-usage [21]

Bertin et Cummings [6] distinguent au moins trois types de missions qui nécessitent des véhicules hypersoniques :

1. Les attaques décisives au début des hostilités, par diminution de la capacité de combat adverse.
2. Les systèmes de défenses efficaces et la supériorité des armes en cas de conflit inévitable.
3. La réduction des coûts d'accès à l'espace.

En plus de son rôle déterminant concernant ces trois mission cruciales pour les forces militaires, cette technologie dispose également d'un fort potentiel dans les domaines civils et en particulier dans le domaine spatial pour réduire l'énergie nécessaire à la mise en orbite et permettre ainsi l'augmentation de la charge utile et la réduction des coûts, et dans le domaine aéronautique civil afin de réduire considérablement les temps de vol intercontinentaux.

Plusieurs concepts utilisant des super-statoréacteurs sont en cours de développement le monde, tels que X-43 and X-51 (États-Unis, figures 1a et 1b, respectivement), HIFiRE (Australie/États-Unis, figure 1c), LEA (France, figure 1d), SABRE (Angleterre, figure 1e) and 14-X (Brésil, figure 1f).

(a) X-43 [38]

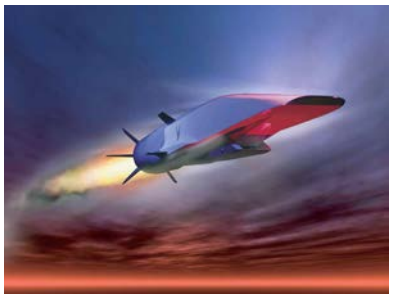

(b) X-51 [37]

(c) HIFiRE [54]

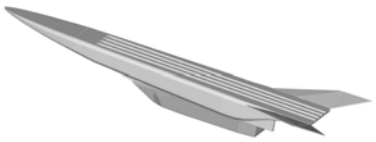

(d) LEA [16]

(e) SABRE [46]

(f) 14-X [19]

FIGURE 1 – Démonstrateurs de la technologie scramjet

L'optimisation de l'intégration du système de propulsion dans le véhicule devient obligatoire puisqu'un petit changement dans les paramètres de vol affecte de manière significative la performance du moteur.

Le manuscrit est organisé de la manière suivante, dans un premier temps, le super-statoréacteur est présenté en incluant sa conception historique, certains des programmes de recherche qui l'on amené à son état actuel de développement, de même que les caractéristiques du moteur et leurs rôles dans son fonctionnement. Ensuite, nous présentons

les équations générales utilisées en simulation, le solveur et ses caractéristiques. Nous abordons plus particulièrement les méthodes numériques, le filtrage `LES`, les conditions de fermetures et la validation du code. La méthode de frontières immergées (`IBM`) et le modèle de réacteur partiellement mélangé instationnaire (`U-PaSR`) sont également présentés et discutés. Enfin, la dernière partie de ce manuscrit est consacrée aux simulations d'un écoulement supersonique avec injection transversale d'hydrogène et une cavité. Les analyses de ces simulations portent sur l'écoulement turbulent, le développement de la combustion turbulente, le mécanisme de stabilisation de la combustion et les interactions chimie-turbulence.

L'objectif de cette thèse est de contribuer à l'étude numérique de l'allumage et de la combustion turbulente dans des situations génériques représentatives de la combustion dans les scramjets.

2 Développement du travail

La propulsion d'un aéronef au moyen d'un moteur à réaction a été envisagée en premier lieu par René Lorin, qui a déposé un brevet en 1908. Il a publié plusieurs articles dans la revue l'Aérophile entre 1908 et 1913, décrivant, à des fins d'utilisation comme systèmes de propulsion, les avantages de la conversion directe de l'énergie des produits de combustion en une forme cinétique (détente des gaz de combustion dans une tuyère) au lieu d'utiliser une forme mécanique comme intermédiaire (arbre mécanique relié à une hélice).

« *Il y aurait un grand avantage à pouvoir supprimer l'intermédiaire de la puissance mécanique. C'est ce que l'on obtient par l'emploi du propulseur à échappement* » (Lorin [27])

En 1913 il a publié un article décrivant le principe d'un propulsion, qu'on appellera plus tard statoréacteur, mais il a conclu que ce moteur ne conviendrait pas pour les vols subsoniques en raison des faibles niveaux de pression dynamique obtenus.

Maxime Guillaume, en 1921, résolut le problème des faibles performances du statoréacteur en suggérant l'utilisation de turburéacteurs pour augmenter la pression jusqu'à la valeur nécessaire à son fonctionnement.

Finalement, ce n'est qu'en 1935 que René Leduc a obtenu le brevet d'un avion à propulsion scramjet, qui devint l'avion expérimental `Leduc 010`, figure 2, dont le premier vol propulsé eut lieu le 21 avril 1949, atteignant Mach 0.84.

Au début des années 90, les études relatives à la propulsion par statoréacteurs ont repris et il en a résulté des missiles dotés de systèmes de propulsion mixte avancés.

Les statoréacteurs conviennent aux vols dont le nombre de Mach est compris entre 3 et 6 car la pression dynamique y est suffisante pour générer une poussée. Cependant, à des

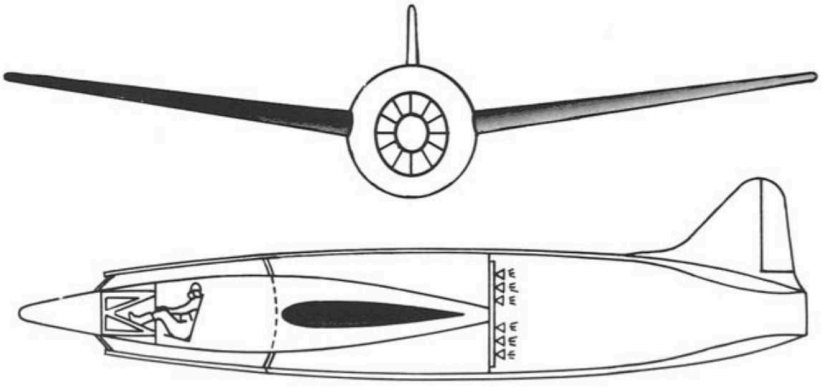

FIGURE 2 – Avion à propulsion ramjet de Leduc (reproduit du brevet français original) [26]

vitesses supersoniques, il n'est plus avantageux de réduire l'écoulement aux vitesses subsoniques et la combustion doit avoir lieu à des conditions supersoniques [21], là où la couche de cisaillement devient chimiquement réactive du fait de l'élévation de la température induite par le frottement de l'air sur le fuselage de l'avion [2].

Les super-statoréacteurs se différencient par une combustion, à l'intérieur du moteur, qui s'effectue à des vitesses supersoniques. Cela limite le ralentissement nécessaire de l'air extérieur et permet donc théoriquement d'atteindre des vitesses supérieures. Il a été étudié pour la première fois par Weber et MacKay [56] en 1958, qui analysaient la performance de combustion aux écoulements supersoniques visant à dépasser la limite de vitesse des statoréacteurs. Ses travaux sont toujours utilisées comme référence, sans beaucoup de changements.

Le super-statoréacteur est actuellement un moteur expérimental : les rares vols hypersoniques réalisés n'ont duré que quelques secondes, durant lesquelles l'appareil a simplement maintenu sa vitesse. Le programme le plus ambitieux impliquant des super-statoréacteurs était le NASP (*National Space Program*), dont le but était de développer l'avion `X-30` : un lanceur orbital monoétage capable de décoller et d'atterrir dans un aéroport conventionnel. Son système propulsif était composé de plusieurs cycles différents pour accélérer l'ensemble jusqu'à des vitesses hypersoniques. Malgré le développement fructueux des technologies nécessaires à la conception de la structure et de l'installation propulsive de l'appareil, il restait aux ingénieurs de nombreuses difficultés techniques à résoudre. Le programme a été abandonné en 1995 en raison de son coût élevé et son manque d'expertise technologique pour développer son moteur de base.

Les recherches se poursuivirent et aboutirent à la création du programme `Hyper X`, qui visait initialement à explorer les performances générales d'un moteur intégré à la structure du véhicule et capable de fonctionner comme un statoréacteur à des vitesse supersoniques et comme un super-statoréacteur à des vitesses hypersoniques. Dans le

cadre de ce programme, deux véhicules ont été développés et désignés : ce sont le `X-43` et le `X-51`.

Même si sa conception est simple, le super-statoréacteur doit faire face à des défis technologiques complexes. Le vol à grande vitesse dans l'atmosphère pose plusieurs problèmes structurels liés au chauffage aérodynamique et à la force de traînée du véhicule, imposant la nécessité de refroidir le véhicule et le moteur lors des opérations prolongées.

Dans un moteur scramjet l'écoulement est compressé en plusieurs étapes, en passant par des ondes de choc obliques générées par l'avant du véhicule et décélérant dans un conduit convergent-divergent. Contrairement au statoréacteur, l'écoulement est maintenu supersonique. Il convient de noter que ce type de moteur ne comporte aucune pièce mobile, car l'écoulement est comprimé par l'avant du véhicule, ce qui implique qu'il n'est pas nécessaire qu'il soit symétrique axialement suivante l'axe central.

Quand l'écoulement est décéléré, la vitesse relative et l'énergie cinétique diminuent, réapparaissant sous forme d'énergie interne, ce qui entraîne une augmentation significative de la pression, de la température et de la densité. Comme l'air reste très peu de temps entre l'entrée et la sortie du moteur (de l'ordre de quelques millisecondes), garantir le mélange entre le combustible et l'oxydant jusqu'à l'échelle moléculaire devient difficile. Cela impose également des complications pour la stabilité de la flamme, en raison des gradients intenses de composition et de température dans la région de la flamme.

La figure 3 présente le schéma d'un moteur scramjet, qui peut être divisé en 4 parties principales : admission, isolateur, chambre de combustion et tuyère d'échappement.

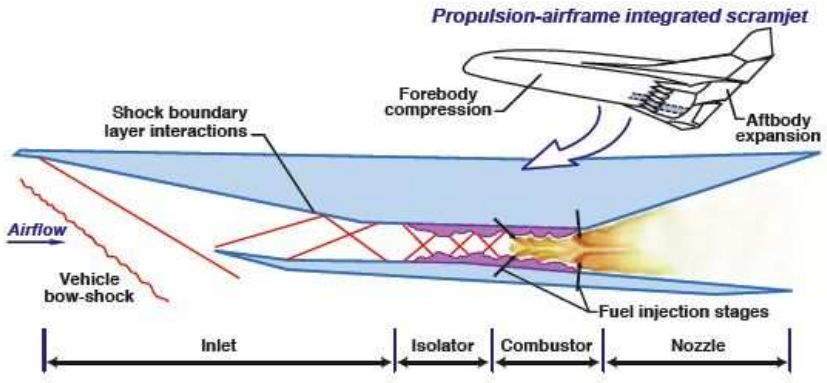

FIGURE 3 – Schéma de principe d'un super-statoréacteur [36]

L'intégration avec le système propulsif nécessite que l'avant du véhicule comprime l'air aspiré afin d'obtenir une pression et une température adéquates pour la combustion et d'optimiser la récupération de pression. L'admission doit pouvoir capter la quantité exacte d'air requise par le moteur pour le décélérer ensuite à la vitesse requise, sans distorsion d'écoulement ni perte de pression et en produisant le moins de traînée possible

[49, 55]. Sa conception est essentielle au bon fonctionnement du moteur, car il est le seul fournisseur de flux d'air et de compression. Il existe plusieurs types de géométrie pour l'admission, chacune avec ses avantages et ses inconvénients, et dont leur choix dépend des caractéristiques de la mission. Les types les plus courants sont :

- externe
- isentropique externe
- mixte
- symétrique interne
- paroi latérale mixte

Un moteur scramjet qui fonctionne dans le régime hypersonique inférieur est appelé scramjet bimode, où l'écoulement est caractérisé par des régions de régimes subsoniques et supersoniques dans la chambre de combustion. Il peut fonctionner de trois manières différentes : mode ram, mode scram précoce et mode scram tardif.

En mode ram, le moteur fonctionne comme un ramjet : l'air est comprimé et ralenti à un nombre de Mach subsonique par l'admission et les ondes de choc génèrent un train de choc de pré-combustion (`PCST`) qui peut séparer la couche limite de la surface du conduit de la chambre de combustion. Lorsque la vitesse atteint un nombre de Mach compris entre 5 et 7, le moteur fonctionne en mode scram précoce : la combustion est considérée supersonique, mais la combustion subsonique peut se produire près de la paroi. Enfin, lorsque le nombre de Mach est supérieur à 7, seule la combustion supersonique se produit et le moteur fonctionne dans ce que l'on appelle mode scram tardif : il n'y a pas de train de choc de pré-combustion puisque l'écoulement est complètement supersonique.

Afin de contenir ces trains de choc, un conduit court est ajouté à la voie de passage d'écoulement en amont de la chambre de combustion. Ce conduit s'appelle isolateur et évite aux trains de choc de perturber le fonctionnement de l'admission, en contribuant ainsi à maintenir un flux d'air stable dans la chambre de combustion.

Quel que soit le système de compression, l'écoulement doit être chauffé dans la chambre de combustion et la poussée est générée par l'accélération des produits de combustion dans une tuyère. La chambre de combustion est l'un des composants les plus critiques d'un moteur scramjet, car elle entraîne des phénomènes complexes tels que les effets de compressibilité, de dégagement de chaleur, de temps de séjour limité, d'interaction des chocs et le mélange turbulent. Les principaux défis de son développement sont liés à l'amélioration de l'efficacité du mélange et de la combustion pour des temps de séjour courts (ordre des millisecondes [22]) afin de stabiliser la flamme et de minimiser la perte de pression totale.

Au cours des dernières années, plusieurs techniques d'injection de carburant ont été proposées pour favoriser l'allumage et la stabilisation des processus de combustion [34],

telles que l'injection transversale de carburant à partir d'un orifice pariétal [28], l'injection inclinée et la cavité accroche-flamme [4].

Selon Ben-Yakar et Hanson [4], qui ont fait la synthèse des travaux en cours sur les cavités accroche-flamme, la magnitude du rapport longueur / profondeur (L/D) permet de caractériser l'écoulement dans une cavité suivant deux régimes différents : cavité ouverte ($L/D < 7-10$), lorsque la couche de cisaillement se rattache au bord de fuite en aval (fig. 4a), et cavité fermée ($L/D > 7-13$), lorsque la couche de cisaillement supérieure se rattache à la face de plancher (fig. 4b).

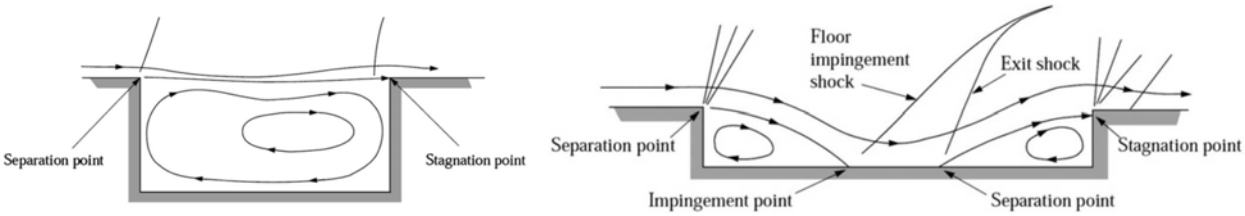

(a) Cavité ouverte

(b) Cavité fermée

FIGURE 4 – Régimes d'écoulement par cavité [25]

Une caractéristique de la technique de la stabilisation par cavité est qu'elle peut intégrer l'injection de carburant et la capacité de maintien de la combustion simultanément.

Enfin, la conception de la tuyère soulève plusieurs difficultés, telles que la détermination de la composition des produits de combustion, qui implique le calcul de la concentration de centaines d'espèces chimiques. Son objectif est de diriger et d'accélérer les produits de combustion afin de maximiser la vitesse à l'échappement, et cela se fait uniquement avec sa géométrie.

Le système d'équations reporté ci-dessous décrit un écoulement 3D, instationnaire, compressible, turbulent et visqueux composé de $\mathcal{N}_{sp}$ espèces réactives, où les forces volumiques et le transfert d'énergie par rayonnement sont supposées négligeables. Ce système de lois de conservation est basé sur les variables indépendantes suivantes (appelées aussi variables conservées) : la densité ρ, les quantités de mouvement ρu_i, l'énergie spécifique totale pondérée par la densité ρe_t et les fractions massiques d'espèces pondérées par la densité ρY_α.

$$\frac{\partial \rho}{\partial t} + \frac{\partial \rho u_i}{\partial x_i} = 0 \tag{1}$$

$$\frac{\partial \rho u_i}{\partial t} + \frac{\partial \rho u_i u_j}{\partial x_j} = -\frac{\partial p}{\partial x_i} + \frac{\partial \tau_{ij}}{\partial x_j} \tag{2}$$

$$\frac{\partial \rho e_t}{\partial t} + \frac{\partial \rho e_t u_i}{\partial x_i} = -\frac{\partial p u_i}{\partial x_i} - \frac{\partial q_i}{\partial x_i} + \frac{\partial u_i \tau_{ij}}{\partial x_j} \tag{3}$$

$$\frac{\partial \rho Y_\alpha}{\partial t} + \frac{\partial \rho Y_\alpha u_i}{\partial x_i} = -\frac{\partial J_{\alpha i}}{\partial x_i} + \rho \dot{\omega}_\alpha \quad , \quad \alpha = 1, \ldots, \mathcal{N}_{sp} \tag{4}$$

La première équation du modèle de Navier-Stokes (eq. 1) traduit la conservation de la masse du mélange. Les trois équations suivantes (représenté par eq. 2) traduisent la variation de la quantité de mouvement d'un système physique due aux forces auxquelles il est soumis. Le premier principe de la thermodynamique, i.e. la variation de l'énergie totale d'un système physique due à la somme des travaux de toutes les forces appliquées à ce système est représenté par l'équation 3. L'équation restante (équation 4) traduit la conservation des espèces. La densité ρ et la pression p sont reliées à la température T par l'équation d'état relative au mélange de gaz idéaux :

$$p = \frac{\rho \mathcal{R} T}{\mathcal{W}} \tag{5}$$

où $\mathcal{R} = 8.314\ {}^{J}/_{\text{mol·K}}$ est la constante universelle des gaz parfaits et

$$\mathcal{W} = \sum_{\alpha=1}^{\mathcal{N}_{sp}} X_\alpha \mathcal{W}_\alpha = \left(\sum_{\alpha=1}^{\mathcal{N}_{sp}} \frac{Y_\alpha}{\mathcal{W}_\alpha} \right)^{-1} \tag{6}$$

est la masse molaire du mélange, calculée à partir des masses molaires de chaque espèce $\mathcal{W}_\alpha$ et leur fractions molaires ou massiques, X_α ou Y_α, respectivement.

Le tenseur des contraintes visqueuses, en considérant un fluide newtonien, est donnée par

$$\tau_{ij} = \kappa S_{kk} \delta_{ij} + 2\mu \left(S_{ij} - \frac{1}{3} S_{kk} \delta_{ij} \right) \tag{7}$$

où κ est la viscosité volumique (*bulk viscosity*) et μ est la viscosité dynamique, $S_{ij} = {}^{1}/_{2} \left({}^{\partial u_i}/_{\partial x_j} + {}^{\partial u_j}/_{\partial x_i} \right)$ est la partie symétrique du tenseur de taux de déformation et δ_{ij} est le symbole de Kronecker.

Les flux de diffusion d'espèces est donnée par

$$J_{\alpha i} = \rho Y_\alpha V_{\alpha i} \tag{8a}$$

$$= -\sum_{\beta=1}^{\mathcal{N}_{sp}} \left(\rho \mathring{D}_{\alpha\beta} d_{\beta i} \right) - \rho Y_\alpha \theta_\alpha \frac{\partial \ln T}{\partial x_i} \tag{8b}$$

$$= -\sum_{\beta=1}^{\mathcal{N}_{sp}} \rho \mathring{D}_{\alpha\beta} \Bigg[\underbrace{\frac{\partial X_\beta}{\partial x_i}}_{(I)} + \underbrace{\left(X_\beta - Y_\beta \right) \frac{\partial \ln p}{\partial x_i}}_{(II)} \Bigg] - \underbrace{\rho Y_\alpha \theta_\alpha \frac{\partial \ln T}{\partial x_i}}_{(III)} \tag{8c}$$

où $d_{\beta i}$ est le vecteur de diffusion, $\mathring{D}_{\alpha\beta} = Y_\alpha D_{\alpha\beta}$ est le coefficient du flux de diffusion, $\mathring{\mathcal{X}}_\alpha = {}^{\mathcal{X}_\alpha}/_{X_\alpha}$ est le rapport de la diffusion thermique normalisé, et θ_α est le coefficient de diffusion thermique de l'espèce α.

Le flux de chaleur peut s'exprimer comme

$$q_i = -\underbrace{\lambda \frac{\partial T}{\partial x_i}}_{(I)} + \sum_{\alpha=1}^{\mathcal{N}_{sp}} J_{\alpha i} \left(\underbrace{h_\alpha}_{(II)} + \underbrace{\frac{RT\mathring{\mathcal{X}}_\alpha}{\mathcal{W}_\alpha}}_{(III)} \right) \tag{9}$$

avec λ la conductivité thermique du mélange.

Les énergies spécifiques totale et internet de l'écoulement sont reliées par l'équation

$$e_t = e + \frac{1}{2} u_i u_i \tag{10}$$

où $e = h - {}^{p}/_{\rho}$. L'enthalpie spécifique du mélange est obtenue à partir de la somme pondérée des enthalpies de chaque espèce par la fraction massique correspondante

$$h = \sum_{\alpha=1}^{\mathcal{N}_{sp}} Y_\alpha h_\alpha \tag{11}$$

La même procédure est utilisée pour retrouver la chaleur spécifique à pression constante du mélange

$$c_{p\alpha}(T) = \frac{\mathcal{R}}{\mathcal{W}_\alpha} \left(a_{1\alpha} + a_{2\alpha} T + a_{3\alpha} T^2 + a_{4\alpha} T^3 + a_{5\alpha} T^4 \right) \tag{12}$$

tandis que la chaleur spécifique à volume constant du mélange est donnée par la relation

$$c_v = c_p - \frac{\mathcal{R}}{\mathcal{W}} \tag{13}$$

Finalement, le taux de dégagement de chaleur est calculé comme

$$\dot{\omega}_T = -\sum_{\alpha=1}^{\mathcal{N}_{sp}} \Delta h^0_{f\alpha} \dot{\omega}_\alpha \tag{14}$$

Ces différentes loi de conservation et de comportement ont été implémentées, testées et étudiées avec le solveur `CREAMS` [11, 29].

Afin de séparer les petites échelles de turbulence des plus grandes, un filtre spatial doit être utilisé. L'opérateur de filtrage de Favre [17] permet de décomposer les termes non linéaires impliquant la masse volumique en une partie résolue (filtrée) et une partie non résolue dite de sous-maille (`SGS`) :

$$\widetilde{\phi} = \frac{\overline{\rho\phi}}{\bar{\rho}} \tag{15}$$

En conséquence, les équations filtrées de masse, de quantité de mouvement, de l'énergie et de conservation des espèces se déduisent facilement et s'écrivent

$$\frac{\partial \bar{\rho}}{\partial t} + \frac{\partial \bar{\rho} \widetilde{u}_i}{\partial x_i} = 0 \tag{16}$$

$$\frac{\partial \bar{\rho}\widetilde{u}_i}{\partial t} + \frac{\partial \bar{\rho}\widetilde{u}_i\widetilde{u}_j}{\partial x_j} = -\frac{\partial \bar{p}}{\partial x_i} + \frac{\partial \check{\tau}_{ij}}{\partial x_j} - \frac{\partial \tau_{ij}^{sgs}}{\partial x_j} + \frac{\partial}{\partial x_j}\left(\bar{\tau}_{ij} - \check{\tau}_{ij}\right) \tag{17}$$

$$\frac{\partial \bar{\rho}\widetilde{e}_t}{\partial t} + \frac{\partial \bar{\rho}\widetilde{e}_t\widetilde{u}_j}{\partial x_j} = -\frac{\partial \bar{p}\widetilde{u}_j}{\partial x_j} + \frac{\partial \check{\tau}_{ij}\widetilde{u}_i}{\partial x_j} - \frac{\partial \check{q}_j}{\partial x_j} - \frac{\partial \mathcal{L}_j^A}{\partial x_j} + B_6 - B_7 \tag{18}$$

$$\frac{\partial \bar{\rho}\widetilde{Y}_\alpha}{\partial t} + \frac{\partial \bar{\rho}\widetilde{Y}_\alpha\widetilde{u}_i}{\partial x_i} = -\frac{\partial \check{J}_{\alpha i}}{\partial x_i} - \frac{\partial J_{\alpha i}^{sgs}}{\partial x_i} - \frac{\partial}{\partial x_i}\left(\bar{J}_{\alpha i} - \check{J}_{\alpha i}\right) + \bar{\rho}\widetilde{\dot{\omega}}_\alpha \quad , \quad \alpha = 1, \ldots, \mathcal{N}_{sp} \tag{19}$$

On considère l'approximation suivante de la loi d'état filtrée

$$\bar{p} = \frac{\bar{\rho}\mathcal{R}\widetilde{T}}{\widetilde{\mathcal{W}}} \tag{20}$$

ainsi que celle décrivant le mélange, sachant que $\widetilde{X}_\alpha\mathcal{W}_\alpha \approx \widetilde{Y}_\alpha\widetilde{W}$

$$\widetilde{\mathcal{W}} = \left(\sum_{\alpha=1}^{\mathcal{N}_{sp}} \frac{\widetilde{Y}_\alpha}{\mathcal{W}_\alpha}\right)^{-1} \tag{21}$$

La formulation pour l'équation de l'énergie retenue est celle de Ragab *et al.* [45], où on exprime l'énergie totale filtrée par

$$\bar{\rho}\widetilde{e}_t = \bar{\rho}\widetilde{e} + \frac{1}{2}\bar{\rho}\widetilde{u}_i\widetilde{u}_i + \frac{1}{2}\tau_{ii}^{sgs} \tag{22}$$

avec $\tau_{ii}^{sgs} = \overline{\rho u_i u_i} - \bar{\rho}\widetilde{u}_i\widetilde{u}_i$ est le terme isotrope du tenseur de viscosité de sous-maille.

Ces équations de bilan filtrées ont été implémentées, testées et étudiés avec le solveur `CREAMS` par Techer [53] au cours sa thèse.

Le modèle de viscosité de sous-maille de `WALE` (*Wall-Adapting Local Eddy*), introduit par Nicoud et Ducros [39] s'exprime avec l'expression suivante

$$\mu_{sgs} = \bar{\rho}\left(C_w\Delta\right)^2 \frac{\left(S_{ij}^d S_{ij}^d\right)^{3/2}}{\left(\widetilde{S}_{ij}\widetilde{S}_{ij}\right)^{5/2} + \left(S_{ij}^d S_{ij}^d\right)^{5/4}} \tag{23}$$

où $C_w = C_s\sqrt{10.6}$ est la constante du modèle `WALE`, $\Delta = \left(\Delta x_1 \Delta x_2 \Delta x_3\right)^{1/3}$ est la taille caractéristique de maille, and S_{ij}^d correspond à la partie symétrique déviatrice du carré du tenseur des déformations résolus, il s'écrit :

$$S_{ij}^d = \frac{1}{2}\left(\frac{\partial \widetilde{u}_i}{\partial x_k}\frac{\partial \widetilde{u}_k}{\partial x_j} + \frac{\partial \widetilde{u}_j}{\partial x_k}\frac{\partial \widetilde{u}_k}{\partial x_i}\right) - \frac{1}{3}\frac{\partial \widetilde{u}_m}{\partial x_l}\frac{\partial \widetilde{u}_l}{\partial x_m}\delta_{ij} \tag{24}$$

Cette formulation a été choisie parce qu'elle permet d'avoir un bon comportement asymptotique en proche paroi, i.e. $\mu_{sgs} = \mathcal{O}\left(y^3\right)$.

Le modèle de Yoshizawa [57] est l'un des modèles les plus classiques utilisé pour fermer la partie isotrope du tenseur de viscosité de sous-maille. Il exprime ce terme isotrope par

$$\tau_{kk}^{sgs} = 2C_I\bar{\rho}\Delta^2\left\|\widetilde{S}\right\|^2 \tag{25}$$

où C_I est la constante du modèle de Yoshizawa, prise généralement à 0.066 selon Erlebacher *et al.* [14]. Cette valeur semble faiblement dépendante du nombre de Mach de l'écoulement.

Le solveur `CREAMS` est un solveur Navier-Stokes compressible, instationnaire, visqueux, multi-espèces, 3D et parallèlisé. Il est couplé aux solveurs `CVODE` [10] et la librairie `EGLIB` [15] afin de calculer les flux et coefficients de transport multi-espèces dans le cas d'une description détaillée des propriétés de transport. Le couplage avec la librairie `CHEMKIN` [24] permet d'évaluer les coefficients de transports avec une description simplifiée, il permet en autre l'utilisation des tables thermodynamiques `JANAF` [52].

L'integration temporelle est basée sur la combinaison d'un schéma `TVD` (*Total Variation Diminishing*) Runge-Kutta d'ordre 3 [20] (contribution non réactive, i.e. inerte) et de l'intégrateur `CVODE` (contribution réactive) via l'emploi d'un découpage (`splitting`) de Strang [51].

La discrétisation spatiale des flux convectifs (non-visqueux) s'appuie sur une procédure de pondération non-linéaire `WENO` (*Weighted Essentially Non-Oscillatory*) d'ordre 7 [30]. L'application de la procédure de pondération non-linéaire du schéma `WENO7` est conditionnée par la présence de discontinuité (choc principalement), estimée à partir du senseur de choc modifié d'Adams et Shariff [1]. Un schéma centré d'ordre 8 est adopté dans la discrétisation spatiale des flux diffusifs (visqueux) moléculaires.

Enfin, étant donnée la dépendance non linéaire de l'énergie à la température, cette dernière est déterminée à l'aide de la méthode de Newton-Raphson [3] à partir de la définition de l'énergie totale, comme étant la racine de la fonction

$$f\left(T\right) = e_t + \frac{\mathcal{R}T}{\mathcal{W}} - h\left(T\right) - \frac{u_i u_i}{2} \tag{26}$$

Le solveur a été validé par des cas tests académiques, dont le tube à choc multi-espèces inerte. Ce cas test, proposé par Fedkiw *et al.* [18], est une version modifiée du tube à choc 1D de Sod [50] en utilisant un mélange multi-espèces non réactif.

On considère un tube de 10.0 cm de longeur, discrétisé avec 400 points. Le mélange gazeux est composé des fraction molaires suivantes $(\mathrm{H_2}, \mathrm{O_2}, \mathrm{Ar}) = (0.2, 0.1, 0.7)$ et le mélange est initialement au repos et réparti de manière uniforme dans le tube. Les conditions initiales correspondent au problème de Riemann suivant :

$$\text{à } t = 0 \begin{cases} (T_L, p_L) = (400\text{ K}, 8.0\text{ kPa}) & \text{si } x < 5.0\text{ cm} \\ (T_R, p_R) = (1200\text{ K}, 80.0\text{ kPa}) & \text{sinon} \end{cases} \tag{27}$$

Les résultats obtenus sont présentés sur la figure 5 et montrent que les positions respectives du choc ($x = 2.0$ cm), de la discontinuité de contact ($x = 3.5$ cm) ainsi que de la détente (6.0 cm $\leq x \leq$ 8.0 cm) coïncident avec celles obtenues par les travaux numériques de Fedkiw *et al.* [18].

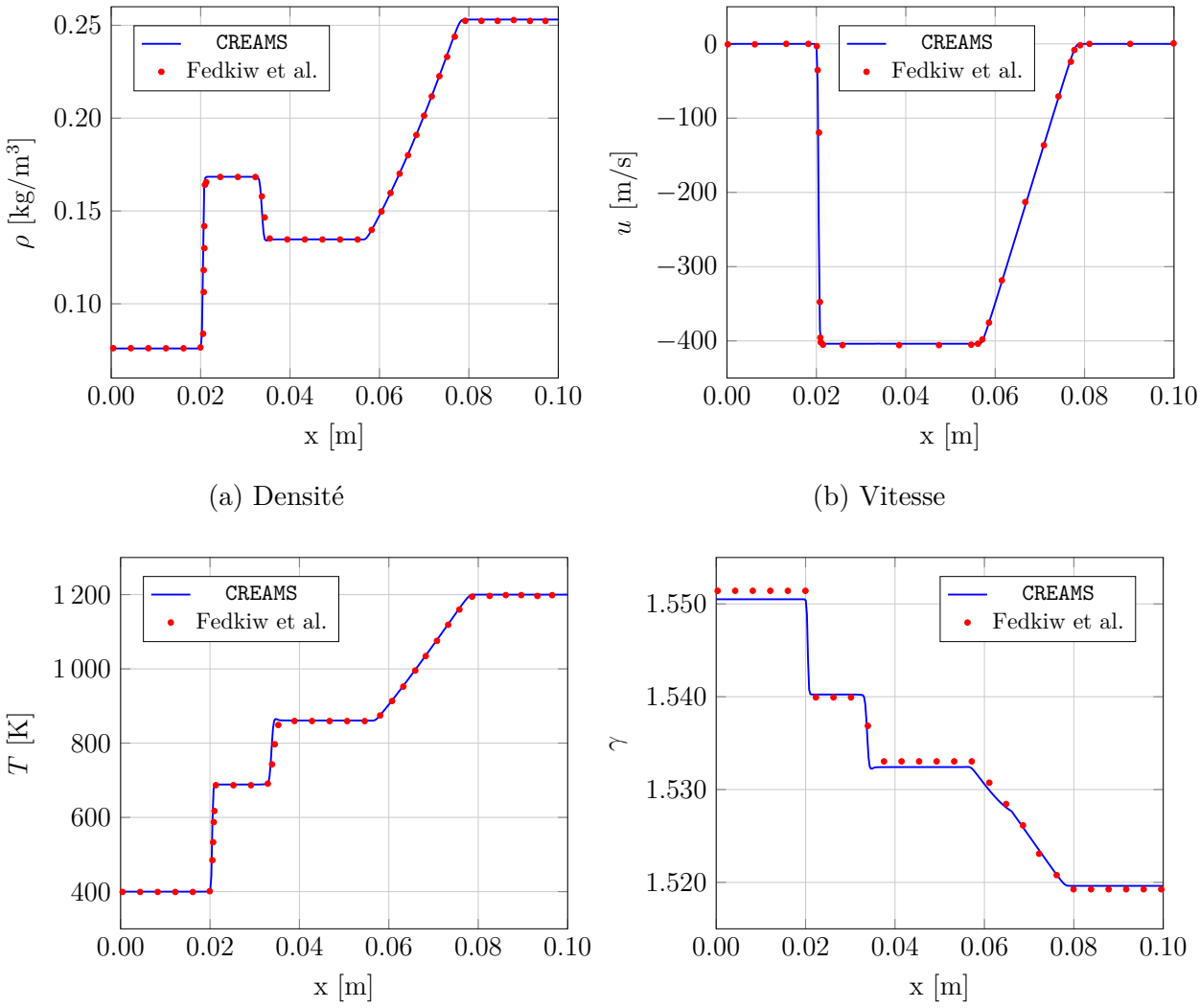

(a) Densité

(b) Vitesse

(c) Température

(d) Rapport des capacités calorifiques

FIGURE 5 – Profils de densité, vitesse, température et rapport des capacités calorifiques à $t = 40\mu s$

D'autres cas de test de validation ont été réalisés, tels que la couche limite de Blasius, pour vérifier le développement de la couche limite ou encore le vortex de Taylor-Green, pour vérifier la précision numérique du solveur.

La simulation d'écoulement autour d'un objet de géométrie complexe nécessite souvent le recours à un maillage adapté qui est susceptible d'être notablement distordu. La chambre de combustion, considérée ici comme un obstacle à l'écoulement, peut être modélisée à l'aide de plusieurs techniques, telles que les transformations de coordonnées,

l'utilisation des mailles structurées et non structurées adaptées à l'obstacle, les frontières immergées ou encore les approches de domaines fictifs.

Afin de rester en phase avec l'utilisation de schémas de différences finies d'ordre élevé appliqués sur un maillage cartésien, la méthode des frontières immergées (`IBM`) est finalement choisie pour être utilisée conjointement avec le solveur `CREAMS`. Cette méthode a été étudiée et implémentée dans le solveur dans le cadre de la thèse de Boukharfane [9] et de mes propres travaux.

Peskin [41] a développé cette méthode pour simuler initialement des écoulements de sang autour des valves de cœur, suivi de plusieurs stratégies proposées et développées. L'originalité de cette méthode réside dans le fait qu'elle permet de simuler l'écoulement sanguin du cœur sur un maillage cartésien structuré, et ce en résolvant un seul système d'équation, en l'occurrence celui du fluide. L'écoulement fluide est résolu suivant une approche Eulérienne, alors que le solide est décrit par le biais d'une formulation Lagrangienne.

Pour décrire cette méthode, on considère un domaine de calcul Ω contenant un corps immergé, dans lequel évolue un écoulement incompressible visqueux. Ce domaine peut se décomposer en un domaine fluide Ω_F, un domaine solide Ω_S et l'une interface fluide/solide notée Γ, telle que $\Gamma = \Omega_F \cap \Omega_S$, comme le montre la figure 6.

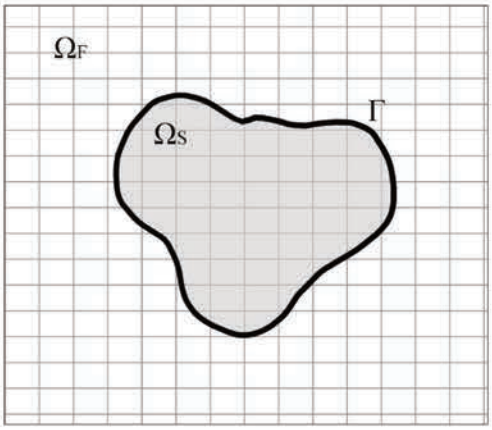

FIGURE 6 – Maillage structuré et frontière immergée

Dans le cas d'un écoulement incompressible, les équations régissant le fluide sont données par le système suivant :

$$\begin{cases} \dfrac{\partial u_i}{\partial t} + u_j \dfrac{\partial u_i}{\partial x_j} = -\dfrac{1}{\rho}\dfrac{\partial p}{\partial x_i} + \nu \dfrac{\partial^2 u_i}{\partial x_j^2} & \text{dans } \Omega_F \quad (28a) \\ \dfrac{\partial u_i}{\partial x_i} = 0 & \text{dans } \Omega_F \quad (28b) \\ u_i = u_{s,i} & \text{dans } \Omega_S \quad (28c) \end{cases}$$

où $u_{s,i}$ sont les composantes de la vitesse du solide.

Le principe des méthodes de frontières immergées consiste à discretiser les équations 28a et 28b sur un maillage cartésien tout en imposant la condition de bord 28c. Il existe plusieurs méthodes pour imposer cette condition limite au corps immergé, mais selon Iaccarino et Verzicco [23] elles peuvent être divisées en deux classes principales : forçage continu (`CFM`) et forçage discret (`GPM`). Ces deux méthodes diffèrent par la façon dont le terme de forçage est appliqué aux équations de Navier-Stokes.

La méthode de forçage continu consiste à ajouter un terme source dans l'équation 28a sous la forme d'une fonction de forçage. L'équation 28a prendra ainsi la forme suivante :

$$\frac{\partial u_i}{\partial t} + u_j \frac{\partial u_i}{\partial x_j} = -\frac{1}{\rho}\frac{\partial p}{\partial x_i} + \nu \frac{\partial^2 u_i}{\partial x_j^2} + f_i^L \qquad \text{dans } \Omega_F \tag{29}$$

où $f^L = \left(f_1^L, f_2^L, f_3^L\right)$ est le terme de forçage.

La méthode de forçage discret consiste à laisser inchangée l'équation 28a dans le domaine continu. Les équations sont discrétisées et le forçage est implicitement ou explicitement appliqué aux équations discrétisées au niveau des mailles proches de l'interface Γ. La discrétisation peut être ajustée pour prendre en compte la présence de l'interface et le système linéaire à résoudre devient :

$$\left[\mathcal{A}'(u)\right]\{U\} = \{\mathcal{F}^L\} \qquad \text{dans } \Omega \tag{30}$$

où $[\mathcal{A}'(u)]$ est l'opérateur discret modifié des équations de Navier-Stokes incompressibles, $\{U\} = \{u, p\}$ et $\{\mathcal{F}^L\}$ sont les termes permettant l'imposition des conditions de bord.

La mise en œuvre de la méthode de forçage continu est basée sur les travaux de Silva *et al.* [48], qui a envisagé une approche appelée *Physical Virtual Model* (`PVM`). La méthode de forçage discret est basée sur les travaux de Chaudhuri *et al.* [13], qui mettent au point une méthode de point fantôme (`GPM` - *Ghost-Point Method*).

Pour réussir l'implémentation de ces deux méthodes dans le code `CREAMS`, certaines étapes doivent être suivies :

- Identification des points Lagrangien, afin d'identifier les points solides et fluides sur le maillage Eulérien.
- Identification des points d'interpolation, des points fantômes et image (`GPM`).
- Calcul du terme de forçage continu et traitement des points fantômes (`GPM`).
- Validation de la méthode couplée `CFM-GPM` sur une série de cas tests bien documentés.

La présente stratégie des frontières immergées combine les méthodes `CFM` et `GPM` suivant l'algorithme ci-dessous :

1. Déterminer si le point est dans le domaine solide (Ω_S) où dans le fluide (Ω_F).
2. Chercher le support d'interpolation pour la méthode CFM.
3. Déterminer les points fantômes (Ω_{GP}) et les points images (Ω_{IP}).
4. Calculer la vitesse aux points Lagrangiennes de l'interface solide/fluid Γ.
5. Calculer les variables conservatives mises à jour en ajoutant le terme source $f^L(x)$ aux équations de quantité de mouvement à chaque étape de Runge-Kutta.
6. Metre à jour les points fantômes selon les conditions limites.

Une attention particulière est requise pour les coins d'angle vif car un point fantôme peut avoir plus d'un point image. En considérant un système avec un sous-ensemble de nœuds 3×3, voir la figure 7, une condition limite d'absence de flux doit être imposée à chaque stencil s_i $(i = 1, \ldots, 5)$, voir la figure 7a. Les stencils s_i $(i = 6, \ldots, 9)$ sont calculées en utilisant le polynôme de Lagrange $l_{i,4}$ $(i = 1, ..., 4)$.

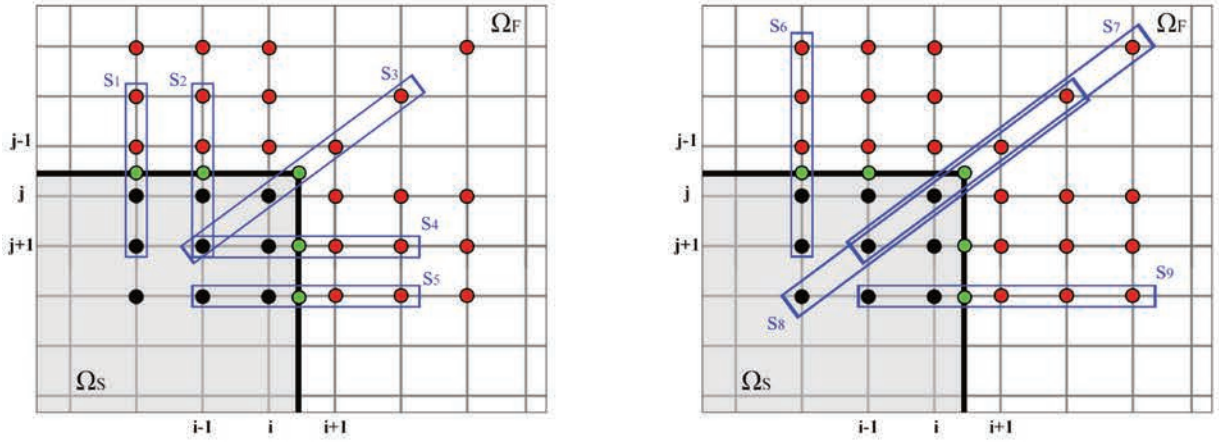

FIGURE 7 – Schéma d'une région d'angle et définition des stencils utilisés dans la procédure d'interpolation

En imposant la nullité du flux au bord du domaine de définition, ce système se réduit à $AT = B$, où

$$A = \begin{bmatrix} 0 & 0 & 0 & 0 & 1 & -27 & 0 & 0 & 0 \\ 0 & 1 & -27 & 0 & 0 & 0 & 0 & 0 & 0 \\ 0 & 0 & 0 & 0 & 1 & 0 & 0 & 27 & 0 \\ 0 & 0 & 0 & 1 & 0 & 0 & -27 & 0 & 0 \\ 0 & 0 & 0 & 0 & 1 & 0 & 0 & 0 & 27 \\ 0 & 0 & 0 & 1 & 0 & 0 & -4 & 0 & 0 \\ 0 & 1 & -4 & 0 & 0 & 0 & 0 & 0 & 0 \\ 0 & 0 & 0 & 1 & 0 & 0 & 0 & 0 & -4 \\ 1 & 0 & 0 & 0 & -4 & 0 & 0 & 0 & 6 \end{bmatrix} \tag{31}$$

$$T = \begin{bmatrix} T_{i-2,j-2} \\ T_{i-2,j-1} \\ T_{i-2,j} \\ T_{i-1,j-3} \\ T_{i-1,j-2} \\ T_{i-1,j-1} \\ T_{i,j-2} \\ T_{i,j-1} \\ T_{i,j} \end{bmatrix} \tag{32}$$

et

$$B = \begin{bmatrix} -27T_{i-1,j+1} + T_{i-1,j+2} \\ -27T_{i-2,j+1} + T_{i-2,j+2} \\ -27T_{i+1,j-1} + T_{i+2,j-1} \\ -27T_{i+1,j-2} + T_{i+2,j-2} \\ -27T_{i+1,j+1} + T_{i+2,j+2} \\ -6T_{i+1,j-2} + 4T_{i+2,j-2} - T_{i+3,j-2} \\ -6T_{i-2,j+1} + 4T_{i-2,j+2} - T_{i-2,j+3} \\ -6T_{i+1,j+1} + 4T_{i+2,j+2} - T_{i+3,j+3} \\ 4T_{i+1,j+1} - T_{i+2,j+2} \end{bmatrix} \tag{33}$$

L'implémentation d'`IBM` est validée avec quelques cas de tests, tels qu'un écoulement autour d'un cylindre carré, un écoulement autour d'un profil `NACA 0012` et écoulement sur une cavité.

L'interaction fluide-solide d'un écoulement supersonique est vérifiée avec la simulation d'un écoulement supersonique autour d'un cylindre carré de taille $a = 10.0$ mm. L'écoulement a une vitesse $M_0 = 2.43$, température $T_0 = 300$ K et pression $p_0 = 101325.0$ kPa.

La maillage est 4000 × 800, avec une distribution uniforme des points, et les données de référence sont celles obtenues à partir des travaux de Shterev et Stefanov [47].

La figure 8 montre les distributions de pression (fig. 8a) et de température (fig. 8b) le long de l'axe des ordonnées dans 3 sections différentes perpendiculaires à l'axe du canal : devant, au milieu et derrière le cylindre carré. Les données de référence sont indiquées par des lignes et les données du solveur `CREAMS` par des symboles.

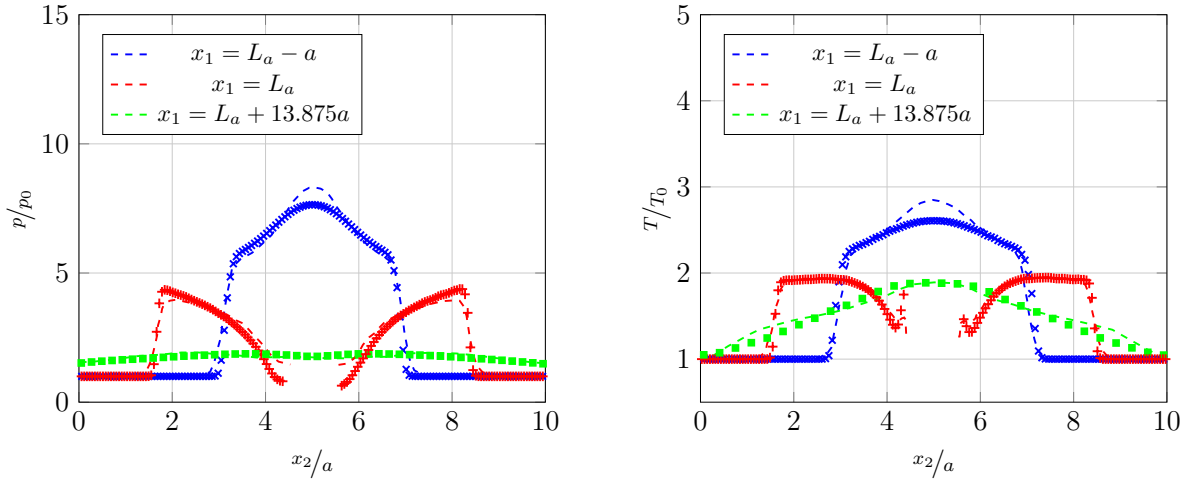

(a) Pression (b) Température

FIGURE 8 – Pression et température dans les sections normales à l'axe du canal

Les résultats obtenus sont en accord avec ceux de Shterev et Stefanov [47] concernant l'emplacement du choc. Cependant, les résultats du solveur `CREAMS` ont fourni un détecteur de choc légèrement plus sensible, ce qui peut être vérifié par le changement plus abrupt et plus rapide des variables par rapport aux courbes de référence.

Dans un moteur scramjet, l'écoulement d'air comprimé provenant de l'admission est maintenu supersonique suivant l'intégralité de la trajectoire. La méthode de chimie rapide devient moins appropriée lorsqu'il s'agit de combustion supersonique car les échelles de temps des réactions chimiques tendent à être du même ordre de grandeur que les échelles de temps turbulents dans ces conditions, ce qui conduit à des valeurs du nombre de Damköhler tendant ver l'unité. Une approche basée sur la chimie finie semble mieux appropriée décrire ce type de régime de combustion, dominé par des processus chimiques en présence de phénomènes d'auto-allumage.

L'approche de réacteur partiellement mélangé instationnaire (`U-PaSR` - *Unsteady Partially Stirred Reactor*) permet de prendre en compte les effects de micromélange, de chimie finie ainsi que de l'interaction entre les deux. Il apparaît alors comme un cadre théorique approprié pour modéliser les effets de sous-maille avec une approche `LES`.

Ce modèle est basée sur le modèle `EDC` (*Eddy Dissipation Concept*) et considère que les

réactions chimiques ne se produisent que dans les zones dissipatives, où le mélange moléculaire est plus intense. Chaque volume fluide de l'écoulement est alors traité comme un réacteur partiellement prémélangé (PaSR - *Partially Stirred Reactor*) avec des zones dissipatives, mélangées à l'échelle moléculaire (noté *), et une zone non-réactive environnante (noté ^{0}), comme le montre la figure 9. La zone bien mélangé se comporte alors comme un réacteur parfaitement mélangé, où les termes sources chimiques sont potentiellement élevés en raison des conditions favorables de mélange alors que la zone environnante reste chimiquement inerte.

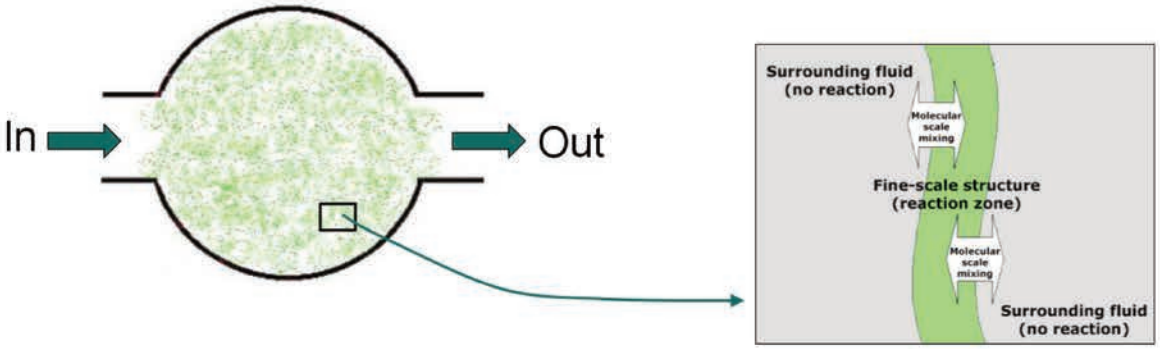

FIGURE 9 – Volume fini fluide comportant des structures à échelle fine et une zone non réactive environnante

Le terme de source chimique moyen s'écrit de manière générale :

$$\bar{\dot{\omega}}_\alpha = \int_\Psi \mathtt{PDF}\left(\psi\right) \dot{\omega}_\alpha\left(\psi\right) \, \mathrm{d}\psi \tag{34}$$

où Ψ désigne le domaine de définition de la PDF et $\psi = \left[T, Y_\alpha\right]^T$. La PDF est supposée bimodale avec une contribution de la zone micromélangée (*) et une contribution environnante (^{0}), de telle sorte que le terme source chimique moyen se simplifie comme :

$$\bar{\dot{\omega}}_\alpha \approx \gamma^* \dot{\omega}_\alpha\left(\psi^*\right) + \left(1-\gamma^*\right) \dot{\omega}_\alpha\left(\psi^0\right) \approx \gamma^* \dot{\omega}_\alpha\left(\psi^*\right) \tag{35}$$

où γ^* est la fraction volumique des structures bien mélangées, i.e., la fraction de chaque cellule de calcul au sein de laquelle se déroule la réaction chimique.

Les conditions dans les deux zones définies * et ^{0} sont liées par une équation de quasi-équilibre entre micromélange et production chimique, se traduisant pour la masse par :

$$\bar{\rho}\left(Y_\alpha^* - Y_\alpha^0\right) = \tau_m \dot{\omega}_\alpha\left(T^*, Y_\alpha^*\right) \tag{36}$$

et pour l'énergie par :

$$\bar{\rho} \sum_{\alpha=1}^{\mathcal{N}_{sp}} \left(Y_\alpha^* h_\alpha^* - Y_\alpha^0 h_\alpha^0\right) = \tau_m \sum_{\alpha=1}^{\mathcal{N}_{sp}} h_{\alpha,f}^\theta \dot{\omega}_\alpha\left(T^*, Y_\alpha^*\right) \tag{37}$$

où h_α est l'enthalpie de l'espèce α, τ_m est le temps de micromélange et $h^\theta_{\alpha,f}$ est l'enthalpie de formation de l'espèce α.

La fraction volumique de structures bien mélangées γ^* est défini comme le rapport entre le volume de la zone réactive et la somme des volumes des zones réactives et micromélangés, de sorte que

$$\gamma^* = \frac{\tau_{ch}}{\tau_{ch} + \tau_m} \tag{38}$$

où τ_{ch} est le temps caractéristique chimique et τ_m est le temps de micromélange.

Le temps caractéristique chimique τ_{ch} peut être estimé de plusieurs façons. Ici, par souci de simplicité, et en suivant les études de Moule [35], il est assimilé au temps caractéristique d'une flamme stœchiométrique de prémélange laminaire.

$$\tau_{ch} = \frac{\delta^0_L}{S^0_L} \tag{39}$$

Le temps de micromélange τ_m est égal à la moyenne harmonique entre l'échelle de Kolmogorov τ_k et l'échelle intégrale τ_Δ :

$$\tau_m = \sqrt{\tau_k \tau_\Delta} \tag{40}$$

avec $\tau_k = \sqrt{\nu/\varepsilon}$ où $\varepsilon = k^{3/2}/\Delta$ et $k = \left(\nu_{sgs}/0.069\Delta\right)^2$, et $\tau_\Delta = \Delta/\nu'$ où $\nu' = \sqrt{2k/3}$ [5].

Les équations du modèle `U-PaSR` sont ensuite définis comme suit :

$$\begin{cases} \dfrac{\partial \bar{\rho} Y^*_\alpha}{\partial t} + \bar{\rho} \dfrac{\left(Y^*_\alpha - Y^0_\alpha\right)}{\tau_m} = \dot{\omega}_\alpha \left(T^*, Y^*_\alpha\right) & \text{(41a)} \\ \dfrac{\partial \bar{\rho} h^*}{\partial t} + \bar{\rho} \displaystyle\sum_{\alpha=1}^{\mathcal{N}_{sp}} \dfrac{\left(Y^*_\alpha h^*_\alpha - Y^0_\alpha h^0_\alpha\right)}{\tau_m} = \sum_{\alpha=1}^{\mathcal{N}_{sp}} h^\theta_{\alpha,f} \dot{\omega}_\alpha \left(T^*, Y^*_\alpha\right) & \text{(41b)} \end{cases}$$

Ce système peut s'écrire à l'aide des conditions moyennes $(\widetilde{\cdot})$ et micromélangées $(^*)$, en utilisant le changement de variable $\widetilde{\psi} = \gamma^* \psi^* + (1 - \gamma^*)\, \psi^0$ pour une variable ψ donnée :

$$\begin{cases} \dfrac{\partial \bar{\rho} Y^*_\alpha}{\partial t} + \bar{\rho} \dfrac{\left(Y^*_\alpha - \widetilde{Y}_\alpha\right)}{\tau_m \left(1 - \gamma^*\right)} = \dot{\omega}_\alpha \left(T^*, Y^*_\alpha\right) & \text{(42a)} \\ \dfrac{\partial \bar{\rho} h^*}{\partial t} + \bar{\rho} \displaystyle\sum_{\alpha=1}^{\mathcal{N}_{sp}} \dfrac{\left(Y^*_\alpha h^*_\alpha - \widetilde{Y}_\alpha \widetilde{h}_\alpha\right)}{\tau_m \left(1 - \gamma^*\right)} = \sum_{\alpha=1}^{\mathcal{N}_{sp}} h^\theta_{\alpha,f} \dot{\omega}_\alpha \left(T^*, Y^*_\alpha\right) & \text{(42b)} \end{cases}$$

où les conditions moyennes $(\widetilde{\cdot})$ sont imposées par le solveur `CREAMS` et les conditions dans les structures fines $(^*)$ sont calculés avec le système d'équations précédent. Lorsque l'état filtré moyen $\widetilde{\psi}$ et les structures fines (ψ^*) sont connus, le milieu à deux fluides est entièrement déterminé puisque l'état ψ^0 peut être évalué à partir de $\psi^0 = \left(\widetilde{\psi} - \gamma^* \psi^*\right) / \left(1 - \gamma^*\right)$.

Considérant les équations de bilan pour un réacteur `U-PaSR` comme étant continuellement alimentées par un flux de réactifs à la concentration (Y_α^{in}, T^{in}) et avec un temps de séjour à l'intérieur du réacteur τ_{res}, on obtient :

$$\begin{cases} \dfrac{\partial \bar{\rho} Y_\alpha^*}{\partial \tau} + \boldsymbol{\alpha}\bar{\rho}\left(Y_\alpha^* - Y_\alpha^{in}\right) + \boldsymbol{\beta}\bar{\rho}\left(Y_\alpha^* - \widetilde{Y}_\alpha\right) = \boldsymbol{\gamma}\dot{\Omega}_\alpha\left(T^*, Y_\alpha^*\right) & \text{(43a)} \\ \dfrac{\partial \bar{\rho} h^*}{\partial \tau} + \boldsymbol{\alpha}\bar{\rho}\sum_{\alpha=1}^{\mathcal{N}_{sp}}\left(Y_\alpha^* h_\alpha^* - Y_\alpha^{in} h_\alpha^{in}\right) + \boldsymbol{\beta}\bar{\rho}\sum_{\alpha=1}^{\mathcal{N}_{sp}}\left(Y_\alpha^* h_\alpha^* - \widetilde{Y}_\alpha \widetilde{h}_\alpha\right) = \boldsymbol{\gamma}\sum_{\alpha=1}^{\mathcal{N}_{sp}} h_{\alpha,f}^\theta \dot{\Omega}_\alpha\left(T^*, Y_\alpha^*\right) & \text{(43b)} \\ \dfrac{\partial \bar{\rho} \widetilde{Y}_\alpha}{\partial \tau} + \boldsymbol{\alpha}\bar{\rho}\left(\widetilde{Y}_\alpha - Y_\alpha^{in}\right) = \boldsymbol{\gamma}\gamma^*\dot{\Omega}_\alpha\left(T^*, Y_\alpha^*\right) & \text{(43c)} \\ \dfrac{\partial \bar{\rho} \widetilde{h}}{\partial \tau} + \boldsymbol{\alpha}\bar{\rho}\sum_{\alpha=1}^{\mathcal{N}_{sp}}\left(\widetilde{Y}_\alpha \widetilde{h}_\alpha - Y_\alpha^{in} h_\alpha^{in}\right) = \boldsymbol{\gamma}\gamma^*\sum_{\alpha=1}^{\mathcal{N}_{sp}} h_{\alpha,f}^\theta \dot{\Omega}_\alpha\left(T^*, Y_\alpha^*\right) & \text{(43d)} \end{cases}$$

où $h_\alpha^{in}\left(T^{in}\right)$ est l'enthalpie de l'espèce α à la température d'entrée T^{in} de manière à ce que $h^{in} = \sum_\alpha Y_\alpha^{in} h_\alpha^{in}\left(T^{in}\right)$, $\tau = {}^t/_{\tau_{res}}$, $\boldsymbol{\alpha} = {}^{\tau_m}/_{\tau_{res}}$, $\boldsymbol{\beta} = {}^1/_{(1-\gamma^*)}$ et $\boldsymbol{\gamma} = {}^{\tau_m}/_{\tau_{ch}}$ le nombre de Damköhler. Le taux de produit chimique est normalisé par l'échelle de temps chimique τ_{ch}, i.e. $\dot{\Omega}_\alpha\left(T^*, Y_\alpha^*\right) = \tau_{ch}\dot{\omega}_\alpha\left(T^*, Y_\alpha^*\right)$.

Trois paramètres non dimensionnels indépendants sont utilisés pour analyser le comportement limite du modèle de réacteur `U-PaSR` :

$$\boldsymbol{\alpha} = \frac{\tau_m}{\tau_{res}} \tag{44}$$

$$\boldsymbol{\gamma} = \frac{\tau_m}{\tau_{ch}} \tag{45}$$

$$\boldsymbol{\beta} = \frac{1+\boldsymbol{\gamma}}{\boldsymbol{\gamma}} \tag{46}$$

La pression à l'intérieur du réacteur est fixée à 10^5 Pa et l'échelle de temps de micromélange τ_m est fixée à 10^{-3} s. L'enthalpie d'entrée h^{in} est obtenue à partir de sa température T^{in} et de sa composition (rapport d'équivalence Φ^{in}), avec $T^{in} = 298.15$ K et $\Phi^{in} = 0.70$ (2.0% de H_2, 22.8% de O_2 et 75.2% de N_2). Des simulations sont effectuées pour plusieurs valeurs de $\boldsymbol{\alpha}$ et $\boldsymbol{\gamma}$, allant de 10^{-5} à 10^{-1} et de 10^{-1} à 10^1, respectivement.

La figure 10 présente la valeur de la température à l'état d'équilibre en fonction de $\boldsymbol{\alpha}$ (fig. 10a) et $\boldsymbol{\gamma}$ (fig. 10b). On peut remarquer que, lorsque $\boldsymbol{\alpha}$ diminue (i.e. le temps de séjour τ_{res} augmente), la température tend vers la même valeur quelle que soit la valeur de $\boldsymbol{\gamma}$, ce qui signifie que, comme attendu, la température est affectée à la fois par le temps de séjour τ_{res} et par la fraction de structure finie γ^*. Cependant, lorsqu'une valeur de $\boldsymbol{\alpha}$ suffisamment petite est considérée (i.e. valeurs élevées de τ_{res}), la valeur retenue pour $\boldsymbol{\gamma}$ n'affecte plus la température moyenne à l'état d'équilibre : on dispose d'un temps suffisant pour que les processus de réaction chimique aient lieu.

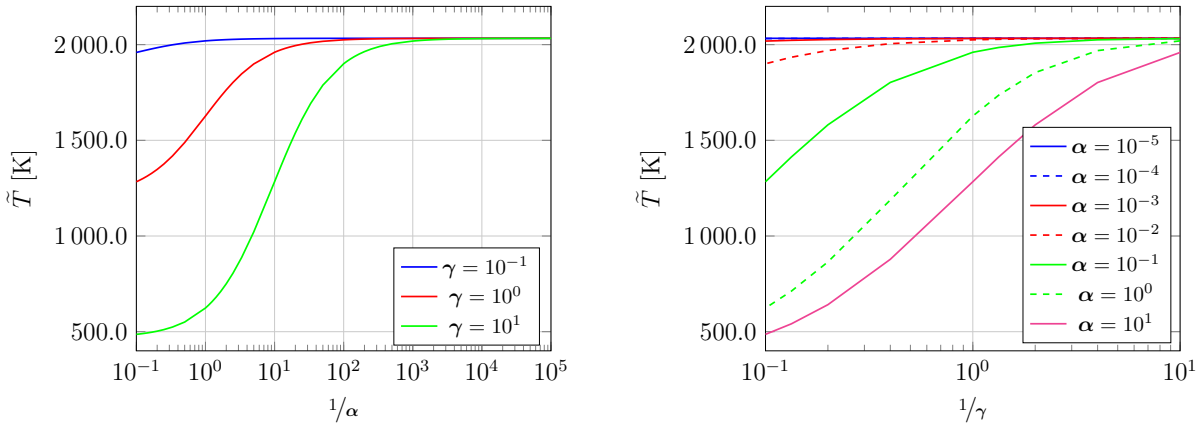

(a) Variation du temps de séjour (b) Variation de la fraction de structure fini

FIGURE 10 – Évolution temporelle de la température

La topologie et la structure de l'écoulement dans un moteur scramjet représentant les expériences effectuée par Micka et Driscoll [34] à l'Université du Michigan sont effectuées, et les régimes de combustion sont étudiés sur la base de diagrammes de combustion turbulente standards. La stabilisation de la combustion est étudiée pour deux niveaux de température différents dans un écoulement d'air vicié en entrée, notés `RFSC-LST` et `RFSC-HST` pour des températures de stagnation à l'admission basse et élevée respectivement.

La figure 11 présente l'installation de combustion expérimentale supersonique, composée d'une tuyère bidimensionnelle à Mach 2.2, d'un isolateur à section constante qui s'étend sur 400.0 mm jusqu'au bord d'attaque d'une cavité rectangulaire et d'une section divergente de 349.00 mm de long qui précède un échappement de 152.00 mm de diamètre.

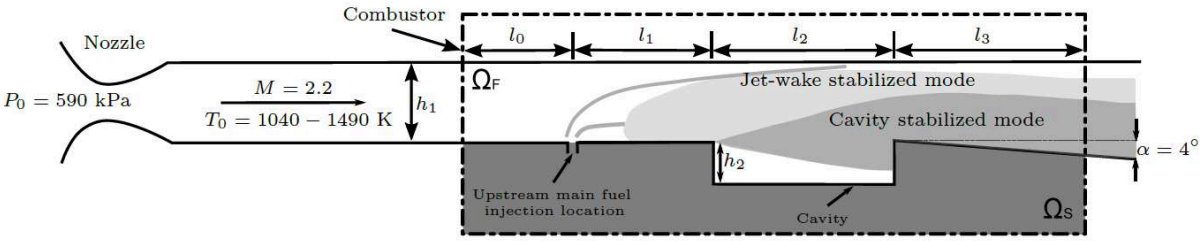

FIGURE 11 – Schémas de l'installation de combustion avec le domaine de calcul mis en évidence

Le domaine de calcul peut être décomposé en trois parties distinctes : un canal de section constante s_1 de longueur $L_{x_1,s_1} = l_0 + l_1 = 94.5$ mm et de hauteur $L_{x_2,s_1} = h_1 = 39.4$ mm, une section s_2 de longueur $L_{x_1,s_2} = 50.8$ mm avec une cavité de profondeur $h_2 = 12.7$ mm, et une section divergente s_3 de $L_{x_1,s_3} = 76.2$ mm de longueur et 4° d'inclinaison. La longueur totale est de $L_{x_1} = 221.5$ mm et il est de $L_{x_3} = 38.1$ mm dans le sens de la largeur. La section S_1 comprend un orifice d'injection de $D_{inj} = 2.5$ mm de

diamètre situé le long de l'axe de la chambre de combustion à 44.5 mm du bord d'attaque de la cavité.

Les simulations sont effectuées dans le cadre `LES` et la viscosité de sous-maille est traitée à l'aide du modèle `WALE`. La cavité est modélise à l'aide d'`IBM` et les conditions limites sont traitées comme une paroi adiabatique. Le temps est normalisé comme $t^* = {}^{(t \cdot u_0)}/_{D_{inj}}$, où u_0 est la vitesse de l'écoulement à l'entrée et D_{inj} est le diamètre de l'orifice d'injection du carburant. Le maillage est raffiné autour de l'injection du carburant, des parois de la cavité et autour de la couche limite qui se développe sur la cavité. Il comporte environ 42 million de points.

La pression de stagnation initiale est $p_0 = 590.0$ kPa et deux valeurs de températures sont considérés dans l'entrée d'air vicié : 1100.0 K (cas `RFSC-LST`) et 1400.0 K (cas `RFSC-HST`). Le tableau 2 regroupe les principaux paramètres caractérisant les écoulements d'entrée d'air vicié et de combustible dans les deux cas.

		Cas `RFSC-LST`	**Cas `RFSC-HST`**
Entrée d'air vicié	T_0 (K)	1100.0	1400.0
	Y_{O_2}	0.244	0.251
	Y_{N_2}	0.671	0.607
	Y_{H_2O}	0.085	0.142
Entrée de combustible	p_{inj} (kPa)	845.0	755.0
	T_{inj} (K)	288.0	288.0
	Y_{H_2}	1.0	1.0

Tableau 2 – Caractéristiques des écoulements d'air vicié et de combustible

La figure 12 présente la distribution des mailles du cas `RFSC-LST`, en unités de paroi, au dessus de la paroi `IBM`, selon une présentation similaire à celle réalisée par Techer [53]. En considérant uniquement la zone où le combustible et l'oxydant ne sont plus séparés, comme le montre la figure 12b, on peut en conclure que le maillage satisfait aux critères recommandés pour une `LES` résolue à la paroi [42].

Le modèle WALE change de manière satisfaisante son comportement dans la couche tampon qui sépare la zone logarithmique ($y^+ > 30.0$) de la sous-couche visqueuse ($y^+ < 5.0$), comme indiqué dans la figure 13.

L'évaluation de la résolution de calcul est complétée par une analyse de la qualité du maillage, permettant de vérifier sa résolution dans l'écoulement. Deux indices ont donc été considérés, variants de zéro (faible résolution de maillage) à l'unité (bonne résolution de maillage) : l'indice de qualité modifié de Pope IQ_k [43] et l'indice de qualité de Celik IQ_η [12].

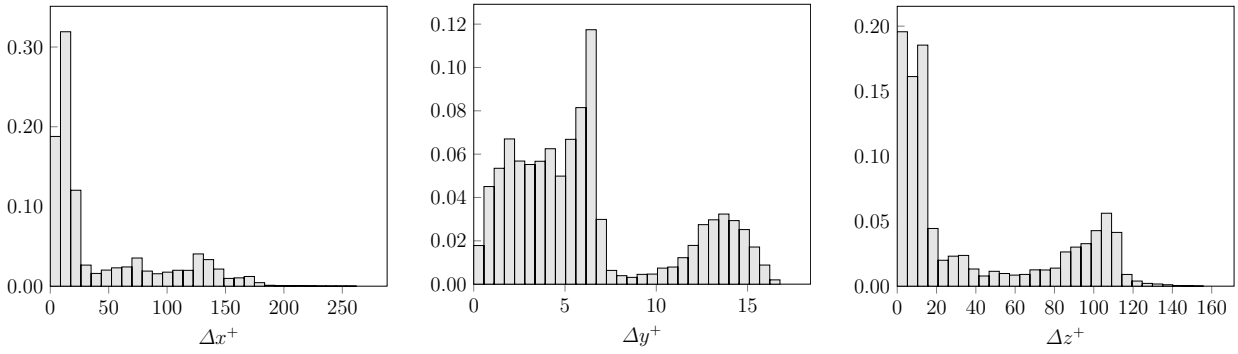

(a) Sur toutes les parois `IBM`

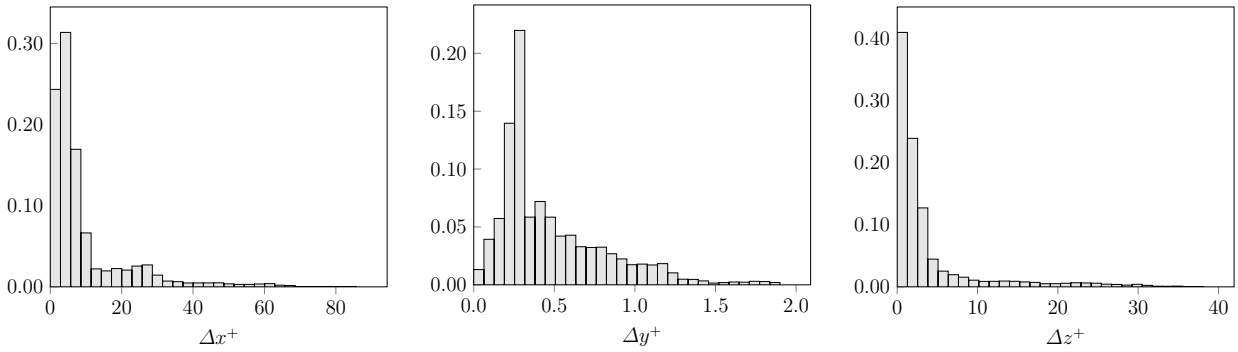

(b) À l'exclusion des régions associées au combustible pur et à l'oxydant pur

FIGURE 12 – Histogramme de distribution de taille de maille (cas `RFSC-LST`)

La figure 14 présente la `PDF` obtenue avec les deux indices de qualités, indiquant que la plupart des valeurs des indices de qualité IQ_k et IQ_η sont bien supérieures à 0.80 et 0.93, respectivement.

Près de 98% des valeurs obtenues pour l'indice de qualité de Pope IQ_k sont supérieures à 0.80 et 95% des valeurs obtenues pour l'indice de qualité Celik IQ_η sont supérieures à 0.93.

En ce qui concerne l'analyse de convergence statistique, la solution converge de $t^* = 450$ et $t^* = 500$ pour les cas `RFSC-LST` et `RFSC-HST`, respectivement.

L'efficacité du mélange, i.e. le degré de mélange entre le combustible et l'air, peut être définie par le rapport de débit massique du réactive susceptible d'avoir réagi et le débit massique total :

$$\eta_m = \frac{\int Y_r \rho \, \mathrm{d}A}{\int Y_f \rho \, \mathrm{d}A} \tag{47}$$

où la fraction massique Y_r est calculée comme suit :

$$Y_r = \begin{cases} Y_f & Y_f \leq Y_{f,st} \\ Y_{f,st} \left(\dfrac{1 - Y_f}{1 - Y_{f,st}} \right) & Y_f > Y_{f,st} \end{cases} \tag{48}$$

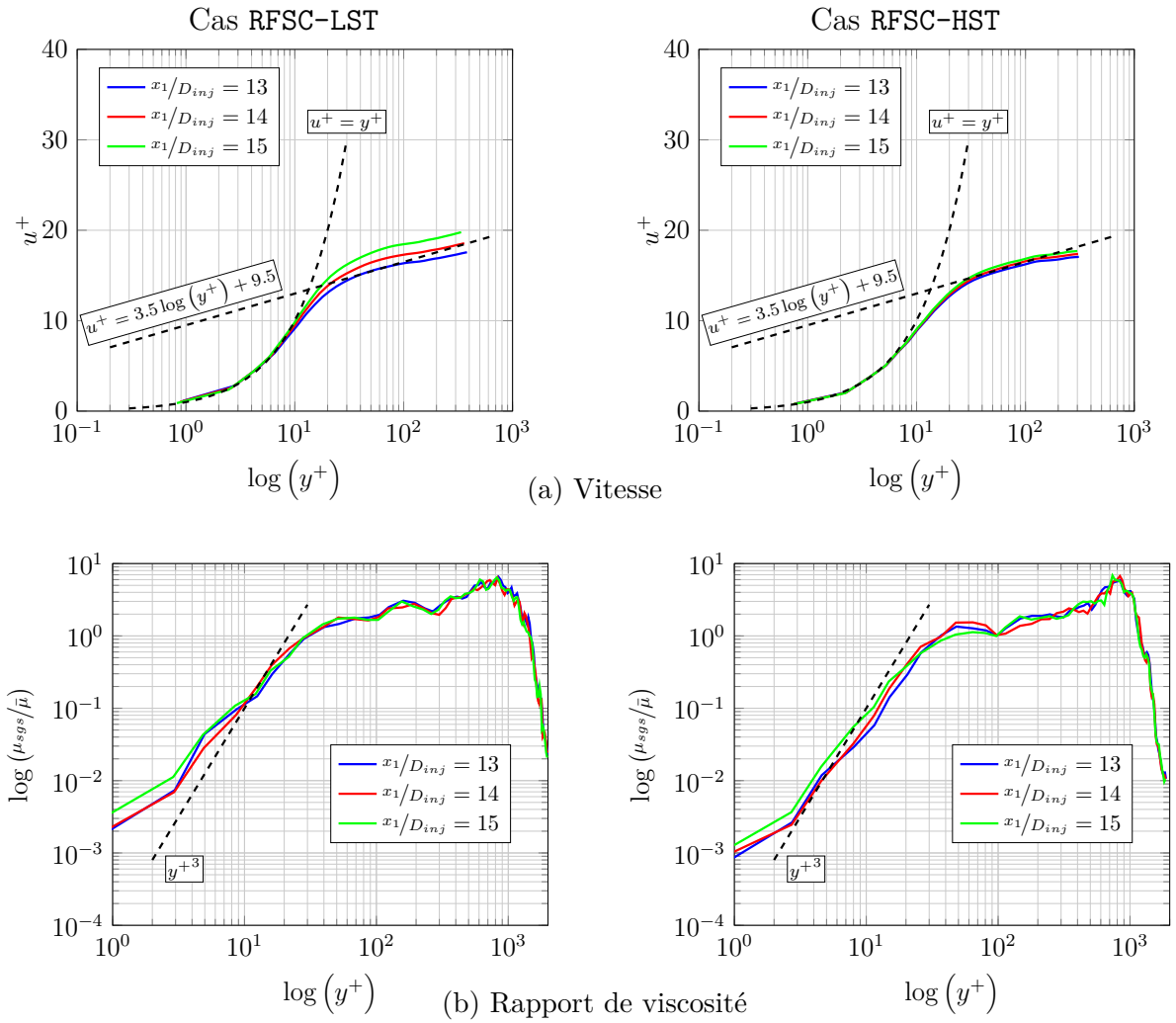

FIGURE 13 – Profil adimensionné de vitesse en unités de paroi et rapport de viscosité à plusieurs abscisses x_1/D_{inj} le long de $x_3/D_{inj} = 0$ pour les cas `RFSC-LST` (à gauche) et `RFSC-HST` (à droit)

avec Y_f la fraction massique du combustible, $Y_{f,st}$ la fraction massique stœchiométrique du combustible et Y_r la fraction de combustible prenant part à la réaction.

La figure 15 présente l'efficacité du mélange dans le sens du courant, en considérant l'injection de combustible et la cavité murale, i.e. $4 \leq x_1/D_{inj} \leq 38$. L'efficacité du mélange est proche de 100% avant l'injection de combustible car une petite partie du combustible se propage en amont le long de la couche limite turbulente et est suffisamment mélangée avec l'air. Un minimum de l'efficacité est obtenu avant l'injection du jet de combustible car le mélange y est dominé par des tourbillons à grande échelle dans la couche de cisaillement. L'efficacité du mélange augmente ensuite plus rapidement le long de la cavité, ce qui signifie que le mélange est amélioré, atteignant presque 100% à la fin de la cavité.

Considérant la simulation de l'écoulement réactif en utilisant le mécanisme détaillé

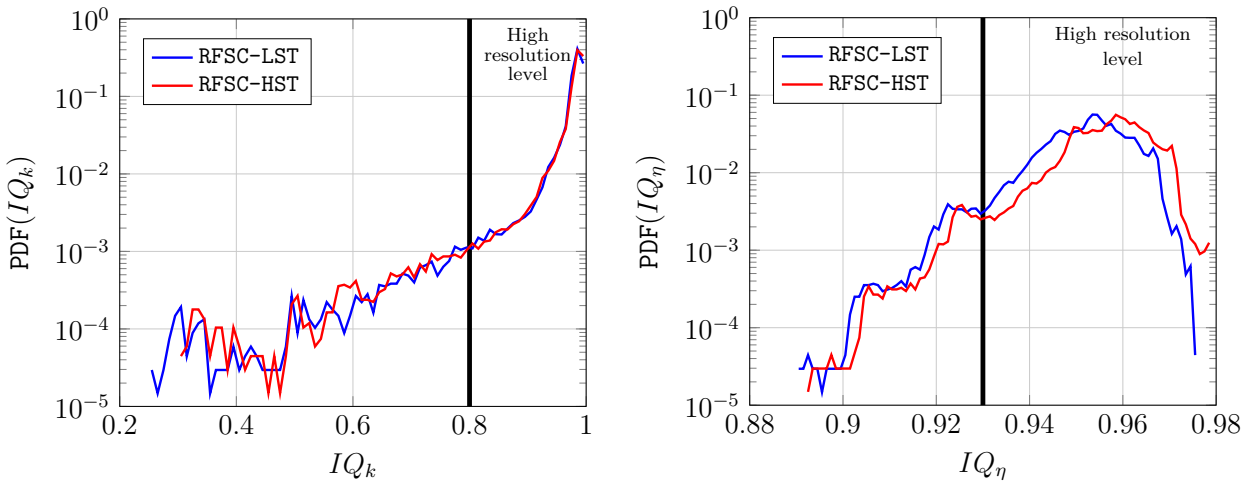

(a) Pope (b) Celik

FIGURE 14 – PDF de l'indice de qualité obtenu dans le plan médian dans le sens de l'envergure ($x_3/D_{inj} = 0$)

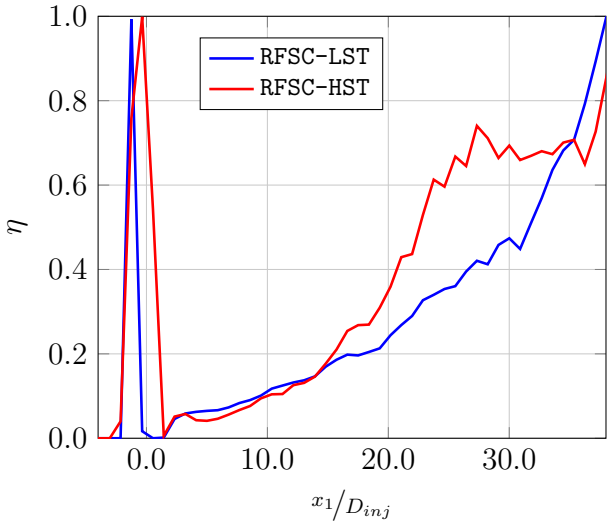

FIGURE 15 – Evaluation longitudinale de l'efficacité de mélange

d'O'Conaire *et al.* [40], composé de 9 espèces chimiques (H_2, O_2, H_2O, H, O, OH, HO_2, H_2O_2 et N_2) et 21 étapes de réaction élémentaires pour représenter la cinétique chimique H_2-air. Dans ces cas, la simulation est conduite de $t^* = 800$ et $t^* = 900$ pour cas RFSC-LST et RFSC-HST, respectivement.

La mode de combustion stabilisé par cavité est caractérisé par une zone de réaction ancrée au bord d'attaque de la cavité et se propageant dans l'écoulement principal selon un angle approximativement constant. En mode de stabilisation de type jet, la zone de réaction est stabilisée en amont de la cavité et le bord d'attaque est incurvé.

La figure 16 compare le taux moyen de dégagement de chaleur des cas RFSC-LST et

RFSC-HST avec la luminosité de la flamme obtenue expérimentalement. Ils sont relativement similaires à ceux obtenus expérimentalement par Micka [33].

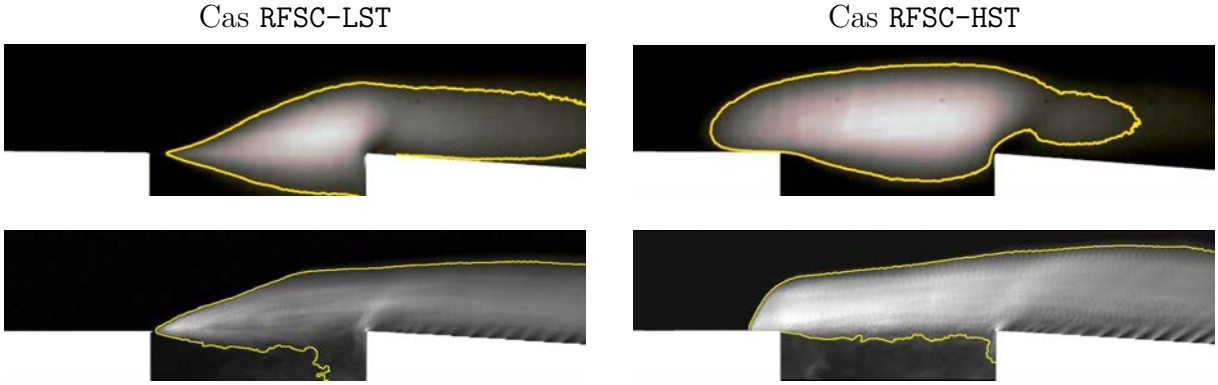

FIGURE 16 – Comparaison avec des résultats expérimentaux : luminosité de flamme adaptée de Micka [33] (en haut) et taux moyen de dégagement de chaleur (en bas)

Comme les réactions chimiques ont lieu loin en aval de l'injection de carburant, il est intéressant de déterminer les contributions du mode de combustion prémélangées et non prémélangées (i.e. par diffusion). Un indice de prémélange $\check{\zeta}_p$ est considéré à cet effet, il est défini comme suit :

$$\check{\zeta}_p = \frac{1}{2}\left(1 + \mathbf{n}_F \cdot \mathbf{n}_O\right) \tag{49}$$

où $\mathbf{n}_F$ et $\mathbf{n}_O$ sont les vecteurs unitaires normaux associés au flux de diffusion moléculaire du combustible et de l'oxydant.

Cet indice devrait s'approcher de zéro pour la combustion par diffusion et de l'unité pour la combustion prémélangée. Il est largement utilisé dans les analyses préliminaires des caractéristiques de combustion partiellement prémélangées, malgré certaines situations particulières dans lesquelles sa représentativité peut être mise en défaut [31].

La figure 17 présente la PDF de cet indice à des moments différents pour les cas RFSC-LST et RFSC-HST, pour un volume limité à $0.01 \leq \widetilde{\xi} \leq 0.99$ et un taux de dégagement de chaleur supérieur à 10^9 $^W/_{\mathrm{kg}}$, et confirme que les modes diffusif et prémélangé sont tous deux significatifs.

Étant donné qu'une proportion non négligeable de de réaction chimique se déroule en mode de combustion prémélangé, les régimes de combustion prémélangés turbulents sont analysés dans le diagramme standard de Barrère et de Borghi [7, 8]. Les données sont représentées sur la figure 18 en utilisant un rapport d'échelle de longueur normalisé $^{\mathcal{L}_t}/_{\delta_L^0}$ et un rapport de vitesse $^{u_{rms}}/_{S_L^0}$ en abscisse et en ordonnée.

On trouve plusieurs régimes de combustion prémélanges, tels que des flammes épaisses, des flammes plissées et même des flammes laminaires. Dans le cas RFSC-LST, la plu-

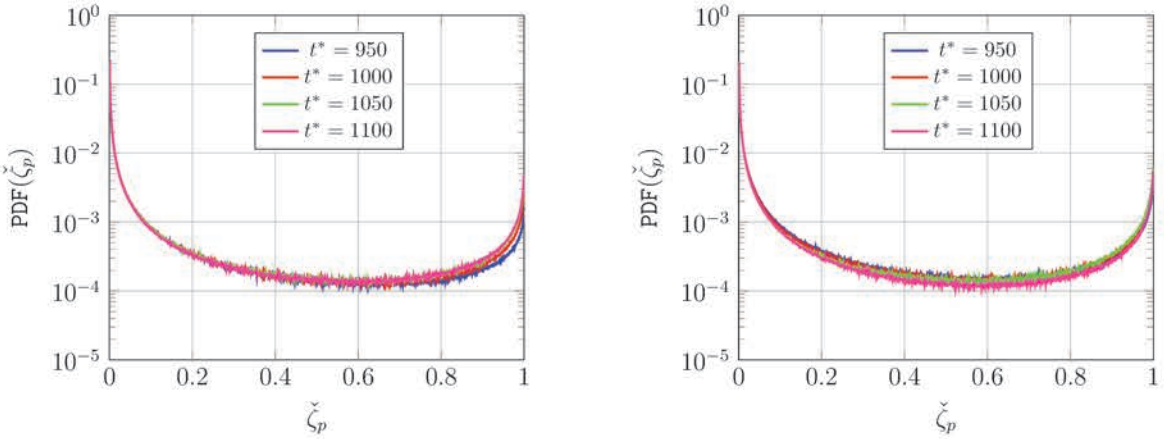

(a) Cas RFSC-LST (b) Cas RFSC-HST

FIGURE 17 – PDF de l'indice de prémélange $\check{\zeta}_p$

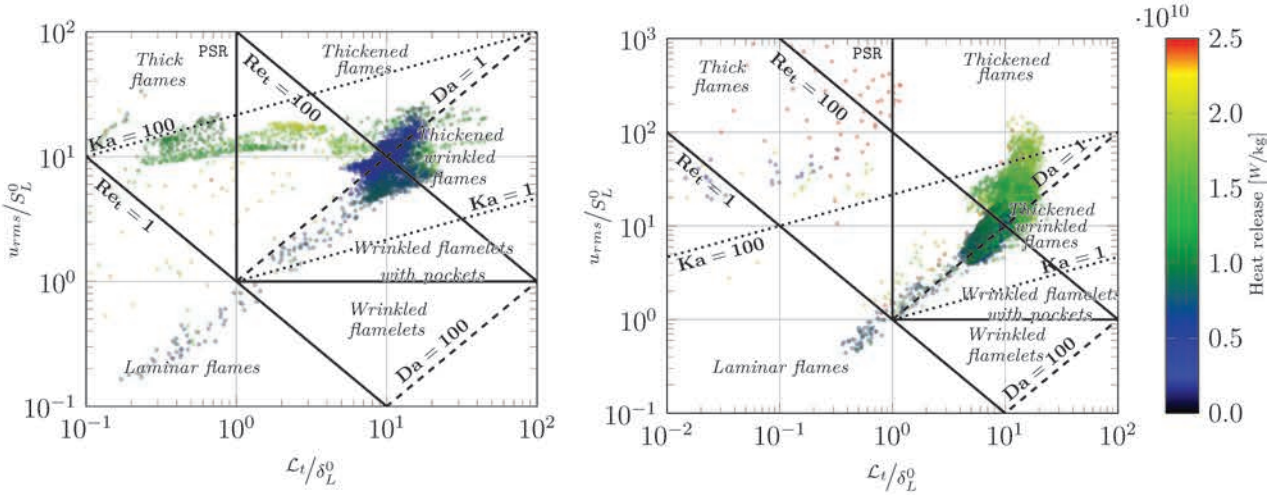

(a) Cas RFSC-LST (b) Cas RFSC-HST

FIGURE 18 – Diagramme de combustion turbulente prémélangée basé sur les coordonnées de Borghi-Barrère [8]

part des points sont situés à proximité du régime de flammes plissées épaissies (*thickened-wrinkled flame*), entre la limite de Klimov-Williams (Ka = 1) et la ligne correspondant à Da = 1, autour de la ligne horizontale correspondant à $u_{rms}/S_L^0 = 10$, avec certains points présentant un taux de dégagement de chaleur non négligeable situé dans la région des flammes épaisses (*thick flame*). Le cas RFSC-HST présente un taux de dégagement de chaleur plus élevé, avec ses pointes s'étendant vers les régimes de flammes épaissies (*thickened flame*) et plissées (*thickened-wrinkled flame*), ce qui correspond à un nombre de Damköhler plus modéré. De plus, il y a des effets de cinétique chimique finie non négligeables.

L'analyse des régimes de combustion confirme la présence de flammes prémélangées

très turbulentes. La distribution des points pour le cas `RFSC-LST` est semblable aux résultats obtenus par Quinlan *et al.* [44] et Techer [53], avec l'ensemble de points déplacé vers une zone associée à un nombre de Karlovitz plus grand. Ces différences peuvent s'expliquer par une configuration différente, notamment la pression, la température, la fraction de mélange et le carburant considéré. Pour le cas `RFSC-HST`, toutefois, la distribution des points est plus concentrée le long de la région de flamme plissées épaissies (*thickened-wrinkled flame*) avec un nombre de Damköhler proche de l'unité, ce qui signifie que la vitesse de réaction est du même ordre de grandeur que la vitesse de diffusion.

3 Conclusions et perspectives

Cette thèse a été conduite à l'Institut Pprime avec pour objectif de contribuer à la compréhension de la combustion turbulente supersonique, en se concentrant sur ses applications aux moteurs scramjet.

En introduction, une brève description du moteur scramjet, de sa conception et de son comportement, ainsi que certains aspects historiques de son développement technologique sont présentés. Le statoréacteur (ramjet) et le super-statoréacteur (scramjet) ont l'avantage de pouvoir transporter une charge utile plus lourde puisque, du fait de l'utilisation de l'oxygène atmosphérique, le transport de leur propre oxydant devient inutile. Fondamentalement, le moteur scramjet peut être divisé en quatre parties : admission, responsable de la compression et de l'accélération de manière à obtenir la pression et la température nécessaires à la combustion, isolateur, responsable du confinement des trains de choc qui peuvent apparaître lorsque le véhicule accélère à la vitesse opérationnelle, la chambre de combustion, où le carburant et l'oxydant sont brûlés, et enfin la tuyère d'échappement, où la poussée est générée par l'accélération des produits de combustion.

Les équations de Navier-Stokes ont été présentées dans leur forme compressible, réactive et multi-espèces. La modélisation de la turbulence est également introduite, y compris les équations filtrées de Navier-Stokes et les termes de fermeture de sous-maille. Le solveur `CREAMS` utilise le méthode de Strang pour coupler les termes non réactifs aux termes réactifs, et l'intégration temporelle est effectuée avec un schéma `TVD` pour les termes non réactifs et `CVODE` pour les termes réactifs.

La cavité est modélisée à l'aide de la méthode `IBM` récemment implémentée. Cette méthode fonctionne avec un maillage cartésien et permet d'insérer un objet solide dans le domaine de calcul sans modifier la maillage. Deux classes différentes d'`IBM` sont présentées, dont les différences résident dans l'ajout du terme de forçage aux équations de Navier-Stokes pour simuler la paroi solide : forçage continu et forçage discret.

Étant donné que l'écoulement est maintenu supersonique à l'intérieur de la chambre

de combustion du scramjet, les échelles de temps de réaction chimique ont tendance à être du même ordre de grandeur que les échelles de temps turbulents, ce qui rend l'approche de chimie rapide moins appropriée. suivant le modèle `U-PaSR`, la réaction chimique a lieu dans des régions fines ("*worms*"), où se déroulent la plupart des processus de dissipation visqueuse et de mélange moléculaire. Ce modèle prend en compte les inhomogénéités de composition et de température dans la région de la flamme ainsi que les effets du micromélange, de la chimie finie et des interaction entre eux.

Deux simulations, dont les conditions correspondent aux expériences effectuées à l'Université du Michigan, sont effectuées : une avec une température d'écoulement en entrée limitée (cas `RFSC-LST`) et une autre avec une température d'écoulement en entrée plus élevée (`RFSC-HST`). Plusieurs critères ont été utilisés pour vérifier la résolution du calcul et des efforts ont été déployés pour capturer l'écoulement près des parois `IBM` aussi précisément que possible. L'efficacité du mélange est déterminée dans les deux cas entre l'injection de combustible et la région de la cavité. Il est vérifié que la présence de la cavité augmente considérablement l'efficacité du mélange.

Finalement, nous avons étudié les interactions chimie-turbulence et le mécanisme de stabilisation de la flamme sur la même configuration. Deux modèles de réacteur ont été examinés : `PSR` et `U-PaSR`, et les deux modèles fournissent des résultats similaires, confirmant la qualité du maillage retenu et le fait qu'il permet de restituer à l'échelle résolue les effets de micro-mélange. Deux modes de stabilisation de la combustion ont été retrouvés : le mode stabilisé par cavité (cas `RFSC-LST`) et le mode stabilisé par jet (cas `RFSC-HST`), ce qui concorde avec les résultats expérimentaux de Micka et Driscoll [32]. Des conditions de flammes prémélangées très turbulentes se produisent dans les deux cas.

Parmi les perspectives liées à cette étude, nous indiquons l'utilisation d'un maillage moins raffiné afin de mieux analyser et discriminer le comportement du modèle `U-PaSR`. Des simulations complémentaires pourraient aussi être conduites pour des valeurs intermédiaires de température de fonctionnement afin de comprendre comment peuvent se produisent les oscillations entre les deux modes de stabilisation de la combustion et la durée pendant laquelle chacune d'elles est active. Enfin, l'analyse des régimes de combustion confirmant la présence de flammes prémélangées très turbulentes, il peut être intéressant de travailler sur la représentation des interactions turbulence-chimie et de proposer des modèles encore mieux adaptés à ces conditions.

Références

[1] Adams, N. A. et Shariff, K. (1996). A high-resolution hybrid compact-ENO scheme for shock-turbulence interaction problems. *Journal of Computational Physics*, 127(1) :

27–51.

[2] Anderson, J. D. (1990). *Modern compressible flow : with historical perspective*, volume 12. McGraw-Hill New York.

[3] Atkinson, K. E. (2008). *An introduction to numerical analysis*. John Wiley & Sons.

[4] Ben-Yakar, A. et Hanson, R. K. (2001). Cavity flame-holders for ignition and flame stabilization in scramjets : an overview. *Journal of propulsion and power*, 17(4) : 869–877.

[5] Berglund, M., Fedina, E., Fureby, C., Tegnér, J. et Sabelnikov, V. (2010). Finite rate chemistry large-eddy simulation of self-ignition in supersonic combustion ramjet. *AIAA journal*, 48(3) :540–550.

[6] Bertin, J. J. et Cummings, R. M. (2003). Fifty years of hypersonics : where we've been, where we're going. *Progress in Aerospace Sciences*, 39(6-7) :511–536.

[7] Borghi, R. (1984). Sur la structure des flammes turbulentes. *Journal de chimie physique*, 81 :361–370.

[8] Borghi, R. (1985). On the structure and morphology of turbulent premixed flames. *In Recent advances in the Aerospace Sciences*, pages 117–138. Springer.

[9] Boukharfane, R. (2018). *Contribution à la simulation numérique d'écoulements turbulents compressibles canoniques*. Thèse de doctorat, ISAE-ENSMA Ecole Nationale Supérieure de Mécanique et d'Aérotechique-Poitiers.

[10] Brown, P. N., Byrne, G. D. et Hindmarsh, A. C. (1989). VODE : A variable-coefficient ODE solver. *SIAM journal on scientific and statistical computing*, 10(5) : 1038–1051.

[11] Buttay, R. (2015). *Etude de l'interaction choc/turbulence/combustion en écoulement cisaillé réactif : analyse des jets réactifs fortement sous-détendus*. Thèse de doctorat, ISAE-ENSMA Ecole Nationale Supérieure de Mécanique et d'Aérotechique-Poitiers.

[12] Celik, I., Cehreli, Z. et Yavuz, I. (2005). Index of resolution quality for large eddy simulations. *Journal of fluids engineering*, 127(5) :949–958.

[13] Chaudhuri, A., Hadjadj, A. et Chinnayya, A. (2011). On the use of immersed boundary methods for shock/obstacle interactions. *Journal of Computational Physics*, 230(5) :1731–1748.

[14] Erlebacher, G., Hussaini, M. Y., Speziale, C. G. et Zang, T. A. (1992). Toward the large-eddy simulation of compressible turbulent flows. *Journal of Fluid Mechanics*, 238 :155–185.

[15] Ern, A. et Giovangigli, V. (2004). Eglib : A general-purpose fortran library for multicomponent transport property evaluation. *Manual of EGlib version*, 3 :12.

[16] Falempin, F. et Serre, L. (2010). French flight test program LEA status. Rapport technique, MBDA Le Plessis Robinson (France).

[17] Favre, A. (1983). Turbulence : Space-time statistical properties and behavior in supersonic flows. *The Physics of fluids*, 26(10) :2851–2863.

[18] Fedkiw, R. P., Merriman, B. et Osher, S. (1996). *Numerical methods for a mixture of thermally perfect and/or calorically perfect gaseous species with chemical reactions*. Department of Mathematics, University of California, Los Angeles.

[19] Força Aérea Brasileira (2017). *Brasil quer testar nos próximos anos velocidade hipersônica em voo*. Available at : `https://www.fab.mil.br/noticias/mostra/29437/LAAD%202017%20%E2%80%93%20Brasil%20quer%20testar%20nos%20pr%C3%B3ximos%20anos%20velocidade%20hipers%C3%B4nica%20em%20voo`.

[20] Gottlieb, S. et Shu, C. (1998). Total variation diminishing Runge-Kutta schemes. *Mathematics of computation of the American Mathematical Society*, 67(221) :73–85.

[21] Heiser, W. H. et Pratt, D. T. (1994). *Hypersonic airbreathing propulsion*. AIAA.

[22] Huang, W., Qin, H., Luo, S.-B. et Wang, Z.-G. (2010). Research status of key techniques for shock-induced combustion ramjet (scramjet) engine. *Science in China Series E : Technological Sciences*, 53(1) :220–226.

[23] Iaccarino, G. et Verzicco, R. (2003). Immersed boundary technique for turbulent flow simulations. *Applied Mechanics Reviews*, 56(3) :331–347.

[24] Kee, R. J., Dixon-Lewis, G., Warnatz, J., Coltrin, M. E. et Miller, J. A. (1986). A fortran computer code package for the evaluation of gas-phase multicomponent transport properties. *Sandia National Laboratories Report SAND86-8246*, 13 :80401–1887.

[25] Lawson, S. et Barakos, G. (2011). Review of numerical simulations for high-speed, turbulent cavity flows. *Progress in Aerospace Sciences*, 47(3) :186–216.

[26] Leduc, R. (1935). French patent no. 439,805.

[27] Lorin, R. (1908). Le propulseur à échappement et l'aéroplane à grande vitesse. *L'Aérophile*, pages 332–336.

[28] Manna, P. et Chakraborty, D. (2005). Numerical investigation of transverse sonic injection in a non-reacting supersonic combustor. *Proceedings of the Institution of Mechanical Engineers, Part G : Journal of Aerospace Engineering*, 219(3) :205–215.

[29] Martínez-Ferrer, P. J. (2013). *Etude par simulation numérique de l'auto-allumage en écoulement turbulent cisaillé supersonique*. Thèse de doctorat, ISAE-ENSMA École Nationale Supérieure de Mécanique et d'Aérotechique - Poitiers.

[30] Martínez-Ferrer, P. J., Buttay, R., Lehnasch, G. et Mura, A. (2014). A detailed verification procedure for compressible reactive multicomponent Navier–Stokes solvers. *Computers & Fluids*, 89 :88–110.

[31] Martínez-Ferrer, P. J., Lehnasch, G. et Mura, A. (2017). Compressibility and heat release effects in high-speed reactive mixing layers II : Structure of the stabilization zone and modeling issues relevant to turbulent combustion in supersonic flows. *Combustion and Flame*, 180 :304–320.

[32] Micka, D. et Driscoll, J. (2008). Dual-mode combustion of a jet in cross-flow with cavity flameholder. *In 46th AIAA Aerospace Sciences Meeting and Exhibit*, page 1062.

[33] Micka, D. J. (2010). *Combustion stabilization, structure, and spreading in a laboratory dual-mode scramjet combustor*. Thèse de doctorat, University of Michigan.

[34] Micka, D. J. et Driscoll, J. F. (2009). Combustion characteristics of a dual-mode scramjet combustor with cavity flameholder. *Proceedings of the Combustion Institute*, 32(2) :2397–2404.

[35] Moule, Y. (2013). *Modélisation et Simulation de la Combustion dans les Écoulements Rapides : Applications aux Superstatoréacteurs*. Thèse de doctorat, ISAE-ENSMA Ecole Nationale Supérieure de Mécanique et d'Aérotechique-Poitiers.

[36] NASA (2008). *Langley Research Center : How scramjets work*. Available at : `https://www.nasa.gov/centers/langley/news/factsheets/X43A_2006_5.html`.

[37] NASA (2010). *X-51A makes longest scramjet flight*. Available at : `https://www.nasa.gov/topics/aeronautics/features/X-51A.html`.

[38] NASA (2016). *X-43A (Hyper-X)*. Available at : `https://www.nasa.gov/centers/armstrong/history/experimental_aircraft/X-43A.html`.

[39] Nicoud, F. et Ducros, F. (1999). Subgrid-scale stress modelling based on the square of the velocity gradient tensor. *Flow, Turbulence and Combustion*, 62(3) :183–200.

[40] O'Conaire, M., Curran, H. J., Simmie, J. M., Pitz, W. J. et Westbrook, C. K. (2004). A comprehensive modeling study of hydrogen oxidation. *International Journal of Chemical Kinetics*, 36(11) :603–622.

[41] Peskin, C. S. (1972). Flow patterns around heart valves : a numerical method. *Journal of Computational Physics*, 10(2) :252–271.

[42] Piomelli, U. et Chasnov, J. R. (1996). Large-eddy simulations : Theory and applications. *In Turbulence and Transition Modelling*, pages 269–336. Springer.

[43] Pope, S. B. (2004). Ten questions concerning the large-eddy simulation of turbulent flows. *New Journal of Physics*, 6(1). p. 35.

[44] Quinlan, J., McDaniel, J. C., Drozda, T. G., Lacaze, G. et Oefelein, J. C. (2014). A priori analysis of flamelet-based modeling for a dual-mode scramjet combustor. *In 50th AIAA/ASME/SAE/ASEE Joint Propulsion Conference*. AIAA Paper 2014–3743.

[45] Ragab, S., Sheen, S.-C. et Sreedhar, M. (1992). An investigation of finite-difference methods for large-eddy simulation of a mixing layer. *In 30th Aerospace Sciences Meeting and Exhibit*. AIAA Paper 1992–554.

[46] Reaction Engines (2018). *Synergetic Air-Breathing Rocket Engine*. Available at : `https://www.reactionengines.co.uk/sabre`.

[47] Shterev, K. et Stefanov, S. (2008). Finite volume calculations of gaseous slip flow past a confined square in a two-dimensional microchannel. *In Proceedings of the 1st European Conference on Microfluidics, La Societé Hydrotechnique de France*.

[48] Silva, A. L. E., Silveira-Neto, A. et Damasceno, J. (2003). Numerical simulation of two-dimensional flows over a circular cylinder using the immersed boundary method. *Journal of Computational Physics*, 189(2) :351–370.

[49] Smart, M. (2008). Scramjets. Rapport technique, RTO-EN-AVT-150-09.

[50] Sod, G. A. (1978). A survey of several finite difference methods for systems of nonlinear hyperbolic conservation laws. *Journal of Computational Physics*, 27(1) :1–31.

[51] Strikwerda, J. C. (2004). *Finite difference schemes and partial differential equations*, volume 88. Society for Industrial and Applied Mathematics.

[52] Stull, D. et Prophet, H. (1971). JANAF thermodynamic tables. *National Standard Reference Data Series, National Bureau of Standards, Washington, DC.*

[53] Techer, A. (2017). *Simulation aux grandes échelles implicite et explicite de la combustion supersonique.* Thèse de doctorat, ISAE-ENSMA Ecole Nationale Supérieure de Mécanique et d'Aérotechique-Poitiers.

[54] University of Queensland (2016). *Hypersonic flight on the horizon.* Available at : `https://www.eait.uq.edu.au/hypersonic-flight-horizon`.

[55] Van Wie, D. M. (2000). Scramjet inlets. *Scramjet propulsion*, 189 :447–511.

[56] Weber, R. J. et MacKay, J. S. (1958). An analysis of ramjet engines using supersonic combustion. Rapport technique, NACA TN 4386.

[57] Yoshizawa, A. (1986). Statistical theory for compressible turbulent shear flows, with the application to subgrid modeling. *Physics of Fluids*, 29 :2152–2164.

SIMULATION NUMÉRIQUE DE LA COMBUSTION TURBULENT DANS DES SITUATIONS GÉNÉRIQUES REPRÉSENTATIVES À LA PROPULSION D'UN SUPER-STATORÉACTEUR (SCRAMJET)

Résumé : Les super-statoréacteurs sont des systèmes de propulsion aérobie à grande vitesse qui ne nécessitent pas d'éléments rotatifs pour comprimer l'écoulement d'air. Celui-ci est comprimé dynamiquement par un système d'admission intégré dans le véhicule, atteignant la pression et la température requises pour que la combustion puisse s'opérer dans la chambre de combustion. La chambre de combustion est traversée par un écoulement supersonique dans ce type de moteur, ce qui limite considérablement le temps disponible pour injecter le carburant, le mélanger avec un oxydant, enflammer le mélange obtenu et parvenir à une combustion complète. Les cavités peuvent être utilisées pour augmenter le temps de séjour sans perte excessive de pression totale et sont donc utilisées comme éléments de stabilisation dans les chambres de combustion supersonique. Cette thèse se concentre sur l'étude du mécanisme de stabilisation et des interactions chimie-turbulence dans le cas d'une injection pariétale de combustible dans un écoulement supersonique d'air vicié en amont d'une cavité carrée. Les conditions d'écoulement réactif à grande vitesse correspondantes sont examinées sur la base de simulations numériques d'un modèle de scramjet représentatif d'expériences effectuées précédemment à l'Université du Michigan. Les calculs sont effectués avec le solveur `CREAMS`, développé pour effectuer la simulation numérique d'écoulements multi-espèces réactifs compressibles sur des architectures massivement parallèles. Le solveur utilise des schémas numériques d'ordre élevé appliqués sur des maillages structurées et la géométrie de la chambre de combustion est modélisée à l'aide d'une méthode de frontières immergées (`IBM`). Les simulations `LES` font usage du modèle *wall-adapting local eddy* (`WALE`). Deux températures distinctes sont considérées dans l'écoulement entrant d'air vicié pour étudier la stabilisation de la combustion. Une attention particulière est accordée à l'analyse de la topologie et de la structure des écoulements réactifs, les régimes de combustion sont analysés sur la base de diagrammes standards de combustion turbulente.
Mots clés : Turbulence / Chambres de combustion / Statoréacteurs à combustion supersonique / Méthodes des frontières immergées / Simulation des grandes échelles / Jets pariétaux / Compressibilité / Hydrogène (combustible) / Mélange / Cavité / Stabilisation de la combustion

NUMERICAL SIMULATION OF TURBULENT COMBUSTION IN SITUATIONS RELEVANT TO SCRAMJET ENGINE PROPULSION

Abstract: Scramjet engines are high-speed airbreathing propulsion systems that do not require rotating elements to compress the air inlet stream. The flow is compressed dynamically through a supersonic intake system integrated in the aircraft's forebody, reaching the required pressure and temperature for combustion to proceed within the combustor in this kind of engine. The combustion chamber is crossed by a supersonic flow, which limits severely the time available to inject fuel, mix it with oxidizer, ignite the resulting mixture and reach complete combustion. Cavities can be used to increase the residence time without excessive total pressure loss and are therefore used as flameholders in supersonic combustors. This thesis focuses in studying the flame stabilization mechanism and turbulence-chemistry interactions for a jet in a supersonic crossflow (`JISCF`) of vitiated air with hydrogen injection upstream of a wall-mounted squared cavity. The corresponding reactive high-speed flow conditions are scrutinized on the basis of numerical simulations of a scramjet model representative of experiments previously conducted at the University of Michigan. The computations are performed with the high-performance computational solver `CREAMS`, developed to perform the numerical simulation of compressible reactive multi-component flows on massively-parallel architectures. The solver makes use of high-order precision numerical schemes applied on structured meshes and the combustion chamber geometry is modeled by using the Immersed Boundary Method (`IBM`) algorithm. The present set of computations is conducted within the `LES` framework and the subgrid viscosity is treated with the wall-adapting local eddy (`WALE`) model. Two distinct temperatures are considered in the inlet vitiated airstream to study combustion stabilization. Special emphasis is placed on the analysis of the reactive flow topology and structure, and the combustion regimes are analyzed on the basis of standard turbulent combustion diagrams.
Keywords: Turbulence / Combustion chambers / Scramjet / Immersed boundary method / Large-eddy simulation / Wall jets / Compressibility / Hydrogen as fuel / Mixing / Cavity / Combustion stabilization